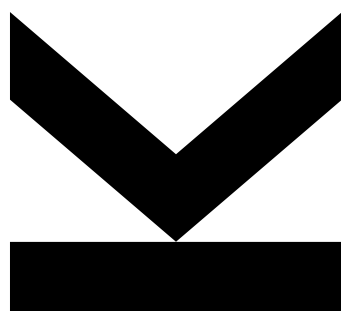Author
DI Dominik Wielend

Submission at
**Linz Institute for Organic
Solar Cells (LIOS) / Institute
of Physical Chemistry**

Supervisor and first evaluator
**Univ. Prof. Dr. Niyazi Serdar
Sariciftci**

Second evaluator
**Priv. Doz.[in] Dr.[in] Yolanda
Salinas**

December 2021

Electrochemical H_2O_2 production using immobilized organic catalysts

Doctoral Thesis

to confer the academic degree of

Doktor der technischen Wissenschaften

in the Doctoral Program

Technische Wissenschaften

SWORN DECLARATION

I hereby declare under oath that the submitted Doctoral Thesis has been written solely by me without any third-party assistance, information other than provided sources or aids have not been used and those used have been fully documented. Sources for literal, paraphrased and cited quotes have been accurately credited.

The submitted document here present is identical to the electronically submitted text document.

Linz, 21.12.2021

Place, Date

Dominik Wielend

Signature

Abstract

As the technological progress and the increased worldwide population demands a steadily increasing energy supply, alternatives to the current main energy source – fossil fuels – are required. Solar energy, wind energy and hydropower are promising candidates for electricity generation. In order to store energy over a long period of time or transport it over long distances, conversion into fuels like hydrogen (H_2), methane (CH_4) or methanol (CH_3OH) are considered as potential solutions. Aside from proton and carbon dioxide (CO_2) reduction also oxygen (O_2) reduction forming hydrogen peroxide (H_2O_2) yields an energy-rich product. In addition to the purely energy related aspect, H_2O_2 is a widely used and important industrial chemical.

This thesis aims at synthesizing and investigating new *immobilized* electrocatalysts for the oxygen reduction reaction (ORR), that are purely organic and metal free. To start with, metal and carbon electrodes were characterized by using cyclic voltammetry (CV) and rotating ring disc electrode (RRDE) techniques. Thereby, bare glassy carbon (GC) was identified as a quite efficient electrode material for the electrochemical O_2 to H_2O_2 reduction. As a result of this aspect, when studying homogenous solutions of anthraquinone for the electrochemical oxygen reduction reaction with conventional GC-platinum RRDE the problem of overlapping redox features occurred. Therefore, a mathematical subtraction method was developed in order to visualize the electrocatalytic effect of homogeneous catalysts using RRDE techniques with a well-known anthraquinone. In order to *immobilize* anthraquinones on electrodes, three poly(anthraquinones) reported in literature were synthesized and investigated. The chemical structure and especially the hydrophilicity of the polymer films appeared to be crucial for the electrochemical responses and electrocatalytic behavior.

An anthraquinone-derivative of a mechanically interlocked carbon nanotube (MINT) recently synthesized and developed by the group of Emilio Pérez was electrochemically investigated. The superior stability and electrocatalytic behavior resulting from combining the best of covalent and non-covalent immobilization techniques demonstrated the benefits of this approach. In addition to anthraquinone-based electrocatalysts, conductive polymers such as polyaniline (PANI) and polypyrrole (PPy) were investigated for their electrochemical O_2 to H_2O_2 performance. Studies involving electrolysis and rotating disc electrode techniques revealed that PANI acts as a peroxide-directing layer enhancing the bare GC electrocatalytic effect. PPy was identified as a real electrocatalyst with a strong selectivity for H_2O_2 production with up to 96% faradaic efficiency.

Kurzfassung

Der, bedingt durch den technologischen Fortschritt und die wachsende Weltbevölkerung steigende Weltenergiebedarf erfordert alternative Energiequellen zu den derzeit überwiegend genutzten fossilen Brennstoffen. Als vielversprechende, erneuerbare Energiequellen zur Stromerzeugung haben sich Solarenergie, Windenergie und Wasserkraft hervorgetan. Um jedoch den erzeugten Strom über weite Distanzen transportieren oder über lange Zeiträume speichern zu können, bedarf es Lösungsansätzen wie der Umwandlung – in chemisch gebundener Form – in Wasserstoff (H_2), Methan (CH_4) oder Methanol (CH_3OH). Neben diesen Ansätzen der Protonen- oder Kohlenstoffdioxid- (CO_2) Reduktion führt auch die Sauerstoff- (O_2) Reduktion zu Wasserstoffperoxid (H_2O_2) zu einem Produkt hoher Energiedichte. Zusätzlich zur rein energetischen Verwendungsmöglichkeit von H_2O_2 ist Wasserstoffperoxid eine für viele technische Anwendungsbereiche bedeutsame Grundchemikalie.

Ziele der vorliegenden Arbeit sind sowohl die Synthese als auch die Untersuchung neuartiger, vollständig organischer und metallfreier immobilisierter Elektrokatalysatoren für die Sauerstoffreduktion (ORR). Zu Beginn wurden verschiedene metallische und kohlenstoffbasierte Elektroden mittels zyklischer Voltammetrie (CV) und der rotierenden Ring-Scheiben-Elektroden (RRDE) Technik untersucht. Dabei wurde reiner Glaskohlenstoff (GC) als relativ effizientes Elektrodenmaterial für die Sauerstoffreduktion zu Wasserstoffperoxid identifiziert. Daraus resultierend zeigt sich bei der Untersuchung homogener Anthrachinon-Lösungen für die elektrochemische Sauerstoffreduktionsreaktion mit einer konventionellen Glaskohlenstoff-Platin Ringscheibenelektrode das Problem der überlappenden Redoxsignale von Glaskohlenstoff und dem Anthrachinon. Um trotzdem die inhärenten elektrokatalytischen Eigenschaften von homogenen Katalysatoren unter Verwendung der RRDE Technik für ein bekanntes Anthrachinon visualisieren zu können, wurde eine mathematische Subtraktionsmethode entwickelt und vorgestellt. Um Anthrachinone auf Elektroden zu immobilisieren, wurden drei aus der Literatur bekannten Poly(Anthrachinone) selbst synthetisiert und charakterisiert. Kernaussage aus dieser vorliegenden Untersuchung war, dass die chemische Struktur und vor allem die Hydrophobizität der Polymere einen essentiellen Einfluss auf die elektrochemische wie auch auf die elektrokatalytische Aktivität haben.

Ein mechanisch-blockiertes Kohlenstoffnanoröhrchen (MINT) auf Basis eines Anthrachinon-Derivats, welches kürzlich durch die Gruppe von Emilio Pérez synthetisiert und entwickelt wurde, war ebenfalls Gegenstand elektrochemischer Untersuchungen. Die hervorragende Stabilität als auch das exzellente elektrokatalytische Verhalten zeigten, dass dieser MINT Ansatz das Beste aus den zwei Welten der kovalenten als auch der nicht-kovalenten Modifikationen vereint. Zusätzlich zu anthrachinon-basierten Elektrokatalysatoren wurden auch leitfähige Polymere wie Polyanilin (PANI) und Polypyrrol (PPy) bezüglich der Sauerstoff zu Wasserstoffperoxid Reduktionen untersucht. Mittels Elektrolysen und Ringscheiben-Experimenten wurde Polyanilin als wasserstoffperoxid-dirigierendes Material identifiziert, welches den elektrokatalytischen Effekt von reinem Glaskohlenstoff nur verstärkt. Polypyrrol hingegen agiert als echter Elektrokatalysator mit extrem hoher Wasserstoffperoxid-Selektivität mit einer Stromeffizienz von knapp 96%.

Acknowledgements

I would like to start by thanking my supervisor Prof. Niyazi Serdar Sariciftci for all his great support and trust in me throughout the last years: Already more than a decade ago, he began inspiring and motivating me for the field of physical chemistry sciences. Without his encouragement and belief in me, I would not have had this great journey in science and not have been able to conduct this thesis.

A big "thank you" goes to Dogukan Hazar Apaydin, Hathaichanok Seelajaroen, Prof. Dong Ryeol Whang, Prof. Markus Clark Scharber and Helmut Neugebauer for their great support from the first days of my PhD time on, helping me find the right scientific questions with special respect to electrochemistry – and teaching me the right way how correctly answers them.

One major awareness I gained throughout this time is that teaching is always a both-way process. Therefore, I am grateful for having the opportunity to guide and work with great students, namely Hannah Rabl, Corina Schimanofsky, Elisabeth Leeb, Angelina Kerschbaumer and Nadine Kleinbruckner.

This study would not have been possible without the support and scientific interaction with numerous in-house, Austrian as well as international collaborators. I am very thankful for the great collaboration with and support from Priv. Doz.^{in} Yolanda Salinas, Prof. Oliver Brüggemann, Maria Würflinger and Paul Strasser from the institute of polymer chemistry (ICP), Prof. Christian Paulik and Felix Leibetseder from the institute for chemical technology of organic materials (CTO) and Matthias Bechmann from the institute of organic chemistry. The interesting discussions and great exchange with Mariano Vera-Hidalgo and Prof. Emilio Pérez from IMDEA in Madrid gave me great insight into the fascinating class of supramolecular interlocked materials. I am very grateful for the multifaceted scientific exchange going even going beyond the topics of this thesis I had with Engelbert Portenkirchner, Daniel Werner, Prof. Thomas Hofer, Daniel Winkler and Prof.^{in} Julia Kunze-Liebhäuser from the University of Innsbruck.

My great thanks also goes to all further members of the "LIOS family" for their continuous support, friendship and the good times we had together. My period at LIOS would not have been the same without: Birgit Paulik, Isolde Wandling and Sara Gusner from the administrative office, Gerda Kalab, Gabriele Hinterberger, Patrick John-Denk and Munise Cobet from the chemical and technical support, Cigdem Yumusak, Nikolas Heitzmann, Liviu Dumitru, Bekele Hailegnaw Teklemariam, Katarina Gugujonovic, Felix Mayr, Jakob Hofinger, Christoph Putz, Wittawat Keawsongsaeng, Jirapong Luangchaiyaporn, Mateusz Bednorz, Serpil Tekoglu, Mihai Irimia-Vladu, Halime Coskun-Aljabour, Abdalaziz Aljabour, Christoph Ulbricht, He Sun, Zoja Lakovic, Fatih Ongül, Prof. Jozef Krajcovic, Anna Prochazkova, Lucia Ivanova, Matous Kratochvil, Alexander Kovalenko, Stefan Pöllner, Melissa Hassel, Ana Cetkovic, Bernhard von Raußendorf, Prof.^{in} Manuela Schiek, Otgonbayar Erdene-Ochir, Katharina Matura, Konstantin Siegel, Lisa Berger, Dominik Böhm, Julia Bicvic, Alexander Planer and Rene Zahrhuber.

Although a PhD is the last but also the lasting part of the university education, undergraduate studies pave the way for the future tasks. Due to that, I want to especially thank all my study colleagues for their help and the great time, in scientific as well as non-scientific terms.

Finally I want to deeply thank my partner, family and friends for all their wonderful support during my whole life. Thank you for your belief in me and your encouragement and understanding all the time!
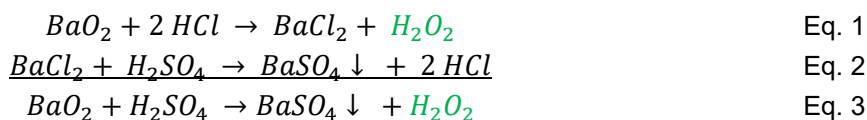
Table of Contents

1. Introduction

Hydrogen peroxide (H_2O_2) is a well-known and highly important base chemical having numerous and versatile application fields. Although H_2O_2 is just simply composed, on a molecular view, from hydrogen and oxygen atoms, it had great contributions in various historic milestones, which will be surveyed within this chapter.
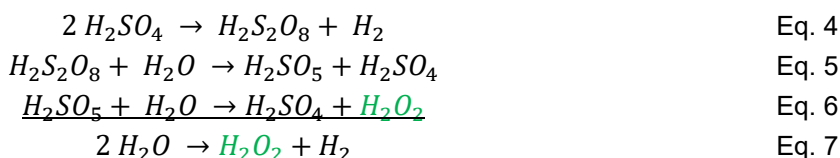
Throughout the last centuries, optimized production processes were developed for a mega-ton scale industry with ongoing market growth. Nevertheless, as the current *state-of-the-art* process, the anthraquinone autooxidation (AO) process has several drawbacks upon ecological consideration, intensive research on alternative production pathways is currently in progress. After a brief summary on the current industrial processes, alternative methods from literature are discussed within this introduction followed by an outlook for future studies.

1.1. Hydrogen peroxide – Historic production

Although the historic description of hydrogen peroxide is rather young in comparison to other inorganic compounds, it is worth mentioning as nearly from the beginning in the 19th century it was always closely related to electrochemical processes. In 1818, Thenard reported the wet chemical synthesis of H_2O_2 for the first time using barium peroxide (BaO_2) and nitric acid (HNO_3) and later on hydrochloric acid (HCl).[1–3] The reaction equations for this process are the following:

$$BaO_2 + 2\,HCl \;\rightarrow\; BaCl_2 + H_2O_2 \qquad\qquad \text{Eq. 1}$$
$$\underline{BaCl_2 + H_2SO_4 \;\rightarrow\; BaSO_4\downarrow\; + \;2\,HCl} \qquad\qquad \text{Eq. 2}$$
$$BaO_2 + H_2SO_4 \;\rightarrow BaSO_4\downarrow\; + H_2O_2 \qquad\qquad \text{Eq. 3}$$

Already in 1880, the first industrial plant for commercial H_2O_2 production using this technology was established which was in operation until around 1950.[1] In 1853 Meidinger experienced for the first time the electrochemical production of H_2O_2 using metal electrodes in sulfuric acid (H_2SO_4) solutions.[1,3,4] With the elucidation of the mechanism by Berthelot in 1878 identifying peroxydisulfuric acid as intermediate, the first industrial plant based on this technology was built in 1908 in Weissenstein in Austria.[1]

$$2\,H_2SO_4 \;\rightarrow\; H_2S_2O_8 + H_2 \qquad\qquad \text{Eq. 4}$$
$$H_2S_2O_8 + H_2O \;\rightarrow H_2SO_5 + H_2SO_4 \qquad\qquad \text{Eq. 5}$$
$$\underline{H_2SO_5 + H_2O \;\rightarrow H_2SO_4 + H_2O_2} \qquad\qquad \text{Eq. 6}$$
$$2\,H_2O \;\rightarrow H_2O_2 + H_2 \qquad\qquad \text{Eq. 7}$$

During the first electrolysis step (Eq. 4), the peroxydisulfuric acid is produced, which then gets further hydrolyzed forming H_2O_2.[1] The overall reaction equation (Eq. 7) shows that during this process H_2O_2 and H_2 are formed as products.

In 1939, Berl discovered the selective electrochemical reduction of oxygen (O_2) to H_2O_2 using carbon-based graphite electrodes, which up to now was not implemented in a large-scale production process.[5]

A highly important work was done by Manchot upon his report in 1901 where some organic molecules like quinones and azobenzenes in their reduced state were identified of being capable of selective H_2O_2 production, as depicted in the following Figure 1:[1,3,6]
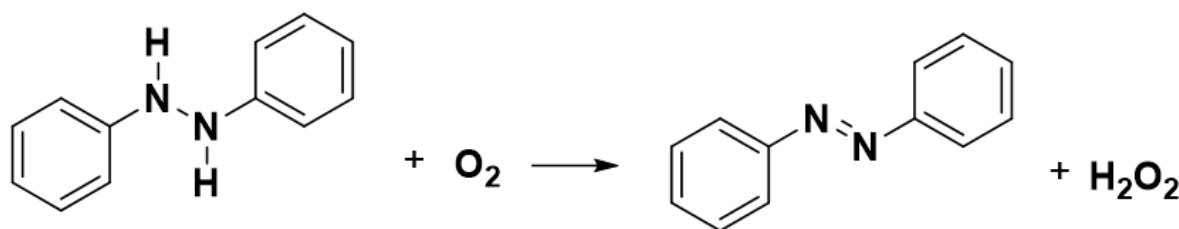

Figure 1: Schematic illustration of the oxygen reduction of a hydrazobenzene yielding H_2O_2 and the oxidized azobenzene.

Based on this fundamental work, in the 1920s Pfleiderer at IG Farbenindustrie/BASF (Germany) developed a cyclic, industrial process based on azobenzene working with amalgam electrodes in highly alkaline solutions, which was used under license in Finland by Kymmene AB.[1] In 1939, Riedel and Pfleiderer at IG Farbenindustrie (Germany) developed an improved process circumventing the use of amalgam and highly alkaline solutions.[1–3,7] During this so-called Riedel-Pfleiderer-Process instead of azobenzene alkylated anthraquinones (AQs) were used in solvent mixtures, which is why this process is also often referred to as anthraquinone autoxidation process (AO), as depicted in the following Figure 2:[1–3,7]
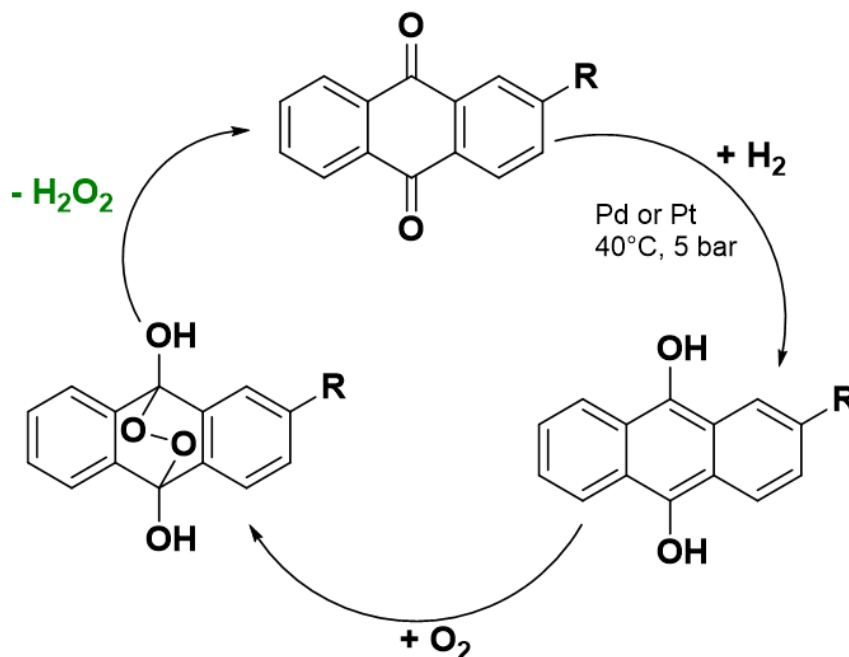
Figure 2: Reaction scheme of the Riedel-Pfleiderer or anthraquinone autoxidation process (AO) producing H_2O_2 via hydrogenation and consecutive oxidation of alkylated anthraquinones in homogeneous solution. The side group R stands for an alkyl group for improved solubility. Scheme adapted from Wielend (2017).[8]

As illustrated in Figure 2, this first reaction of this process involves the hydrogenation at slightly elevated temperatures using pressures of around 4-5 bar over a noble metal catalyst bed. The resulting hydroquinone molecules undergo oxidation with O_2 which finally leads to the release of H_2O_2 and the initial AQ molecule. Besides the use of noble metal catalyst beds for the hydrogenation, the use of special solvents which have to be tuned for the quinone and

hydroquinone species is a major drawback of this process. In addition, the separation of H_2O_2 from the solvents is also challenging and quite energy demanding.[1–3,7]

After World War II, the pilot plants based on this AO process were closed by the Allies and in 1953 the first Riedel-Pfleiderer process plant was built in US by DuPont.[1] Throughout the following centuries, this AO process became the market dominating one until today. A rough sketch of such an AO process plant illustrating the single steps is shown in Figure 3:
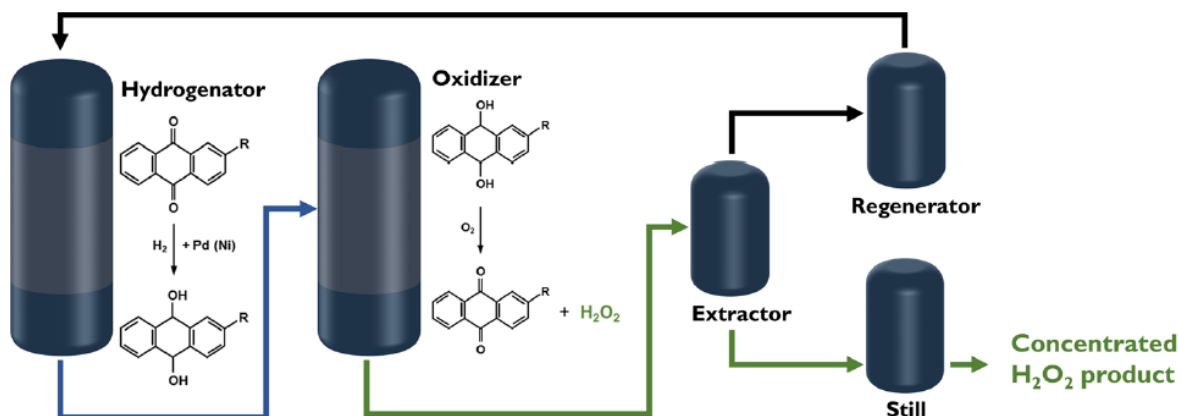
Figure 3: Scheme of an AO process industrial plant depicting all relevant steps. Reproduced with permission from Yang *et al.* (https://pubs.acs.org/doi/10.1021/acscatal.8b00217)[9] © 2018 American Chemical Society.

Besides the actual chemical reaction forming H_2O_2 in Figure 3, also the consecutive steps including H_2O_2 extraction followed by concentration as well as the solvent regeneration is shown.

Although it has several drawbacks like the large solvent quantities, stability issue of the AQs used and the use of noble metals, it still remains the most economic process.[1–3,7]
Nevertheless intensive research focusses on finding alternatives to this AO process where either the direct and selective reaction of hydrogen gas (H_2) and O_2 or electrochemical methods are promising candidates.[2,3,7,9]

1.2. Hydrogen peroxide – Historic applications

Since the first industrial plants producing H_2O_2 in 1880 with a world annual production of around 2000 t a^{-1}, the demand as well as the production quantities increased drastically.[1] The following Table 1 depicts some world annual production amounts of H_2O_2:

Table 1: World annual production of H_2O_2 based on pure (100%) H_2O_2.[1–3]

Year	World production / Mt a^{-1}
1990	1.5
2006	2.2
2015	5.5

In comparison to the 2000 tons per year in 1880, already in 1990 this amount was increased by nearly a factor of 10. Furthermore, even from 1990 until 2015 the world annual production increased by nearly a factor of 4 and is predicted to further increase during the next decades.[2,3]

Shortly after the discovery and isolation of H_2O_2 in the end of the 19th century, its applicability in synthesizing organic peroxy compounds was investigated.[10] As an example, the synthesis of organic aromatic peroxycarboxylic acids is depicted in Figure 4:
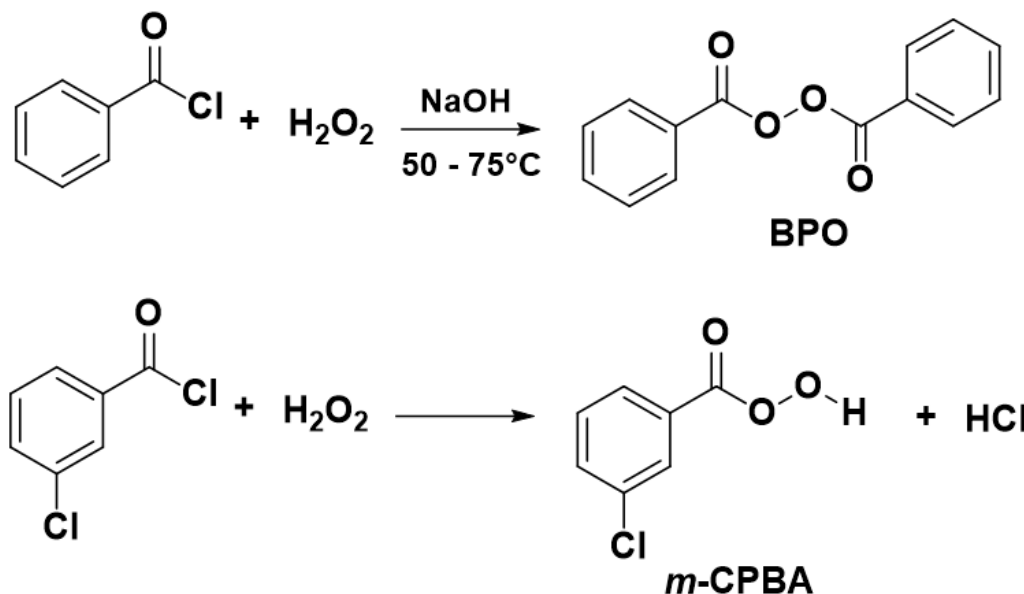
Figure 4: Reaction schemes for the synthesis of organic peroxycarboxylic acids. Synthesis of dibenzoylperoxide (BP) in the upper scheme and synthesis of meta-chloro perbenzoic acid (*m*-CPBA) in the lower scheme.

Following the reactions schemes in Figure 4, peroxycarboxylic acids can be synthesized from carboxylic acid chlorides and H_2O_2. Besides the bleaching behavior of dibenzoyl peroxide (BPO) and meta-chloro perbenzoic acid (*m*-CPBA) during the 20th century the demand of such peroxycarboxylic acids steadily increased due to the application in epoxidation reactions and the use as initiator for radical polymerizations.[10]

One major driving force for the increasing demand of H_2O_2 during the first decades of the 20th century was its possible military use. In the 1930s, the German Hellmuth Walter discovered that concentrated H_2O_2 with around 80% is a potent monopropellant when decomposed over silver catalyst beds or with initiators like potassium permanganate.[11–13]

$$2\,H_2O_{2(l)} \rightarrow O_{2(g)} + 2\,H_2O_{(g)}$$ Eq. 8
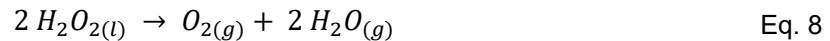
Equation 8 illustrates this strongly exothermic decomposition reaction of H_2O_2. Together with the non-toxicity and high specific heat these were the main reasons for H_2O_2 as first monopropellant used in submarines, torpedos and launching vehicles.[11–13] Later on, H_2O_2 was used as oxidizing agent in bipropellants together with fuels like hydrazine (N_2H_4):[11]

$$N_2H_{4(l)} + 2\,H_2O_{2(l)} \rightarrow N_{2(g)} + 4\,H_2O_{(g)}$$ Eq. 9
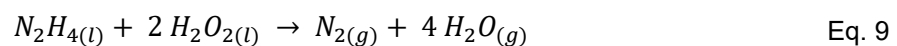
Maybe the most famous military application of H_2O_2 based launching technology was the Black Arrow and Black Knight program of the UK in the 1950s.[11,12] After that time, the use of H_2O_2 as propellant was steadily decreasing and replaced by more powerful compounds like nitrous tetroxide (N_2O_4) and liquid oxygen.[11,12]

Nowadays, the largest industrial application of H_2O_2 is the whole process from wood pulping towards final paper products including bleaching.[2,3,7,14] During the actual wood pulping process, in some technologies already H_2O_2 is used as chemical additive.[14] Within bleaching of paper fibers and also textile fibers, H_2O_2 plays an important global role, especially concerning non-chlorinated bleaching technologies.[2,14] Regarding the largest commercial H_2O_2 production process, the anthraquinone autooxidation process described in chapter 1.1. an interesting fact has to be mentioned. Starting from the 1960s, the addition of anthraquinone during wood pulping processes was discovered to enhance the pulping process by decreasing the carbohydrate degradation while decreasing the required process time and temperature.[14]

Already from the early starting of the industrial H_2O_2 investigation, its potential for cleaning and bleaching purposes was known.[1] Based on the high oxidation power of H_2O_2 throughout the last decades several cleaning and disinfection applications of H_2O_2 were developed.[1,7] Besides classical waste water treatment via inorganic pollutant removal, like hydrogen sulfide (H_2S) and nitrates (NO_3^-) also organic and biological contaminations like phenols, antibiotics, bacteria or viruses can be deactivated in an environmental friendly way.[1–3,7,15] As these disinfecting applications are feasible with rather low H_2O_2 concentrations, especially here the electrochemical H_2O_2 production appears to be a promising alternative for the established AO process.[3,16,17] Known under the term *Fenton process*, this oxidizing power of H_2O_2 can be further boosted by a catalyzed homolytical splitting of H_2O_2 into two hydroxyl radicals:[2,15,16]

$$H_2O_2 \rightarrow 2 \cdot OH$$ Eq. 10

This *Fenton process* can be either induced by UV light or directly coupled to an electrochemical oxygen reduction process followed by iron cation induced hydroxyl radical formation, which are among the most powerful oxidants available.[2,16]

Another cleaning-related application market of H_2O_2 is within the semiconductor industry. Highly pure grade H_2O_2 is used together with sulfuric acid for etching and cleaning printed silicon circuit boards from organic layers.[1–3,7]

As a result of its high energy density and the highly exergonic decomposition reaction depicted in Eq. 8, extensive research is conducted for developing H_2O_2 fuel cells for energy storage and controlled release applications.[3,7,16,18–20] One possible fuel cell geometry is a two-compartment cell using H_2O_2 as liquid and high energy density oxidant, which is beneficial for applications without air supply together with a fuel like for example ethanol, hydrazine, formic acid or borohydrides.[18] Due to the aforementioned unique decomposition property of H_2O_2 depicted in Eq. 8, which historically enabled the first use as propellant, exactly this energy can also be released in a one-compartment fuel cell as illustrated schematically in Figure 5:
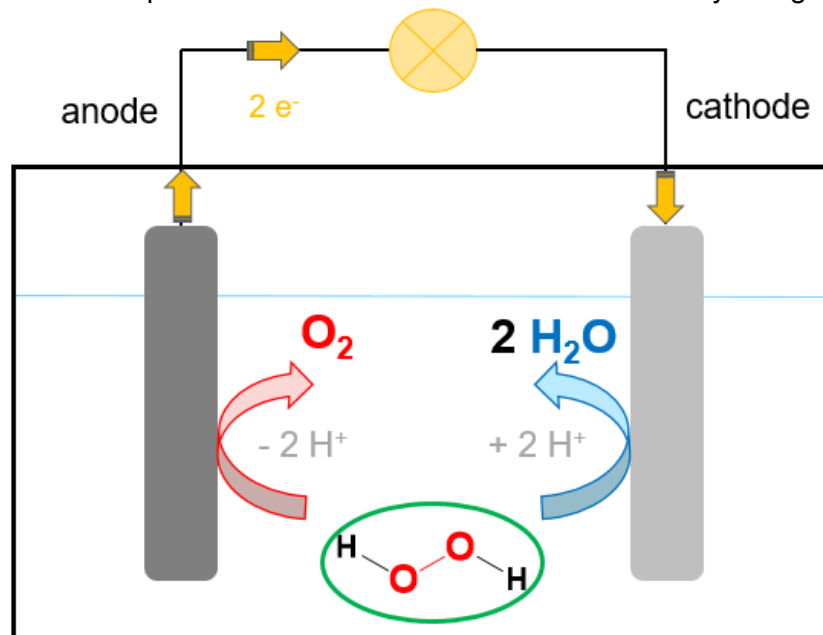

Figure 5: Schematic illustration of the working principle of a H_2O_2 one-compartment cell.

Thereby, H_2O_2 gets oxidized at the anode forming oxygen and simultaneously H_2O_2 gets reduced at the cathode forming water with the overall reaction described by Eq. 8.[7,18–21] Although from a thermodynamic point of view, a theoretical potential of 1.09 V according to Eq. 8 could be reached in real applications, such one-compartment fuel cells usually showed a significantly lower voltage of below 0.7 V and low maximum power densities of around 1 mW cm^{-2}.[18,19] Therefore it has to be kept in mind that in order to operate the reaction according to Figure 5, the only directing participants are the anode and the cathode material. Here, only their tendency towards to reductive or oxidative decomposition reaction of H_2O_2 dictates the performance of such a fuel cell.[18,19] In addition, besides the desired reduction and oxidation reaction the chemical decomposition of H_2O_2 at an electrode might occur without charge generation, which also suppresses the overall performance.[19,21] Nevertheless, Disselkamp suggested a closed-cycle process design for energy storage.[22,23]

Although the use of two-compartment cells with different pH values allows improvement with H_2O_2 only fuel cells with up to nearly 1 V voltage and a maximum power density of around 60 mW cm^{-2}, there is still the requirement of intensive research on efficient electrocatalysts and cell geometries in order to achieve a large-scale application.[18,19,24]

Another merging technology also based on the H_2O_2 decomposition reaction (Eq. 8) are micromotors, [25] as depicted in Figure 6:[26]
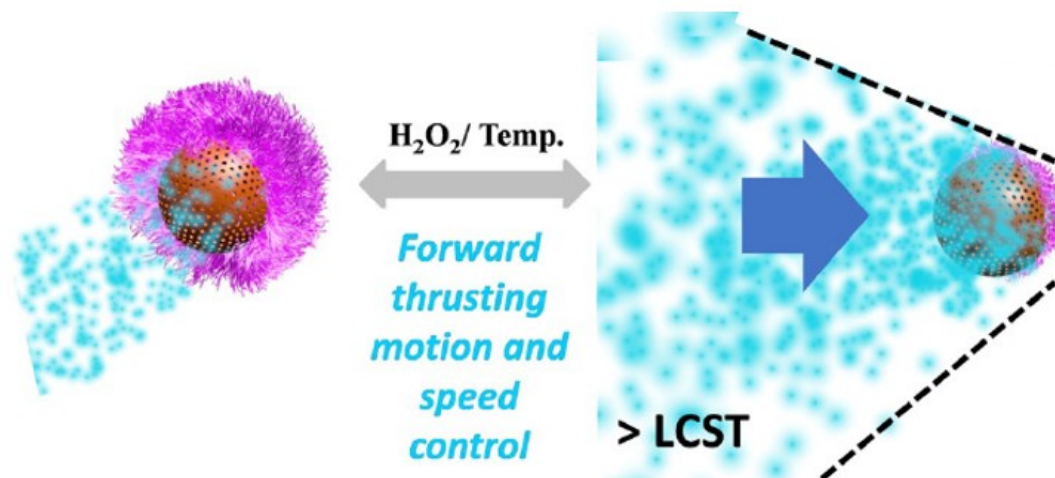

Figure 6: Schematic illustration of a half-grafted (Janus type) micromotor, which undergoes a directed movement via H_2O_2 decomposition above a certain temperature required (Lower critical solution temperature – LCST). Reproduced from Fiedler *et al.*[26] © 2020 the authors.

Micromotors are particles on a micro meter scale that undergo a certain movement due to the H_2O_2 decomposition on metal catalysts[27,28] via temperature[26,29] or light stimuli[30], as recently investigated for medical[31] or environmental application[32,33].

Speaking about numerous application fields of H_2O_2, the question arises where nowadays the majority of H_2O_2 is used. The majority of the global H_2O_2 produced is used for paper and pulp production as well as synthesis of inorganic and organic compounds.[3,7,34] Applications of H_2O_2 for environmental use like wastewater treatment consume around 10% of the global production. Within the remaining 15%, all other scientific and industrial applications mentioned throughout this chapter are considered with textile bleaching, electronic industry, mining and energy storage being some worth mentioning among all others.[3,7,34]

The electrochemical oxygen reduction forming H_2O_2 (as illustrated in the upcoming Figure 7), by also consuming two protons (H^+) is the target reaction throughout this work. Another reaction, which is as atom-economic as the aforementioned one, is the direct synthesis of H_2O_2 from H_2 and O_2 gas over catalyst support beds. As this topic is far beyond the scope of this work, interested readers are referred to specialized literature reports.[35–37]

1.3. Electrochemical hydrogen peroxide production

In addition to the simple atomistic considerations for H_2O_2 production regarding the chemical elements, for the electrochemical H_2O_2 production the following reaction pathways and electrochemical potentials are necessary as depicted in Figure 7:

$$O_2$$
$$(1) \quad +2\ e^- \quad +2\ H^+ \qquad E^0_{(1)} = +0.68\ V$$
$$+4\ e^- \quad +4\ H^+ \quad (3) \quad H_2O_2 \qquad E^0_{(2)} = +1.76\ V$$
$$(2) \quad +2\ e^- \quad +2\ H^+ \qquad E^0_{(3)} = +1.23\ V$$
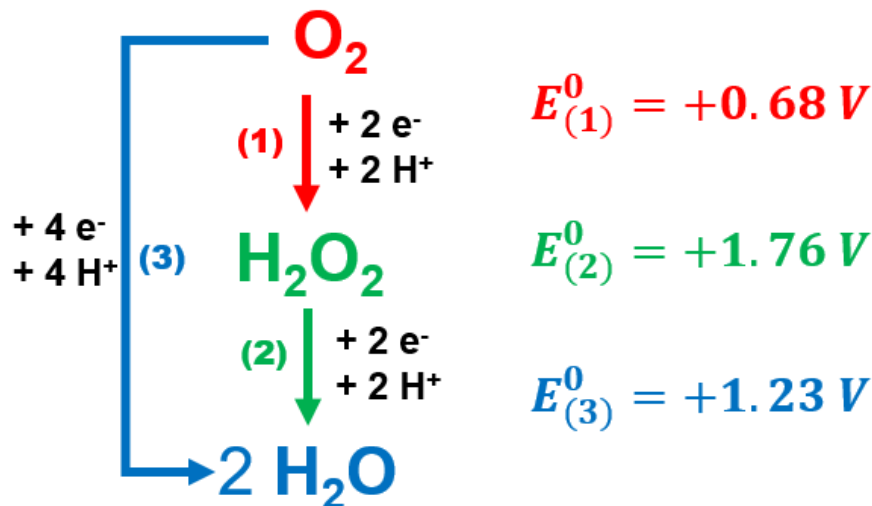$$2\ H_2O$$

Figure 7: Scheme of the oxygen reduction pathways including the according electrochemical potentials versus SHE at standard conditions. Potential values reproduced from literature.[19,38,39]

According to this simplified mechanistic scheme shown involving O_2, H_2O_2 and water (H_2O), those three compounds are in equilibrium during electrochemical treatment. For simplicity reasons, no intermediate species and one-electron reduction products are shown, which will be further discussed in chapter 1.3.1. Depending on the potential applied, either O_2 can be reduced to H_2O_2 (pathway 1) or water oxidized to H_2O_2 (2). In real application, usually the complicated case of further reduction to water or further oxidation to O_2 might occur, or also the direct 4-electron pathway 3.

As the goal of this work is the reduction of O_2 to H_2O_2, the upcoming chapters mostly focus on the possible pathways and mechanisms regarding the reduction reactions. Nevertheless, in chapter 1.3.2. briefly some highlights and challenges of water to H_2O_2 oxidation are summarized.

1.3.1. Electrochemical oxygen reduction reactions

Throughout the last decades, electrochemical reactions like the hydrogen evolution reaction (HER), carbon dioxide reduction reaction (CO_2RR), oxygen evolution reaction (OER) and also the oxygen reduction reaction (ORR) have gained an enormous boost in interest from scientists but also among industry and politics.[40–44] The following graph illustrates the development of the number of papers published referenced by the keywords "oxygen reduction reaction":
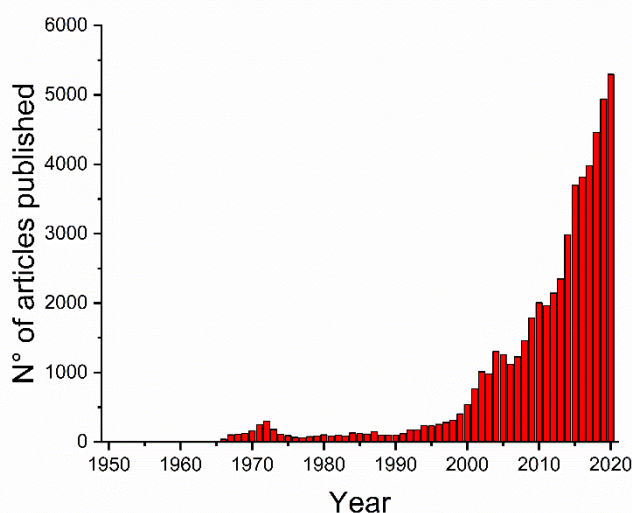

Figure 8: Increasing trend in the number of articles published containing the keyword "oxygen reduction reaction". Source: www.scopus.com[45]

The trend in ORR publications depicted in Figure 8 shows that, with the exception of a local maximum in 1972, the number of publications increased nearly exponentially after 1990, reaching more than 5000 in the year 2020. In contrast to this data, Siahrostami *et al.* identified that only nearly 1% of these publications of ORR in general deal with the 2-electron reduction process forming H_2O_2.[46]

A unique and complicating feature of the ORR is, that one actually has to differentiate between (at least) two cases in aqueous solution regarding the main target product. As illustrated in Figure 7, either H_2O_2 is the product via a 2-electron reduction reaction or water is produced by a full 4-electron reduction reaction. Throughout this work, the 2-electron reduction forming H_2O_2 is the target reaction, but here in brief also the mechanistic basis of the 4-electron reduction is explained, which is highly relevant in oxygen fuel cell applications.[16,46–49] Based on literature reports on ORR on metal surfaces, the molecular steps leading to H_2O_2 and H_2O as product are summarized.[34,38,46,50–54] In the following Figure 9 the steps for the 2-electron pathway forming H_2O_2 are illustrated:

I. $O_2 + *$ $\longrightarrow$ OO^*

II. $OO^* + e^- + H^+$ $\longrightarrow$ HOO^*

III. $HOO^* + e^- + H^+$ $\longrightarrow$ $HOOH^*$

IV. $HOOH^*$ $\longrightarrow$ $H_2O_2 + *$

Figure 9: Mechanistic steps for a 2-electron reduction reaction of O_2 forming H_2O_2 as main product on a metal electrode surface according to literature.[34,38,47,50–54]

The first step of any heterogeneous, electrocatalyzed reaction like the ORR is the adsorption of the O_2 to an active binding site of the electrode material (*). After the formation of a surface-oxygen species (I.) a consecutive 2-electron and 2-proton reduction occurs (II. & III.) yielding a surface-hydrogen peroxide species. During step IV, these species are released from the active surface site as H_2O_2. As illustrated in Figure 9, a side-on binding geometry for the oxygen molecule is assumed.

In order to achieve a full 4-electron ORR, the initial step of adsorption is presumed to be identical, but the consecutive steps differ as illustrated in Figure 10:
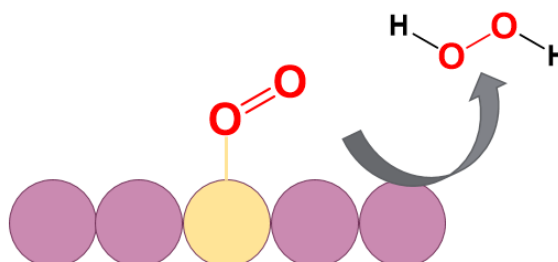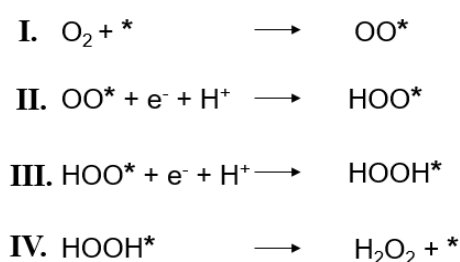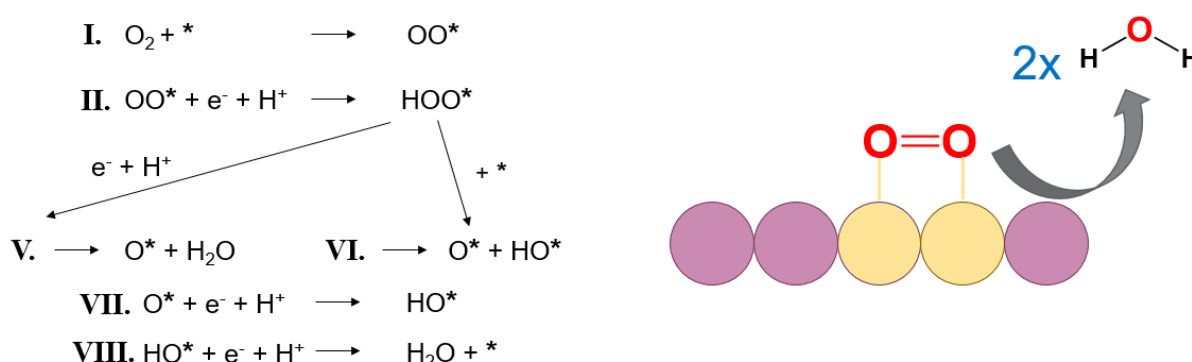

Figure 10: Mechanistic steps for a 4-electron reduction reaction of O_2 forming H_2O as main product on a metal electrode surface according to literature.[34,38,47,50–54]

In the case of a so-called associative process for the 4-electron reduction pathway, the first two steps (I. & II.) are identical to Figure 9. In the case of the 4-electron pathway, the stability of the surface-peroxy species (HOO*) is crucial. Whereas a stable surface-peroxy species enables the 2-electron pathway, instable HOO* species are indications for the 4-electron pathway. This instability refers to the stability of the oxygen-oxygen bond, which is cleaved via the process depicted in Figure 10. One possibility for cleavage is the reduction and release of water while a surface-bound oxygen (O*) remains (V.). The second possibility is a chemical cleavage of the two oxygen molecules resulting in O* and HO* (VI.). Independent on the way how the HO* species are evolved, the further reduction leads to the release of the second water molecule (VIII.)

Besides this associative mechanism, where the oxygen-oxygen bond remains until initial reduction and hydrogenation steps, also the dissociative mechanism exists, where upon adsorption immediately O* forms and the following reduction steps follow the steps VII and VIII.[51] Due to the fact that H_2O_2 is the main goal of this work, only the associative mechanism is of interest, as during a dissociative mechanism only water can be produced as product and no H_2O_2.

Detailed insights into these mechanisms briefly explained above are subject of intensive experimental as well as computational research throughout the last decades. As those details are beyond the scope of this work, it is of utmost importance to mention that in an associative mechanism the stability of the surface-peroxy species (HOO*) is the key element for determining the pathway. Due to the reason, that the intermediate species depicted in Figure 9 and Figure 10 are responsible for the selectivity of the metal electrode, their Gibbs free binding energies ΔG_{*OH} and ΔG_{*OOH} are referred to as thermodynamic descriptors. Plotting these descriptors with respect to experimental values regarding the electrochemical ORR

gives insights into certain trends. Such graphical illustrations of the energetic reaction pathways based on calculations are reported in literature, where platinum and gold are shown as examples in the following Figure 11:
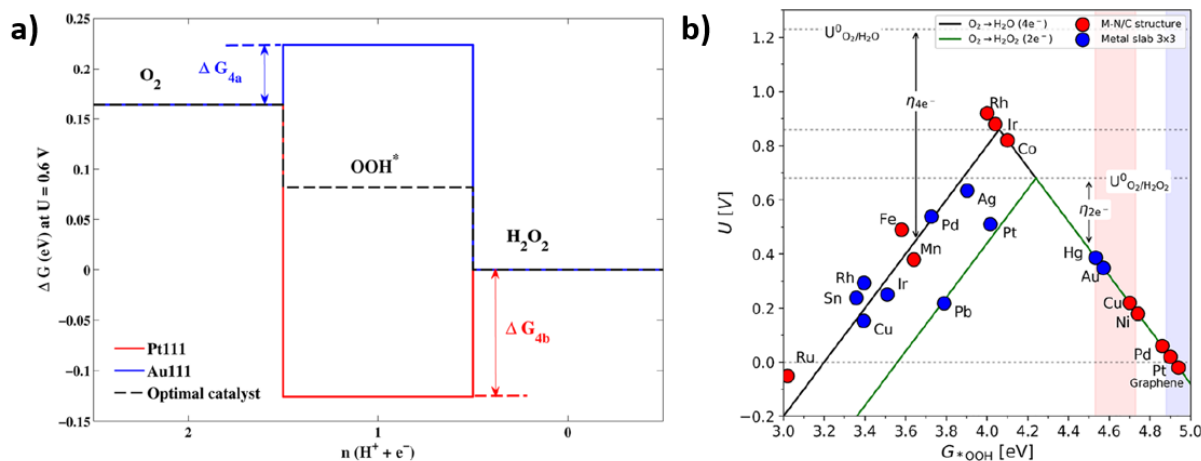

Figure 11: Description of computed properties of metal electrodes towards the ORR. a) Gibbs free-energy diagram for the 2-electron pathway forming H_2O_2 on platinum and gold and b) volcano plot of several metals plotting the limiting potential U_L in dependence of ΔG_{*OOH}. a) Reproduced with permission from Viswanathan *et al.* (https://pubs.acs.org/doi/10.1021/jz301476w)[50] © 2012 American Chemical Society. b) Reproduced with permission from Yang *et al.* (https://pubs.acs.org/doi/10.1021/acscatal.8b00217)[9] © 2018 American Chemical Society.

The computations of the 2-electron reduction pathway in Figure 11a comparing platinum and gold gives an explanation for the different preference during ORR. Gold possess a rather instable *OOH species which leads to the preferred H_2O_2 production whereas platinum stabilizes the *OOH species which dictates the process more to move into dissociation of the oxygen-oxygen bond and therefore facilitating the 4-electron reduction forming water.[50,51] Yang *et al.* constructed a volcano plot for the ORR on computed metal slabs for the 4-electron pathway (black line) and the 2-electron pathway (green line) with respect to ΔG_{*OOH} in Figure 11b. This scheme is also in accordance with the electrocatalytic trends observed on gold, which possesses a low overpotential for the H_2O_2 production, whereas metals like silver, platinum or rhodium show rather low overpotential for the 4-electron reduction with water as main product.[9,38] It should be mentioned here, that besides considering only the energies of *OOH also reports on similar volcano plots referring to *OH and *O exist, which are not shown here as they all provide a similar trend.[50,51]

More in-depth studies not only focusing on one of the energetic values but comparing two of them (ΔG_{*OOH} and ΔG_{*OH}) in one graph recently reported by the group of Nørskov revealing new insights as depicted in the following Figure 12:
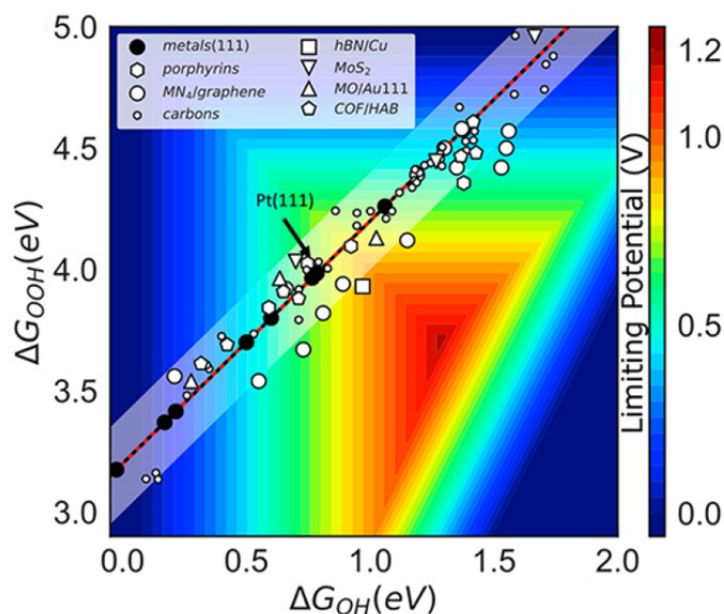
Figure 12: 2D volcano plot relating the ΔG_{*OOH} and ΔG_{*OH} computed energies with the limiting potential U_L for ORR of several compounds including metals, macrocyclic metal complexes, carbon electrodes, boron nitride, etc. Reproduced with permission from Kulkarni *et al.* (https://pubs.acs.org/doi/10.1021/acs.chemrev.7b00488)[53]. © 2018 American Chemical Society.

According to Kulkarni *et al.*, a linear relation between ΔG_{*OOH} and ΔG_{*OH}, as well as ΔG_{*O} is observed.[53] In contrast to previous volcano plots, which often predict platinum to be at an activity maximum[50,51] and according to the predictions in Figure 12, nearly all materials included in this study are still rather away from the maximum activity represented, with the limiting potential in dark red.[53,55] For further details on the mechanistic and atomistic reasons for the results presented in Figure 12, the reader is referred to the literature references given, as this is beyond the scope of this work. Nevertheless, two important conclusions can be drawn from this graph. Firstly, due to the rather large distance of any material included in this graph to an optimum electrocatalytic behavior, further research on the development and investigation of electrocatalysts for the ORR is highly required. Secondly, Figure 12 reveals that not only noble metals are close to the high activity center, but also numerous carbon materials (denoted as small white dots) are presumed to have beneficial properties towards the ORR.

As the main focus of this work is the investigation of organic electrocatalysts for the H_2O_2 production immobilized onto carbon-based electrode materials, some mechanistic insights from literature will be given here. Up to now, the general mechanistic pathways depicted in Figure 9 & Figure 10 are valid for all electrode materials, whereas the references[34,38,47,50–53] explaining the competing 2-electron vs. 4-electron pathway were up to now mainly focused on metal electrode surfaces. An extensive review on transition metal oxide and alloy derived materials for ORR is given by Shao *et al.*[48]

Although the very early reports on the electrochemical H_2O_2 production by Meidinger[4] in 1853 and Traube[56] in 1887 were based on noble metals, already in 1938 Berl[5] reported carbon electrodes as efficient electrocatalyst. Since then, intensive efforts have been made to further investigate and understand the mechanisms of the ORR on carbon materials. One unique property of nearly all carbon materials is that they exhibit a high selectivity for the 2-electron pathway forming H_2O_2.[38] While the mechanistic steps described above on metal surfaces with respective active sites are rather straight-forward to understand, this analogue understanding

for purely carbon electrode surfaces might be startling at first glance. Identification of the actual active sites is a hot topic that has been reported numerous times during the previous years and is still not yet fully understood. Two major explanations moving away from a traditional idealized and planar graphitic (graphene) like purely sp^2 carbon surface are accepted.

In this respect, the carbon materials used nowadays for electrochemical investigations like glassy carbon (GC) and highly-oriented pyrolytic graphite (HOPG) have a degree of ordering close to ideal systems, they still exhibit some corner and terrace structures on a nanometer scale. Exactly those edges were examined by noise-analysis in electrochemical scanning tunneling microscopy (EC-STM)[57] with the mechanism shown in the following Figure 13:
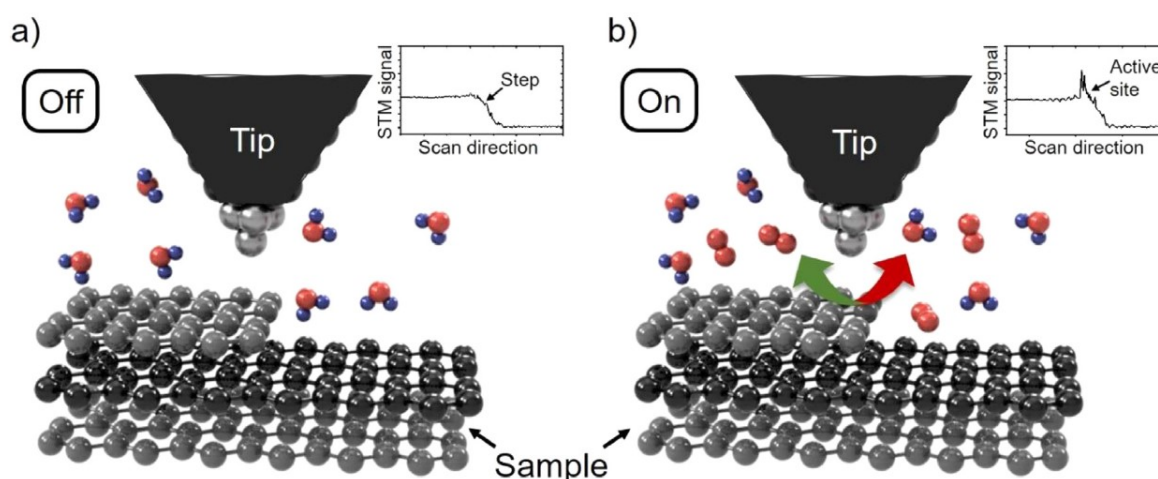

Figure 13: Working principle of a noise analysis EC-STM with a) switched "off" without polarization of the sample electrode and b) polarizing the sample electrode accordingly driving the reaction of interest (ORR; OER or HER). Reproduced with permission from Haid *et al.*[57] © 2021 Elsevier Ltd.

Without any applied potential for electrochemical reactions, resulting from the tunneling currents, the height and according "steps" of layers can be measured by the STM according to Figure 13a. Upon applied bias driving an electrochemical reaction like OER or ORR on the sample electrode while scanning the surface still an STM height profile can be measured. Only at certain positions on the sample showing a high electrocatalytic activity a noise in form of spikes in the STM response is detected as a result of the current flow caused by the electrocatalytic reaction occurring. By using this method, the group of Bandarenka[57] was able to spot active sites for OER and ORR on HOPG samples as depicted in the following Figure 14:
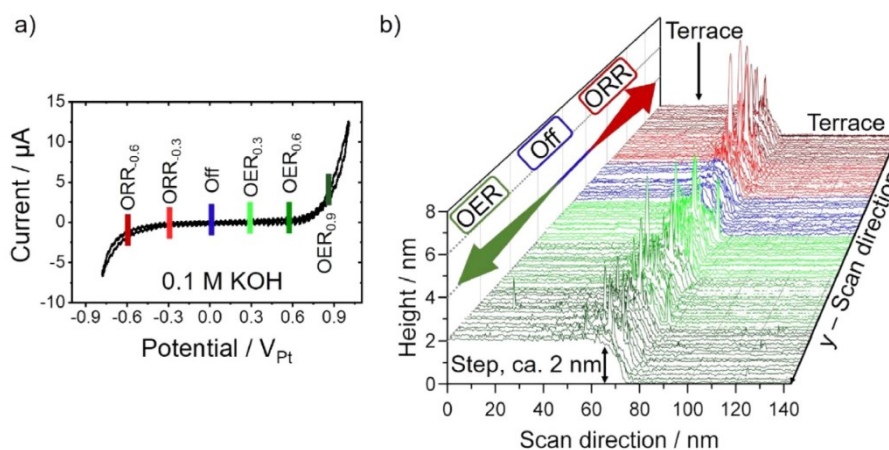

Figure 14: CV and noise-analysis EC-STM result of HOPG in 0.1 M KOH solution for OER and ORR. Reproduced with permission from Haid *et al.*[57] © 2021 Elsevier Ltd.

Following the results in Figure 14 by Haid *et al*., the edge of the HOPG electrode shows the largest noise level for OER and ORR corresponding to the highest electrocatalytic activity.[57] Except for some small noise spikes in the OER on the terraces, which are uniform and nearly ideal carbon surfaces, nearly exclusively the edges are identified as the active sites for electrocatalytic reactions on purely carbon materials. This result is in agreement to previous studies reported in literature.[54,58–60]

In addition to the large electrocatalytic activity of edges in carbon electrode materials as a result of not fully coordinated carbon atoms, also another important chemical aspect is crucial for the electrocatalytic activity for ORR. Uncoordinated carbon atoms have the driving force to form chemical bonds which result in formation of oxygen moieties in ambient atmosphere. Some of these possibilities are illustrated in the following Figure 15:
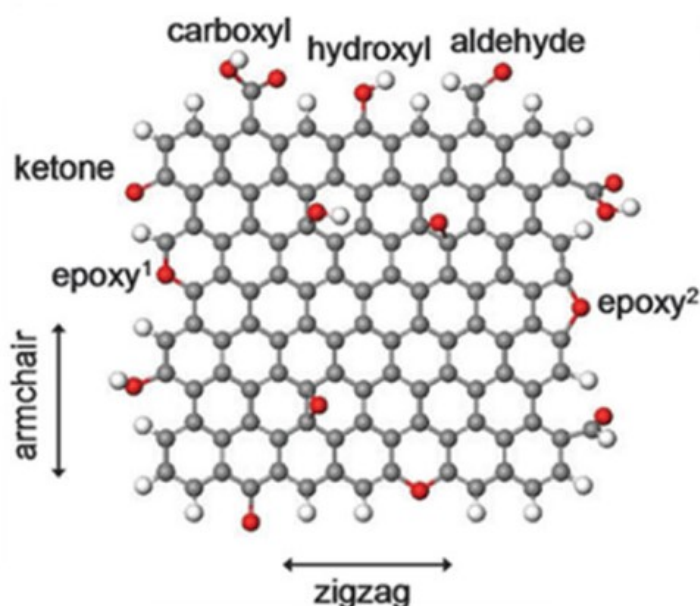

Figure 15: Schematic illustration of some possible oxygen-based edge functional groups on a graphene structure. Reproduced with permission from Ma *et al*. [54] © 2019 these authors.

As depicted in Figure 15, many single bonded oxygen-derived functional groups at the corners of a schematic graphene like epoxy, hydroxyl (or phenolic, depending on the nomenclature) might be present.[54,61] In addition to those single bonded functional groups, also aldehydes, ketones and carboxylic acid groups might occur at such carbon surfaces. According to literature, actually these defect groups at the corners are mainly responsible for the electrocatalytic ORR, by facilitating not only the adsorption but also the stabilization of reaction intermediates.[54,61] The exact mechanistic steps on carbon-oxygen surfaces for ORR are still not yet fully understood, which is why a lot of effort from material scientists as well as computational chemists is required to – hopefully soon – provide a more profound understanding.[62] In this regard, a recent work by Lim *et al.* identified a trend in reactivity towards H_2O_2 to increase from phenol-groups over carbonyl-groups to carboxylic-groups.[61]

Besides focusing on oxygen-carbon systems only, the majority of metal free electrocatalysts reported for ORR is based on nitrogen-doped carbon materials, or other heteroatom doped systems.[34,54,63–68] Within this field, even more and more complex possibilities for mechanistic processes are possible, which are still under investigation. According to Ikeda *et al.* pyridinic

nitrogen atoms adjacent to carbonyl oxygen groups facilitate and direct towards a 2-electron ORR forming H_2O_2.[65] Wang, Sofer and Pumera explained within a perspective that no matter which heteroatom doping increases the electrocatalytic ORR, including pyrolyzed bird droppings.[66] As the mechanistic details on the processes of ORR happening on carbon-based materials are still under investigation and also beyond the scope of this work, several extensive reviews on this topic are reported in literature.[16,69]

Summing up, this brief overview on the mechanistic details of ORR on metal electrode surfaces as well as carbon-based electrodes revealed that especially the binding geometry and stability of the surface-OOH intermediate species determines the pathway for ORR. Whereas noble metal electrode surfaces are already well-studied and quite well-understood, the exact reasons for the high selectivity of carbon-based electrode materials towards the 2-electron process forming H_2O_2 are still under investigation. According to the current state of knowledge, this property is not an intrinsic carbon-only property but more related to heteroatom doping impurities on edges and corners. Nevertheless, one lesson learned is that nearly all electrode materials, especially the carbon-based ones, show some certain activity towards the electrocatalytic H_2O_2 production which always has to be considered throughout any electrochemical experiment.

1.3.2. Electrochemical water oxidation reaction

The technology of electrocatalytic oxygen reduction towards H_2O_2 explained within chapter 1.3.1. is actually only one possible approach to produce H_2O_2. In addition to reduction of oxygen, also the 2-electron oxidation reaction of water yields in H_2O_2 as product, which can be understood as the reverse reaction to H_2O_2 reduction. Although this work focusses on the reduction reaction side, this chapter should provide a short overview on reported materials mainly used for the (photo-) electrochemical oxidation reaction of water to H_2O_2.

During the last years, numerous materials were reported for the electrocatalytic water oxidation reaction, which can be, similar to the reduction reaction described in chapter 1.3.1. split in a 2-electron pathway forming H_2O_2 and a 4-electron pathway for fuel cell application. According to comprehensive reviews,[38,41,46] the most efficient electrocatalysts for the 2-electron reaction are metal oxides, which were also investigated for their *OH intermediate binding energies for a volcano plot comparison (similar to Figure 11 for the ORR):
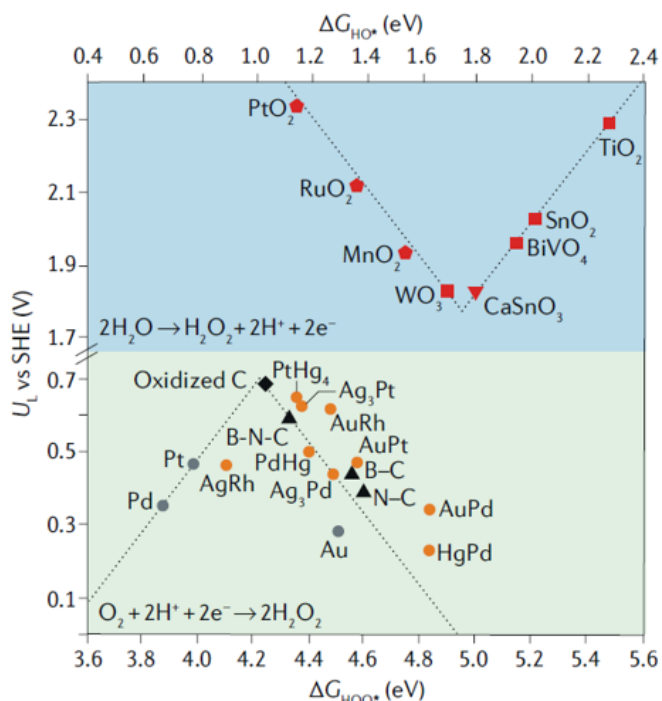

Figure 16: Volcano plot of several metal alloys for the ORR (lower part in green) and volcano plot of several metal oxides for the electrocatalytic water to H_2O_2 oxidation plotting the limiting potential U_L in dependence of ΔG_{*OH} (upper part in blue). Reproduced with permission from Perry *et al.*[38]. © 2019 Springer Nature Limited.

The volcano plot in the lower part of Figure 16 shows few metals, like also Figure 11 does, with some metal alloys in addition. In the upper part of Figure 16, a volcano plot referring to metal oxides for oxidative H_2O_2 production are depicted, like for example tungsten oxide (WO_3), bismuth vanadate ($BiVO_4$) and, manganese(IV) oxide (MnO_2) among others. As nearly all of these metal oxides are well-known for their photo-electrocatalytic activity towards other reaction types, it is no surprise that they are also applied for photo-electrocatalytic water to H_2O_2 oxidation reactions.[38,70] In recent years, perovskite-type metal oxides like $CaSnO_3$[71] and combinations of oxides like $BiVO_4$ and $FeO(OH)$[72] have gained increased interest, reported in several reviews.[38,70]

1.3.3.   Rotating ring-disc electrode technique

The foundations of hydrodynamic voltammetry or, to be more precise, of the rotating disc electrode (RDE) and rotating ring-disc electrode (RRDE) methods, rely on a fascinating historic development, covering aspects of collaboration across political borders, interdisciplinarity and closely related industrial partners. An extensive and illustrative review on this historic stories is reported by Dalton, and within this chapter, only selected key-steps with focus on formalisms for practical ORR experiments are given.[73]

During the 1940s, Russian scientists around Alexander Frumkin and Benjamin Levich investigated the impact of convection on current during electrochemical experiments on rotating disc electrodes.[73,74] Due to political restrictions, their work was published in a book in 1952[75] and in western journals in 1959.[73] In early times only RDE was considered and after 1958 Frumkin developed the idea of putting a concentric ring around the disc electrode.[73]

Only after the publications were accessible to western scientists, pioneers like Stanley Bruckenstein and John Albery starting exploring these topics.[73,74] The mystery of the numerical solutions of the collection efficiency N for RRDEs could only be solved by Bruckenstein in 1965 when he smuggled a book of integrals to Russia when visiting Levich.[73,76]

One of the first western RDE set-ups was built at the Bruckenstein lab in Minnesota by the dental school, as they had the largest knowledge on rotating and drilling devices.[73] In order to simultaneously control the two electrodes required for an RRDE set-up, Bruckenstein developed the first bipotentiostat together with his graduate students Dennis Johnson and Duane Napp.[73,74] Also the commercialization of the first RRDE set-ups and bipotentiostats was done jointly by Bruckenstein and Johnson together with a friend, Ted Hines, who was owner of a small workshop at that time and thereof later created Pine Instruments.[73]

After that, the golden age of the RDE method came including numerous publication series in journals instead of monographies, for example in the 1970s by Alan Bard on digital simulation of RDE curves. [77–80]

Moving from the historic description of the hydrodynamic voltammetry towards the scientific basics, the easiest model to be considered is the one of a RDE as depicted in the following Figure 17:
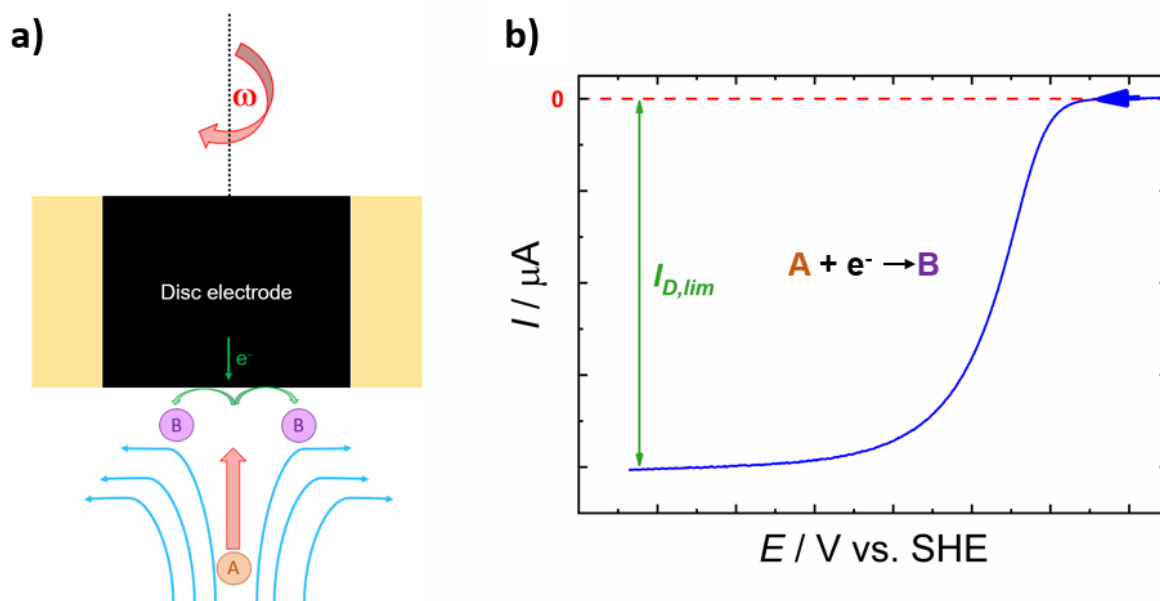
Figure 17: a) Schematic depiction of an RDE experiment involving the electrochemical reduction of molecule A to molecule B. b) Schematic RDE voltammogram graph for such a reduction reaction A→B including the limiting disc current $I_{D,lim}$.

For such a RDE system as illustrated in Figure 17a, upon rotating the disc electrode at a certain rotation speed ω, a stream of electrolyte solution containing the redox active molecule A is forced towards the RDE via convection. At the disc electrode, molecule A gets reduced forming molecule B, which is shown in a schematic voltammogram in Figure 17b. As a result of the convection, the linear sweep voltammogram (LSV) does not show a peak but a step.[81] Upon applying a reductive potential, which corresponds to a movement from right to left in Figure 17b, after a certain cathodic enough potential, a steady-state condition with a constant limiting current $I_{D,lim}$ is observed. This $I_{D,lim}$ depends, amongst other parameters, on the rotation speed ω and follows the famous Levich equation (Eq. 10) initially reported by Benjamin Levich in 1952:[73–76,81,82]

$$I_{D,lim} = 0.62 \cdot A \cdot F \cdot n \cdot D^{2/3} \cdot v^{-1/6} \cdot c^* \cdot \sqrt{\omega} \qquad \text{Eq. 10}$$

Besides the aforementioned dependence of $I_{D,lim}$ on the square root of ω, also the electrode surface area A, the faraday constant F, the number of transferred electrons n, the diffusion coefficient D, the kinematic viscosity of the electrolyte solution v and the initial concentration of the redox-species c^* are relevant. In many real-life measurements, such a limiting current plateau cannot be reached, which is why for determination of important parameters like the number of transferred electrons n often the refined Koutecky-Levich formula is applied. This Koutecky-Levich equation (Eq. 11) describes the part of the LSV curve on the rise before reaching the steady-state conditions and is in addition to the mass transfer also considering the electron transfer kinetics:[73,81,82]

$$\frac{1}{I_{D,lim}} = \frac{1}{I_K} + \left(\frac{1}{0.62 \cdot A \cdot F \cdot n \cdot D^{2/3} \cdot v^{-1/6} \cdot c^*} \cdot \frac{1}{\sqrt{\omega}} \right) \qquad \text{Eq. 11}$$

In accordance with the Levich Eq. 10, the right part of the Koutecky-Levich Eq. 11 is accounting for the mass-transfer limited current contribution. The left part of Eq. 11 is called kinetic current I_K, which corresponds to the current that would flow in absence of any mass transfer limitations and is described as following:[73,81–83]

$$I_K = A \cdot F \cdot k_f(E) \cdot c^*$$

<div align="right">Eq. 12</div>

Following Eq. 12, from this kinetic current I_K, the kinetic parameter, the rate constant k depending on the applied potential E, can be extracted. The practical way in order to determine relevant kinetic parameter from such RDE measurements, frequently but not exclusively for ORR, is to plot $1/I$ versus $1/\sqrt{\omega}$. From these, in an ideal case with linear relations following Eq. 11, the number of transferred electrons n and the rate constant can be obtained.[81–83] One important requirement for all these measurements is the knowledge of all other parameters and constants in the equations, including the electroactive surface area A.

Besides the simple RDE depicted in Figure 17, also rotating ring-disc electrode (RRDE) methods exist for a more detailed experimental set-up, as illustrated in Figure 18:
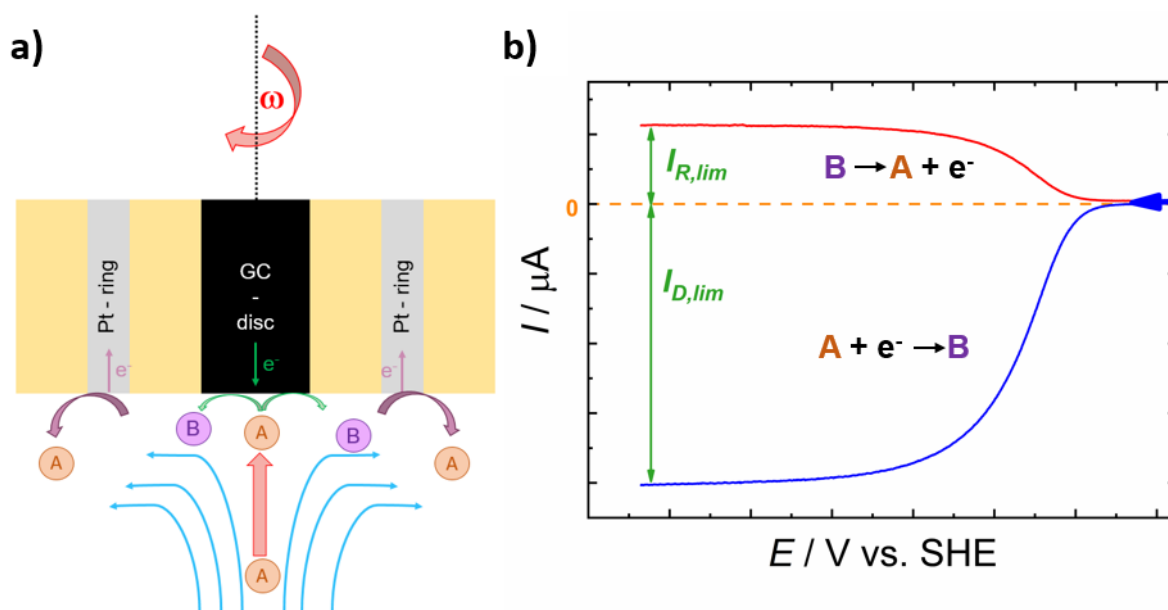

Figure 18: a) Schematic depiction of an RRDE experiment involving the electrochemical reduction of molecule A to molecule B and the back reaction on the ring electrode b) Schematic RRDE voltammogram graph for such a reduction reaction A→B and the reverse reaction including the limiting disc current $I_{D,lim}$ and limiting ring current $I_{R,lim.}$

One important aspect to be mentioned about the LSV curves in Figure 18 is that during sweeping the disc potential as depicted on the x-axis, the ring is kept at a constant and anodic potential in order to drive the re-oxidation of reduced species B → A. As a result of this, the ring current actually corresponds to the potential applied at the disc electrode.
According to the first step shown in Figure 18a, the species A gets reduced to B on the disc electrode, which is identical to the steps depicted in Figure 17. Consecutively, this reduced species B is radially transported along the electrode and then re-oxidized at the positively polarized ring electrode. Thereby a positive ring current is measured, which at very cathodic potentials yields a constant $I_{R,lim}$. When qualitatively comparing the limiting current values for

the disc and the ring, it is obvious that the $I_{R,lim}$ is significantly smaller on an absolute current basis. This is an intrinsic geometric issue, and not due to insufficient anodic potential applied at the ring. Actually, this issue is known since the beginning of Frumkin's and Levich's time and they named this dimensionless ratio collection efficiency N_{max}, of what is the maximum ratio of ring current to disc current.[73] To determine this collection efficiency for certain geometries, sophisticated integrals are required, which caused delay for the early calculations in the 1950s and are even nowadays challenging.[73,77,81–84]

Besides numerical calculation of the collection efficiency, which is often already provided by the vendor companies usually in a range between 25 and 45%, it can also be determined very conveniently and straight forward by using a well-known and highly reversible redox couple like potassium ferricyanide(III) ($K_4[Fe(CN)_6]$). While measuring these LSV curves, similar to the one in Figure 18, at several rotation speeds, the experimental collection efficiency N_{exp} can be determined using the following formula:

$$N_{exp} = \frac{I_R}{|I_D|}$$

Eq. 13

Using this approach, the exact collection efficiency for your system consisting of your RRDE and electrolyte solution can be obtained. This will be demonstrated in the upcoming chapter 3.1. Upon knowledge of the collection efficiency, in-depth analyses beyond the Koutecky-Levich plots and plotting the ratio of disc and ring currents are possible.

Starting around the turn of the millennium, publications introduced the following two formulae, which are especially developed for the ORR calculating the number of transferred electrons n

$$n = \frac{4 \cdot |I_D|}{|I_D| + {I_R}/{N}}$$

Eq. 14

and the faradaic efficiency (*FE*) for the H_2O_2 production:[3,82]

$$FE(\%) = \frac{{I_R}/{N}}{|I_D|} \cdot 100$$

Eq. 15

Following these equations 14 & 15, *n* and *FE* can be determined at any potential measured upon investigation of an electrocatalyst during an RRDE experiment. As besides the ring and disc currents, the collection efficiency is the only further parameter, these formulae open up a very convenient possibility of ORR studies using RRDE.

Although these final formulae given here might suggest the RRDE method to be an easy and plug-and-play method, it is not that trivial. Only to mention two aspects, on the one hand the knowledge of the electroactive surface area is crucial for the Koutecky-Levich equation, even in all other cases surface-modified electrodes hinder the hydrodynamics which causes deviations.[85–88] On the other hand, reproducibility studies on commonly used Pt/C electrode materials in different laboratories revealed significant differences.[89]

Nevertheless, the RDE and RRDE methods are quite powerful when studying the electrochemical H_2O_2 production as in this work – when certain issues are carefully addressed.

1.3.4. Molecular electrocatalysts for the oxygen reduction

From a materials science perspective, development and investigation of a metal (oxide) based electrode material for electrochemical energy conversion reactions like hydrogen evolution reaction (HER), oxygen reduction reaction (ORR), oxygen evolution reaction (OER) or the carbon dioxide reduction reaction (CO_2RR) are already well studied and reviewed.[38,55,90–92] Besides these materials point of view, molecular electrocatalysts with well-defined chemical structure are also of major interest within the scientific community, although direct comparison is by far more difficult as homogeneous cases have to be differentiated from heterogeneous catalysts.

In order to give a comprehensive overview of the important classes of molecular electrocatalysts for the ORR focusing on the 2-electron pathway, another distinguishing feature is highlighted. Whereas in case of HER, CO_2RR and OER the *state-of-the-art* molecular catalysts nearly exclusively contain at least one metal atom, for the ORR numerous metal-free electrocatalysts are reported. Due to this reason, this literature overview is divided into these two following sub-chapters.

1.3.4.1. Metal-based molecular electrocatalysts

One of the most prominent class of metal-complexes for electrochemical ORR are macrocyclic compounds bearing either a porphyrin or a corrole ligand. A scheme of a porphyrin and a corrole structure is shown in Figure 19:

metallo porphyrins

M = Fe, Co
R = phenyl, pyridyl

metallo phthalocyanines

M = Mn, Fe, Co, Ni, Cu

metallo corroles

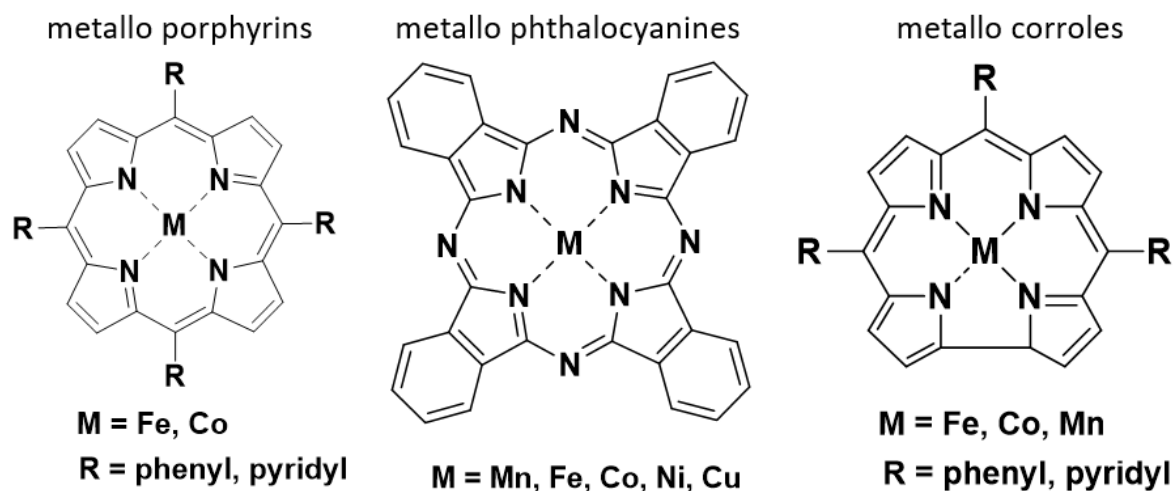M = Fe, Co, Mn
R = phenyl, pyridyl

Figure 19: Chemical structures of porphyrins, phthalocyanines and corroles, as examples of macrocyclic molecules used in ORR.

Inspired by naturally occurring metallo-enzymes bearing an iron metal center, several iron porphyrins are reported as homogeneous electrocatalysts for the ORR as well as other transition metals.[93–97] Upon modification of the macrocycle side groups and the central metal atom, either the 2-electron or 4-electron ORR pathway is preferred, as extensively reviewed by Dey *et al*.[94] A second large molecular group studied for electrocatalytic ORR are metal corroles.[93,98,99] Besides macrocyclic compounds also salen-based, phenolate-based or bipyridinium complexes are reported, sometimes also with multi metal-atom centers often involving copper.[93,94,97] Especially in recent years, synergistic effects of either covalently

linking two macrocycles together or using the so-called hangman complexes were the focus during the development of new molecular catalysts.[94,95]

In addition to homogeneous electrocatalysis, which has several challenges with respect to the ORR concerning adsorption phenomena, electrochemical methodology and separation of the product,[94,100,101] a main goal is the development and characterization of heterogenized systems. Thereby several approaches of heterogenization, also called immobilization, are reported and reviewed by Whang (2020)[102], who reported that molecular catalysts can be covalently linked to metal (oxide) surfaces[103,104] or via coordination of a carboxylic acid group[105,106]. For immobilization onto carbon materials, either direct covalent linking[107,108], physisorption via a pyrene linker[109] or also direct adsorption of the metal complex are described[110].

In addition to these approaches, electropolymerized porphyrin structures are reported, having metal centers for heterogeneous ORR[111,112]. Throughout recent years, metal organic frameworks (MOF) have gained increasing interest in heterogeneous catalysis due to their versatility, high degree of order and nanoporosity, such as porphyrin-based MOFs prepared for ORR.[113–115]

Nearly exclusively in the research of ORR, metal containing carbon-nitrogen materials synthesized via pyrolysis gained increasing interest also due to their high activity and porosity. Although in many cases the precise structure of the active sites is not fully understood, a nitrogen-metal coordination is assumed to play a significant role as many of these compounds are produced from a macrocyclic or polymer (polyaniline or polypyrrole) precursor.[93,116,117] Similar to the results on carbon based materials in chapter 1.3.1. extensive research from computational scientists as well as materials scientists in currently ongoing in order to gain a more in-depth understanding on the role of the active sites in such kinds of composites.

1.3.4.2. Metal-free molecular electrocatalysts

As described in chapter 1.3.1. since decades carbon-based electrode materials are known as efficient electrocatalysts for the oxygen to H_2O_2 reduction reaction.[3,5] On a molecular level, the reasons for this electrocatalytic activity are not the uniform sp^2 graphene layers but heteronuclear defects on edges and corners.[54,57] Thereby carbonyl groups and especially quinone groups have been identified as active centers for selective oxygen to H_2O_2 reduction.[61,118,119] Due to this reason, organic quinones and especially anthraquinone (AQ), were extensively studied for their electrocatalytic properties for ORR forming H_2O_2 throughout the last decades.

Although (anthra-) quinones are already well-studied for their electrochemical properties for many years, quantitative description of homogeneous electrocatalytic studies in organic solvents[120], as well as aqueous solutions[121–123] were thoroughly investigated by the group of Compton during the last 20 years. One reason for this late investigation of homogeneous, aqueous systems might be the overlap of the electrocatalytic ORR features of numerous electrode materials. Due to this reason, the studies mentioned above were all performed at boron-doped diamond (BDD) electrodes[121,122] or surface-modified gold electrodes[123] which help preventing unwanted background ORR currents.

Reports on the heterogenized electrocatalytic effects of quinones on mostly carbon electrode materials already date back much earlier.[119] In particular, Hossain's[119] extensive studies using adsorbed quinones on carbon electrodes done by the group of Tammeveski started with a physiosorbed approach.[124] Thereby they investigated 15 different quinone molecules for their electrocatalytic ORR activity.[124]

Moving towards covalent attachment of the quinone molecule to the carbon surface, the group of Tammeveski developed two approaches for electrochemical grafting as depicted in the following Figure 20:[125,126]
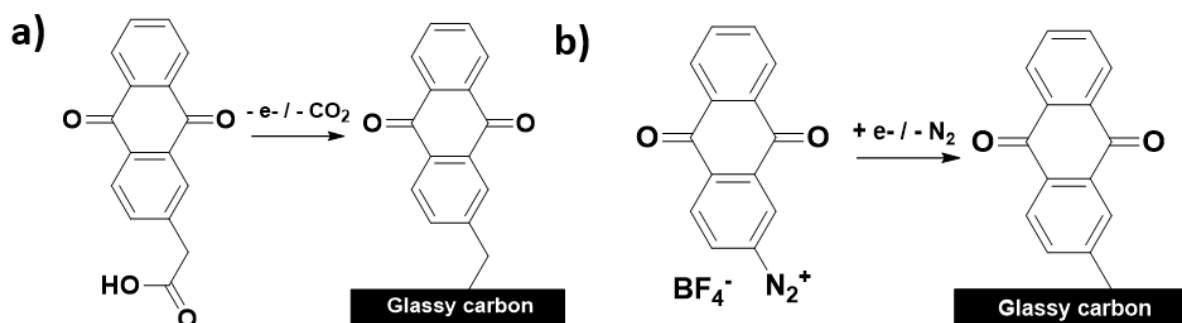

Figure 20: Covalent electrochemical grafting approaches reported by the group of Tammeveski.[125–128] a) oxidative electrochemical grafting of AQ-COOH and b) reductive electrochemical grating of AQ-N_2^+ salt.

According to the reaction schemes in Figure 20, in both cases Tammeveski linked a chemically synthesized AQ precursor to the glassy carbon acting as electrode surface via electrochemical treatment. Thus, via one-electron oxidation, the carboxylic acid group is transformed into a radical species, which decomposes upon CO_2 elimination. The remaining radical species is consecutively reacting with the glassy carbon surface atoms forming a covalent bond. This Kolbe type of reaction is believed to prevent the usually expected dimerization as the formation of radicals is in very close proximity of the glassy carbon within the Helmholtz layer of sub-nanometer.[126]

A similar mechanism via reductive covalent linking of AQ units onto glassy carbon electrodes was reported by the same group.[127,128] Upon electrochemical reduction of the diazonium salt, an aryl radical species is formed under release of nitrogen N_2. This remaining radical species is reacting in the same manner like in the carboxylic acid approach above with the GC electrode surface. [127,128]

During the last 20 years, Tammeveski reported numerous electrocatalytic studies on quinone modified carbon electrodes using this electrochemical grafting approach, further investigating the influence of substituents[127–129], pH value[130] and electrode material used (BDD)[131]. Regarding the pH dependence of quinone modified electrodes for H_2O_2 production several studies have been reported, all agreeing that slightly alkaline conditions are optimum, as in very high pH values desorption of the quinone units might occur.[130,132–134] A detailed study by Lin *et al.* provides insights into the reason for this mechanistic pH behavior using catechol as model compound.[135] Although the exact reaction mechanism during the anthraquinone catalyzed H_2O_2 production is not fully understood yet, some reports about theoretical calculation dealing with this topic are approaching the mechanistic description.[136,137] This approach was later extended by the same group towards linking of AQ units onto multi-walled carbon nanotubes (MW-CNT) and graphene sheets.[138]

A slightly different electrochemical grafting was reported by Wilson *et al.* using an AQ with a carboxylic acid allyl ester group.[139] Already in the 1980s, reports on electropolymerized thin-films using ally-substituted quinones mention their electrocatalytic effect on ORR.[140–142]

Besides anthraquinone, in the following Figure 21 some selected examples from literature are depicted, which were also reported as homogeneous electrocatalysts for the oxygen reduction:
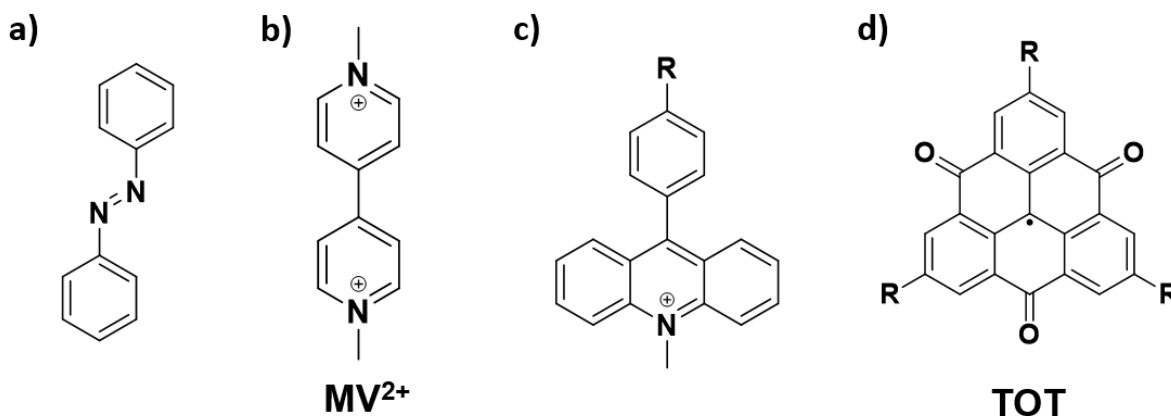

Figure 21: Chemical structures of homogeneous catalysts for the oxygen reduction reaction: a) azobenzene, b) methylviologene (MV), c) 9-(4-R-phenyl)-*N*-methyl-acridinium, where R was H, F or Cl and d) a general trioxotriangulene (TOT) molecule as neutral radical species, where R was H, Cl, Br and phenyl.

Another related class of organic molecules investigated for the electrochemical ORR are the azobenzenes. Together with the first report on chemical H_2O_2 production using anthraquinone by Manchot in 1901 azobenzene was mentioned for the same reaction.[6] Similar to the 1,4-quinone structure, the azobenzene molecule undergoes a reversible 2-electron and 2-proton reduction and is capable as ORR electrocatalyst for H_2O_2 production.[96,143–145] In 1985, Andrieux *et al.* reported that homogeneously dissolved methyl viologene (MV) in dimethylsulphoxide (DMSO) acts as an electrocatalyst for the oxygen reduction.[146] In 1993, Audebert and Hapiot showed the electrocatalytic ability towards oxygen reduction of three different substituted 9-(4-R-phenyl)-*N*-methyl-acridinium salts in homogeneous solution as well as in gels.[147] In 2019, Murata *et al.* reported trioxotriangulenes (TOT) as a new class of electrocatalysts for the oxygen to H_2O_2 reduction reaction. They reported five analogues of TOT, which are able to stabilize multiple redox species. Murata *et al.* investigated them with RDE methods in comparison to anthraquinone analogues.[148]

Quinones, the other molecules shown herein were either oxygen-only or nitrogen-only functionalized organic molecules reported for the electrocatalytic ORR. During the last 5 years hydrogen bonded pigments with amino and carbonyl functional groups, which are well-known organic semiconductors, were intensively studied for their capability for (photo-) electrochemical oxygen to H_2O_2 reduction:

In 2016, Jakesova *et al.* reported an extensive study on the use of two industrially relevant hydrogen-bonded pigments quinacridone (QNC) and epindolidione (EPI) as efficient photo-electrocatalysts for the oxygen to H_2O_2 reduction reaction, with the chemical structures depicted in Figure 22:
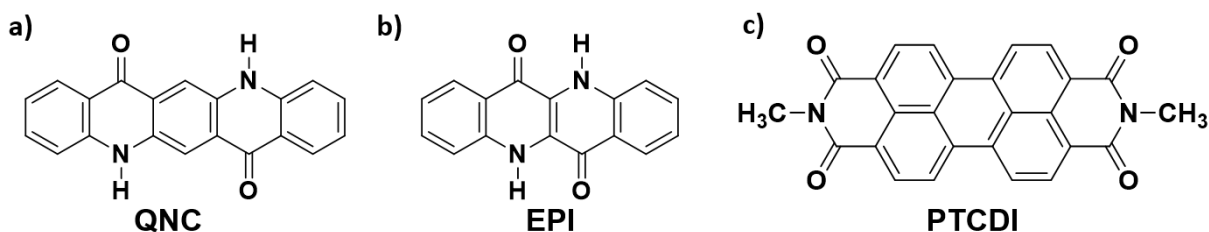
Figure 22: Chemical structures of a) quinacridone (QNC), b) epindolidione (EPI) and c) perylene tetracarbonyl imide (PTCDI).

The chemical structures of QNC and EPI are illustrated in Figure 22 above. Their stability and high sublimation points can be explained by the formation of intermolecular hydrogen bonds between carbonyl and amine groups. Jakesova *et al.* investigated both QNC and EPI as possible photoelectrocatalysts for the H_2O_2 production and found out that EPI is highly stable and efficient (96% faradaic efficiency) at pH=1 throughout several days of operation.[149] QNC on the other hand undergoes recrystallization and degradation after a few hours of electrolysis. For both materials efficiency maxima derived from photocurrent studies were determined to be at highly acidic conditions and at moderately alkaline conditions around pH=10. Mechanistic pathways for the photo-electrochemical reduction of oxygen to H_2O_2 using EPI were proposed to profit from a synergistic interaction of the intramolecular amine and carbonyl groups.[149] In 2020 a more-detailed computational study on this possible mechanistic pathway was published.[150]

Another oxygen and nitrogen containing pigment reported for this electrocatalytic oxygen to H_2O_2 reduction is methyl perylenetetracarboxylic diimide (PTCDI), shown in Figure 22c. Again, acidic conditions at pH=1 were identified as optimum, showing initial faradaic efficiencies around 70%. Over a few hours of electrolysis, this efficiency drastically decreased to around 30%. Measurements at neutral and alkaline conditions demonstrated the potential use of PTCDI also under these conditions, but with lower H_2O_2 production rates and faradaic efficiencies.[151] The exact mechanism for the oxygen reduction is, as often in the case for organic catalysts, not fully clear yet.

In addition to single layer arrangement of such small molecule electrocatalysts, the same group also investigated an organic heterojunction approach using EPI as top-layer and catalyst.[152] Furthermore, these organic pigments and similar molecules do not only show photo-electrocatalytic activity for the H_2O_2 production but also in purely photocatalytic systems, without any electrical wiring.[153,154] This means that, if a suitable excitation wavelength and a suitable sacrificial electron donor is provided, such small organic pigments are able to drive the oxygen to H_2O_2 reduction reaction again over a wide pH spectrum.[154]

1.3.5. Conductive polymers for the oxygen reduction reaction

Throughout this chapter 1.3. up to now several material classes were reviewed, from metals, carbonaceous materials to molecular catalysts with or without metal central atoms. As briefly mentioned in chapter 1.3.4. aliphatic polymer chains with defined redox active side groups are also an interesting pathway to immobilize electrocatalysts.

The polymers presented in this chapter differ from the previous polymers by their intrinsic electric conductivity and redox behavior coming from the conjugated polymer backbone they have. Going back to the 1970s, the history of such conjugated and conductive polymers started by the pioneer work of Alan Heeger, Alan MacDiarmid and Hideki Shirakawa on doping metallic-shiny polymer polyacetylene.[155–157] For this "discovery and development of conductive polymers" they were awarded with the Nobel Prize in 2000 in chemistry.[158] During the last four decades, numerous applications of such conductive polymers have been developed.[159–161] Some of the most prominent example polymers are depicted in the following Figure 23:
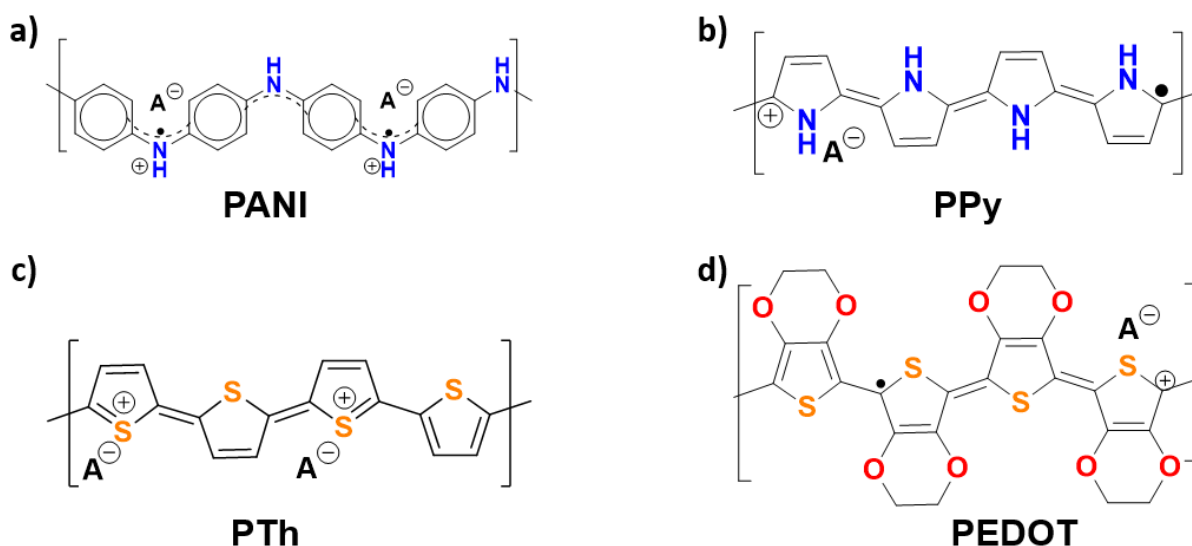

Figure 23: Schematic chemical structures of four conductive polymers: a) polyaniline (PANI), b) polypyrrole (PPy), c) polythiophene (PTh) and d) poly(3,4-ethylenedioxythiophene) (PEDOT).

The chemical structures of the conductive polymers shown in Figure 23 should be considered as schematic hybrids of reduced and oxidized species. Especially polyaniline (PANI) consists of several different states depending on the oxidation and protonation state. The historic development of PANI through the last two centuries is well summarized by a review from Rasmussen.[162] Within this review, and also summarized in the thesis of Heitzmann[163] and Rabl[164], the names and properties of the different PANI states are named, which are beyond the scope of this present work. The other polymers, similar to PANI, possess at least two different redox states for which reason they are reported for numerous applications in energy storage[165], like for example in batteries[166,167], sensors[168,169], supercapacitors[170] or transistors[171].

Exactly because of this reversible redox-behavior of PANI, already in the 1980s several groups reported on the interaction of oxygen during electrochemical treatment, namely the oxygen reduction reaction.[172–174] Although these reports are quite extensive and accurate, they all lack of quantification of H_2O_2 produced. In 2005, Khomenko *et al.* reported a comprehensive work

on the comparison of the oxygen reduction ability of PANI, PPy, PTh and PEDOT.[175] The main part of this work is based on quantumchemical calculations, but also stationary electrochemical experiments were performed. As a main conclusion, Khomenko *et al.* suggested that all those polymers with the exception of PEDOT are good electrocatalysts, with PANI as the best candidate. Two years later in 2007, Wu *et al.* reported a comparison between PANI and PPy for which they chose the different name of oxygen reversible electrodes.[176] Thereby PPy was identified to be the superior electrocatalyst in comparison to PANI.[176] In order to enhance the electrocatalytic ORR of PANI, the group of Azzaroni developed a method based on zinc-based MOFs. Therefore, they fabricated a top-layer of a MOF on PANI electrodes, which are adsorbing oxygen molecules and thereby increasing the local oxygen concentration in the proximity of the electrode.[177–179] Very recently, composite materials of surface functionalized PANI and carbon nanotubes (CNT) were reported by Hu *et al.* as efficient electrocatalysts for the H_2O_2 production.[180]

In 2011, Winther-Jensen and MacFarlane investigated PEDOT electrodes as potential candidates for replacing noble metal electrodes for several redox processes including the oxygen reduction reaction.[181] Later, Mitraka *et al.* described the effect of oxygen-induced doping of PEDOT films with respect to chemical structure and conductivity.[182] Especially concerning the ORR activity and selectivity of PEDOT somehow the existing reports are not yet fully clear. Miglbauer *et al.* reported a selective H_2O_2 to water reduction behavior in fuel cells using 0.1 mM concentration of the H_2O_2.[183] One year later the same group described an electrolysis system using PEDOT to selectively reducing oxygen to H_2O_2 up to concentrations reaching 0.3 mM.[184] A very recent publication by Vagin *et al.* suggested that PEDOT is actually a selective electrocatalyst for the O_2 to H_2O_2 reduction reaction.[185] Very recently, Cui *et al.* reported composite nanomaterial fibers based on PEDOT and CNTs for electrochemical H_2O_2 production.[186]

In addition to these common conductive polymers, more exotic ones like eumelanin and polyindole thin-films were reported for oxygen to H_2O_2 reduction. [187,188] Oka *et al.* investigated co-polymers of thiophene and phenylene for photoelectrocatalytic H_2O_2 production in a device structure.[189] Also, Long *et al.* reported a similar linear conjugated polymer (LCP) backbone as composite with graphene, but introducing a heteroatom bridging with boron and nitrogen atoms for enhanced electrocatalysis.[190] Patnaik *et al.* synthesized a co-polymer from paraphenylene diamine and acenaphthequinone resulting in a bis(aryl)-acenaphthenequinone (BIAN) polymer showing promising ORR electrocatalysis.[191] The schematic repeating units of the polymers explained within this paragraph are illustrated in the following Figure 24:
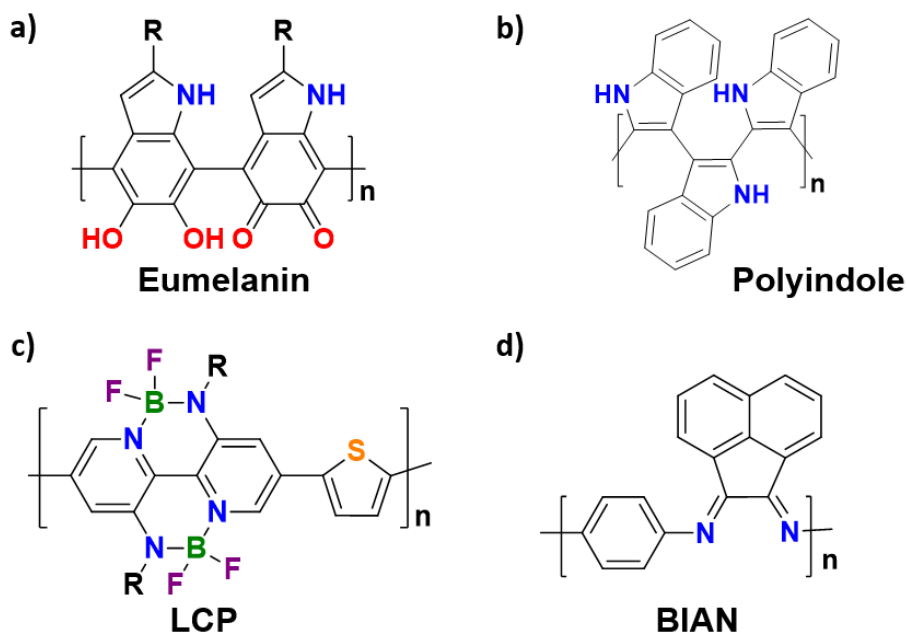
Figure 24: Schematic chemical structures of four conductive polymers: a) Eumelanin[187] , b) Polyindole[188] , c) the linear chain polymer (LCP)[190] and d) the bis(aryl)-acenaphthenequinone (BIAN) polymer.[191]

One general bottleneck in dealing with all conductive polymers are the trace amounts of metal impurities, as also addressed by Winther-Jensen and MacFarlane.[181] As during chemical polymerization often metal impurities are still within the polymer thin-films, they might disturb the real electrocatalytic activity of the polymer. Another aspect is, that the electrocatalytic activity background of the electrode material should also be always taken into account, which is unfortunately still not always the case within the scientific community.

2. Experimental Materials & Methods

2.1. Materials & Chemicals

All the chemicals, gases, solvents and other materials used are summarized in **Table 2**:

Table 2: List of chemicals and materials used

Material	Formula	Supplier	Purity	Abbreviation
Acetone	C_3H_6O	VWR Chemicals	technical	-
Acetonitrile	C_2H_3N	Roth	>99.9%	MeCN
Alpha,alpha-Azoisobutyronitrile	$C_8H_{12}N_4$	Molekula		AIBN
Aniline	C_6H_7N	Sigma Aldrich	(99%), Freshly distilled	-
Sodium anthraquinone 2-sulfonate monohydrate	$C_{14}H_7NaO_5S$ * H_2O	TCI Chemicals	>98%	AQS
Benzoylperoxide	$C_{14}H_{10}O_4$	Merck	for synthesis, 25% H_2O	BPO
2,2'-bipyridyl	$C_{10}H_9N_2$	Sigma Aldrich	>99%	Bpy
1,4-dichloro anthraquinone	$C_{14}H_6Cl_2O_2$	TCI Chemicals	98%	DCAQ
Chloroform	$CHCl_3$	VWR Chemicals	for analysis	$CHCl_3$
Bis(1,5-cyclooctadiene) nickel(0)	$C_{16}H_{24}Ni$	Alfa Aesar	96%	Ni(COD)$_2$
Cis,cis-1,5-cyclooctadiene	C_8H_{12}	Alfa Aesar	99%, stabilized with 50-200ppm Irganox	COD
N,N-dimethyl formamide	C_3H_7NO	Sigma Aldrich	anhydr., 99.8%	DMF
Dimethylsulphoxide	C_2H_6SO	VWR	rectapur, 99.7%	DMSO
Ferrocene	$C_{10}H_{10}Fe$	Sigma Aldrich	98%	Fc
Glassy carbon plate, 2mm		Alfa Aesar	Type 1	GC
Hydrochloric acid	HCl	Merck	37%	HCl
Hydrogen peroxide	H_2O_2	Merck	for synthesis, 30%	H_2O_2
Methanol	CH_4O	VWR Chemicals	AnalaR NORMAPUR	MeOH
Nitrogen	N_2	JKU houseline		N_2
Iso-propanol	C_3H_8O	VWR Chemicals	technical	IPA
Oxygen	O_2	Linde	5.0	O_2
P-nitrophenyl boronic acid	$C_6H_6BNO_4$	Alfa Aesar	95%	*p*NBA
Poly(diallyldimethylammonium chlorid) (M_w=200.000-350.000)	$[C_8H_{16}ClN]_n$	Sigma Aldrich	20% (*m/m*) in H_2O	PDADMAC
Potassium chloride	KCl	Alfa Aesar	99%	KCl
Potassium dihydrogen phosphate	KH_2PO_4	Sigma Aldrich	puriss, 99.5-100.5%	
Potassium hydrogen phosphate	K_2HPO_4	Sigma Aldrich	>98%	
Potassium hexacyanoferrate (III)	$K_3[Fe(CN)_6]$	Sigma Aldrich	>99%	

Pyrrole	C_4H_5N	Sigma Aldrich	(98%), Freshly distilled	-
Silver wire	Ag	Alfa Aesar		
Sodium carbonate	Na_2CO_3	Fluka	>99.5%	
Sodium hydrogen carbonate	$NaHCO_3$	Sigma Aldrich	99.7 – 100.3%	
Sodium hydrogen sulphate monohydrate	$NaHSO_4$ * H_2O	Alfa Aesar	reagent grade	
Sodium hydroxide	NaOH	Alfa Aesar	98%	
Sodium sulphate	Na_2SO_4	Sigma Aldrich	>99.0%	
Sulphuric acid	H_2SO_4	J. T. Baker	95 – 97%	
Tetrabutylammonium hexafluorophosphate	$C_{16}H_{36}F_6NP$	Sigma Aldrich	>99.0%	$TBAPF_6$
Toluene	C_7H_8	VWR Chemicals	AnalaR NORMAPUR	
2-vinyl anthraquinone	$C_{16}H_{10}O_2$	Sigma Aldrich	>98%	

2.2. Electrode preparation

The disc-type electrodes like the RDE as well as the GC/Pt RRDE and the 3 mm diameter GC electrode (PalmSens) were polished prior to being used with Buehler Micropolish II deagglomerated alumina pastes. For this method, an Al_2O_3 paste with decreasing particle size from 1.0 to 0.3 and 0.05 µm was used for 30 sec each on a polishing pad (Figure 25a). In between, the electrodes were rinsed with 18 MΩ water (MQ water) and isopropanol (IPA).
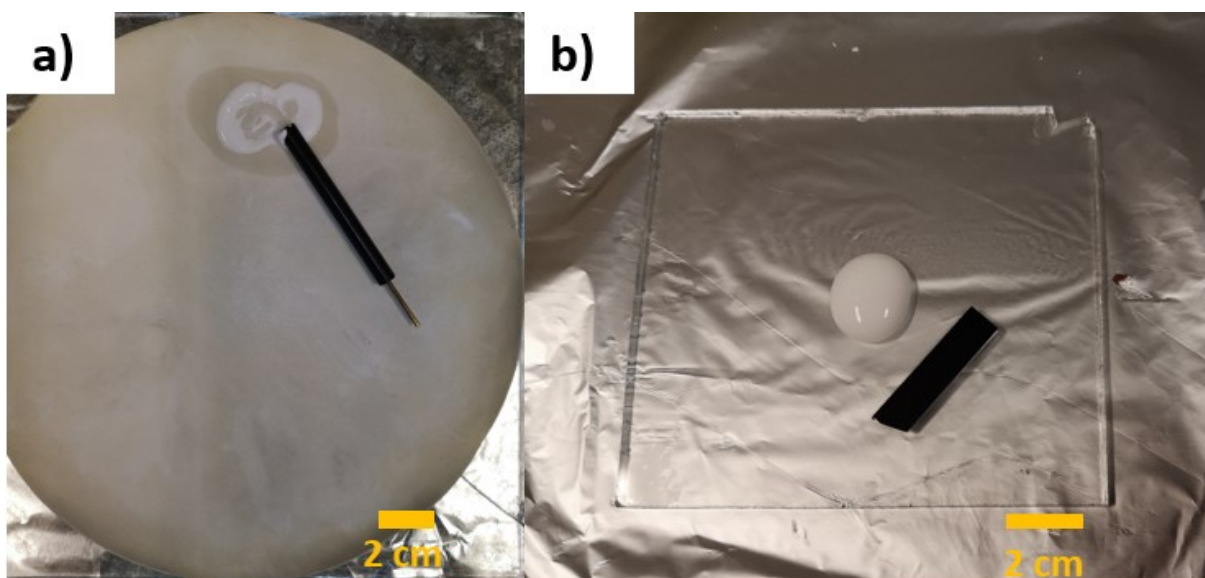

Figure 25: Polishing of GC electrodes with alumina pastes for a) disc-type GC electrode (black rod) with a polishing pad and the white Al_2O_3 polishing paste and b) a 1x4 cm GC plate (black) on a glass plate with white Al_2O_3 polishing paste.

For chronoamperometric studies, 2 mm thick GC electrodes (Alfa Aesar, Type 1) cut in the size of 1 x 4 cm were also polished with the same polishing pastes in sequence of decreased particle size for 1 min each, on a glass plate (Figure 25b). In between, cleaning was performed with sonication in MQ and IPA for 15 min each. In order to remove excess alumina particles, a last polishing step using toothpaste was done for 1 min each, followed again by sonication in MQ water and IPA for 15 min each.

As final step, electrochemical treatment was performed by sweeping the potential between +1.5 V and -1.0 V vs. Ag/AgCl (3M KCl) for 30 cycles at a scan rate of 50 mV s^{-1}.

2.3. Electrochemical characterization

2.3.1. Cyclic Voltammetry

For the electrochemical experiments in this work, either a Jaissle Potentiostat-Galvanostat PGU10V-100 mA, a Jaissle Potentiostat-Galvanostat 1030 PC-T or an Ivium Vertex One.EIS were used as shown in Figure 26.
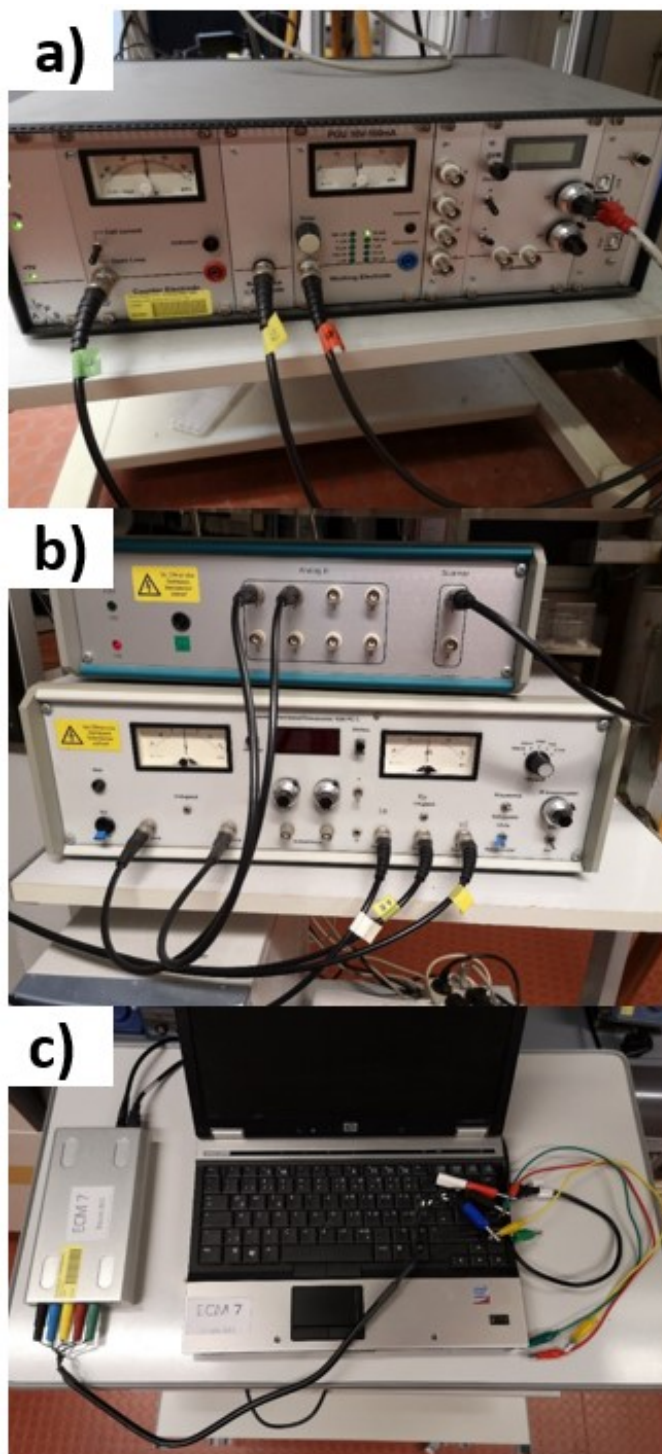

Figure 26: Images of the potentiostats used. a) Jaissle Potentiostat-Galvanostat PGU10V-100 mA, b) Jaissle Potentiostat-Galvanostat 1030 PC-T with a 10 V application voltage but a maximum current range of 1 A and c) Ivium Vertex One.EIS with 10 V application voltage and a maximum current range of 100 mA.

Cyclic voltammetry (CV) experiments in aprotic, organic solvents were all performed in a 0.1 M TBAPF$_6$ solution in acetonitrile (MeCN) in a one-compartment cell (Figure 27a).
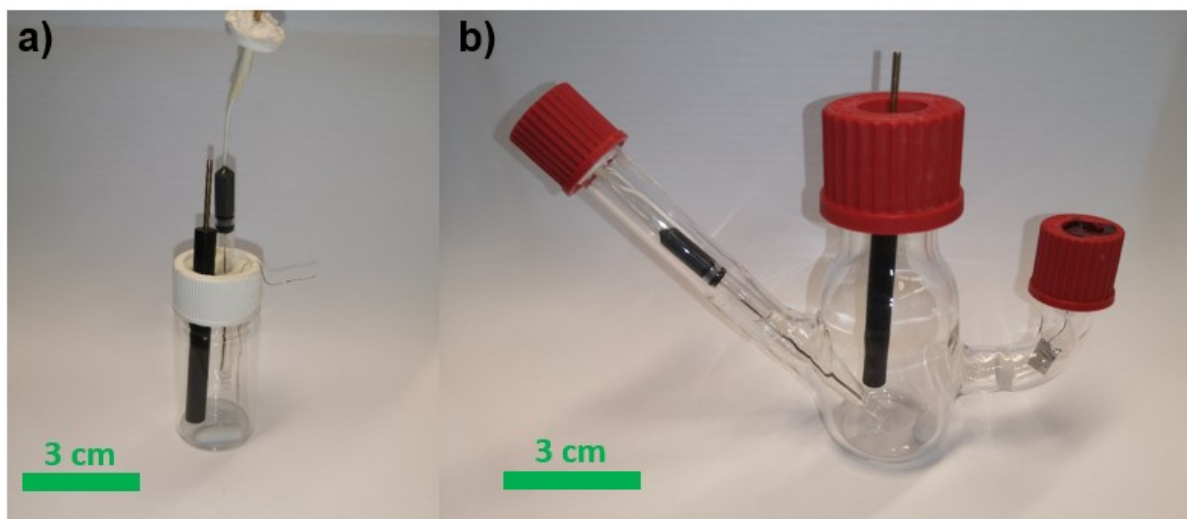
Figure 27: a) One-compartment electrochemical cell with GC as WE, Pt as CE and Ag/AgCl (3M KCl) as RE and b) two-compartment electrochemical cell separated with a glass frit and GC as WE, Pt as CE and Ag/AgCl (3M KCl) as RE.

10 mL of the electrolyte solution were used with a 3 mm GC disc-type electrode as WE (see section 2.2. for polishing details), a platinum plate as CE and a silver wire covered with silver chloride (denoted as Ag/AgCl) as quasi-reference electrode (QRE). All CV experiments in MeCN were performed in a nitrogen filled glove box to enable inert conditions throughout the experiment. Directly after the experiment, ferrocene was added and the QRE calibrated versus this ferrocene standard. The graphical illustration of this conversion calculation together with the conversion potential is given in the following Figure 28:
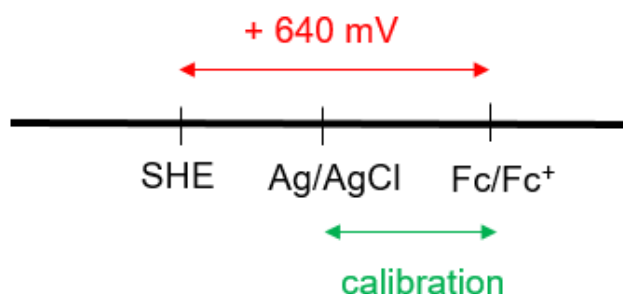

Figure 28: Conversion of potentials vs. QRE into vs. SHE via ferrocene calibration. Conversion potentials are reproduced from literature.[81,192]

Due to this reason, all potentials mentioned throughout this work are recalculated and referenced versus the standard hydrogen electrode (SHE). CV experiments in aqueous solution were performed as electrolyte solutions with the salts, concentration and pH values as stated. 20 mL of the electrolyte solution were used in a 2-compartment (see Figure 27b) cell separated by a sintered glass frit using glassy carbon as working electrode (WE) and a platinum plate as counter electrode (CE). In nearly all electrochemical experiments in aqueous solutions, commercial Ag/AgCl (3M KCl) (BASi) electrodes were used as RE and thereby all potentials mentioned throughout this work are recalculated and referenced versus the SHE. The only exception is the potentiodynamic electropolymerization of aniline where a saturated calomel electrode (SCE) was used as RE (see chapter 3.5.

As the experiments in aqueous solution were performed under ambient conditions, the sealed cell was purged prior the electrochemical measurements with the respective gas (either nitrogen or oxygen) for 1 h to achieve the conditions stated.

2.3.2. Chronoamperometry

As already mentioned in chapter 2.3.1. the chronoamperometric electrochemical experiments were all performed in aqueous solution on either a Jaissle Potentiostat-Galvanostat PGU10V-100 mA or a Jaissle Potentiostat-Galvanostat 1030 PC-T.

Like for the CV experiments in aqueous solutions, also the chronoamperometries were performed in these 2-compartment cells with 20 mL electrolyte solution. Throughout the electrolysis time, the cell was gently stirred while applying a constant potential which was recalculated versus the SHE. Before starting the chronoamperometry and after certain times, 150 µL aliquots of the electrolyte solution were taken and analyzed for the quantities H_2O_2 produced as described in the next chapter 2.4.

From the current measured over time and the electric charge respectively, the moles H_2O_2 produced can be recalculated as so-called faradaic efficiency using the following equation:

$$FE(\%) = \frac{v_{reaction} \cdot n_{product}}{moles\ of\ electrons} \cdot 100$$

Eq. 16

As the electrochemical reduction of oxygen to H_2O_2 is a 2-electron reduction process, $v=2$ in this case. This faradaic efficiency indicates how many percent of all charges induced were directly used for the desired H_2O_2 production reaction. Although the meaning of the faradaic efficiency is always the same, the formula in Eq. 16 differs from the one in chapter 1.3.3. Eq. 15 just by the experimental method approach, as Eq. 16 is the universal formula whereas Eq. 15 is an adjusted one used for RRDE experiments.

2.3.3. Rotating (ring) disc electrochemistry

For experiments involving hydrodynamic convection, an IPS Jaissle PGU BI-1000 Bipotentiostat-Galvanostat attached to an IPS PI-ControllerTouch unit and an IPS Rotator 2016 rotating unit was used as shown in Figure 29a:
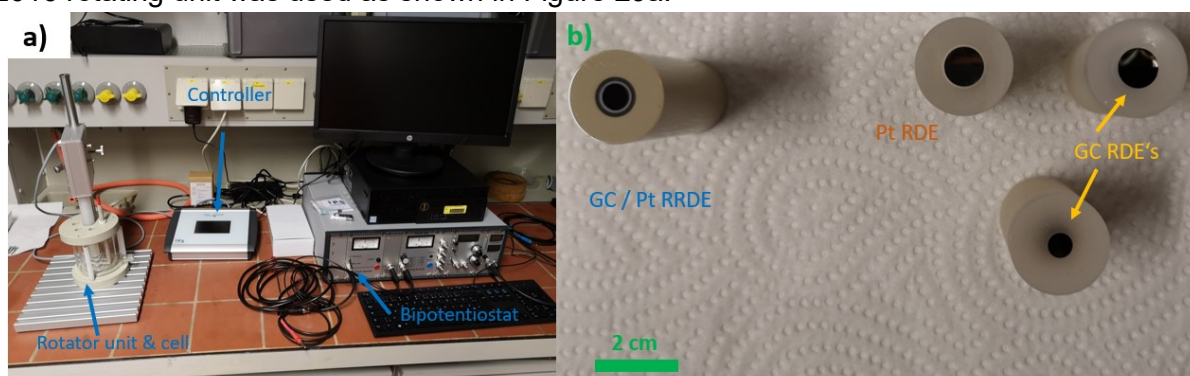

Figure 29: a) Picture of the rotating (ring) disc electrode setup including the bipotentiostat, the rotator unit and the rotation controller and b) picture of the GC/Pt RRDE in PEEK and GC and Pt RDE's in PTCFE.

As stated in the respective chapter, either an 8 mm diameter GC or Pt disc in poly(chloroflouroethylene) (PTCFE) or the RRDE consisting of a GC disc (Ø = 5 mm) in polyether ether ketone (PEEK) with a Pt ring (Ø$_m$ = 7 mm) was used as WE. The electrode preparation via polishing was done according to the procedure described in chapter 2.2. In all cases a platinized electrode was used as CE and an Ag/AgCl (3M KCl) electrode mounted in a Luggin capillary was used as RE in the cell shown in Figure 29a. 120 mL of electrolyte solution were used in all experiments, the cell was tightly closed and prior the experiment purged for 1 h with N_2 or O_2 to achieve saturated conditions. For all linear sweep voltammograms (LSV), a scan rate of 10 mV s^{-1} was used throughout the whole work.

Throughout all RRDE measurements, the potential given on the *x*-axis corresponds to the one applied at the disc while the ring potential was always kept constant throughout a sequence of measurements. Which ring potential was actually required for a certain type of measurement was experimentally determined via CV before (as illustrated in the results chapter, Figure 42)

2.4. H_2O_2 quantification

The quantification of the amounts of H_2O_2 produced during electrolysis in the electrolyte solution was done via a photometric method initially reported by Su, Wei and Guo[193] and adapted at the LIOS by Apaydin and collaborators.[105]

The reaction solution consists of a 1:1 volumetric ratio of 4 mM *p*-nitrophenyl boronic acid (*p*NBA) in DMSO solution and 150 mM Na_2CO_3/$NaHCO_3$ aqueous buffer solution at pH=9, which was filtered through a syringe filter (0.45 µm, RC). Throughout an electrolysis, (see chapter 2.3.2. aliquots of 150 µL electrolyte solution were taken with a needle and a 1 mL syringe at certain times. 50 µL of each aliquot were mixed with 2.0 mL of the reaction solution in a 4 mL brown vial and incubated for 36 min at room temperature under these dark conditions. Thereby the following reaction, according to Figure 30, occurs:
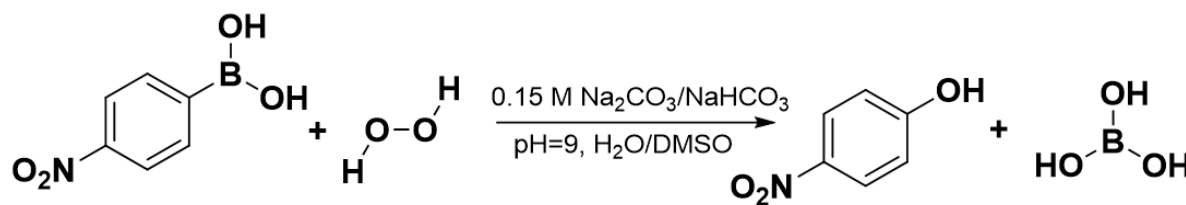

Figure 30: Reaction equation for the stoichiometric reaction of H_2O_2 with the *p*NBA forming *p*-nitrophenol.

As the *p*NBA only absorbs light in the UV region whereas the *p*-nitrophenol has an absorption maximum at 411 nm, this color change upon reaction with H_2O_2 can be used for quantification. In order to do so, after this 36 min reaction time, 100 µL aliquots were transferred onto a microplate as triplicates and the absorbance values at 411 nm for all samples simultaneously recorded on a Thermo Fischer Multiskan Go Microplate Spectrophotometer. In order to quantify the amounts of H_2O_2, a calibration curve was made from H_2O_2 standard solutions following the same procedure as shown in Figure 31. In all cases, the measured absorbance values were subtracted by the absorbance values of a blank sample and this Δabsorbance was used for the actual calculations- also considering the total electrolyte solution volume.
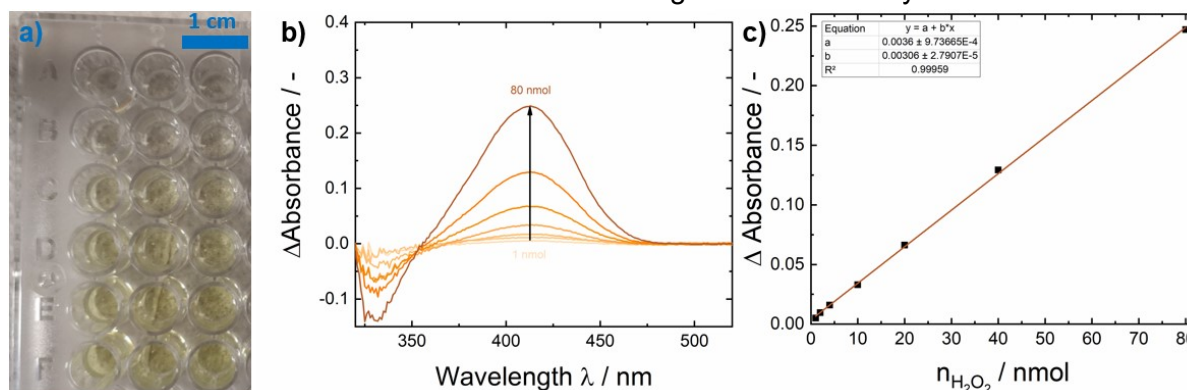

Figure 31: a) Picture of the microplate with samples of increasing [H_2O_2], b) subtracted absorbance spectra of the H_2O_2 calibration and c) calibration curve of H_2O_2 for quantification.

2.5. Scanning electron microscopy

Scanning electron microscopy (SEM) is a powerful technique for imaging sub-millimeter features. In contrast to common light microscopes, instead of electromagnetic radiation (light), electrons are used for focusing and imaging. Due to the better resolution of electrons, based on quantum mechanics, higher resolutions far below the wavelength of visible light are possible. The first electron microscope was already built in the early 1930s by Ruska and Knoll, for which Ruska was awarded the Nobel Prize in Physics in 1986.[194,195]
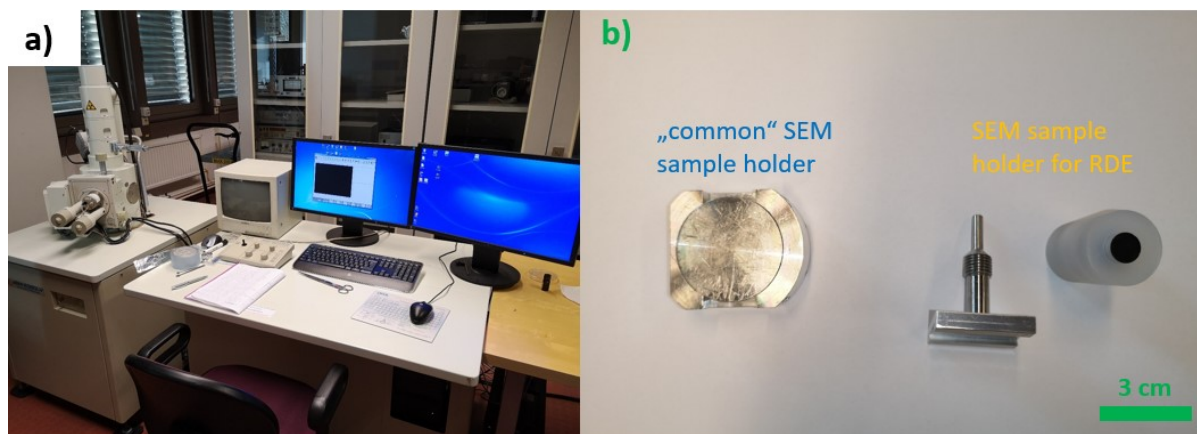

Figure 32: a) Picture of the mainly used scanning electron microscope (SEM): JEOL JSM-6360LV, and b) sample holders used for SEM.

Throughout this work, all SEM images were almost exclusively recorded on this JEOL JSM-6360LV scanning electron microscope shown in Figure 32a. The samples were mounted in the vacuum chamber in such a way, that sufficient electric conductivity was preserved for high quality imaging with one of the sample holders shown in Figure 32b. Optimized settings for imaging conductive carbon-based substrate materials are an acceleration voltage of 7 kV and a working distance of 12 mm under high vacuum conditions.

For higher resolution images, a SEM ZEISS 1540 XB cross beam scanning electron microscope, equipped with a vacuum antechamber, was operated at an acceleration voltage of 3 kV and a working distance of 3.5 mm.

2.6. Nuclear magnetic resonance spectroscopy

^{1}H-NMR spectra were recorded by dissolving approximately 5 mg of the compound in 600 µL deuterated chloroform ($CDCl_3$), transferring into an NMR tube and measuring on a Bruker® Advance 300 spectrometer. Diffusion ordered spectroscopy (DOSY) NMR spectra were recorded on a Bruker Avance III 500 spectrometer.

The 1D ^{1}H-NMR spectra were recorded by Yolanda Salinas. The 2D DOSY spectra were recorded and fitted by Matthias Bechmann.

2.7. UV-Vis spectroscopy

The equipment described in this chapter was used to determine the optical properties like absorption maxima and extinction coefficients of materials in solution and thin-films as well as for in-situ spectroelectrochemistry. In contrast to these photophysical characterizations, the quantification of H_2O_2 via the boronic acid method and the microplate reader are described in detail in chapter 2.4.

All measurements of dissolved samples were recorded on a Varian Cary 3G UV-Visible spectrophotometer as shown in Figure 33:
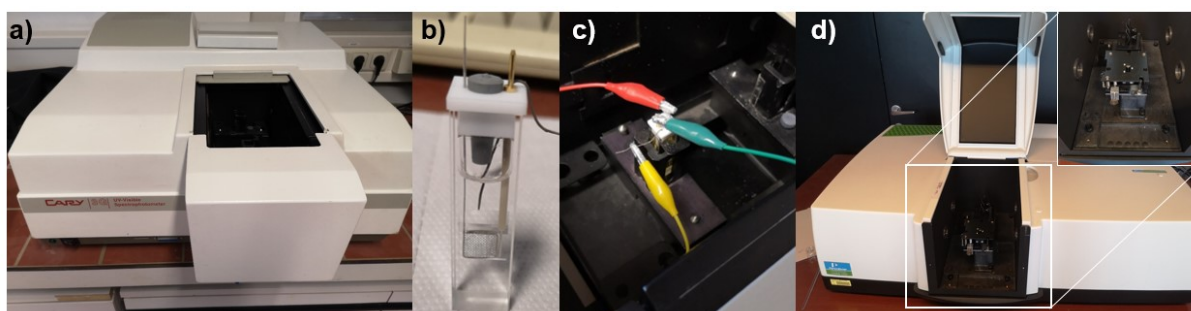

Figure 33: a) Photo of the Varian Cary 3G UV-Visible spectrophotometer, b) picture of the UV-Vis spectroelectrochemical cell, c) illustration of the mounting of the spectroelectrochemical cell inside the spectrophotometer and d) photo of the Perkin Elmer Lambda 1050 UV/VIS/NIR spectrometer with the reflectance unit mounted.

Standard UV-Vis absorption spectra of homogeneously dissolved compounds were recorded in a quartz cuvette with 10 mm path length between 250 and 700 nm at a scan rate of 600 nm s^{-1}. For in-situ spectroelectrochemical studies, the spectroelectrochemical cell (BASi) shown in Figure 33b with 1 mm path length, a Pt mesh as WE, a Pt rod as CE and an Ag/AgCl as QRE was used. An Ivium Vertex One.EIS (Figure 26c) was used to modify the applied potential in -100 mV steps every 40 s where meanwhile absorption spectra were recorded between 300 and 700 nm with a scan rate of 1515 nm s^{-1}.

UV-Vis absorptance spectra of blade coated polymer films on quartz glass were recorded on a PerkinElmer Lambda 1050 spectrophotometer (Figure 33d). UV-Vis transmittance spectra were recorded in a standard thin-film sample holder whereas the reflectance measurements were recorded using a 6° specular reflectance accessory.

The UV-Vis transmittance and reflectance spectra were recorded and re-calculated for absorptance values by Felix Mayr.

2.8. Fourier-transform infrared spectroscopy

Fourier transform infrared spectroscopy (FTIR) has become the most-prominent IR measurement technique throughout the last 70 years.[196] As a result of the longer wavelength of IR radiation compared to the visible light, the FTIR uses a Michelson interferometer with beam splitter and a moveable mirror for recording the data as illustrated in Figure 34.[196,197] Due to this unique setup, multiple measurements can be recorded in reasonable time frames and by averaging several scans, a high spectral resolution can be obtained. [196,197] A mercury-cadmium-telluride (MCT) detector, which has to be cooled prior measurement with liquid nitrogen was used.
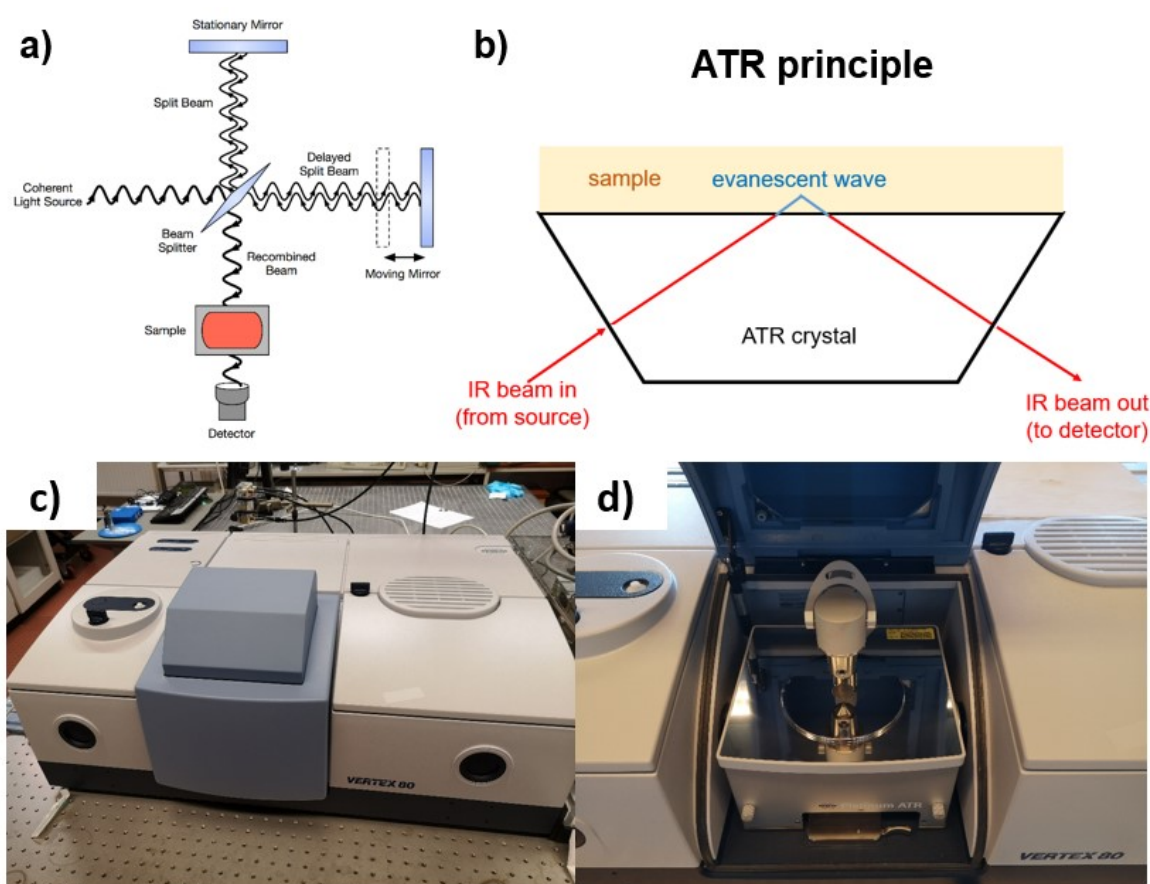

Figure 34: a) Scheme of an FTIR, reproduced from Wikimedia Commons[198], b) scheme of an ATR spectroscopy measurement mode, c) picture of the Vertex 80 FTIR and d) picture of the Platinum ATR unit.

The Bruker Vertex 80 spectrometer shown in Figure 34 was used for measurements in an attenuated total reflection (ATR) mode as it is equipped with a Platinum ATR module. Thereby the sample can be loaded as either liquid or solid (as powder or thin-film on an electrode) on a diamond crystal. In an ATR geometry according to Figure 34b, the IR beam is reflected by the crystal and sample interface, where some frequencies are absorbed by the sample, which is called evanescent wave. These bands missing via attenuation are the ones analyzed and detected. By applying moderate pressure with the lever on the sample and purging the whole measurement chamber for 2 min with N_2 gas, precise measurements avoiding fluctuations by trapped air can be performed.

ATR-FTIR measurements were performed at a resolution of 2 cm^{-1} between 4000 and 500 cm^{-1} averaging 32 scans.

2.9. Contact angle measurements

The contact angle of blank GC and drop-casted polymer films was determined by an Ossila Angle Goniometer as shown in Figure 35:
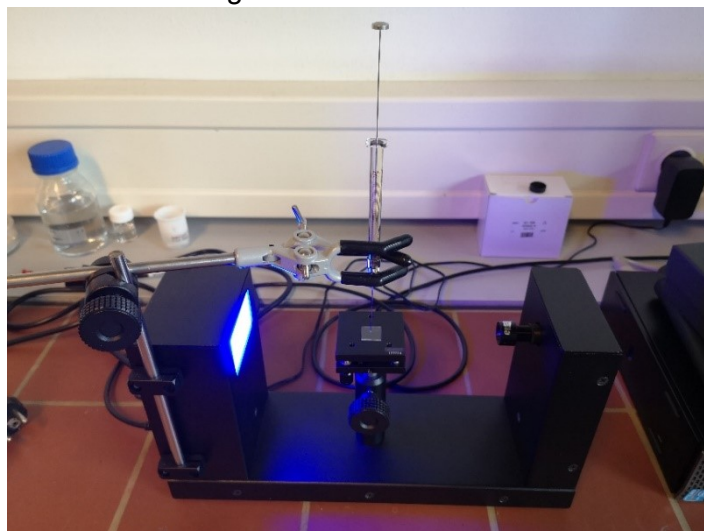

Figure 35: Ossila Angle Goniometer setup for contact angle determination.

All measurements were performed at room temperature using MQ water and the fitting calculations and determination of the contact angle was done within the integrated Ossila Contact Angle v.3.0.4.0 software.

2.10. Thermogravimetric analysis (TGA)

The thermogravimetric analyses of the monomers and polymers were performed in platinum pans using approximately 1-10 mg per measurement. A TGA/PerkinElmer Q5000 was used for measurements between 50 and 900 °C at a heating rate of 10 °C min^{-1} under nitrogen (N$_2$) flow (25 mL min^{-1}) as depicted in Figure 36:
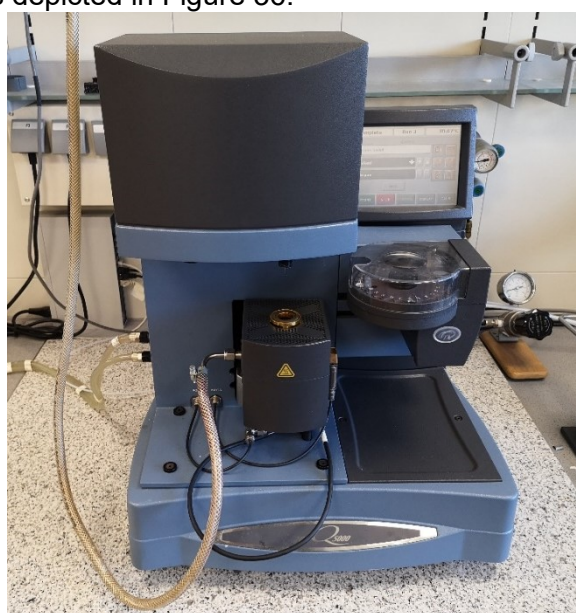

Figure 36: TGA/Perkin Elmer Q5000.

The sample preparation was done by Maria Würflinger and the TGA measurements were performed and fitted by Yolanda Salinas.

3. Results and Discussion

As outlined in the introductory chapter 1.2. the electrochemical oxygen reduction reaction forming H_2O_2 is a promising technological route within the scope of renewable energy storage. Although the 2-electron reduction reaction forming H_2O_2 seems to be facile, the further reduction forming water as unwanted side product is challenging.

Therefore the key-challenge for efficient reductive electrochemical H_2O_2 production is to develop and characterize electrocatalysts, which are highly selective for the O_2 to H_2O_2 reaction and suppress the further reduction to water.

3.1. Electrochemical oxygen reduction on common electrode materials

Like for all electrocatalytic investigations, the selection of inert supporting electrode materials is crucial. In the ideal case, this material has a large electrochemical potential window and shows no intrinsic electrocatalytic behavior towards the target reaction. Within the scope of this work, this target reaction is the O_2 to H_2O_2 reduction reaction.

In contrast to other target reactions like to hydrogen evolution reaction (HER) or the CO_2 reduction reaction (CO_2RR) where common electrode materials like glassy carbon (GC) or conductive oxide materials exhibit the desired properties, for the oxygen reduction reaction the situation is more complicated.

Since decades, carbon-based electrode materials are well known electrocatalysts for the O_2 to H_2O_2 reduction reaction giving high H_2O_2 selectivity.[5] The reason for this catalytic behavior on an atomistic scale is beyond the scope of this work, but already thoroughly studied in literature.[62,65,67,69,199]

Screening the periodic table of elements for possible metal electrodes shows that numerous research groups found out via experiments, as well as theoretical calculations, that the metals can all be classified in two groups: some metals like platinum and palladium prefer the direct 4-electron reduction to water, whereas some metals like gold and silver show high selectivity towards to 2-electron process forming H_2O_2.[50,51,200,201]

Checking literature reports on electrocatalytic investigations for the oxygen reduction reaction reveals that the majority uses GC[68,125,129] electrodes, although also some report fluorine doped tin oxide (FTO)[153,187], titanium dioxide (TiO_2)[105,106] or gold electrodes[151,202]. Surprisingly, in most of the reports no blank electrode reports on the amounts of H_2O_2 produced or sometimes even no CVs are given. Only some recent papers report boron-doped diamond (BDD) electrodes as prime candidate for studying the oxygen reduction, as this material itself has a high overpotential for ORR.[121,122]

The goal within this work is the use of common commercially available electrode materials, thus the background ORR of GC, platinum, titanium and gold was investigated:
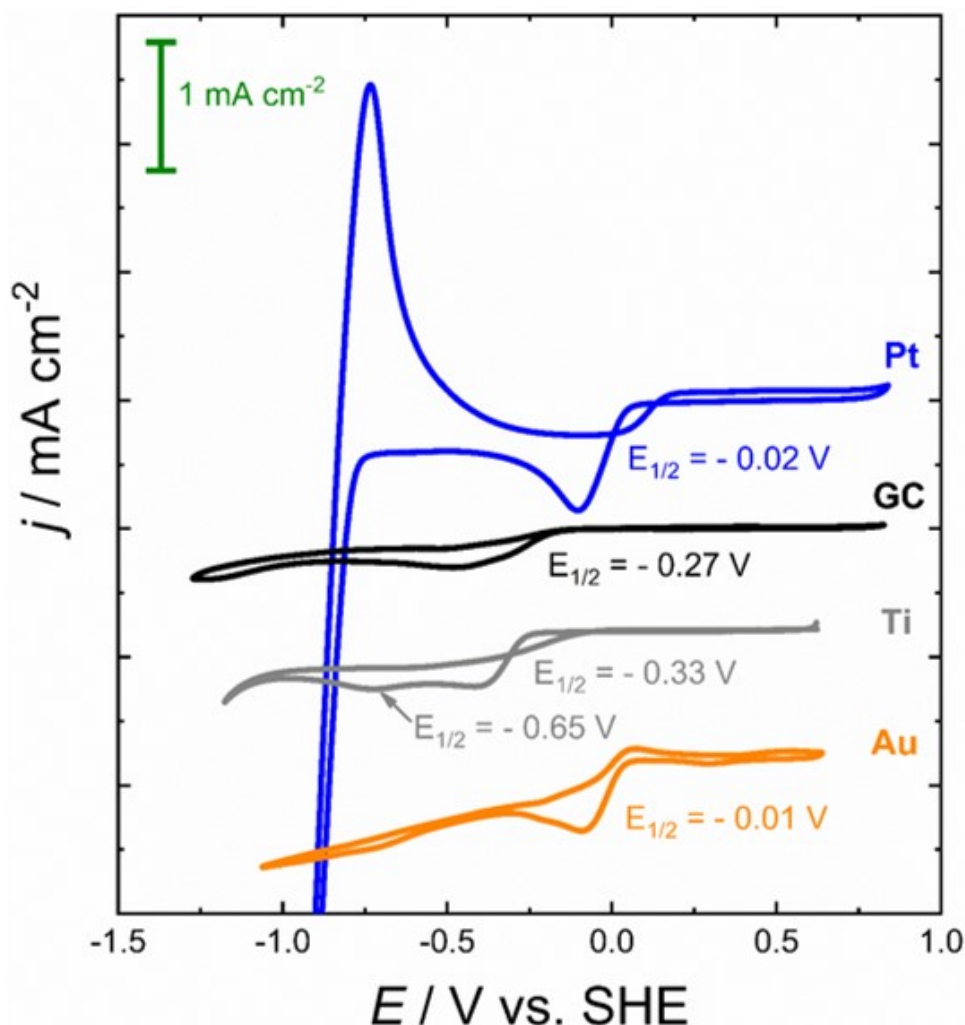
Figure 37: CV of Pt, GC, Ti and 5 nm Cr / 80 nm Au on glass electrodes recorded in 0.1 M NaOH under O_2 saturated conditions at a scan rate of 20 mV s^{-1}. For clarification, the large current responses from the platinum hydrogen evolution phenomena are not shown in detail here.

As can be seen from Figure 37, all four materials studied (Pt, GC, Ti and Au) showed an electrocatalytic effect towards the oxygen reduction in the potential region between ca. 0.0 V and -0.33 V. Thereby glassy carbon is the least active electrode material with the most negative ORR potential and the lowest current density whereas platinum shows the highest current density for ORR at nearly the same potential like gold.

Further results on mechanistic details on the ORR steps on these materials can be found in literature.[118,200,203–207]

In addition to CV studies under unstirred conditions, introducing electrochemical experiments with hydrodynamic control, namely rotating disc electrodes (RDE), allow further insights into the ORR mechanisms. As outlined in chapter 1.3.3. performing the so-called Koutecky-Levich analysis on LSV's at different rotation rates ω allows the determination of the number of electrons transferred per reduction reaction n. According to the reactions equations in Figure 7, an n value of 2 corresponds to only H_2O_2 as product whereas an n value of 4 means that water is the only product of the ORR.

Comparing commercial RDEs with GC and platinum, the LSV curves as well as the according Koutecky-Levich plots in 0.1 M phosphate buffer (PB) are depicted in the following Figure 38:
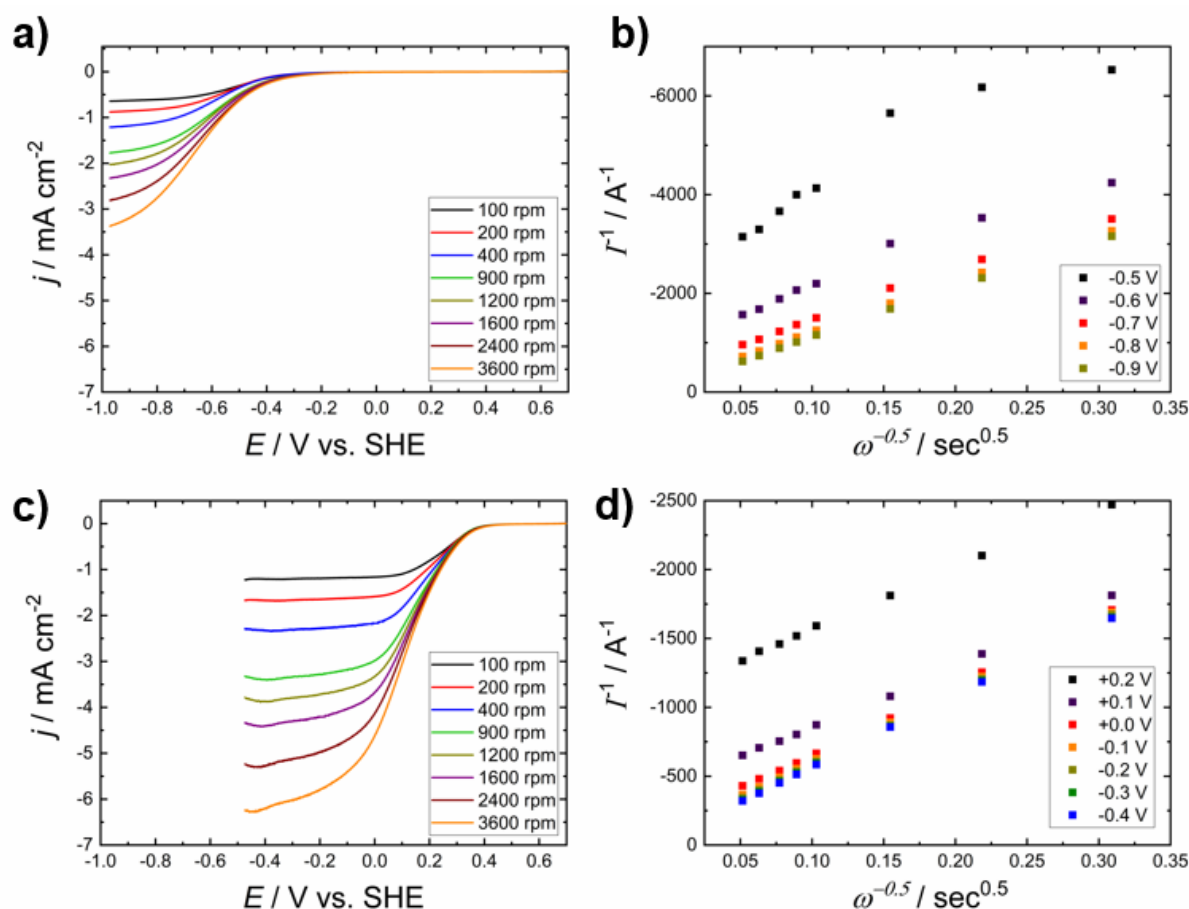
Figure 38: RDE-LSV curves of a) GC and c) Pt electrode recorded in 0.1 M PB at pH=7 at the rotation speeds given. The Koutecky-Levich plots are illustrated in the part b) and d).

In accordance with the CV curves in Figure 37, also the onset potentials of GC and Pt in Figure 38 are quite apart. At platinum the oxygen reduction reaction already starts around +0.2 V whereas in case of GC the onset is around -0.4 V. In case of Pt already at around -0.4 V the mass transfer only limited regime is reached. Starting at potentials slightly more negative than these onsets, the Koutecky-Levich analysis can be performed. As depicted in Figure 38, in case the curves of GC and Pt, the data points follow the Koutecky-Levich equation as shown in Eq. 11. Based on these experimental results, the number of transferred electrons per reduction reaction n was determined for GC and platinum at different pH values from pH=2 to pH=13:
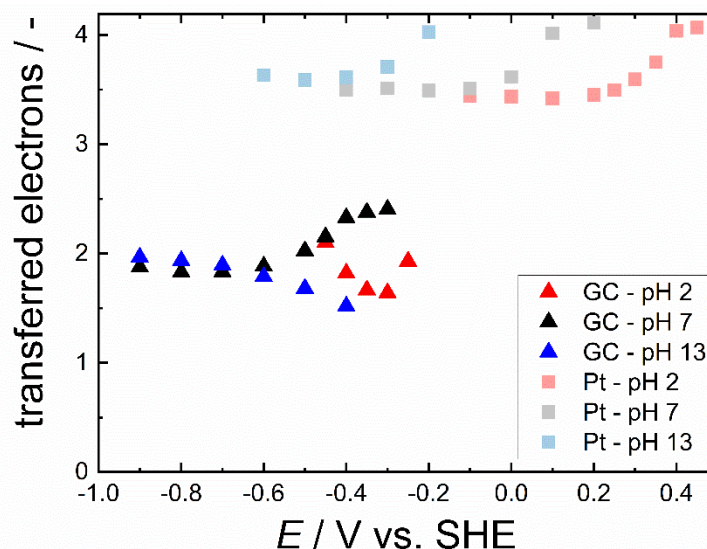
Figure 39: Number of transferred electrons per reduction reaction *n* for GC and platinum determined in 0.1 M NaHSO₄ solution (pH=2), 0.1 M PB solution (pH=7) and 0.1 M NaOH solution (pH=13).

The underlying LSV curves (at pH=7) for the *n* values calculated in Figure 39 are shown in Figure 38.These results depicted in Figure 39 clearly show, that nearly independent on the pH value, GC prefers the 2-electron reduction step to H_2O_2 whereas in case of platinum the 4-electron reduction to water dominates. As expected from thermodynamics as a result of the Nernst equation, the onset for the ORR is pH dependent. Values above 4 in case of platinum and values below 2 for GC are an indication, that this RDE method involves multiple experimental as well as calculation steps which cause some errors. Obviously, such values cannot be explained chemically, but a distinct difference between GC and platinum can be clearly demonstrated with this graph.

For further hydrodynamic electrochemistry measurements using rotating ring-disc electrodes (RRDE), a commercial electrode with a GC disc and a platinum ring was used. As stated in chapter 1.3.3. / Eq. 13, one important parameter of each RRDE for quantitative measurements is its collection efficiency *N*. Although sophisticated formulae exist for calculating this *N* for certain RRDE systems[73,84,208], the more convenient way is to determine the experimental collection efficiency N_{exp} via calibration using a known redox couple, for example $K_3[Fe(CN)_6]$ following Eq. 13, as shown in the following Figure 40:
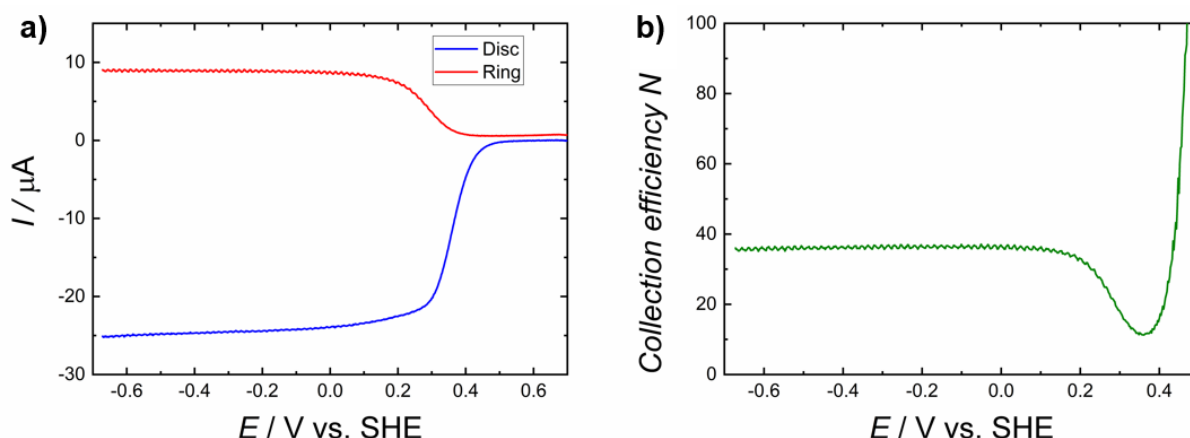
Figure 40: a) RRDE-LSV recorded in 1 mM $K_3[Fe(CN)_6]$ in 0.1 M PB at 100 rpm (Ring potential at +0.73 V) and b) the according plot of the experimental collection efficiency N_{exp}.

As can be seen from the LSV curve and the trend of N_{exp}, at potentials more negative than +0.1 V a very stable mass-transport limited regime is observed at 100 rpm. At faster rotation speeds, this onset is slightly, cathodically shifted and therefore an average of the N_{exp} values between -0.4 and -0.7 V are used for determination of the N_{exp} value at certain rotation speeds as depicted in Figure 41:
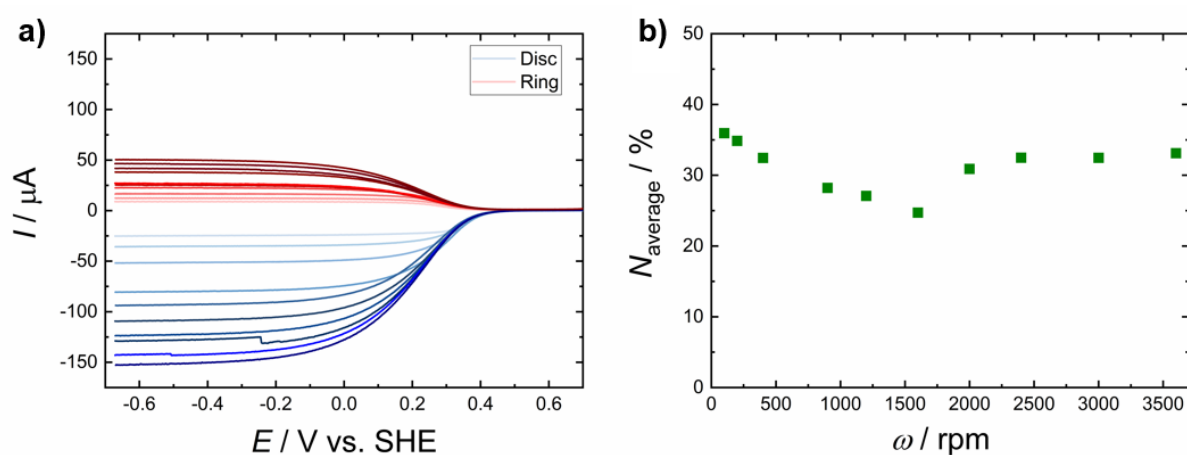

Figure 41: a) RRDE-LSV curves in 1 mM $K_3[Fe(CN)_6]$ in 0.1 M PB at rotation speeds between 100 and 3600 rpm and b) according average values of N_{exp} at the rotation speeds stated. Reproduced with permission from Rabl *et al.* (https://pubs.acs.org/doi/abs/10.1021/acsaem.0c01663)[209] © 2020 American Chemical Society.

The RRDE-LSV curves in Figure 41 at all rotation speeds investigated follow the trend of reaching a mass-transport limited plateau with increased current at faster ω. Based on these disc and ring current values, N_{exp} values for each rotation speed were calculated and used for further calculations. The values ranged from 25 % to 36 %, which is in good agreement to literature reports.[68,82,84]

Prior the RRDE experiments for investigating the oxygen reduction reaction, the oxidation potential of H_2O_2 on the platinum ring was determined according to Figure 42:
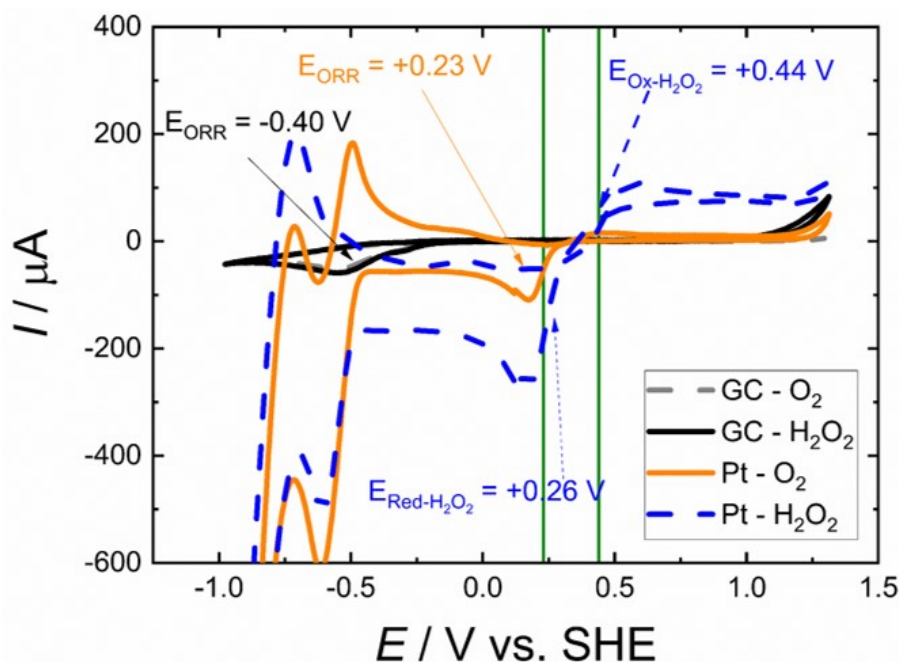
Figure 42: CV of GC and Pt from the RRDE in 0.1 M PB under O_2 saturated conditions and with 5 mM H_2O_2 added

Similar to Figure 37, the reduction potential for oxygen reduction of GC is significantly cathodically shifted compared to platinum. Furthermore, in case of GC (as shown in the black curve) the addition of H_2O_2 does not change the reduction behavior at all and in the potential range shown only the onset of the H_2O_2 oxidation. On the other hand, in case of platinum, the addition of H_2O_2 increases the reductive current but leaves the reduction potential at a nearly unchanged position.

Based on these results from Figure 42, one can deduce the required potentials to be applied at the ring electrode. As the goal of RRDE when studying the ORR is the detection of the H_2O_2 produced at the disc via re-oxidation, the ring potential has to be more positive than +0.44 V in order to enable this. Usually, an even slightly more positive potential is used in order to avoid kinetic limitations. Interestingly, from a thermodynamic point of view an area exists between the potential window marked by green lines in Figure 42, where in theory a potential could be applied without reducing oxygen or oxidizing H_2O_2 – which would be interesting for experiments described in chapter 3.2. These experiments showed, that from a practical point of view, such a condition could not be achieved, which means that on platinum electrodes you always either reduce oxygen or oxidize H_2O_2.

With this knowledge in mind, the blank GC/Pt RRDE was characterized for the electrocatalytic behavior towards the oxygen reduction reaction with LSV. The LSV curves from the disc currents (I_D) and ring currents (I_R) were recalculated with Eq. 15 to obtain the faradaic efficiency (FE) for H_2O_2 produced as shown in Figure 43:
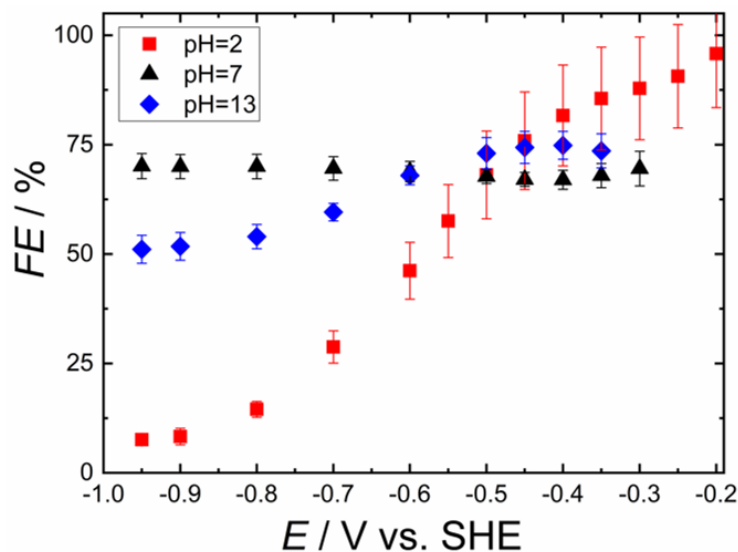
Figure 43: Faradaic efficiency values for H_2O_2 produced on a GC/Pt RRDE in various pH conditions: 0.1 M NaHSO4 solution at pH=2, 0.1 M PB at pH=7 and 0.1 M NaOH solution at pH=13. The error bars indicate the deviations from different rotation speeds. Reproduced with permission from Rabl *et al.* (https://pubs.acs.org/doi/abs/10.1021/acsaem.0c01663)[209]. © 2020 American Chemical Society.

As can be seen from Figure 43, under neutral conditions, GC produces H_2O_2 at a nearly unchanged *FE* over the potential range measured of around 70%. In alkaline media, GC shows a higher faradaic efficiency for H_2O_2 at moderate potentials down to -0.5 V of around 75%, which declines down to 50% at -1.0 V. This higher selectivity, at low overpotentials for H_2O_2 but further reduction to water at negative potentials in alkaline conditions, is in agreement with literature reports.[204,205,210] This deceasing trend is even more pronounced at pH=2, where at more positive potentials starting at -0.2 V a very high *FE* close to unity was measured which decays to nearly 0% at -1.0 V. The reason for this is the earlier onset for the competing hydrogen evolution reaction (HER) under acidic conditions. Furthermore, the values at pH=2 should be considered with caution, as for unknown reason the deviations and errors were larger compared to the other conditions.

When studying any electrocatalytic properties – of either homogenously dissolved or heterogenized catalysts – this background behavior of the GC electrode always has to be kept in mind.

3.2. Homogeneous anthraquinone for oxygen reduction

According to literature and the findings reported here in chapter 3.1. glassy carbon as a typical commercial carbon-based electrode material shows quite high selectivity for electrochemical oxygen to H_2O_2 reduction.[211] As this oxygen reduction to H_2O_2 is the target reaction within this work, this background catalytic activity of the GC is not desirable. Nevertheless, the majority of literature reports on these electrocatalytic studies used conventional electrode materials like GC, FTO or gold, which all show quite high background catalytic activity. Thus, GC was also chosen as electrode material within this work. Furthermore, it should be mentioned that, although numerous literature reports do not mention these background activities, in this work great care is taken on explicitly considering the background ORR of the GC electrode material.

Literature reports by the group of Compton recommend two strategies on how to circumvent any disturbance by such background activities. One way would be the use of special boron-doped diamond (BDD) electrodes, which shows quite high overpotential for undesired ORR by the electrode material and thereby enables facile investigation of homogeneous electrocatalysts.[121,122,131,212] As a second approach these authors reported the surface-modification by organic compounds and thereby suppress the ORR by blocking the surface active states.[123,213]

Although we believe that these two approaches will be of great importance in future studies, within this work, typical and commercially available electrode materials are used.

As outlined in the introductory chapter 1.2. the majority of H_2O_2 produced on industrial scale is done via the anthraquinone autooxidation process. Although thereby alkylated anthraquinones (AQ) are used as chemical catalysts, they are also the most studied class of organic molecules for electrocatalytic oxygen to H_2O_2 reduction.[96,124,139] For an industrial process of electrochemical H_2O_2 production, heterogeneous electrodes with immobilized catalysts are desirable. Nevertheless, extensive studies of electrocatalysts in homogeneous solution prior immobilization are inevitable for a better understanding on a molecular level.

Due to this reason, the well-known homogenous electrocatalyst anthraquinone sulfonate (AQS)[121,122] was chosen as case-study material for the electrochemical oxygen to H_2O_2 reduction reaction. Here, the main goal was to prove and investigate this electrocatalytic behavior with hydrodynamic electrochemical methods under special consideration of the background catalytic activity of the GC electrode material.

The results presented in this subsequent chapter were already published by Wielend *et al.* (2021) in *Electrochemistry Communications*.[214]

To start with, normal CV graphs were recorded comparing nitrogen saturated conditions with oxygen saturated conditions, represented in Figure 44:
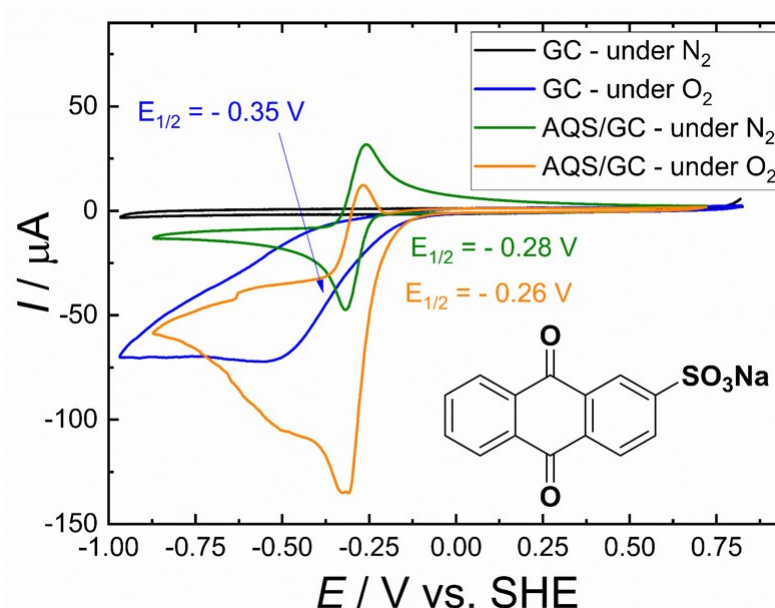
Figure 44: CV curves of GC and 1 mM solutions of AQS under N_2 and O_2 saturated conditions. In all cases, 0.1 M PB at pH=7 was used as electrolyte solution. Reproduced from Wielend et al.[214]. © 2021 the authors.

In contrast to the CV curve of GC in alkaline solution in Figure 37 under neutral conditions as shown in Figure 44, the ORR peak of GC is shifted cathodically, which is in accordance to literature reports[118,204,205]. Homogeneously dissolved AQS (structure shown in inset of Figure 44) under inert conditions shows a nicely reversible redox-behavior at -0.28 V, which is very close to the redox potential of the ORR obtained by using glassy carbon. The CV graph of AQS under O_2 saturated conditions shown in orange at a first glance only shows one reduction peak at -0.26 V, where the re-oxidation peak is significantly smaller. In order to gain a better understanding of the process, CV studies at different scan rates were performed:
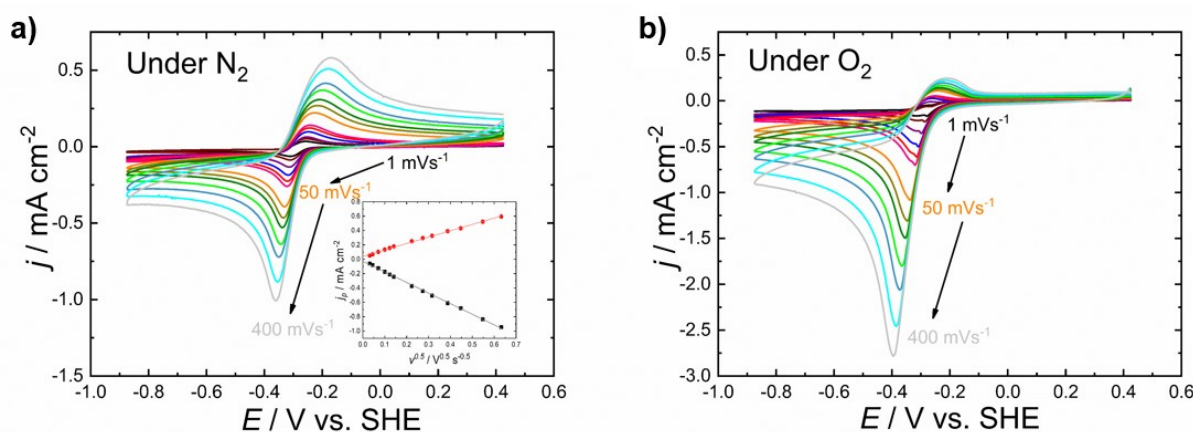

Figure 45: CV studies of 1mM AQS in 0.1 M PB at different scan rates under a) N_2 saturated conditions and b) O_2 saturated conditions. Reproduced from Wielend et al.[214]. © 2021 the authors.

The CV curves under N_2 in Figure 45a reveal a nearly ideal, reversible behavior at all scan rates investigated, which is also proven by Randles-Sevcik plots (Eq. 17)[81,215] shown in the inset.

$$I_p = 2.69 \cdot 10^5 \cdot A \cdot n^{3/2} \cdot \sqrt{D} \cdot c^* \cdot \sqrt{v}$$

Eq. 17

At fast scan rates under O_2, it appears as if one not fully reversible reduction peak is present. In contrast, the CV studies at slower scan rates (below 20 mV s⁻¹) reveal that this supposed one reduction peak is actually composed of two peaks, in close proximity. This behavior can be explained by comparison between the graphs shown in Figure 44, as these two peaks correspond to the ORR of the glassy carbon and the reduction of AQS.

Summing up, these CV studies did not reveal a clear electrocatalytic behavior of AQS towards the oxygen reduction. Nevertheless, qualitatively comparing the peak current values in Figure 44 reveals by bare eye, that the AQS/O_2 system shows a similar current like the sum of GC/O_2 and AQS/N_2, but already at more positive potentials.

As these qualitative observations are insufficient for the scientific proof of the catalytic activity, rotating ring-disc electrode (RRDE) measurements at the same conditions as illustrated in Figure 44 were performed as depicted in Figure 46:
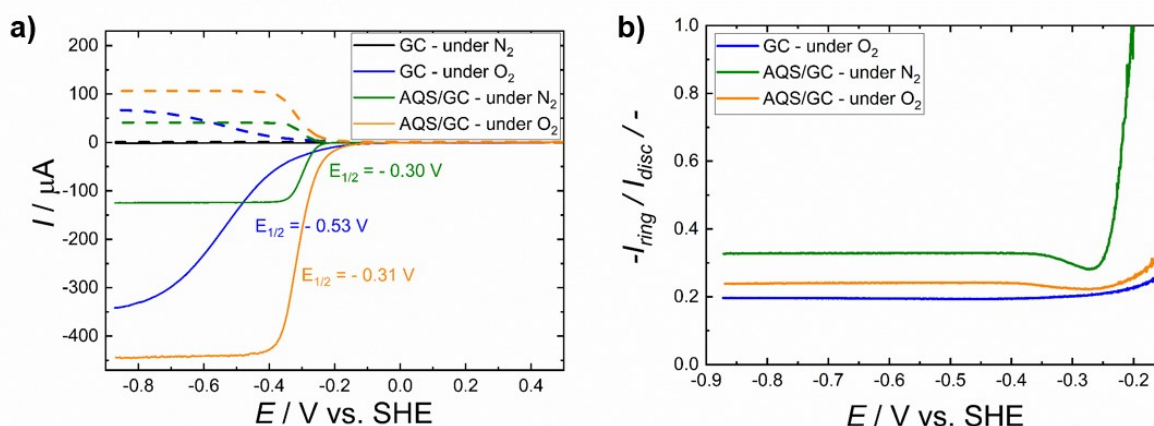

Figure 46: a) RRDE-LSV curves of blank GC electrodes in comparison with 1 mM AQS in 0.1 M PB solution under N_2 saturated conditions in comparison with O_2 saturated conditions, b) Ratio of ring current I_R and I_D from the LSV curves shown in a). For all measurements the ring was kept at +0.64 V and the rotation speed was 900 rpm. Figure a) was reproduced from Wielend *et al*.[214]. © 2021 the authors.

In accordance to the CV graphs from Figure 44, also the LSV curves in Figure 46a for AQS under N_2 show an ideal behavior expressed by a steep reductive current step followed by a very stable mass-transport limited regime below -0.5 V. In contrast, GC under O_2 shows a broader step which does not fully reach a mass-transport limited regime within the potential range investigated. The AQS under O_2 conditions shows a slightly anodically shifted onset of the reduction step and reaches a highly negative mass-transport limited current at moderate potentials more negative than -0.4 V. Interestingly, this plateau current can be described as the sum of the GC under O_2 and the AQS under N_2 current values at -0.85 V.

As this overall current of AQS under O_2 seems to be linearly composed of the current values of the single components, at first glance no electrocatalytic effect can be described. Only the slightly anodically shifted reduction onset is a hint for catalysis, which is not reflected by comparing the half-step potentials. Furthermore, also analysis of the ratios between I_R and I_D in Figure 46b does not reveal any clear hint for electrocatalysis. AQS under N_2 appears to be the most reversible redox couple as it shows the highest ratio.

The only hint for an electrocatalytic effect is, that although the AQS under O_2 current is composed from its single components at -0.85 V, this current plateau is already established at -0.4 V. As a result, at negative potentials like -0.85 V no catalytic effect can be observed whereas at low overpotentials significant excess currents are observed, which can be mathematically described by the following formula (Eq. 18):

$$I_{excess} = I_{AQS/O_2} - \left(I_{GC/O_2} + I_{AQS/N_2}\right)$$

By using this mathematical approach of Eq. 18, this behavior of electrocatalytic excess currents at moderate overpotentials can be quantified. As the sum of the currents from GC under O_2 and AQS under N_2 are subtracted from the AQS under O_2 conditions, these resulting current values are those exceeding the simple linear combination of the single components. This approach was applied to the disc currents I_D as well as to the ring currents I_R for the RRDE-LSV measurements at all rotation speeds performed. One inspiration for this linear dependence which allows subtraction is given in an Oxford Chemistry Primer by A. C. Fisher.[215] In addition, the group of Koper reported a similar RRDE subtraction method to determine the contribution of HER to the overall current on gold electrodes by subtracting the CO_2 to CO reduction current from the overall current.[216,217]

Following this approach using Eq. 19, the graphs at 100 and 3600 rpm are shown in the following Figure 47 as representative results:
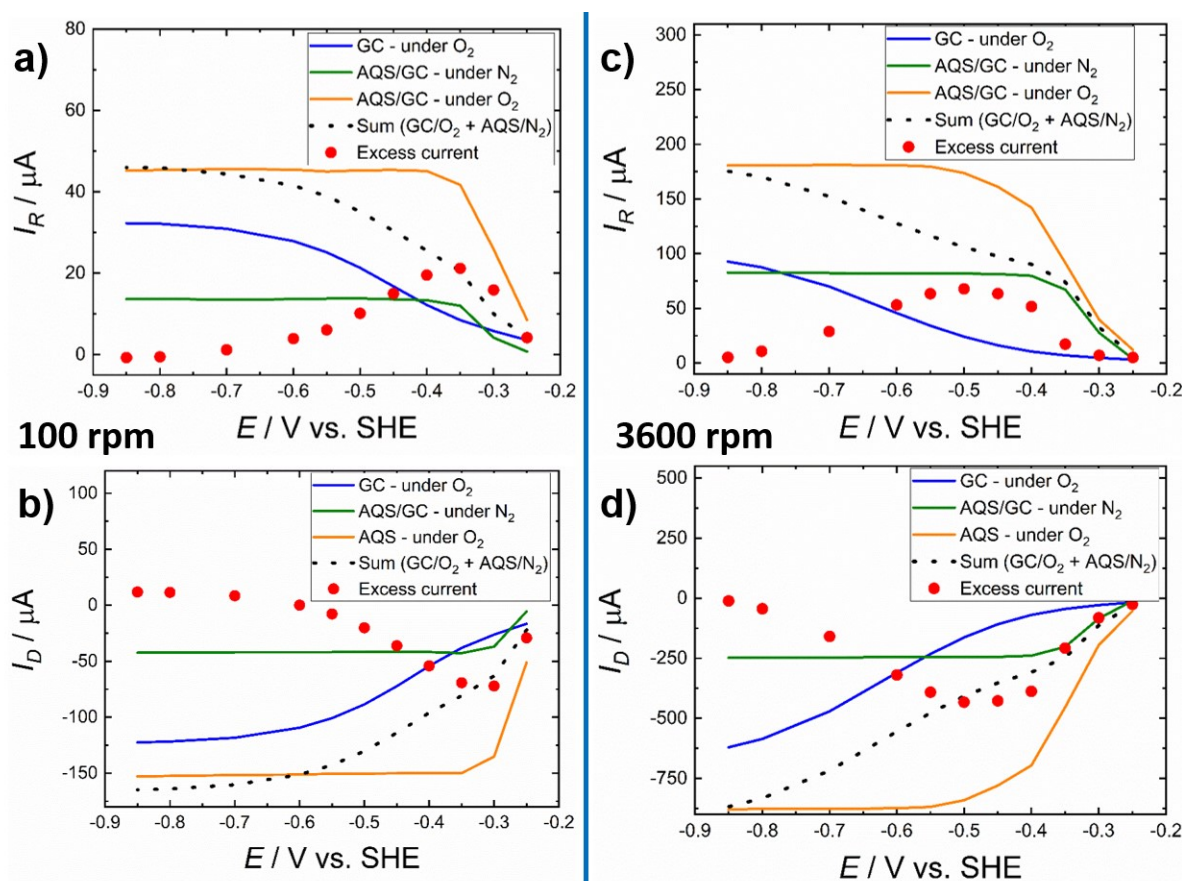

Figure 47: RRDE-LSV curves at 100 rpm (a & b) and 3600 rpm (c &d), where the excess currents were calculated and illustrated as red dots.

The graphs depicted in Figure 47 clearly illustrate how the excess currents were calculated for the ring currents (Figure 47a&c) and the disc currents (Figure 47b&d). Both, the excess currents on the disc and on the ring exhibit a gaussian and inverse-gaussian like shape. When comparing the shapes at different rotation speeds, some differences regarding width and position of the current maximum were observed, which are more clearly visualized in the following Figure 48:
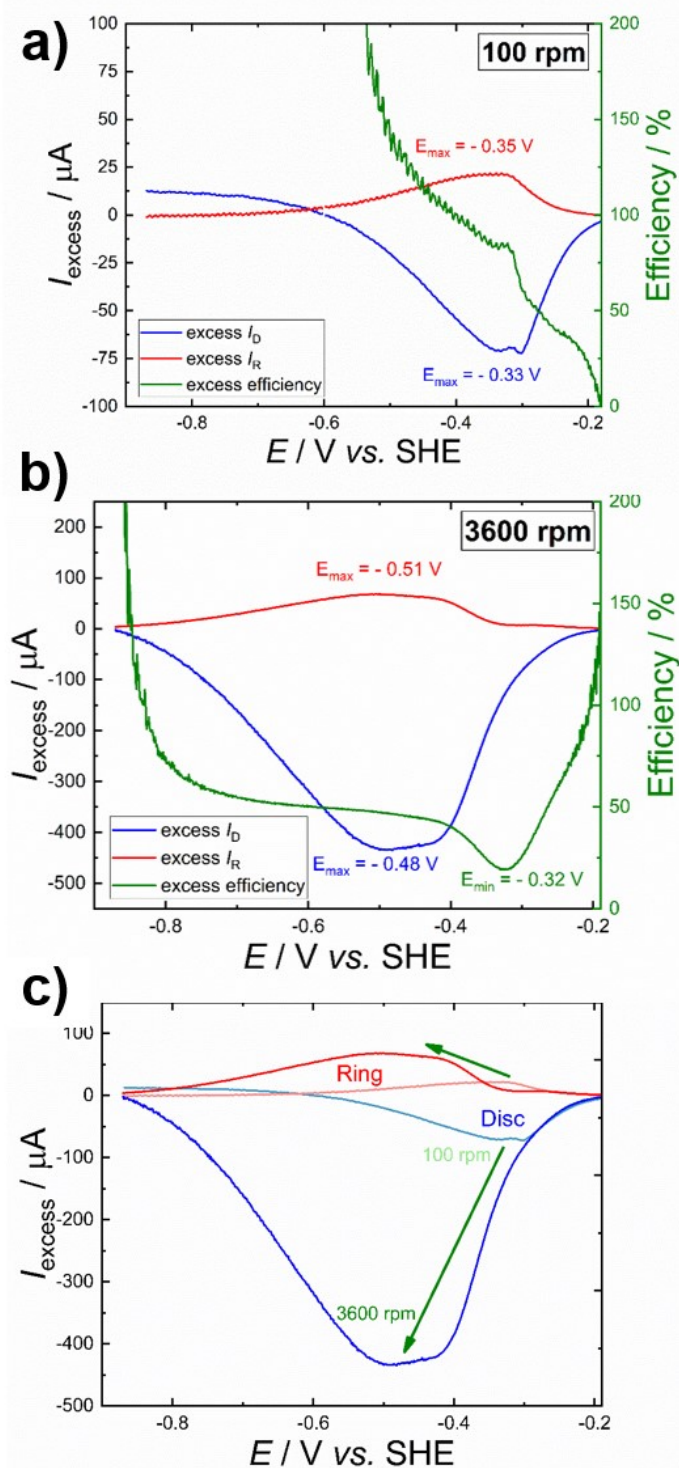
Figure 48: Illustration of the excess currents at the disc and ring at 100 rpm (a) and 3600 rpm (b) including the excess efficiency, c) Visualization of the excess current shifts upon increasing the rotation speed from 100 to 2600 rpm in one graph. Reproduced from Wielend *et al.*[214]. © 2021 the authors.

In Figure 48a&b, the curves of the excess currents calculated in Figure 47 are shown again. Therefore it can be clearly seen that upon higher rotation speed, significantly higher excess current values are observed. Besides this expected behavior, also the position of the peak current values significantly shifts. Upon higher rotations speed, this maximum is shifted towards more negative potentials. Furthermore, this potential of the peak is always slightly

cathodically shifted comparing the ring with disc currents due to hydrodynamic delay of the redox active species. Especially at slow rotation speeds, the shape of the disc excess current values is clearly composed of two peaks which are merged upon increased rotation speed. This behavior mentioned is comparatively illustrated in Figure 48c for 100 and 3600 rpm, but it can be stated that the experiments recorded at rotation speeds in between are analogous. Especially at quite negative potentials, the values for the excess currents get very close to 0 or even in the opposite direction. As there is no clear physical meaning behind such values, the excess current values should only be trusted down to this regime and below that attributed to mathematical calculation deviations.

Inspired by the Eq. 15 for faradaic efficiencies in heterogeneous RRDE catalytic studies, exactly this formula was used to calculate an excess efficiency from the excess current values shown in Figure 47 and Figure 48. It has to be mentioned, as these are not experimental values but subtracted ones, this excess efficiency cannot be referred to as a real faradaic efficiency but more to a semi-qualitative measure for the processes occurring at the RRDE. As illustrated in Figure 48a&b, this excess efficiency increases steadily upon decreasing the applied potential until slightly below the maximum excess current values. Afterwards, the excess current curves get less smooth and abruptly increase to values significantly exceeding unity. As mentioned in the previous paragraph, this behavior has to be attributed to mathematical deviations, as after these potential values the excess current values are very small and lead to such behavior upon division calculations.

For further analysis, the trends of maximum current peak potentials and the excess efficiency graphs for all rotation speeds examined are shown in the following Figure 49:
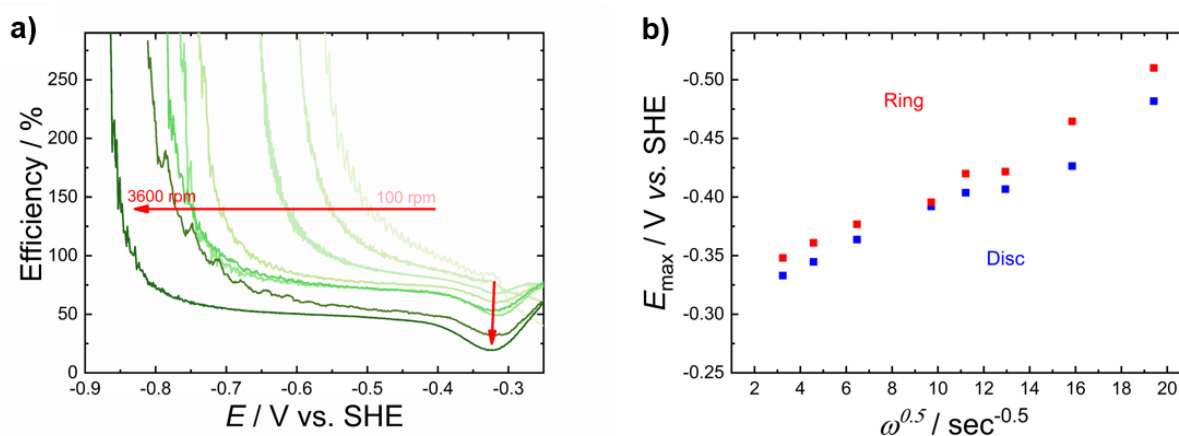

Figure 49: a) Graphs of the excess efficiencies for all rotation speeds recorded between 100 and 3600 rpm, b) maximum current potentials of I_D and I_R at various rotation speeds vs. $\omega^{0.5}$. Reproduced from Wielend *et al.*[214]. © 2021 the authors.

As explained above, the excess efficiencies depicted in Figure 49a show the following trend: upon increasing rotation speed, a more negative potential is required to achieve high efficiency values. One interesting observation is that for all curves recorded at speeds faster than 200 rpm a minimum of the efficiency curve was observed at exactly the same potential of -0.32 V. The reason for this highly stable behavior is not fully understood, but one possible explanation is that this corresponds exactly to the thermodynamic potential of the oxygen reduction in this system.

Upon further investigation of the shift, in the excess current maximum potentials in Figure 48c, revealed an unexpected trend illustrated in Figure 49b. Plotting the potentials of these maximum current points versus the square root of the angular rotation speed revealed a nearly linear behavior. Although such linear trends versus $\omega^{0.5}$ are well-known in hydrodynamic voltammetry studies for limiting current values (Eq. 10) since the historic beginning[75], the reason for this trend observed on the potential is unknown and will require further investigations.

Besides pure electrochemical studies, insights into the molecular processes of such electrocatalytic reactions can also be gained by the combination of spectroscopy and electrochemistry, so-called spectroelectrochemistry. Many organic molecules undergo a color change upon electrochemical reduction, which can be readily observed by naked eye and certain spectroelectrochemcial setups *in-situ* or *ex-situ*. Especially, the unsubstituted anthraquinone was already thoroughly studied in literature for its spectroelectrochemical changes in the UV-Vis regime upon reduction in aprotic solvents.[218,219] As it is well known from CO_2 reduction electrocatalysis with metal complexes, catalytic intermediates can be observed by *in-situ* spectroelectrochemistry.[220–223] In order to investigate whether the AQS species also forms an intermediate with O_2 upon reduction, *in-situ* spectroelectrochemistry in homogeneous solution was performed using the special cuvette cell shown in Figure 33b.
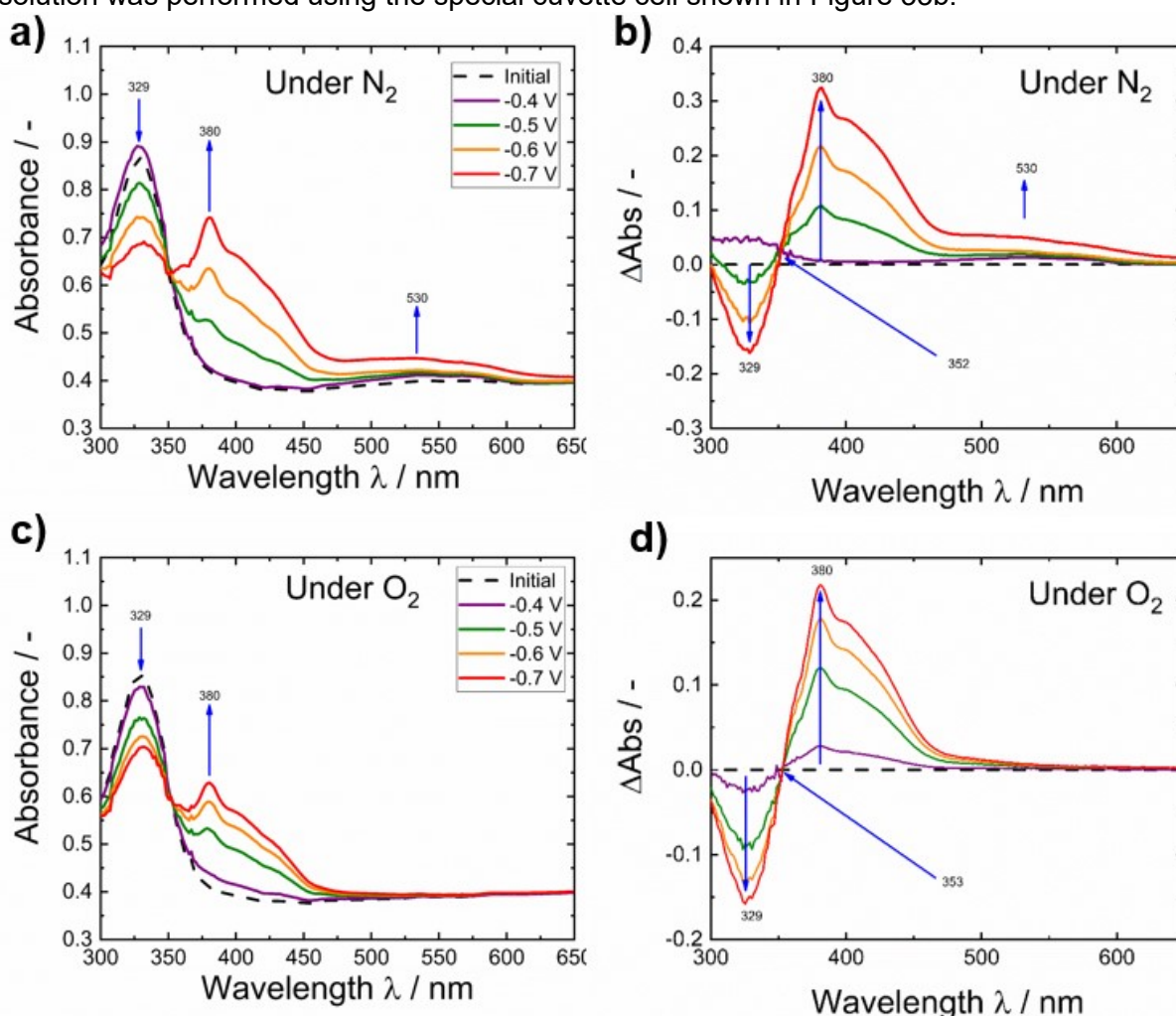

Figure 50: In-situ UV-Vis spectroelectrochemistry graphs of 1 mM AQS in 0.1 M PB upon electrochemical reduction in a) &b) N_2 saturated conditions and c) & d) O_2 saturated conditions.

Upon electrochemical reduction under N_2 in Figure 50a, AQS revealed a decrease in the band at 329 nm, which corresponds to the ground state absorption of AQS. Simultaneously, two broad bands with maxima at 380 nm and 530 nm could be seen. According to literature[224,225], the band at 380 nm corresponds to the protonated, reduced form of $AQSH_2$ whereas the small, broad band at 530 nm corresponds to the reduced and deprotonated form AQS^{2-}. In contrast to the N_2 conditions, under O_2 only the band at 380 nm evolves whereas the one at 530 nm is missing. As in addition also no new bands arise, these results show that no AQS-O_2 species is formed, but that the catalytically active AQS^{2-} species cannot be detected as it is immediately quenched by the O_2 present. These results are in good agreement to literature investigations *in-situ*[224] and *ex-situ*[225].

Summing up, the results presented herein clearly demonstrated the importance of considering the background currents as a result from the selected electrode material. Although a great contribution of literature in the field of electrocatalytic O_2 to H_2O_2 reduction is based on common glassy carbon electrodes, one must not forget the significant oxygen reduction capability of glassy carbon alone.

Besides overestimating the electrocatalytic activity of your target material (see chapters 3.4. & 3.5. one might also overlook an electrocatalytic contribution of a homogeneous catalyst in CV studies (Figure 44) or LSV studies (Figure 46). The RRDE subtraction method presented herein reveals and semi-quantitatively illustrates this electrocatalytic behavior of the well-studied electrocatalyst AQS. Nevertheless, the alternative method to study the ORR behavior of homogeneous electrocatalysts reported in literature[122,131] by using boron-doped diamond electrodes with suppressed ORR activity also seems to be a feasible complementary technique.

The results presented within this chapter were already published by Wielend *et al.* (2021) in *Electrochemistry Communications*.[214]

Nevertheless, further in-depth studies building on these initial observations by this RRDE subtraction method are required and in progress. More results using this method for evaluating the electrocatalytic behavior of homogeneous, organic electrocatalysts can be found in the bachelor thesis of Angelina Kerschbaumer, conducted under the supervision of Dominik Wielend at the JKU Linz.
In addition to the evaluation of the electrocatalytic behavior via the RRDE method, studies involving CV and chronoamperometry of aqueous, homogeneous solutions of organic molecules for the oxygen to H_2O_2 production were performed by Corina Schimanofsky[226] and Elisabeth Leeb under the supervision of Dominik Wielend.

3.3. Immobilization of anthraquinones via polymerization

The experimental results presented and discussed in chapter 3.2. clearly show the capability of homogeneously dissolved anthraquinone for the electrocatalytic O_2 to H_2O_2 reduction, which is also in agreement with literature reports.[121,122,224] Due to this renowned electrocatalytic effect, besides the use of dissolved anthraquinones in the industrial anthraquinone autooxidation process[3,7], a logic step towards immobilized organic catalysts is the heterogenization of anthraquinones. Exactly on the topic of immobilized monomers, different derivatives of anthraquinone immobilized on GC electrodes has been investigated by the groups of Tammeveski and Schiffrin throughout the last 20 years. Their extensive studies can be roughly classified in two approaches. The first approach is based on physical adsorption of quinones on carbon-based electrodes which apparently already demonstrates quite high stability.[124] In a second approach they grafted quinones covalently to the carbon electrode materials via electrochemical reduction of diazonium compounds[127,130,138] or anodic attachment of carboxylated compounds[126].

As such direct covalent modification approaches have already been extensively studied, the approach examined within this work is focused on the immobilization of anthraquinones within a polymeric system. Such so-called poly(anthraquinones) have also already been extensively studied in literature, but mostly towards their application in organic battery application.[227–230] Since only limited reports on the electrocatalytic oxygen reduction usage of such poly(anthraquinones) exist[231], selected polymers from battery research were synthesized and investigated for the electrocatalytic behavior.

The results presented here in this subsequent chapter were recently published by Wielend *et al.* (2021) in *ChemElectroChem*.[232]

It should be mentioned, that in early literature reports by Pietron *et al.* (1999), polymeric or oligomeric structures of anthraquinones were identified to show a higher electroactivity compared to their monomeric pendants.[213]

3.3.1. Synthesis of poly(anthraquinones)

For this study, the three different polymers PDDA-SAQ, P14AQ and PVAQ were prepared. The synthesis of poly(diallyldimethylammonium sulfonic acid anthraquinone) (PDDA-SAQ) was performed according to a reported procedure by Hernández *et al.* (2017).[231] As this report does not give exact concentrations of educts used but only molar ratios, initially the solubility of sodium anthraquinone 2-sulfonate (AQS) was determined. As a result of that, a concentration of 25 mmol per liter in MilliQ (MQ) water was determined to be reasonable within 15 min of sonication, which is why 50 mL of such a solution were prepared for the ion exchange polymerization. 500 µL of a poly(diallyldimethylammonium chloride) (PDADMAC) solution (20% in water) were diluted with 500 µL of MQ water in a 100 mL flask and stirred. While intensively stirring the polymer solution, the AQS solution was added dropwise over a time of 20 min. During this procedure, the solution turned milky-turbid and became very viscous due to gelation. This can be understood by the anion exchange which transformed the soluble chloride-polymer into an insoluble AQS-polymer. Finally, this suspension was left for 3 h under stirring and further 3 h unstirred to complete the reaction.

After this reaction time, the polymer was filter over paper and washed six times with 5 mL MQ water each. Finally, the filter with the polymer precipitate was dried in a vacuum oven at 50 °C for 6 h. Subsequently, amorphous looking yellow flakes were collected at a yield of nearly 70%. The reaction scheme of this ion-exchange reaction as well as pictures taken during the synthesis are depicted in Figure 51:
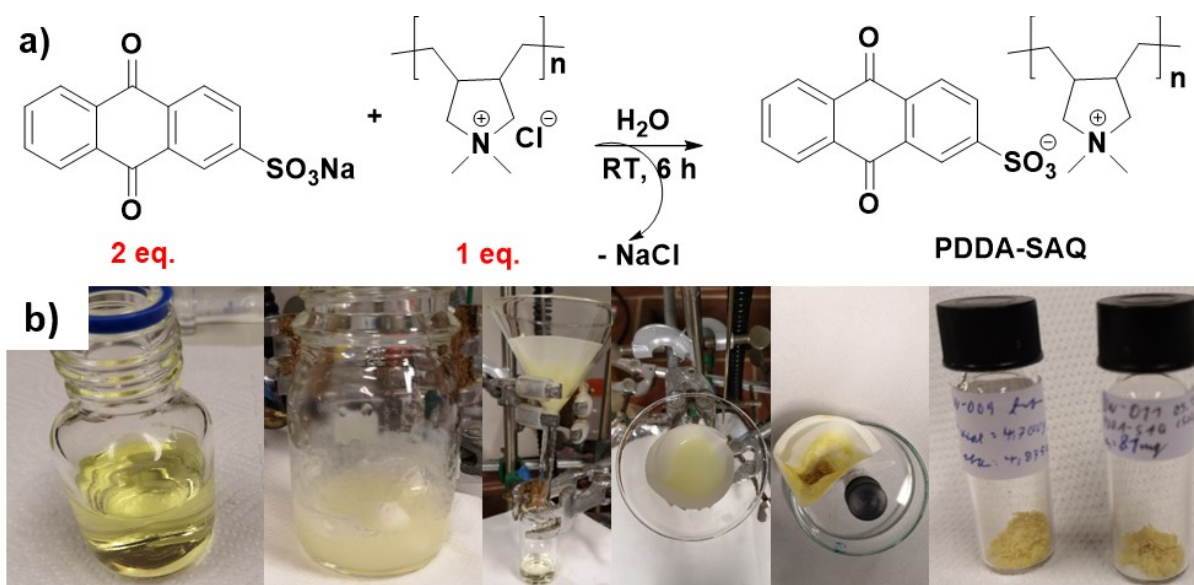

Figure 51: a) Reaction scheme for the synthesis of PDDA-SAQ, b) photographs taken during the synthesis of PDDA-SAQ. On the left picture, the 25 mM AQS solution is shown, then the reaction mixture is shown which is subsequently filtered with a filter paper and funnel, afterwards washed with MQ, dried and finally the yellow polymer collected as flakes.

The reaction scheme in Figure 51 illustrates the exchange of the initial chloride ion by the AQS anion upon salt formation with the positively charged ammonium units on the polymer backbone. In order to achieve a full or at least high exchange yield, 2 mol equivalent AQS was used.

Poly(1,4-anthraquinone) (P14AQ) was synthesized via an organometallic condensation reaction initially reported by Yamamoto and Etori (1995)[233], improved afterwards by Song *et al.* (2015)[234] in a 1:10 reduced scale approach. As a starting point, 83.1 mg of 1,4-dichloro anthraquinone (DCAQ) were weighed into a 20 mL glass vial, which was then immediately transferred into a glove box under N_2 atmosphere. Afterwards, 2.0 mL of dry DMF were added and the solution was stirred for 2 h.

In a second 20 mL glass vial, 63.2 mg 2,2'-bipyridine (Bpy), 110.5 mg bis(1,5-cyclooctadiene)nickel(0) and 37.0 µL cis,cis-1,5-cyclooctadiene were weighed inside the glove box and dissolved in 3.0 mL DMF. Thereby, an intensively deep-purple colored solution was obtained. The previously prepared DCAQ solution was added to this 2nd glass vial inside the glove box, which resulted in a dark-blue color. Afterwards, the vial was sealed and transferred outside the glove box. Under stirring, it was heated in an oil bath at 60°C and keeping the vial under inert conditions, this mixture was reacted for 48 h. After cooling down to room temperature, the reaction was quenched with 10 mL of a 0.5 M hydrochloric acid (HCl) solution. This resulted in brown precipitation, which was left for 30 min to separate from the solution. This precipitated polymer was filtered over paper with a Büchner funnel under vacuum and washed with the following steps: 4 x 5 mL DMF each, 5 x 5 mL 0.5 M HCl each, 5 x 5 mL MQ

water each and finally 5 x 5 mL methanol (MeOH) each. Consecutively, the product was dried at room temperature overnight and then re-dissolved in 3 mL chloroform (CHCl$_3$). The polymer was then precipitated from this yellow solution upon addition of 10 mL MeOH, which yielded a large, fluffy, yellow precipitate. This polymer precipitate was collected by filtration over paper with a Büchner funnel under vacuum and washed 3 times with 5 mL MeOH each. This final P14AQ polymer was dried at room temperature for 6 h and the fine yellow powder was collected at a yield of nearly 80%. The reaction scheme of this organometallic polycondensation as well as pictures taken during the synthesis are shown in the following Figure 52:
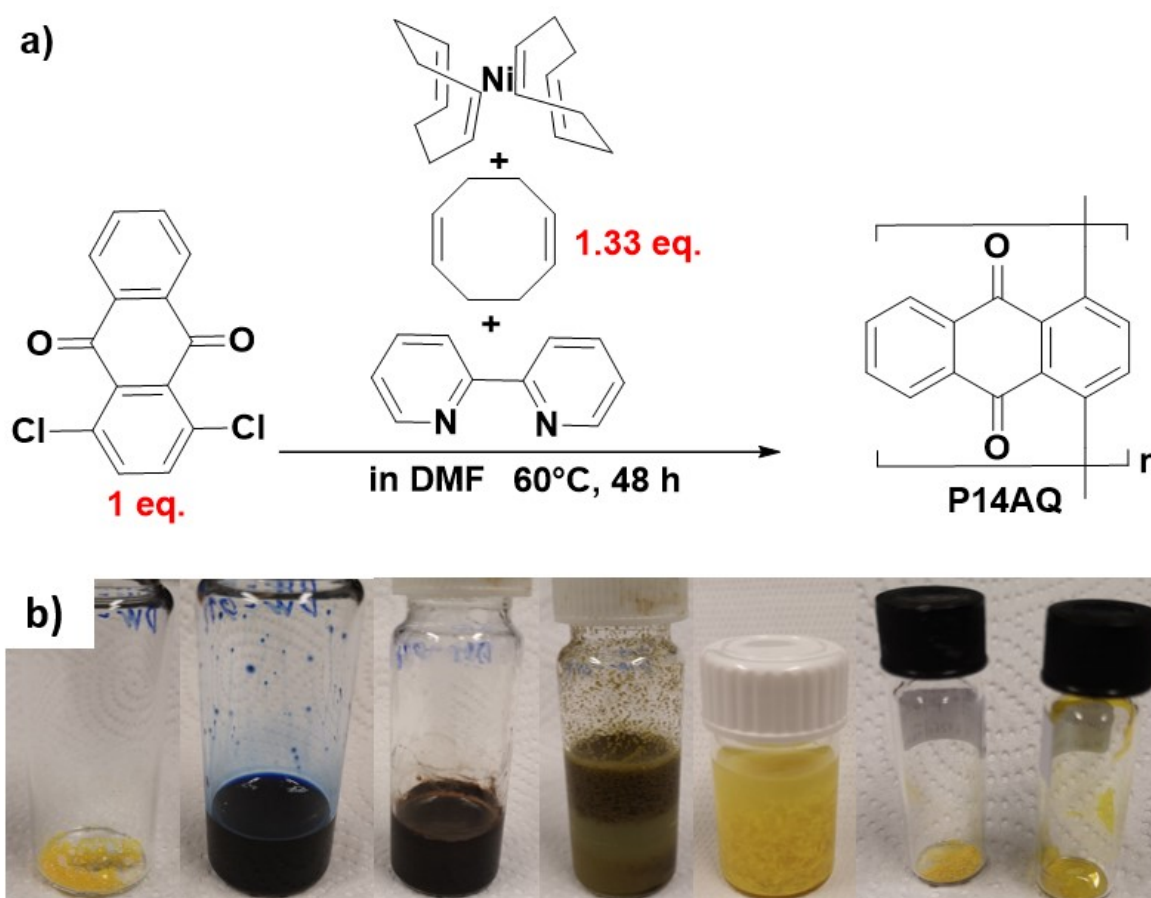

Figure 52: a) Reaction scheme for the synthesis of P14AQ, b) photographs taken during the synthesis of P14AQ. The left image shows DCAQ, the blue color is observed for the reaction mixture right before the reaction start, during which the solution turns dark brown. After quenching with HCl, on top of the blue-green solution the brown polymer was precipitated. After washing, re-dissolving in CHCl$_3$ and precipitation with MeOH the polymer appears as yellow precipitate which can then be collected as powder via filtration or as film after slow evaporation when dissolved in CHCl$_3$.

The images shown in Figure 52b show the color change described above throughout this polymerization reaction. As can be seen in the picture on the right side, the fine, yellow powder is not the only way in which P14AQ is obtained. According to literature[234], P14AQ forms nice free-standing films, which will be discussed in further detail in chapter 3.3.2.

The third polymer was poly(2-vinyl anthraquinone) (PVAQ), following the reported procedure of Choi *et al.* (2011).[235] Unfortunately, this radical polymerization procedure using *alpha,alpha*-azobisisobutyronitril) (AIBN) in tetrahydrofuran (THF) did not result in any polymer. Therefore, this method was adapted by using benzoylperoxide (BPO) in CHCl$_3$ according to Clausen *et*

al. (2017).[236] As the authors[236] reportedly aimed for oligomeric structures with lower molecular weight, the principle reaction conditions were kept from Choi *et al.*[235].

There, 93.7 mg of the monomer 2-vinyl anthraquinone and 6.45 mg of the initiator benzoyl peroxide were weighed into a Wheaton bottle including a magnetic stirrer bar. After closing this bottle, the flask was evacuated and flushed with N_2 three times before addition of 5 mL $CHCl_3$ via a septum. After sonication for 5 min, the headspace was purged with N_2 for 5 min. Subsequently, this reaction mixture was stirred and heated in an oil bath at 60°C for 24 h under N_2 atmosphere.

After the reaction mixture was cooled down to room temperature, it was filled into a centrifuge tube and the liquid level reduced to ~2 mL by evaporation at ambient conditions. Afterwards, precipitation of the polymer was induced by the addition of 2 mL toluene and continued for 2 h. The polymer PVAQ was purified by centrifugation at 5500 rpm and after removing the supernatant, washed 3 times with 2 mL toluene each. Finally, the precipitated polymer was dried in this centrifuge tube at 50°C under vacuum for 4 h. Then, the polymer was transferred into a glass vial and further dried at 60°C for 8 h under vacuum. The PVAQ polymer was collected as a yellow-white fine powder at a yield of 46%.

The reaction scheme of this radical polymerization as well as pictures taken during the synthesis are illustrated in the following Figure 53:
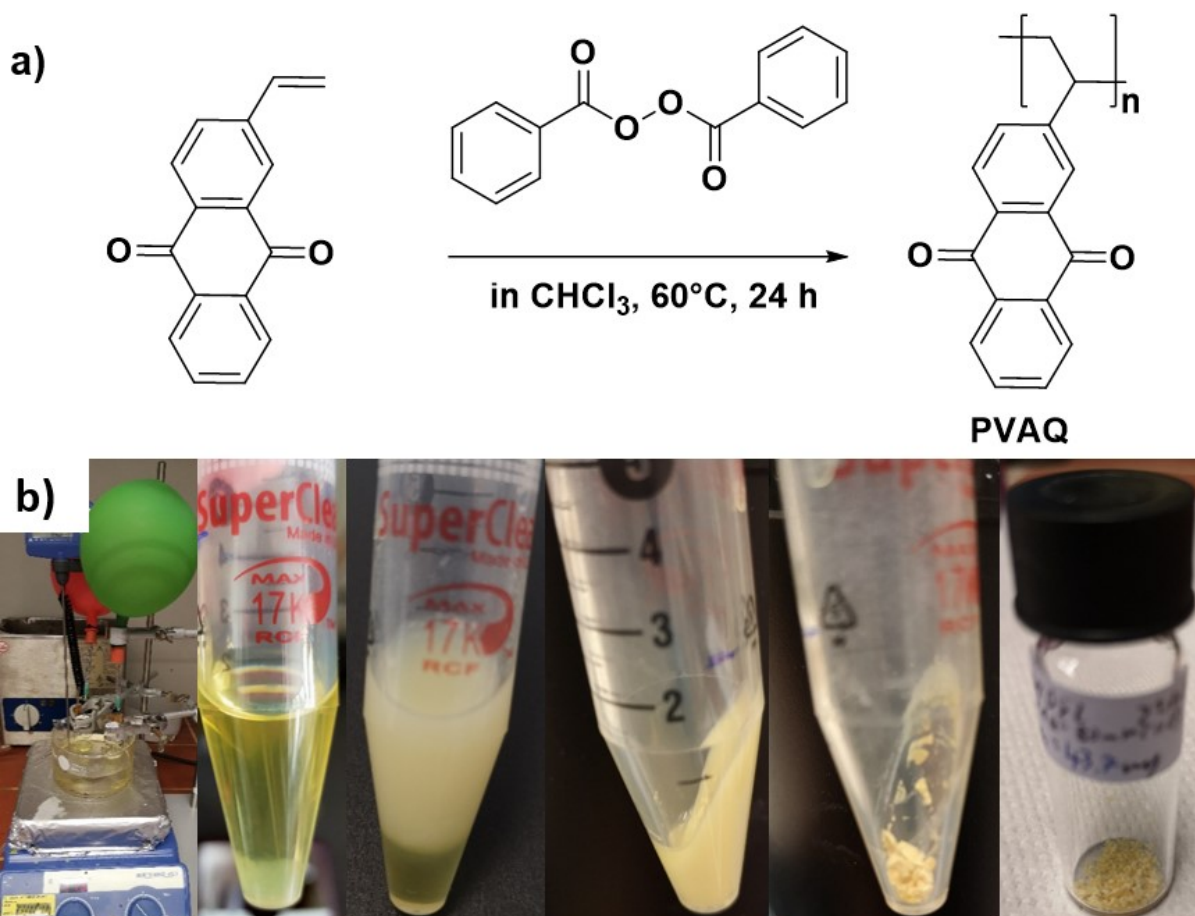

Figure 53: a) Reaction scheme for the synthesis of PVAQ, b) photographs taken during the synthesis of PVAQ. On the left image the reaction setup is shown, then the reaction tube with already concentrated solution and faint polymer precipitation. The third image from the left shows the precipitated polymer upon toluene addition followed by centrifugation and drying, before collecting the light-yellow polymer powder.

3.3.2. General characterization of poly(anthraquinones)

Recapitulating the chemical structures of the three synthesized polymers, PDDA-SAQ, P14AQ and PVAQ in Figure 51 to Figure 53 one significant chemical difference between the polymers is that PDDA-SAQ does not contain any covalently bound AQ units. Most likely due to this fact, PDDA-SAQ was the only polymer which could not be fully dissolved in any solvent. Therefore, for application onto electrodes, the polymer was swollen and suspended in DMF. Nevertheless, this suspension could not be investigated with common characterization methods for dissolved samples like NMR or solution UV-Vis absorption.

The conventional 1D ^{1}H-NMR spectra of the monomers DCAQ and the respective polymer P14AQ are shown in the following Figure 54:

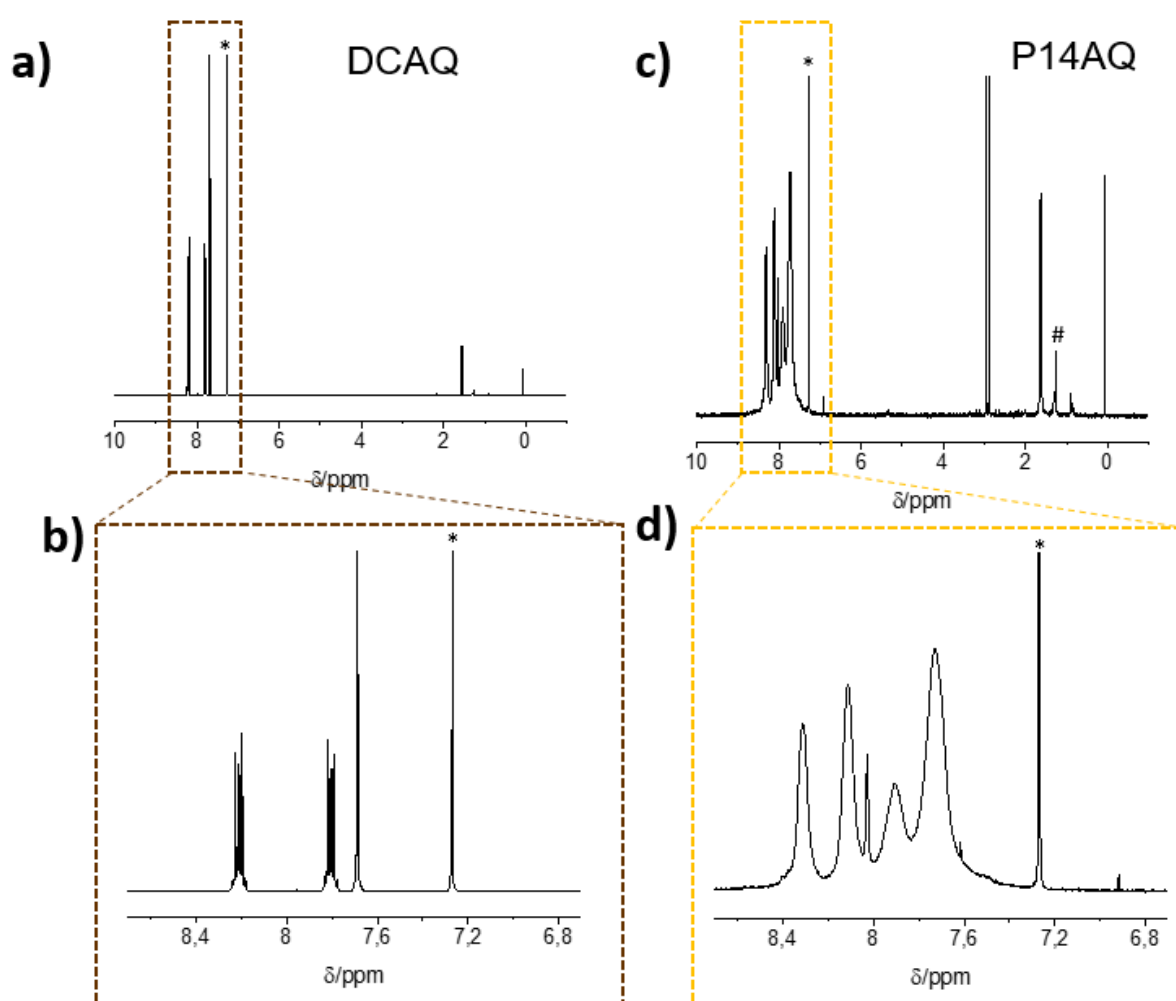Figure 54: a&b) ^{1}H-NMR spectra of monomer DCAQ and c&d) ^{1}H-NMR spectra of polymer P14AQ recorded as solution in CDCl$_3$ (marked as *). The presence of water in c) is marked with #. Spectra were recorded by Yolanda Salinas. Adapted from the Supporting Information of Wielend *et al.*[232] © 2021 the authors.

Especially the region of the aromatic protons between 7 and 9 ppm shift in Figure 54b&d reveals a significant change upon polymerization. The sharp multiplets of DCAQ disappear and instead, 4 broad singlet peaks of the P14AQ are detected. This is in good accordance to the brief statement on NMR of Choi *et al.* (2011)[235] and nearly identical to the spectrum reported by Li *et al.* (2019)[237]. The peaks below 3 ppm cannot be directly correlated to the

P14AQ structure, but as the complete drying of such polymer is challenging it is presumed, that they are originating from solvent residues, like for example water, as indicated.

The following Figure 55 shows the 1D ^{1}H-NMR spectra of the monomer 2-vinyl anthraquinone and its respective prepared polymer PVAQ:

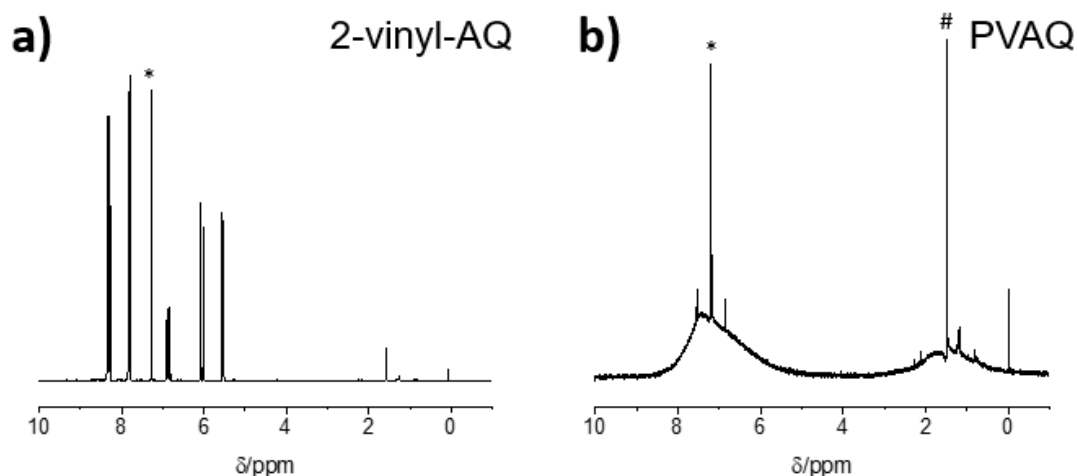Figure 55: a) ^{1}H-NMR spectrum of monomer 2-vinyl AQ and b) ^{1}H-NMR spectrum of polymer PVAQ recorded as solution in CDCl$_3$ (marked as *). The presence of water in b) is marked with #. Spectra were recorded by Yolanda Salinas. Adapted from the Supporting Information of Wielend et al.[232] © 2021 the authors.

When comparing the NMR spectra of the monomer and polymer PVAQ in Figure 55, the situation is not as clear as in case of P14AQ in Figure 54. Although the majority of the monomer peaks, including the significant doublets of the protons adjacent to the vinyl group between 5.5 and 7.5 ppm are not observed in the PVAQ spectrum, no significant new peaks are observed. As can be seen from the relative height of the CDCl$_3$ peak, only 2 broad but faint peaks around 7 and 1.5 ppm are observed, which are overlapping with the expected positions of the aromatic groups and the aliphatic polymer backbone.
In order to clarify, if these broad peaks are actually originating from the polymer and are not just simple measurement artefacts, diffusion correlated spectroscopy (DOSY) was done, as shown in the following Figure 56:
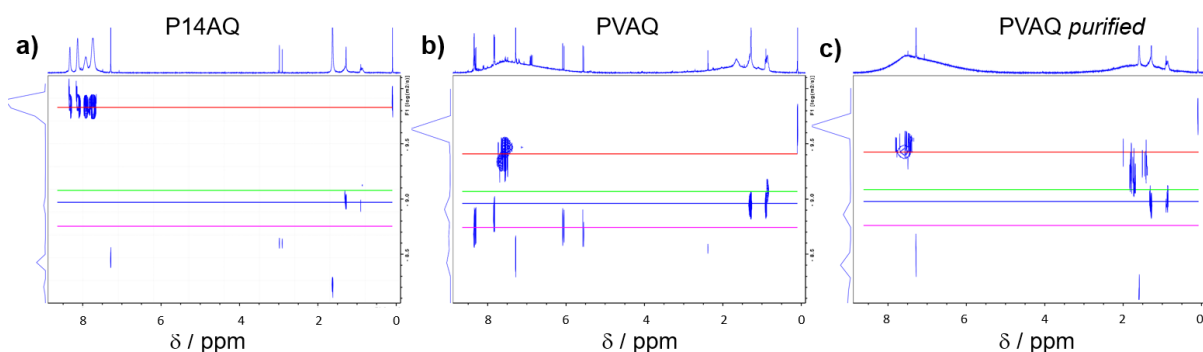

Figure 56: DOSY spectra a) P14AQ and two different samples of PVAQ. b) less purified PVAQ and c) more purified PVAQ. Spectra were recorded and fitted by Matthias Bechmann. a) & c) Reproduced from the Supporting Information of Wielend et al.[232] © 2021 the authors.

In such 2D-DOSY spectra like shown in Figure 56, the *y*-axis can be understood in terms of a diffusion ability, where high (upper) values correspond to diffusion-hindered species like polymers. More freely diffusing species like small molecules are detected in the lower regimes. The magenta lines mark the area of small organic molecules whereas the red lines indicate the position of the least-diffusing species observed in every graph.

As expected from the 1D NMR spectra of P14AQ in Figure 54c&d, also the DOSY spectrum of P14AQ in Figure 56a demonstrated that the 4 peaks between 7.5 and 8.5 ppm occur in the hindered-diffusing area. No monomer peaks are detected, only artefacts from $CDCl_3$ and H_2O which occurred below the magenta line due to their high diffusion properties. In contrast to P14AQ, the PVAQ was recovered after only one washing step (instead of the usual 3 washings steps as described in chapter 3.3.1. in Figure 56b, where significant peak contributions from the 2-vinly anthraquinone monomer is still present. However, the intensive and broad peak at 7.5 ppm at the top of the spectrum is a clear indication that a polymer PVAQ is present. In contrast to this, the fully washed sample shown in Figure 56c did not show any signals from remaining monomer, but in addition also some broad signals at 1.5 ppm in a diffusion hindered region slightly below the red line. This is an indication, that this broad peak is originating from a polymeric structure but shows less hindrance towards the measurement setup.

Summing up, the ^{1}H-NMR spectra and in addition the DOSY spectra clearly proved the successful formation of the polymers. When comparing the red lines marked in the DOSY spectra, one can even qualitatively state that according to these measurement parameters P14AQ might have a larger molecular weight compared to PVAQ. This is in agreement to the values stated in literature.[234,235]

UV-Vis absorption spectroscopy was done for homogenous solutions of the monomers used as well as P14AQ as comparatively shown in the following Figure 57:
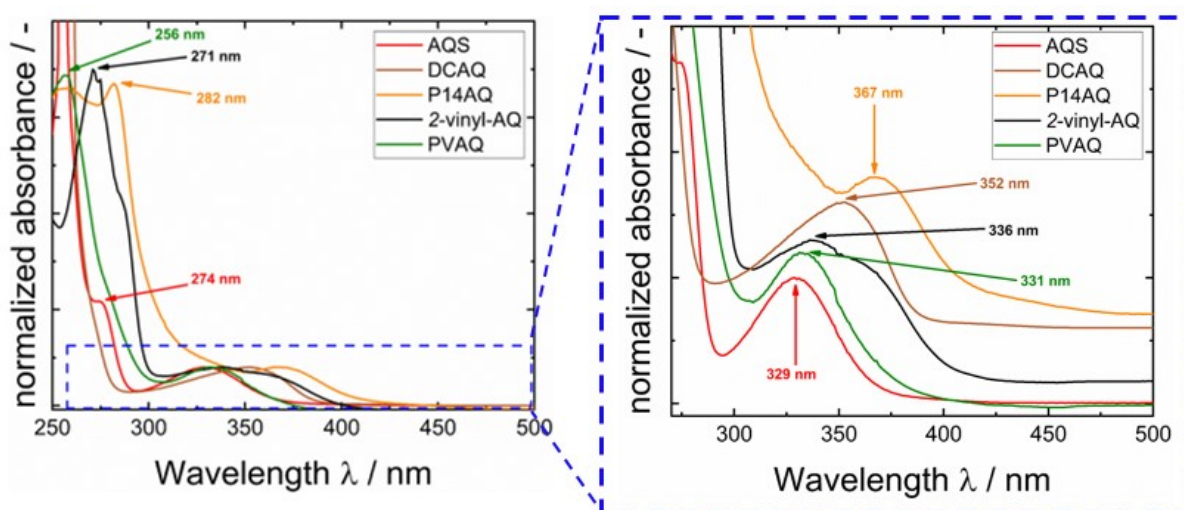

Figure 57 : UV-Vis absorption spectra of P14AQ and PVAQ dissolved in $CHCl_3$, the monomers DCAQ and 2-vinyl-AQ also dissolved in $CHCl_3$ whereas the monomer AQS was measured in homogeneous aqueous solution. The right graph shows a closer look at the regime between 250 and 500 nm. Reproduced from Wielend *et al.*[232] © the authors.

The UV-Vis spectra in Figure 57 revealed that all monomers and polymers measured show an absorption maximum of the lowest-frequency π-π* transition between 300 and 400 nm, as one would expect from the yellow color of all substances. When comparing λ_{max}=336 nm of 2-vinyl anthraquinone with PVAQ (λ_{max}=331 nm), a slight blue shift by 5 nm is observed. Considering

the chemical structure shown in Figure 53, the decrease of the conjugated π-system upon loss of the vinyl double bond is responsible for this hypsochromic shift in absorption upon polymerization. Besides the simple position of the absorption maximum, the 2-vinyl anthraquinone also shows the absorption shoulder of a second transition at around 360 nm, which results in an extended absorption tail towards higher wavelengths. In contrast to this behavior, PVAQ only shows one quite Gaussian-shaped peak in this regime. Furthermore, also in the far UV region below 300 nm a hypsochromic shift from the monomer of 271 nm to 256 nm observed for the PVAQ was measured.

In contrast, polymerization of the DCAQ to the P14AQ resulted in a significant bathochromic shift from 352 nm to 367 nm, which is in agreement to the extension of the conjugated π-system upon polymerization and literature reports[233]. Besides the shift of the absorption maximum, also qualitatively P14AQ shows a broader tailing behavior towards high wavelengths compared to all other materials investigated. In addition to the peaks at 350 nm, also the peak in the far UV region of P14AQ at 282 nm is shifted to higher wavelengths compared to DCAQ. In the case of DCAQ, this peak is below 260 nm and at those measurement conditions it could not be detected due to a too low light intensity passing through.

The aqueous solution of AQS showed a nice gaussian-shaped peak at 329 nm with an additional absorption shoulder at 274 nm.

During these measurements, the PDDA-SAQ polymer could not be observed due to solubility reasons. In addition, the free-standing film of P14AQ in particular, but also drop-casted P14AQ films showed a much more intensive yellow color by eye compared to the other two polymers.

In order to prove that in PDDA-SAQ no stacking of AQ units occurs but on the other hand, in case of the P14AQ film a π-π stacking of the AQ units is expected, the three polymers were casted onto quartz glass slides via doctor-blading, as can be seen on the image in the following Figure 58 with a logo of JKU below:
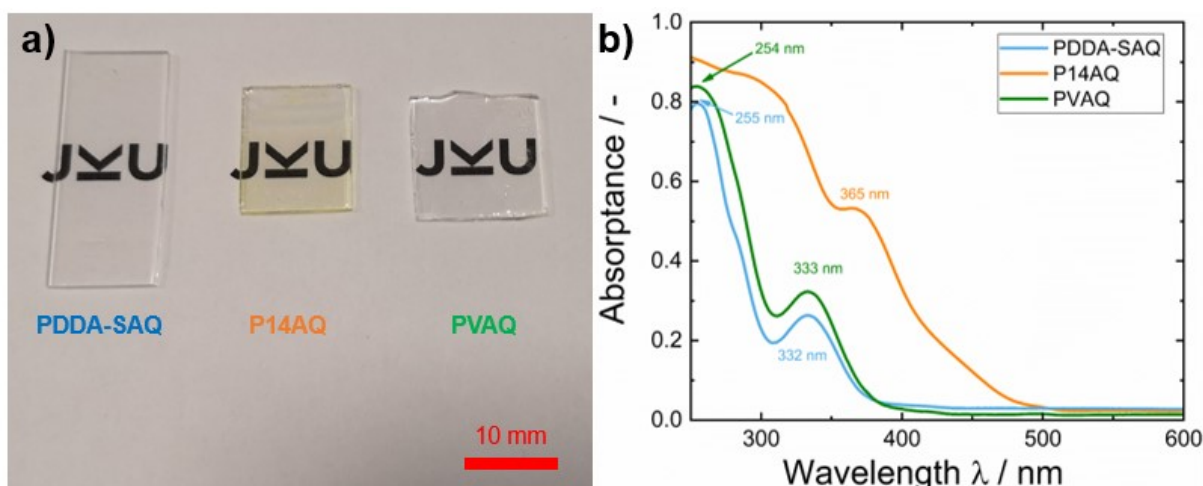

Figure 58: a) Photograph of the thin-films on quartz glass of PDDA-SAQ, P14AQ and PVAQ, b) Absorptance spectra measured of these polymer thin-films. Absorptance spectra were recorded and corrected for reflection by Felix Mayr. b) Reproduced from Wielend *et al.*[232] © 2021 the authors.

The polymer films of PDDA-SAQ and PVAQ in Figure 58a show no color appearance, whereas the P14AQ film is clearly yellow. This behavior is in agreement with the absorptance spectra, where PDDA-SAQ shows an absorptance maximum at 332 nm, which is nearly exactly at the

position of homogeneously dissolved AQS in water (λ_{max}=329 nm). Also in case of PVAQ, the film absorptance maximum values of 254 and 333 nm are within ±2 nm of the measurements done in CHCl$_3$ solutions in Figure 57. This unchanged behavior as well as the quite steep absorptance onset at around 390 nm are indications, that in PDDA-SAQ and PVAQ no π-π stacking of the AQ is present.

In case of P14AQ, surprisingly the position of the absorption peak of the thin film also does not differ significantly from the solution spectra. Nevertheless, in addition to the single absorption peak at 365 nm, P14AQ shows a broad and long tail towards the low frequency regime. Due to this onset of absorption starting at around 500 nm, the P14AQ has this yellow appearance. In addition to the position of the absorption maxima, also the absorptance value of P14AQ is nearly twice of the values of PDDA-SAQ and PVAQ. As in all cases, the films were casted from solutions having 10 mg mL^{-1} polymer content, this is an indication of an improved absorption behavior of P14AQ especially in comparison to PVAQ. For PDDA-SAQ the gravimetric AQ content, which corresponds to the fraction of AQ within the whole polymer mass, is significantly lower compared to the other two polymers as a result of the large allyl-polymer backbone.

As a next step towards spectroscopic material characterization and thereby proving the formation of polymeric species, ATR-FTIR spectra of all monomers as well as the three polymers in solid state were recorded:
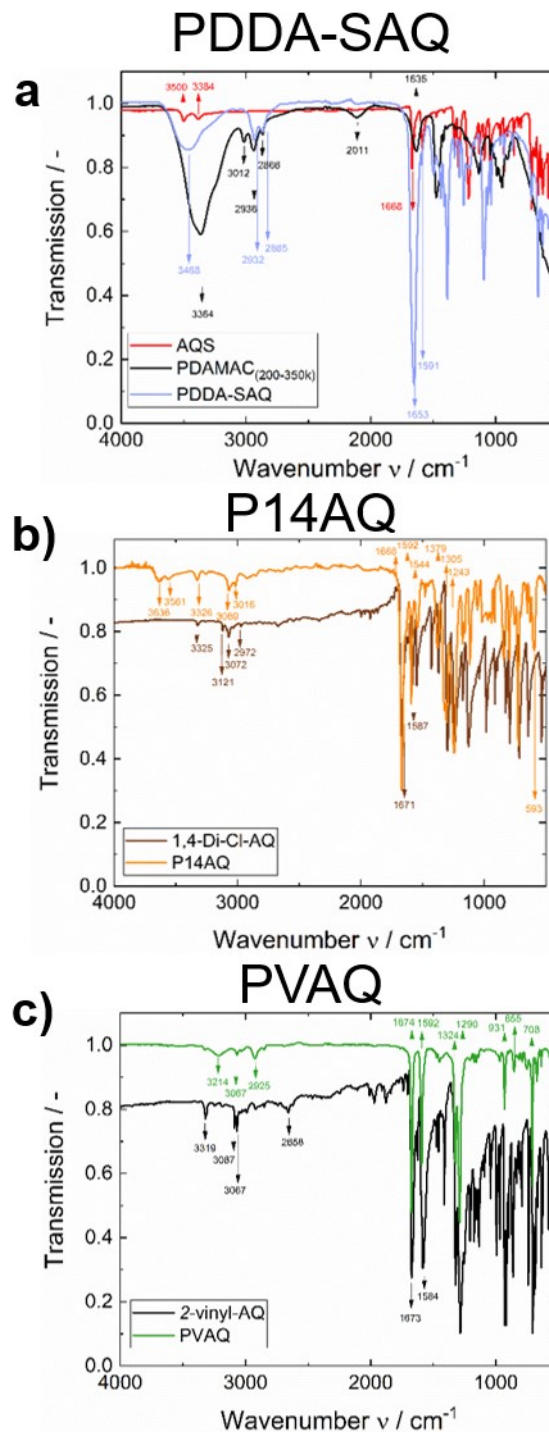
Figure 59: ATR-FTIR spectra of the polymers a) PDDA-SAQ, b) P14AQ and c) PVAQ in comparison with the respective monomers. Reproduced from the Supporting Information of Wielend *et al.*[232] © the authors.

For all three polymers shown in Figure 59, the polymers show distinct peaks in comparison to their building blocks. In addition, the polymers also show less but smoother and well-resolved peaks in comparison to the small molecules, which is a general observation for polymeric structures. The only exception to this is the PDAMAC, which is also a polymer and shows even broader and smoother curves compared to PDDA-SAQ. Due to this mentioned large number of sharp peaks of the AQ monomers, especially in the low frequency regime below 1600 cm^{-1}, the spectra of the three polymers are illustrated in the following Figure 60b for better visibility:
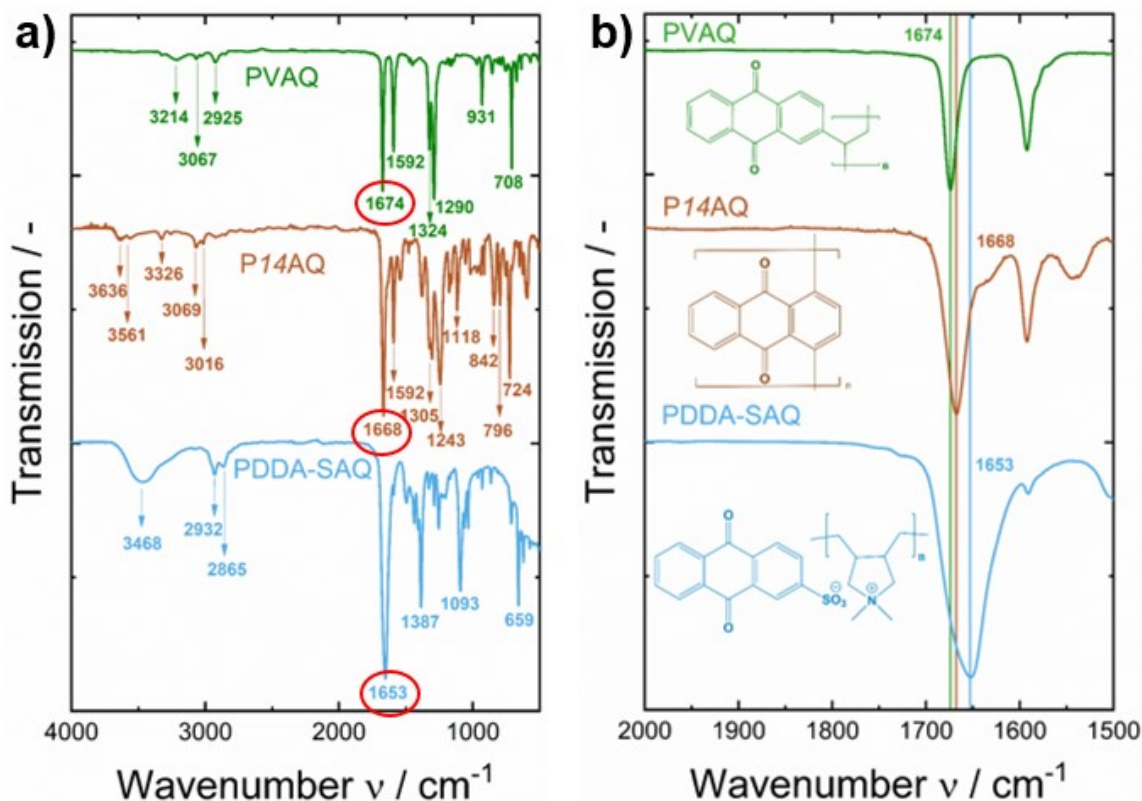
Figure 60 :a) ATR-FTIR spectra of the three anthraquinone polymers where some of the most prominent bands are marked. The bands encircled in red correspond to the C=O vibration, where a further zoomed area of these bands is shown in b). Reproduced from Wielend *et al.*[232] © 2021 the authors.

The characteristic IR bands of PDDA-SAQ, P14AQ and PVAQ are presented in a better resolved way in Figure 60 compared to Figure 59 before. It was found out, that the bands obtained for PDDA-SAQ and P14AQ are in good agreement to literature.[231,234] Among the characteristic bands examined, the ones originating from the C=O vibration modes around 1650 cm^{-1} are of special interest. The carbonyl bands of the three polymers differ by 21 wavenumbers, which will be discussed in further detail in comparison to other properties later in the upcoming chapter 3.3.3.

In order to determine the thermal stability of the materials as well as another proof of successful chemical synthesis, thermogravimetric analysis (TGA) was performed:

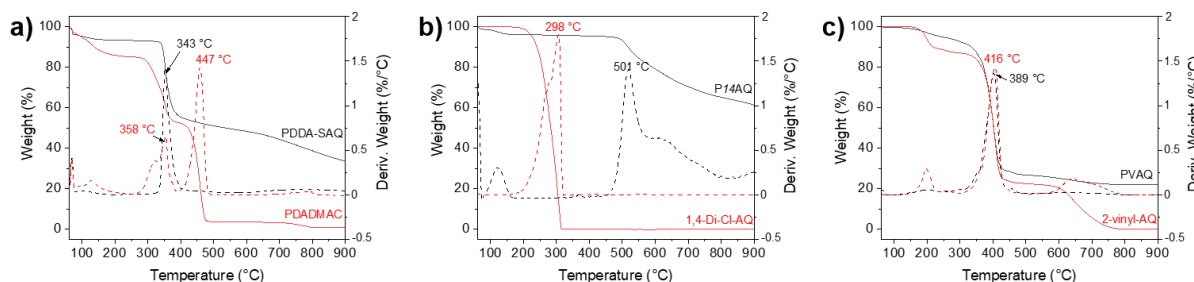Figure 61: TGA graphs of a) PDADMAC and PDDA-SAQ, b) DCAQ and P14AQ and c) 2-vinyl AQ and PVAQ. The left y-axis and the solid lines refer to the weight whereas the right y-axis and the dashed lines refer to the derivatives of the weight. The TGA measurements were done and fitted by Maria Würflinger and Yolanda Salinas. Reproduced from the Supporting Information of Wielend *et al.*[232] © 2021 the authors.

In Figure 61 the TGA graphs of all polymers and monomers with the exception of AQS are shown and analyzed. The reason, why no TGA for AQS could be performed is that this compound upon the heat treatment spontaneously distributed within the whole TGA machine, maybe due to uncontrolled release of the crystal water content. For better clarity, the decomposition temperatures T_d from the maximum points of the derivation curve are summarized in the following Table 3:

Table 3: Comparison of the decomposition temperatures T_d and the weight loss between 100 and 600°C.

Sample	T_d / °C	Weight loss / % (100°C – 600°C)
PDADMAC (*initial polymer*)	358/447	99.17
PDDA-SAQ	343	46.94
DCAQ (*monomer*)	298	99.72
P14AQ	501	19.18
2-vinyl-AQ (*monomer*)	416	79.70
PVAQ	389	74.42

The TGA results of PDADAMAC and PDDA-SAQ in Figure 61 and Table 3 reveals that PDDA-SAQ has an even lower T_d as the first T_d of PDADMAC. At 400°C both polymers have still a comparable mass. At more elevated temperatures PDDA-SAQ only shows a slight further decrease in mass whereas almost no mass remains for PDADMAC at temperatures above 500 °C. Interestingly, PVAQ also has a slightly lower T_d compared to its monomer, but otherwise a nearly identical thermal behavior up to 600°C. At higher temperatures, the mass of PVAQ stays almost constant whereas no 2-vinyl AQ remains at temperatures above.

In contrast to these polymers, P14AQ exhibits a very high thermal stability up to 501°C followed by a slow decrease in mass. The monomer DCAQ has a very sharp and complete step at 298°C, which can be attributed to a controlled sublimation phase transition.

These results described above can also be clearly deduced from the weight loss up to 600°C in Table 3 which shows the complete decomposition of PDADMAC and DCAQ and the surprisingly high thermal stability of P14AQ, which is in agreement to literature[234].

As electrochemistry investigates the solid-liquid interface, which is strongly depending on the surface energies, the contact angle of water drops was determined for a blank GC electrode and the polymers as can be seen in the following Figure 62:
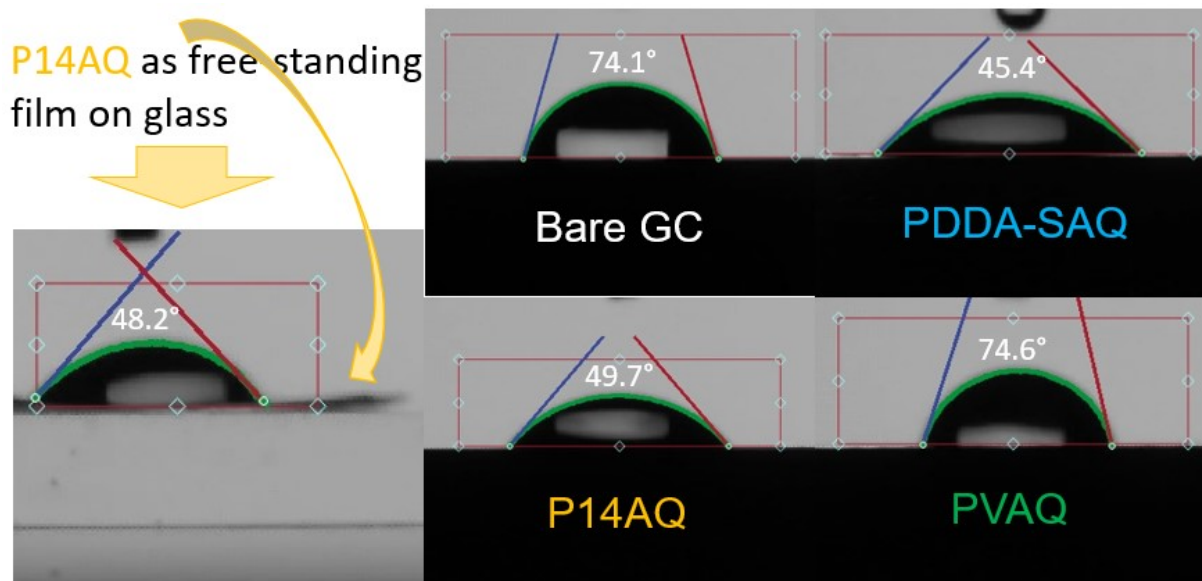
Figure 62: Contact angle measurement with a water drop on blank GC, PDDA-SAQ, P14AQ and PVAQ on GC as well as on a P14AQ film on glass. Adapted from Wielend *et al.*[232] © 2021 the authors.

In accordance with literature reports[238], blank GC shows a quite large contact angle of 74.1 °, which is an indication of a significant intrinsic hydrophobicity. As expected from the molecular structure, PDDA-SAQ is quite hydrophilic and PVAQ is rather hydrophobic with a contact angle slightly larger than bare GC. As the chemical structure of P14AQ would also suggest a quite hydrophobic behavior, the rather small contact angle of 49.7 ° suggesting a more hydrophilic surface is unexpected. As can be seen in Figure 62 on the left side, nearly the same contact angle was also measured on a free-standing P14AQ film (a picture of the free-standing film is shown in Figure 52 indicated by the yellow arrow), which was only placed on a glass slide for stability reasons.

3.3.3. Electrochemical characterization of poly(anthraquinones)

As outlined in the beginning of chapter 3.3. poly(anthraquinones) are widely studied and a promising class of organic electrode materials for electrochemical energy storage. Therefore, after the thorough synthesis and characterization of the three selected polymers in chapters 3.3.1. & 3.3.2. 0.7 $mg_{polymer}$ cm^{-2} were drop-casted from solutions or suspensions for electrochemical investigation in different aqueous solution. To start the investigations, a 0.1 PB solution at pH=7 was chosen and the CV results are depicted in Figure 63:
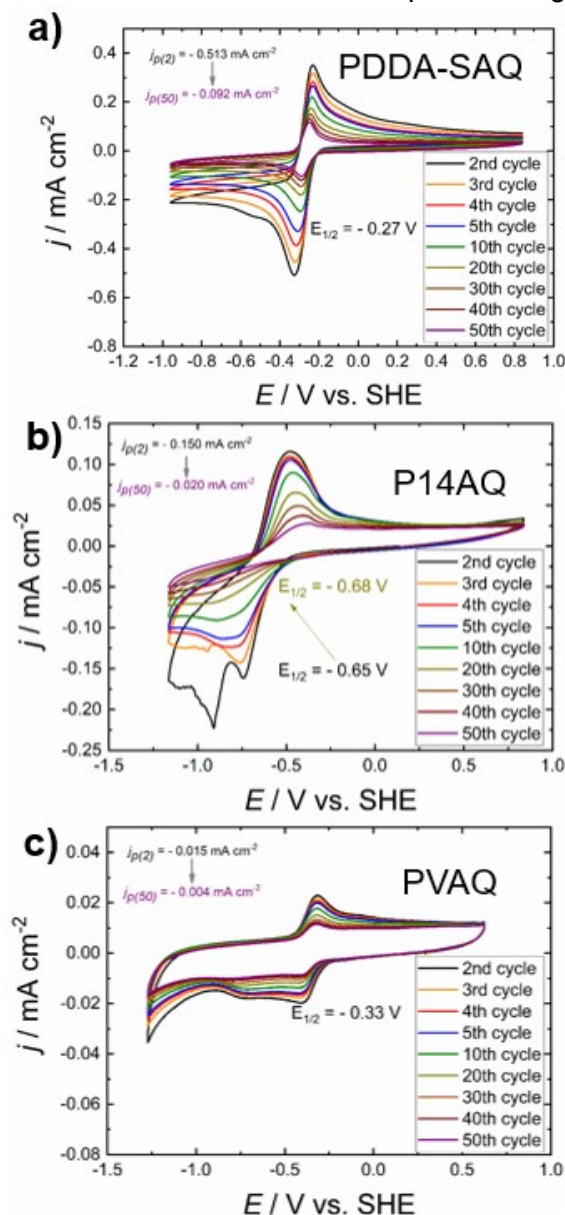

Figure 63: CV graphs testing 50 cycles stability of a) PDDA-SAQ, b) P14AQ and c) PVAQ recorded in 0.1 M PB at neutral pH=7. Reproduced from Wielend *et al.*[232] © 2021 the authors.

At a first glance, Figure 63 reveals that PDDA-SAQ shows the largest faradaic current of all polymers under neutral conditions and at the same time the most reversible redox behavior possessing the smallest peak separation. This high current response is in agreement with the structural properties of poly(ionic liquids) as well as the quite fast decay of the peak currents over cycle time due to dissolution.[239] In case of P14AQ the current is smaller and after the 3rd cycle distinct reduction and re-oxidation peaks develop, which also significantly decrease in

current density over 50 cycles by 87%. In contrast to PDDA-SAQ, where after the CV cycle experiments no polymer film is left on the GC electrode due to dissolution, in case of P14AQ the robust polymer film is still on the electrode. This result suggests, that in case of the P14AQ film, the loss in current density is not due to dissolution but most likely due to deactivation of the redox active sites. The PVAQ films shows a faradaic current response, which is one order of magnitude lower compared to P14AQ. In addition, the reduction peak is composed of two merged peaks whereas the re-oxidation peak has a nicely reversible shape. Similar to PDDA-SAQ and P14AQ, the peak current density significantly decreased over 50 cycles by 73%. After this cycle study, the PVAQ film was still attached to the GC surface, but in contrast to P14AQ very easy to remove in one piece.

Due to the fact that the degree of protonation of the reduced carbonyl groups as well as the solubility heavily depend on the pH value of the electrolyte solution, similar CV cycle experiments were also performed in alkaline 0.1 M NaOH solution:
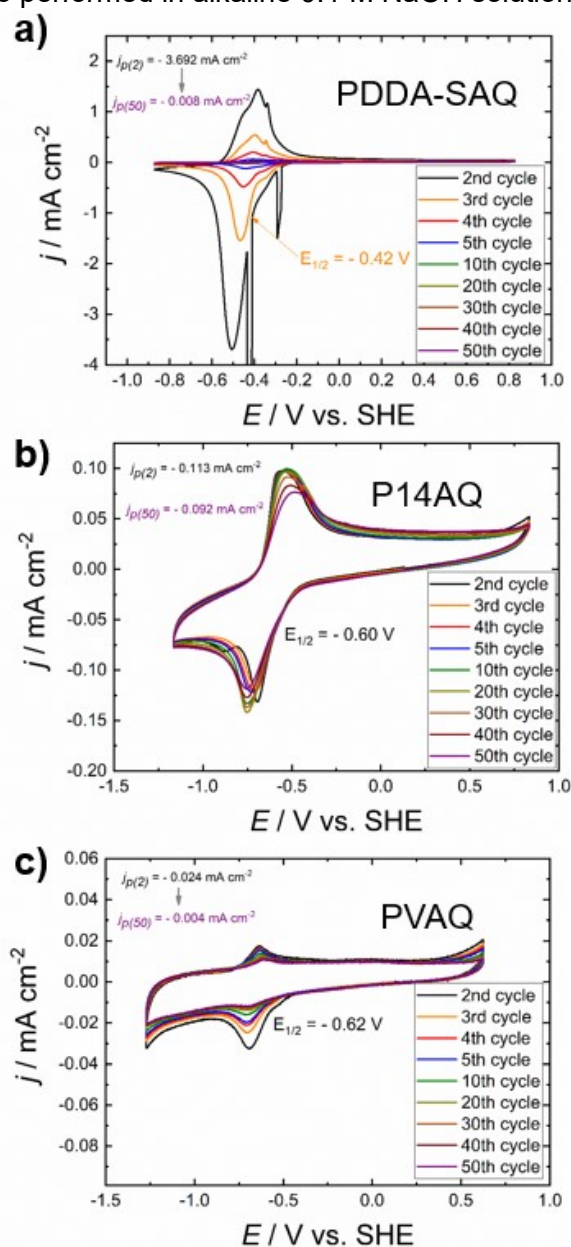

Figure 64: CV graphs testing 50 cycles stability of a) PDDA-SAQ, b) P14AQ and c) PVAQ recorded in 0.1 M NaOH at alkaline pH=13. Reproduced from Wielend et al.[232] © 2021 the authors.

The most obvious difference between the neutral conditions and the CV in alkaline conditions in Figure 64 is the increased j_p in case of PDDA-SAQ by nearly a factor of 10. In these alkaline conditions the j_p although decreases very rapidly within the first 4 CV cycles and some irregularities in the behavior are observed. Both can be most likely attributed to the fast and abrupt dissolution of the AQ moieties upon reduction. Similar, in case of PVAQ a higher j_p followed by faster decay and dissolution is observed in alkaline conditions and after these CV cycles in both cases no polymer film is left on the electrode. As expected from the Nernst equation, the redox potentials of PDDA-SAQ and PVAQ are cathodically shifted upon increased pH. In contrast to these observations, P14AQ shows a comparable current behavior in the NaOH solution but nearly no loss in j_p even after 50 CV cycles. In addition to this stable and reversible current behavior, the redox potential of P14AQ is slightly anodically shifted upon the increased pH. An explanation for both phenomena is an increased swellabilty of the polymer in these alkaline ionic conditions.[235]

Furthermore in Figure 65, similar CV studies at pH=13 were performed in a 2.5 M NaCl solution with increased ionic strength to see if the dissolution behavior of the polymers is affected by the ionic surrounding:
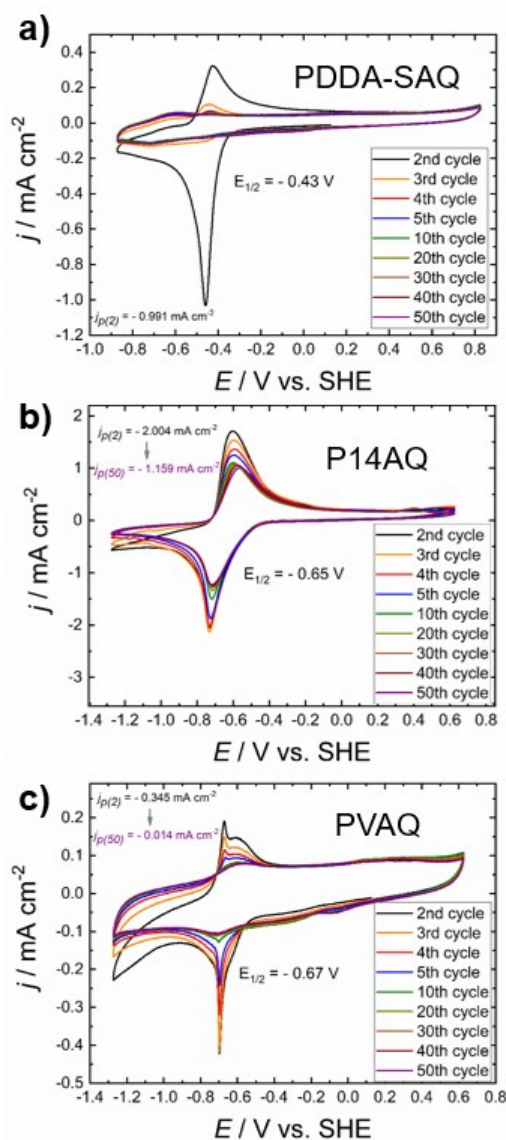

Figure 65: CV graphs testing 50 cycles stability of a) PDDA-SAQ, b) P14AQ and c) PVAQ recorded in 2.5 M NaCl solution in 0.1 M NaOH at alkaline pH=13. Reproduced from the Supporting Information of Wielend *et al.*[232] © 2021 the authors.

As seen in Figure 65, PDDA-SAQ dissolves even faster upon CV cycling in a way that the redox peaks are only observable within the first two cycles. In case of PVAQ the j_p increased by a factor of 14 compared Figure 64 and simultaneously exhibiting sharp and reversible redox peaks. This result demonstrates that the higher ionic strength is beneficial for a more reversible redox behavior in case of PVAQ, but nevertheless the dissolution remains nearly unchanged. In analogy to PVAQ, also P14AQ shows an increased current response by a factor of 18 with a j_p of more than 2 mA cm^{-2} in the 2nd cycle. Again, the high ionic strength assists for a more reversible redox behavior, but also lowers the relative cycle stability.

To finalize the CV cycle stability experiments, the polymer films were also investigated in an acidic electrolyte solution of 0.1 M NaHSO$_4$ at pH=2:

Figure 66: CV graphs testing 50 cycles stability of a) PDDA-SAQ, b) P14AQ and c) PVAQ recorded in 0.1 M NaHSO$_4$ at alkaline pH=2. Reproduced from the Supporting Information of Wielend *et al*.[232] © 2021 the authors.

The redox behavior of PDDA-SAQ in pH=2 appears to be significantly different in comparison to the previous studies due to a larger peak separation. Additionally, between the 20th and 30th cycle a change in CV shape was observed due to delamination of the polymer film. Up to the

20th cycle the AQ redox peaks were observed and no reductive peak in the cathodic region of -0.8 V was observed. After the 30th cycle, the AQ peaks nearly vanished and the hydrogen evolution reaction of GC appeared at -0.8 V, which was suppressed before by the polymer film. P14AQ and PVAQ showed no faradaic current behavior in these acidic conditions and only very low capacitive current response. Only PVAQ showed a slight increase in a peak during the 50 CV cycles, but at a very low j_p close to the detection limit.

Concluding, for all three polymers studied, such acidic conditions seem to be unfavorable for reversible redox response investigations. Out of the three polymers, only PDDA-SAQ showed a faradaic response with hindered and shifted re-oxidation peaks.

In addition to the CV studies in aqueous solution – which is the main target of this work – also CV studies in the organic, aprotic solvent acetonitrile (MeCN) were performed as shown in the following Figure 67:
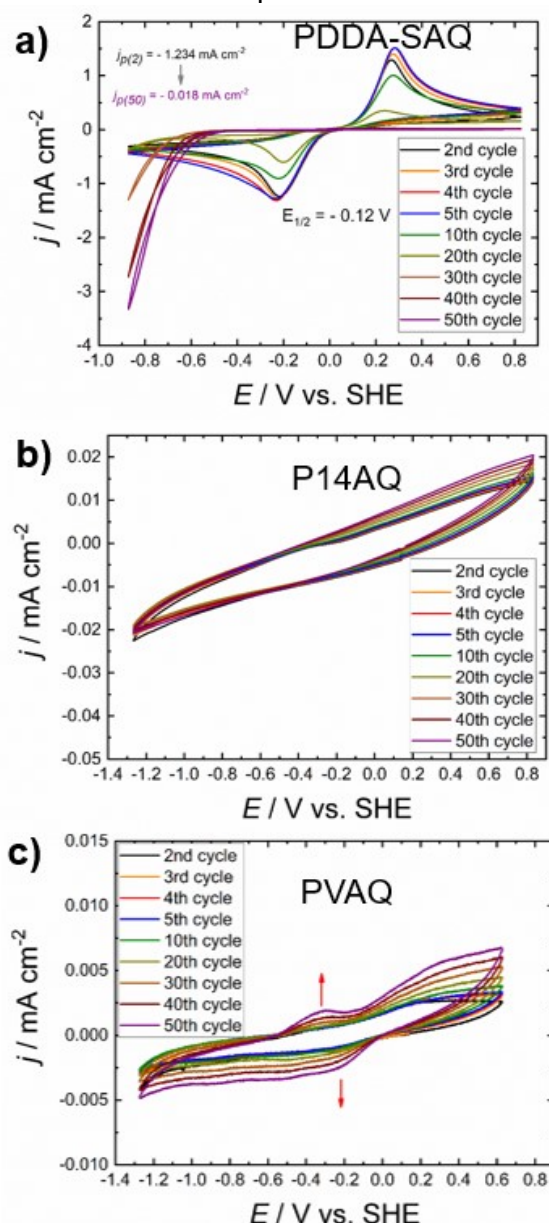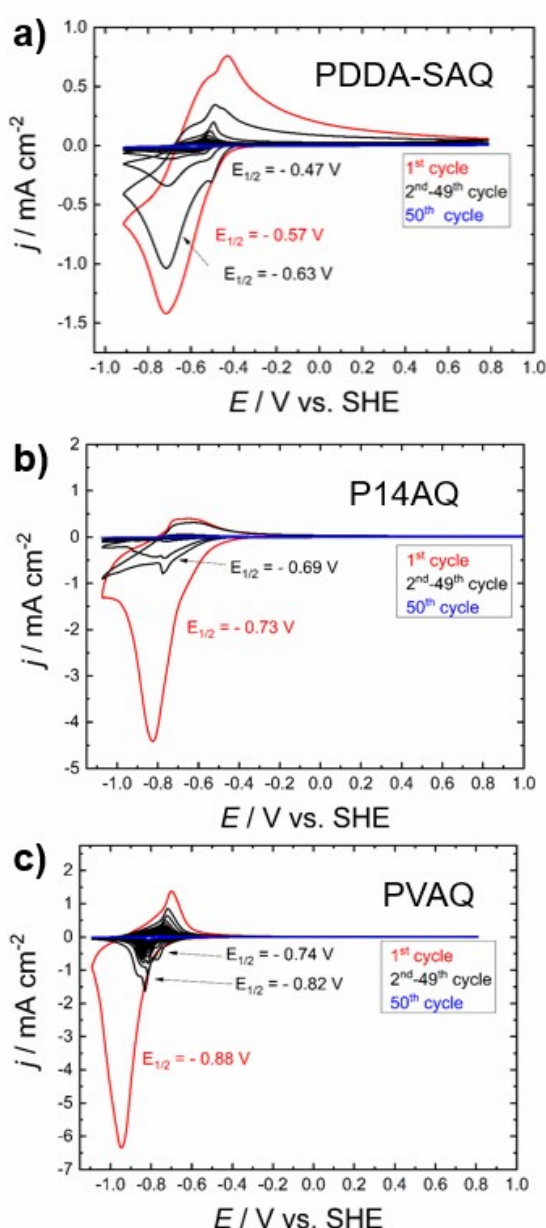

Figure 67: CV graphs testing 50 cycles stability of a) PDDA-SAQ, b) P14AQ and c) PVAQ recorded in 0.1 M TBAPF$_6$ in MeCN solution. Reproduced from the Supporting Information of Wielend *et al.*[232] © 2021 the authors.

The CV cycle experiments in MeCN in Figure 67 show the opposite trend compared to the ones performed in 2.5 M NaCl with 0.1 M NaOH. In MeCN PDDA-SAQ shows moderate cycle stability with one reduction peak at -0.57 V in the first cycle which splits up into two waves in the consecutive cycles. The CV cycles of P14AQ in MeCN are only detectable within the first 3 cycles before complete dissolution. In case of PVAQ, the first cycle occurs at a negative potential of -0.88 V with high j_p and the consecutive ones consist of 2 reduction peaks at lower current density. Nevertheless, PVAQ shows the highest cycle stability of all three polymers with even partial faradaic current of -0.085 mA cm^{-2} in the 50th cycle.

While discussing the CV cycle stability in terms of remaining polymer on GC, the question of how to analyze this remaining polymer arose. In order to answer the question, scanning electron microscopy (SEM) images of drop-casted polymer films on GC electrodes were recorded. After CV cycle treatment under the most stable pH conditions (according to Figure 63 & Figure 64), also SEM images after this cycle treatment were recorded and compared in Figure 68:
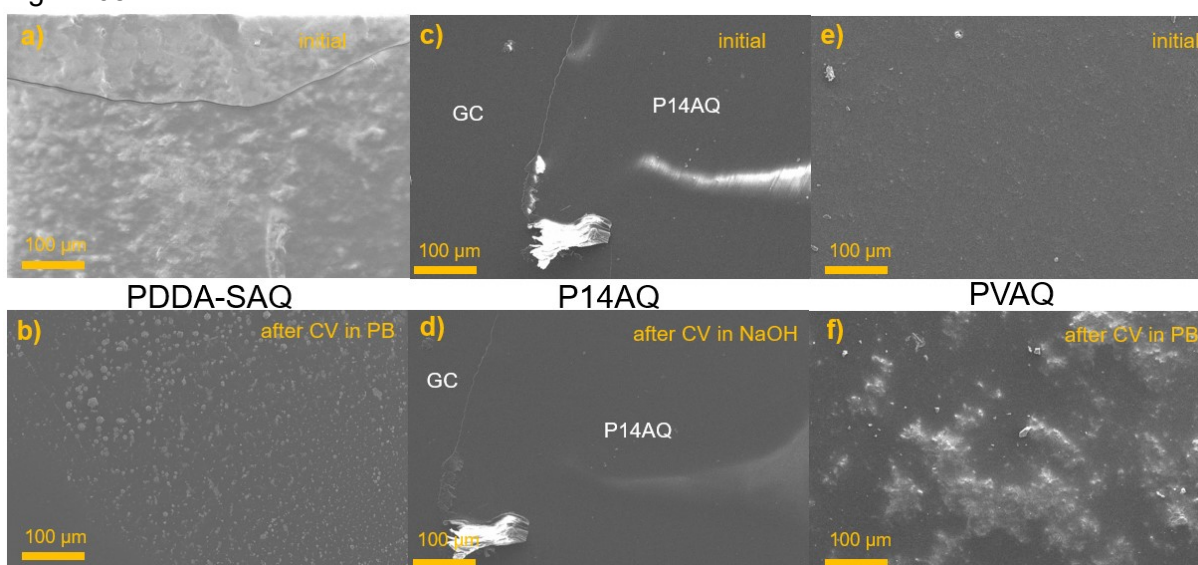

Figure 68: SEM images of polymer films on GC electrode before and after the electrochemical treatment as stated: a-b) PDDA-SAQ, c-d) P14AQ and e-f) PVAQ. Reproduced from Wielend et al.[232] © 2021 the authors.

P14AQ shows no change in morphology according to the SEM images in Figure 68 before and after CV's in 0.1 M NaOH, which is why the areas of GC and P14AQ are marked within the images. In case of PVAQ the as-casted film is quite smooth which turns into a rougher appearance after cycling in 0.1 M PB. Only in case of PDDA-SAQ, the as-casted film is quite thick and rough and shows a crack as a result from the solvent evaporation. After the CV treatment, only very few polymer islands are left, which is in good agreement to the nearly complete dissolution shown in Figure 63.

As Hernández et al.[231] reported PDDA-SAQ films as electrocatalyst for the oxygen reduction reaction, CV cycles of PDDA-SAQ were recorded under N_2 and O_2 saturated conditions in neutral 0.1 M PB and 0.1 M NaOH solution as depicted in the following Figure 69:
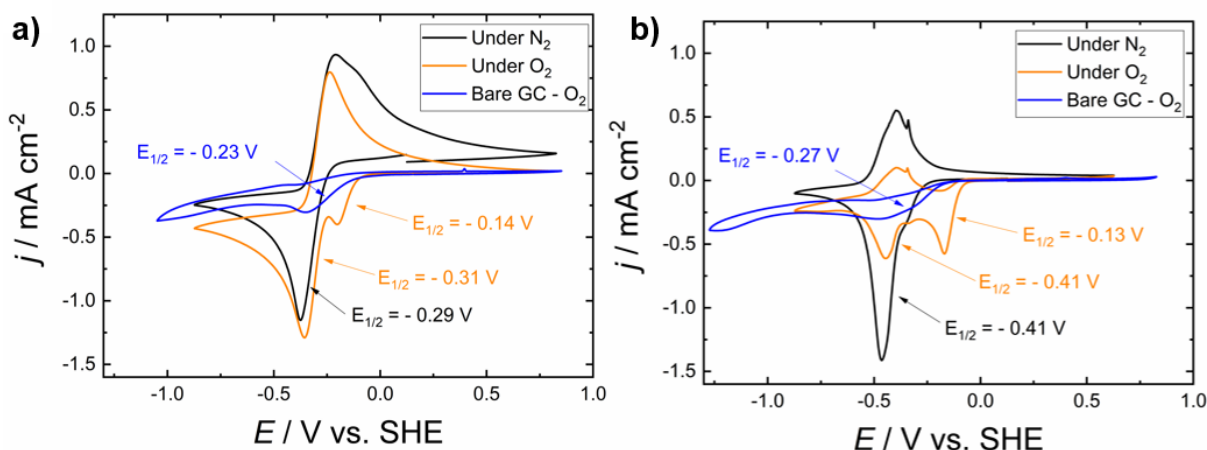
Figure 69: CV comparison of PDDA-SAQ comparing N_2 saturated conditions with O_2 saturated conditions with GC under O_2 in a) 0.1 M PB at pH=7 and b) 0.1 M NaOH at pH=13. Reproduced from Wielend *et al.*[232] © 2021 the authors.

After the studies on ORR on GC electrodes in chapters 3.1. & 3.2. the CV curves of a blank GC under O_2 is plotted for comparison in Figure 69 for both electrolyte solutions. The shape and potentials of the graphs recorded under N_2 are nearly identical to the ones in Figure 63 & Figure 64. Upon addition of O_2, at pH=7 the PDDA-SAQ redox peak remains unchanged and an additional peak at -0.14 V evolves. This additional peak can be correlated to oxygen reduction at a lower overpotential compared to GC. This result is in agreement with literature[231] and demonstrates the electrocatalytic effect of immobilizing the AQS in PDDA-SAQ in comparison to the studies with homogenously dissolved AQS in chapter 3.2. The homogeneously dissolved AQS did not alter the potential nor the limiting current, but only with help of RRDE catalytic excess currents could be observed.[214] On the other hand, the immobilized PDDA-SAQ still has a nearly unchanged AQS peak and the additional catalytic peak with more positive potential and higher current than blank GC.

Considering the alkaline conditions, this positively shifted additional peak is also present. Although under O_2 the PDDA-SAQ peak is significantly smaller than under N_2 due to dissolution, this extra electrocatalytic peak at -0.13 V has even larger j_p compared to the neutral conditions or even the GC under O_2 peak in 0.1 M NaOH.

As P14AQ and PVAQ did not show a reversible redox behavior in neutral conditions, the following electrocatalytic CV studies for oxygen reduction were only performed in 0.1 M NaOH as illustrated in the following Figure 70:
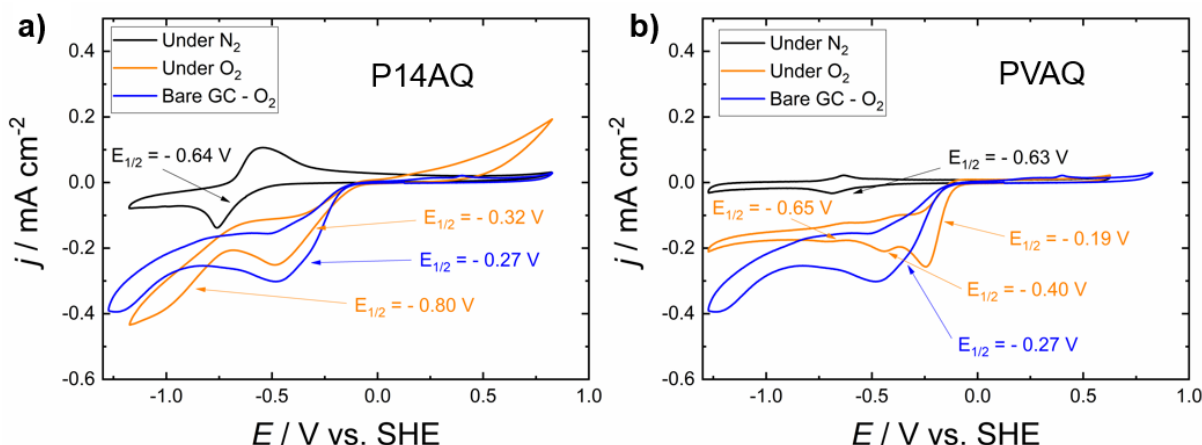
Figure 70: CV comparison of a) P14AQ and b) PVAQ comparing N_2 saturated conditions with O_2 saturated conditions with GC under O_2 in 0.1 M NaOH at pH=13. Reproduced from Wielend *et al.*[232] © 2021 the authors.

Here, P14AQ shows a CV curve under O_2 which seems to be additively composed of the polymer under N_2 and GC under O_2. In contrast to PDDA-SAQ, no additional peak is observed and the ORR peak of GC appears at a more negative potential and lower current density. This means that P14AQ is not active towards electrochemical oxygen reduction but acts as a blocking layer. As the peak at -0.80 V is not identical to the redox response of P14AQ, this might be a hint for the O_2 to water reduction reaction. Nevertheless, as the goal of this work is the production of H_2O_2, this behavior is not studied in further detail.

In accordance with the previous CV studies of PVAQ under N_2 in Figure 64 also in Figure 70 the redox peak of PVAQ at -0.63 V is quite small in comparison to GC. Nevertheless, this PVAQ peak is still observable in the CV recorded under O_2, in contrast to P14AQ. In addition, the onset of the oxygen reduction peak is slightly positively shifted with the PVAQ present in comparison to bare GC while the PVAQ on the other hand reduces the ORR current density.

Given that PVAQ and PDDA-SAQ suffer from reduction dissolution due to the AQ moieties, CV studies under N_2 and O_2 were also tried with a reduced potential range without reducing the AQ moieties. After 50 cycles under N_2 and O_2 each, only at the end a full CV cycle was recorded in order to check if the polymers themselves are stable in alkaline solution without reducing the AQ polymers:
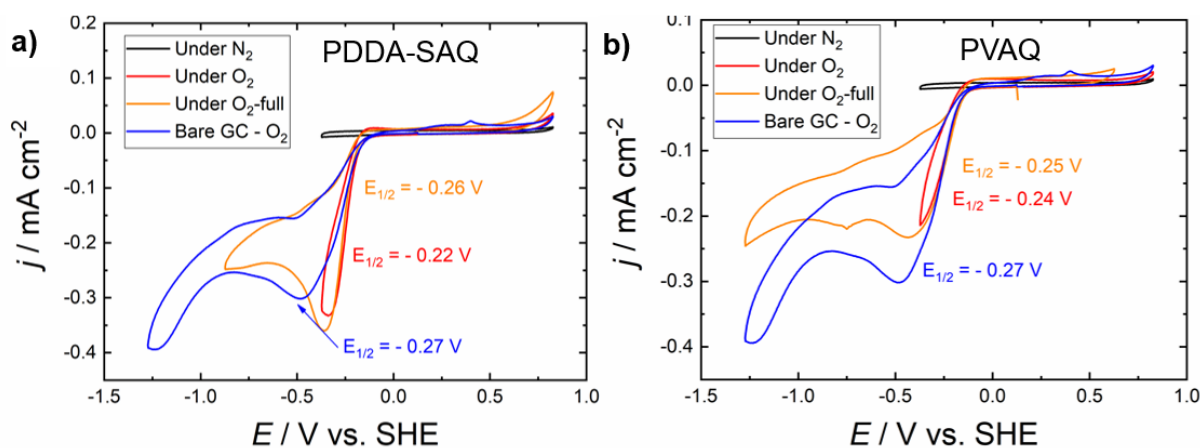

Figure 71: CV comparison of a) PDDA-SAQ and b) PVAQ comparing N_2 saturated conditions with O_2 saturated conditions with GC under O_2 in 0.1 M NaOH at pH=13. "Full" refers to scans going beyond the onset of reduction of the polymer whereas the other scans were stopped at the edge of GC ORR.

For the first CV cycles under N_2 and O_2 seen, the reductive return potential was set to -0.4 V to prevent the AQ reduction. Only after this treatment, one full CV scan (shown in red) is recorded to check if there is still electrocatalytically active polymer left. For both, PDDA-SAQ and PVAQ these results reveal that the polymer is dissolving also without reducing the AQ moieties and thereby losing the catalytic activity over time. This is demonstrated by the more negative reduction potentials (see orange curves in Figure 71) in contrast to the one recorded after shorter treatment.

Due to this stability issue, further studies exploring the electrocatalytic activity of PDDA-SAQ and PVAQ like RDE measurements or electrolysis for H_2O_2 production are unfeasible. However, surprisingly Hernández *at al.* reported RDE-LSV curves for PDDA-SAQ without noticing any stability problems.[231]

After thorough investigation of the three polymers with spectroscopic characterization methods and electrochemistry, structure property relations between these techniques are attempted. As the chemical structure affects the electrochemical properties, such relations would be beneficial for future development of poly(anthraquinones) and other related redox active polymers as this would facilitate the screening. In a first correlation attempt, the redox potentials of the polymers recorded in different electrolyte solutions were compared relative to the C=O IR bands from Figure 60, as exactly these carbonyl groups of the AQ moieties are electrochemically reduced at these certain redox potentials:
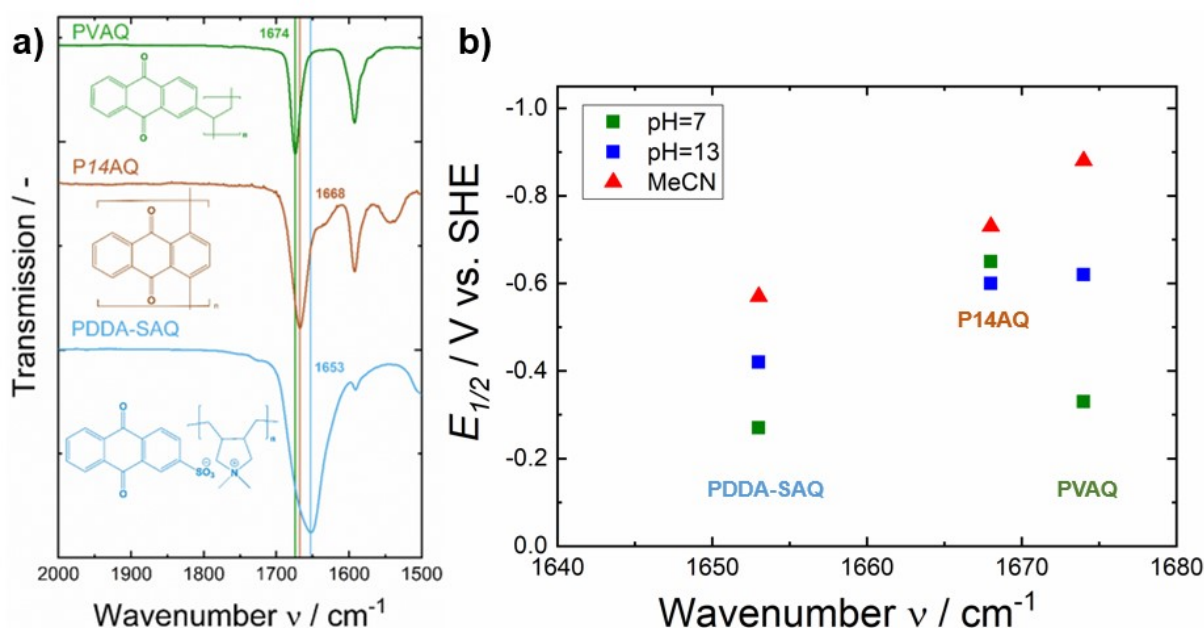
Figure 72: a) ATR-FTIR spectra of the three anthraquinone polymers in the ragne of the C=O vibration modes and b) graphical illustration of the redox potentials at various electrolyte soltutions in dependece of the C=O wavenumbers. Reproduced from the Supporting Information of Wielend *et al.*[232] © the authors.

As can be seen from the potential vs. wavenumber plot in Figure 72, especially the redox potentials of the CV scans extracted from Figure 67 correlate nearly linearly with the $\nu_{C=O}$ of the according polymer. A similar trend is observed for the results in alkaline solution, whereas the ones recorded in PB do not follow this trend. One reason for the difference of the pH=7 measurements is the instability of the redox behavior due to an unknown deactivation process. The trend in MeCN and NaOH solution can be understood by referring to chemical bonds

acting as springs described with *Hooke's law* and the approach of a harmonic oscillator from quantum mechanics:[240]

$$F = -k \cdot \Delta x$$

$$\nu_0 = \frac{1}{2\pi} \cdot \sqrt{\frac{k}{\mu}}$$

Hereby μ corresponds to the reduced mass of the system and k to a force constant. A higher $\nu_{C=O}$ corresponds to a stronger bond (or from Hooke's law to a larger spring constant k) which requires a higher driving force as a more cathodic potential for electrochemical reduction. Furthermore, this weaker C=O bond is most likely arising from a stronger π-conjugation throughout the covalently bound molecules in case of P14AQ and PVAQ.

In electrochemical studies, the interface between the electrode material and the electrolyte solution is studied, which is why the wetting properties of the electrode and solution is crucial. This might be one explanation, why in neutral PB, having large phosphate anions, this interface is somehow less reversible in comparison to the small and nucleophilic hydroxide anions. Figure 73 illustrates, whether these wetting properties exemplified as contact angle also correlate with electrochemical properties:
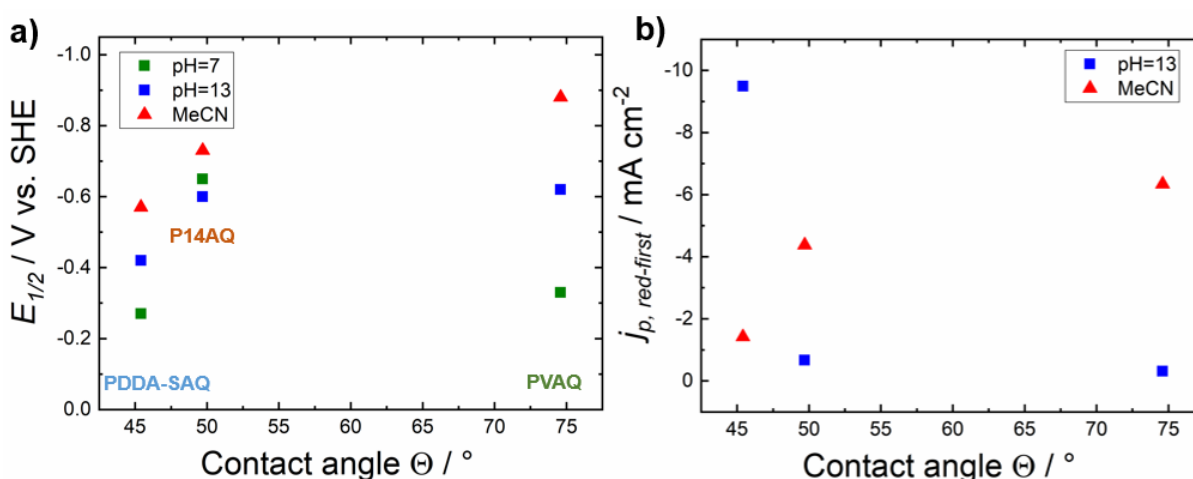

Figure 73: Graphical correlation plots of a) redox potential *vs.* the contact angle θ and b) peak current density of the first reduction peak in MeCN *vs.* the contact angle θ. Part b) is reproduced from the Supporting Information of Wielend *et al.*[232] © 2021 the authors.

Similar to the correlation of the redox potential with the detected carbonyl IR bands, the comparison of the redox potential vs. the contact angle reveals a comparable trend. A polymer with a higher contact angle θ is regarded as more hydrophobic. The more hydrophobic a polymer is, a more cathodic potential is required for the electrochemical reduction. Again, under neutral media, deviations from this behavior are observed, which are likely due to the unfavorable polymer-ion interactions, as mentioned above. As a result of these irregularities in form of multiple-peak reductions, the results from pH=7 could not be referred to as reliable which is why they are omitted in Figure 73b. Based on the reorganization energy from Marcus theory[215,240–242], correlations of the electrochemical redox potentials in dependence of the hydrophobicity of the molecules were already reported in literature for redox-active enzymes[243,244]. Very recently, Ma *et al.*[245] described a very similar correlation but not naming

the polymer parameter *hydrophobicity* but *polymer-water affinity*. Furthermore, Oka *et al.*[246] from the same research group which described the PVAQ application for energy storage for the first time, explicitly emphasized the importance of a hydrophilic backbone in a newly synthesized poly(anthraquinone) system.

The findings reported here as well as the described latest publications on redox-active polymers clearly demonstrate the importance of knowing the hydrophobicity of the polymer material. Nevertheless, it appears that the terminology as well as the experimental quantifications for this parameter still requires some unification within the community. Therefore, it is proposed to include the contact angle measurement into the "pool of standard characterization methods" for such redox active polymers. We believe that this will not only help for new compounds but also help to understand the properties of already synthesized polymers.

In addition to the correlation of the redox potential, also qualitative trends for the reduction current densities can be deduced from Figure 73b. When considering the very first cycle upon electrochemical reduction in MeCN, the more hydrophobic polymers show a larger j_p. On the other hand in 0.1 M NaOH solution, the opposite trend was observed where the most hydrophilic polymer PDDA-SAQ shows the highest j_p. These trends can be understood by means of the tendency of the reduced polymers to dissolve into the electrolyte solution. As the graph does not show a linear correlation, further in-depth studies are required to understand and model this behavior in detail. Possible suggestions on the way to a deeper understanding are considering the cosine function part of the formula for the contact angle as well as a frequently used logarithmic plot for current densities in Tafel plots.

Summing up, three selected poly(anthraquinones) were synthesized and characterized for their spectroscopic, thermal and surface properties, as well as for their electrochemical and electrocatalytic behavior in aqueous solution. Although the redox-active center of all three polymers is chemically nearly identical, significant differences in the electrochemical and electrocatalytic behavior were observed and could be explained by spectroscopic and surface related techniques.

In particular, P14AQ as polymer with a π-conjugated backbone, shows the highest solubility in CHCl$_3$ and highest stability upon CV cycling in alkaline medium whereas the quinone moieties seem to be unable to catalyze the oxygen reduction reaction. Furthermore, P14AQ shows unexpected high thermal stability and quite hydrophilic behavior. In contrast, PDDA-SAQ is quite electrocatalytically active towards the oxygen reduction but shows low CV cycle stability. Both properties seem to be a result of the non-covalent ionic bond of the quinone moieties. PVAQ is a hydrophobic polymer with quite hindered quinone groups for electrocatalysis and even pure redox chemistry. Due to a certain hindered structure, which was even visible in the DOSY-NMR, no sufficient ion permeation is possible, which causes very low faradaic currents and fast reductive dissolution.

Besides correlation of the $v_{C=O}$ from FTIR measurements with the redox potential, the hydrophobicity of the polymer representing the electrode-electrolyte interface is identified as a key parameter. Therefore it is recommend to include the contact angle measurement in future studies on new poly(anthraquinones).

Furthermore, determination of the hydrophobicity via contact angle measurements of already reported poly(anthraquinones) are easy to perform and could further help the community via verifying or falsifying the structure-property relations proposed herein. As a rather easy and cheap table-top experiment the contact angle measurement is beneficial compared to the determination of partition coefficients[243,244] or determination of a water mass uptake with the help of a quartz-crystal microbalance (QCMB) technique[245].

These outcomes are in agreement with literature that consideration of the hydrophobicity of the electrode materials is crucial for battery research[247,248] but also in electrocatalysis[60,199,249]. Therefore, the integration of hydrophobicity measurements during material characterization is recommended.

The results presented within this chapter were recently published in *ChemElectroChem* by Wielend *et al.* (2021).[232]

3.4. Non-covalent immobilization of anthraquinone on carbon nanotubes

It is well known from literature and the results in chapter 3.2. that homogeneously dissolved anthraquinones can catalyze the oxygen to hydrogen peroxide reduction reaction. Although aforementioned literature reports[125–127] on covalently grafted anthraquinones onto GC electrodes report improved electrocatalysis, the studies shown in chapter 3.3.3. on poly(anthraquinones) for the oxygen reduction reaction revealed an ambiguous behavior. While in case of PDDA-SAQ, where the AQ units are ionically bound to the polymer backbone, shows a strong electrocatalytic effect, covalently bound AQ units in P14AQ and PVAQ are not accessible for the oxygen reduction reaction. Furthermore, differences in hydrophobicity are also identified as key-parameters for the electrochemical addressability of the quinone moieties.

This balancing of chemical stability and electrochemical addressability in heterogenized systems applied in electrocatalysis is one of the key challenges for designing durable and sustainable electrocatalysts.[55,94,102,104,250–252] Throughout the last 10 years, the Spanish group of Emilio Pérez developed and reported several non-covalent architectures on carbon materials. Starting with macrocyclic host molecules for fullerenes[253], a further development was the rotaxane-type mechanically interlocking carbon nanotubes (MINTs)[254–257], illustrated in the following Figure 74:
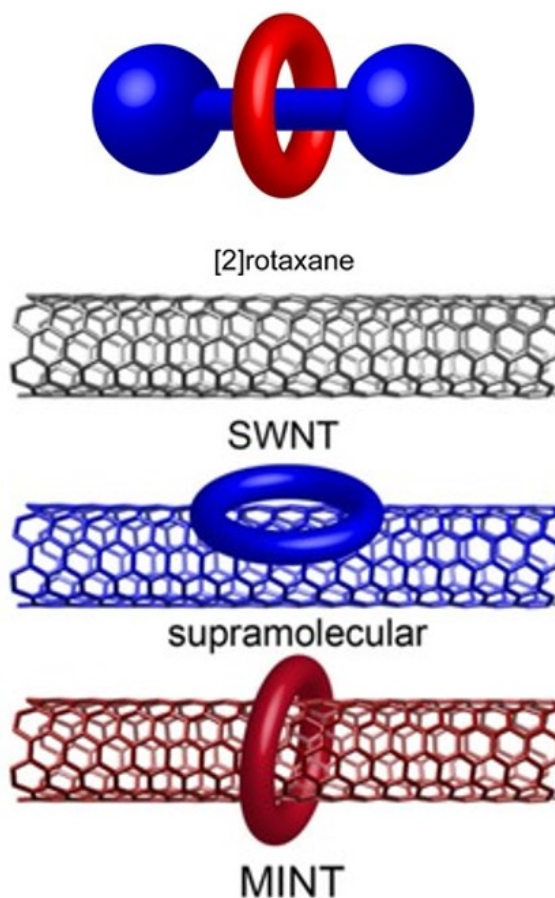

Figure 74: Graphical illustration of a general [2]rotaxane system and a mechanically interlocked carbon nanotube (MINT) system. In addition a single-walled carbon nanotube (SWCNT) and a supramolecular assembly are also depicted. Reproduced with permission from Pérez [256] © 2017 Wiley-VCH Verlag GmbH&Co. KGaA, Weinheim.

Such MINT structures have the unique property of combing the best out of two worlds from immobilization: On the one hand, the redox active molecule is exposed and thereby accessible whereas the SWCNT is not chemically modified and therefore still keeps its good (semi-) conductive properties[108]. On the other hand, this MINT approach also possesses the stability benefits of a covalent attachment, as the macrocycle is covalently closed and this ring cannot easily dispatch.[258]

The goal of this work was to prove the benefits of this non-covalent immobilization as a stable platform for immobilizing electrocatalysts.

The results presented in this subsequent chapter were published by Wielend *et al.* (2020) in *ACS Applied Materials and Interfaces*.[259]

All the material synthesis and spectroscopic characterization was done by Mariano Vera-Hidalgo in IMDEA Nanociencia (Spain) and is explained in detail in his PhD thesis[260] and a publication by Blanco *et al.*[261], as well as in brief form in the supporting information of our joint collaboration paper[259].
Only in brief, in the following Figure 75 the general synthesis steps towards MINTs as well as a scheme are shown:

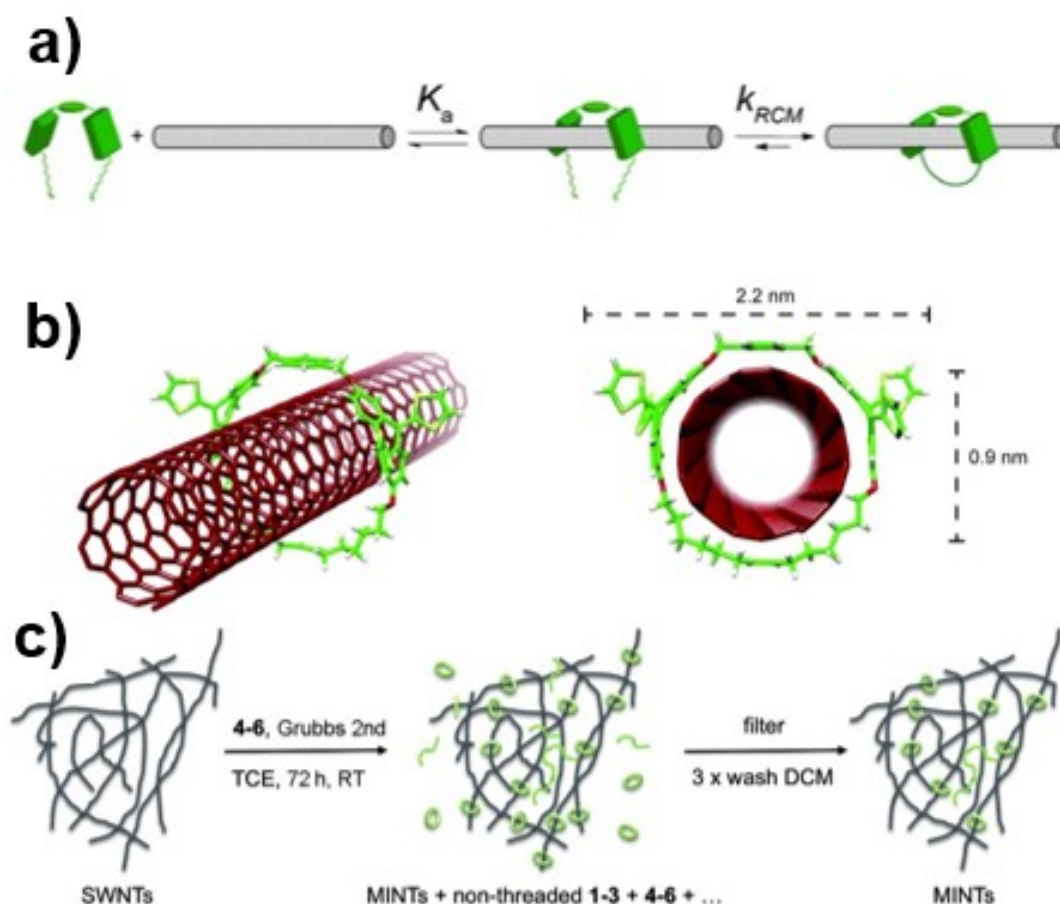Figure 75: a) graphical illustration of the MINT synthesis steps, b) energy-optimized simulation of a general MINT structure on a SWCNT and c) synthesis steps of MINT fabrication. Part a) was reproduced with permission from Pérez [256] © 2017 Wiley-VCH Verlag GmbH&Co. KGaA, Weinheim. And parts b&c) were reproduced with permission from DeJuan *et al.* [254] © 2014 Wiley-VCH Verlag GmbH&Co. KGaA, Weinheim.

As depicted in Figure 75, after synthesis of the U-shaped precursors, this molecule is physisorbed to SWCNTs. The final formation of the MINT is done via a ring closure reaction and the supramolecular forms (which are the ones just simply stuck on SWCNT, as illustrated in Figure 74) are washed away to yield pure MINTs.

For this study on MINTs selected as a platform for electrocatalysis, a macrocycle with two anthraquinone units was prepared, which was previously reported already as a catalyst for other chemical reactions[261]. In order to have a comparable anthraquinone molecule in homogeneous solution, 2,6-bis(oct-7-en-1-yloxy)anthracene-9,10-dione (octenyloxy-AQ) was synthesized by Mariano Vera-Hidalgo as described in the supporting information of Wielend *et al.*[259] and the chemical structure of the MINT macrocycle and this octenyloxy-AQ are shown in Figure 76:
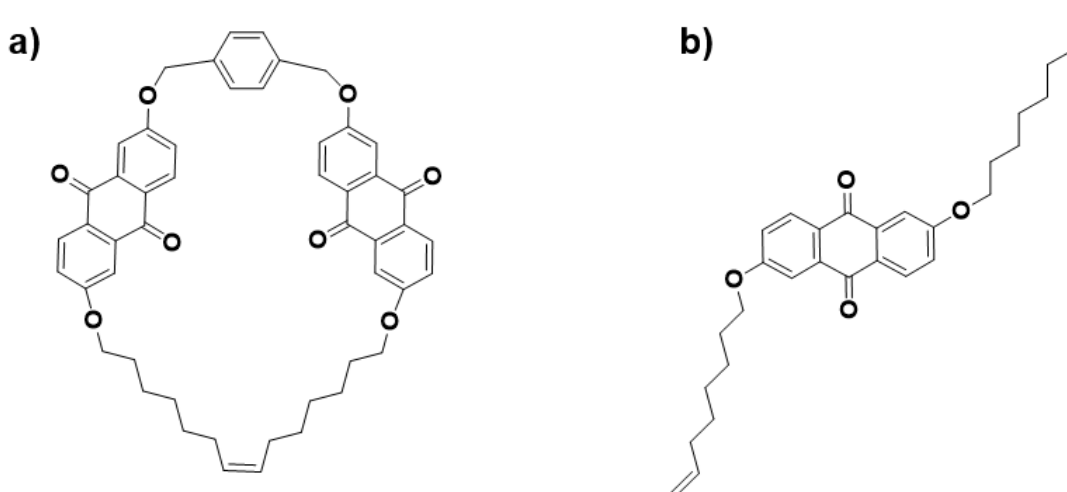
Figure 76: Chemical structure of a) the AQ-MINT macrocycle and b) the octenyloxy-AQ.

Regarding the detailed synthetic procedure as well as the full thermal and spectroscopic characterization of the AQ-MINT as well as the octenyloxy-AQ molecule, as shown in Figure 76, previously published literature is available.[259–261] For a comprehensive understanding on the nano-architecture used herein, the structure of the AQ-MINT is depicted in the following Figure 77:

Figure 77: a) Energy-minimized molecular geometry of AQ-MINT performed via DFT and b) HR-TEM image of AQ-MINT. Reproduced from Blanco *et al.* [261]. © 2018 these authors.

Figure 77 shows that the bonding lengths of the AQ-macrocycle are especially designed for a tight fit around the SWCNTs and that this molecule can even be visualized using a HR-TEM at atomic resolution.

As a starting point, the impact of the alkoxy substituent on the electrochemical behavior of anthraquinone was examined:

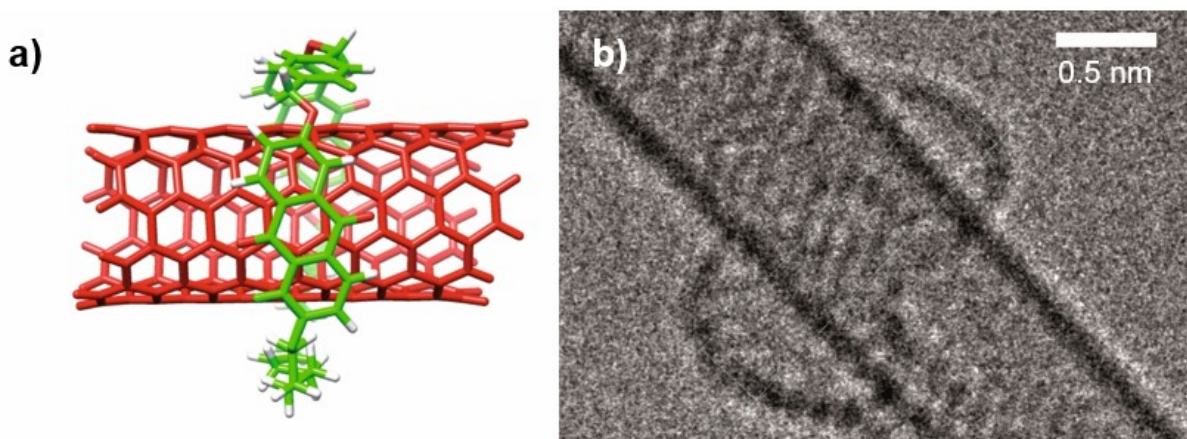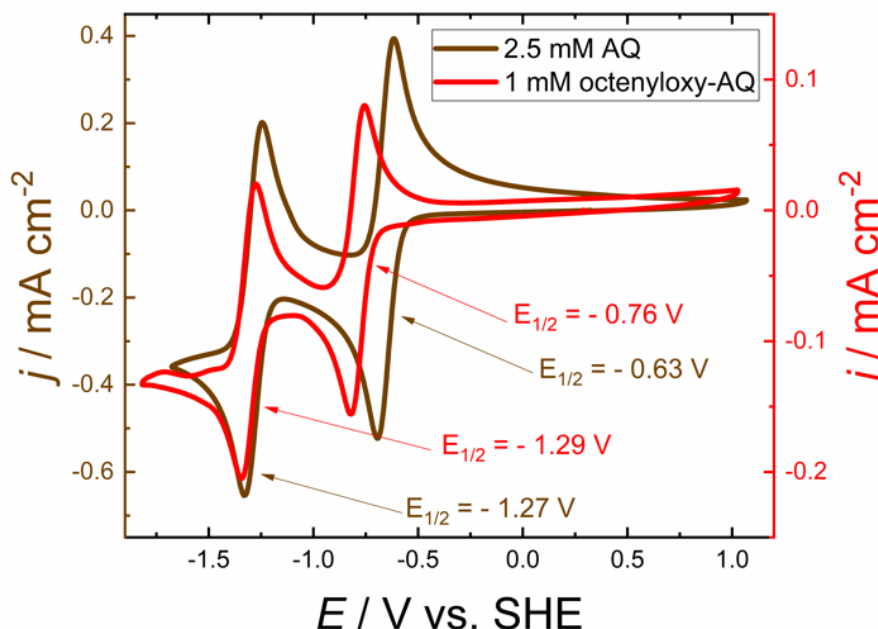Figure 78: CV study of 2.5 mM AQ and 1 mM octenyloxy-AQ in 0.1 M TBAPF$_6$ in MeCN recorded at 20 mV s^{-1}. Reproduced with permission from the supporting information of Wielend *et al.* (https://pubs.acs.org/doi/abs/10.1021/acsami.0c06516)[259].) © 2020 American Chemical Society.

This CV study shows that upon the alkoxy substitution, the first reduction peak of AQ shifts cathodically which is in accordance to literature due to the electron withdrawing effect of the alkoxy groups.[262–265] This behavior is only observed in absence of any substituents capable of hydrogen bonding like for example hydroxyl groups in the position 1, which have an opposite intramolecular effect.[262,263] The second reduction peak is not affected by the alkoxy substitution, which is why the octenyloxy-AQ can be regarded as AQ analogue with closely related chemical structure to the AQ-MINT macrocycle, keeping the reversible electrochemical features of anthraquinones.

In order to verify this statement, CV of the AQ-MINT was performed in aqueous 0.1 M Na$_2$SO$_4$ solution, as well as in 0.1 M TBAPF$_6$ in MeCN solution and compared in Figure 79 with an evaporated AQ thin film and the octenyloxy-AQ CV:

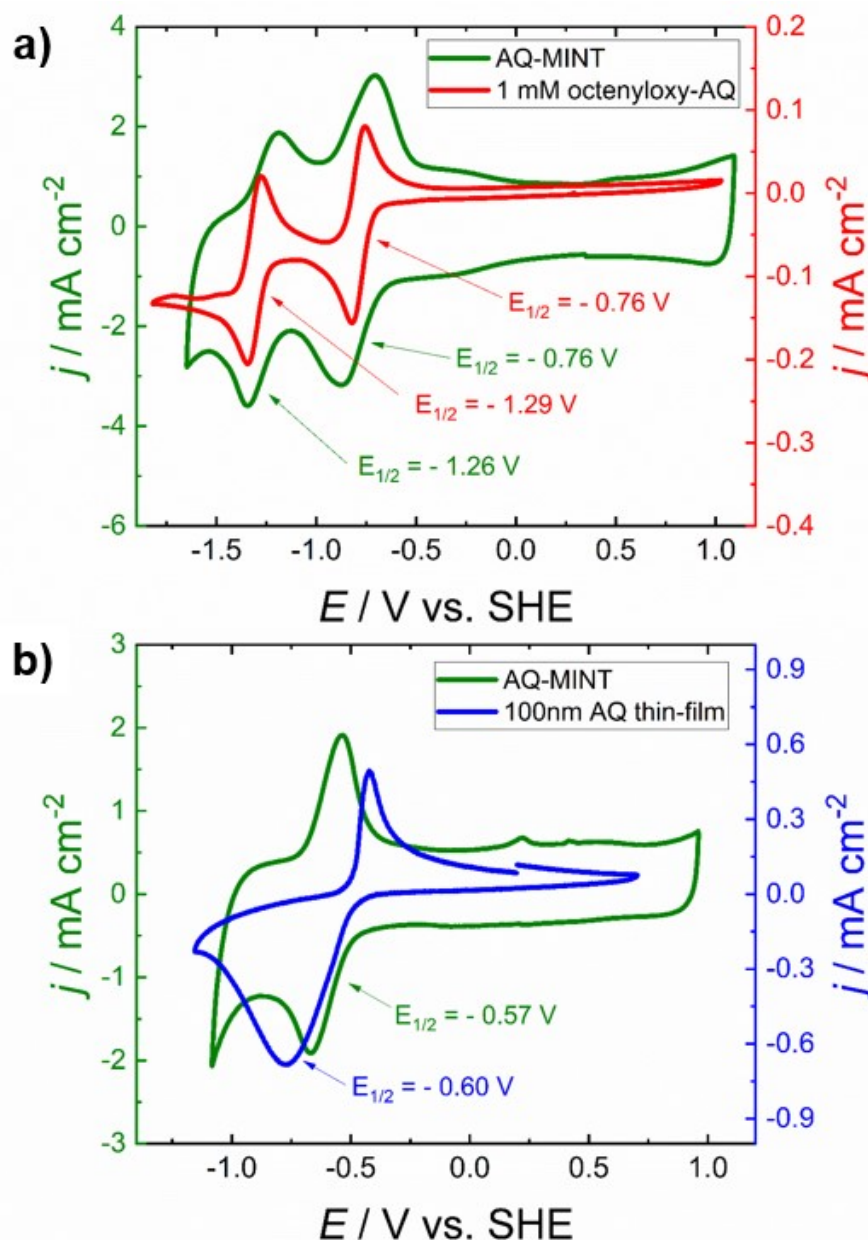Figure 79: CV graphs of a) AQ-MINT and 1 mM octenyloxy-AQ in 0.1 M TBAPF$_6$ in MeCN and b) AQ-MINT and an evaporated 100 nm AQ thin film in 0.1 M Na$_2$SO$_4$ aqueous solution. All CVs were recorded under N$_2$ saturated conditions at a scan rate of 20 mV s^{-1}. Reproduced with permission from Wielend *et al.* (https://pubs.acs.org/doi/abs/10.1021/acsami.0c06516)[259]. © 2020 American Chemical Society.

These results demonstrated that AQ-MINT is indeed a suitable platform for immobilizing a redox active molecule like anthraquinone while retaining a nearly unchanged electrochemical behavior. A similar trend was also reported in literature for adsorbed hydroxyl anthraquinone on MWCNTs.[266] In MeCN as well as aqueous solution, the reduction potentials of AQ-MINT are virtually identical to the ones of octenyloxy-AQ and the AQ thin film. Besides a high current density response, the AQ-MINT also exhibits a quite large faradaic current as a result of the increased electroactive surface due to the SWCNTs. Compared to the homogenous AQ derivative with a peak separation (ΔE_p) of 63 mV, AQ-MINT shows a higher value of 173 mV in MeCN. Nevertheless, the AQ-MINT ΔE_p of 134 mV in aqueous solution is significantly smaller than the 261 mV of the thin film, which demonstrates a more reversible redox system. The fact that adsorbed organic molecules on SWCNTs have faster charge transfer kinetic due

to stacking interactions, which results in a smaller ΔE_p, is well-known in literature.[267] Furthermore, this AQ-MINT systems can be used in both organic and aqueous electrolyte solutions for electrochemical investigations, which was recently also shown for an adsorbed catalyst on MWCNT for electrocatalytic CO_2 reduction.[221]

A third important parameter, in addition to the enhancement of the faradaic current response and elevated electron transfer kinetics, is the stability upon electrochemical CV cycling. For comparison reasons, the AQ-MINT was tested for 50 CV cycles each and compared with the supramolecular form (AQ@SWCNT) as shown in Figure 80:
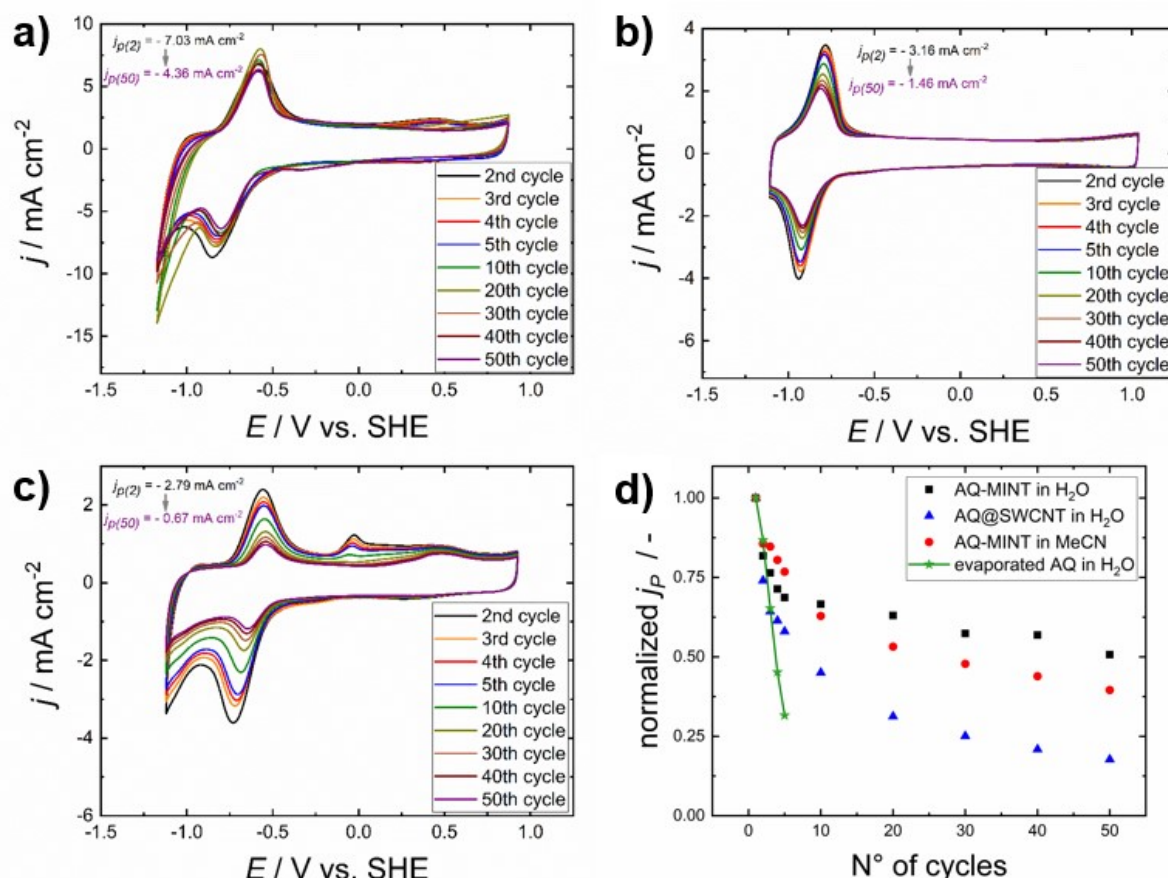
Figure 80: CV curves of a) AQ-MINT in 0.1 M Na_2SO_4, b) AQ-MINT in 0.1 M $TBAPF_6$ in MeCN, c) AQ@SWCNT in 0.1 M Na_2SO_4 and d) Illustration of the normalized peak currents with respect to the first reduction peak. All CV's were recorded under N_2 saturated conditions at a scan rate of 20 mV s^{-1}. Reproduced with permission from Wielend *et al.* (https://pubs.acs.org/doi/abs/10.1021/acsami.0c06516)[259]. © 2020 American Chemical Society.

In order to provide comparable conditions down to around -1.2 V in Figure 80 in aqueous as well as organic conditions, a comparable potential range was chosen. This means that in the graphs a&c, concerted 2 electron steps are shown whereas in graph b only a one electron steps is shown, which is the reason for the lower j_p in MeCN compared to the aqueous system. When comparing the j_p from the 2nd to the 50th cycle, AQ-MINT in aqueous solution only showed a decrease by 38% whereas in case of AQ@SWCNT j_p dropped by 76%. AQ-MINT in MeCN shows surprisingly high stability within the first few cycles followed by a sharp decrease after the 10th cycle. Overall, AQ-MINT in MeCN showed a drop of j_p by 54% from the 2nd to the 50th cycle. AQ thin films are well-know to rapidly dissolve upon electrochemical reduction under N_2

saturated conditions.[268] This fast and nearly linear current drop within the first 5 cycles is also illustrated in Figure 80d as green line.

These results clearly demonstrate the superior stability of the non-covalent AQ-MINT immobilization approach upon electrochemical CV cycling in aqueous solution. In addition to the improved electron transfer kinetic studies, AQ-MINT was also investigated towards the electrochemical oxygen to H_2O_2 production in comparison to SWCNTs and AQ@SWCNTs. As a start, CV cycles under N_2 and O_2 saturated conditions were recorded in 0.1 M Na_2SO_4 and 0.1 M NaOH solutions as depicted in Figure 81:
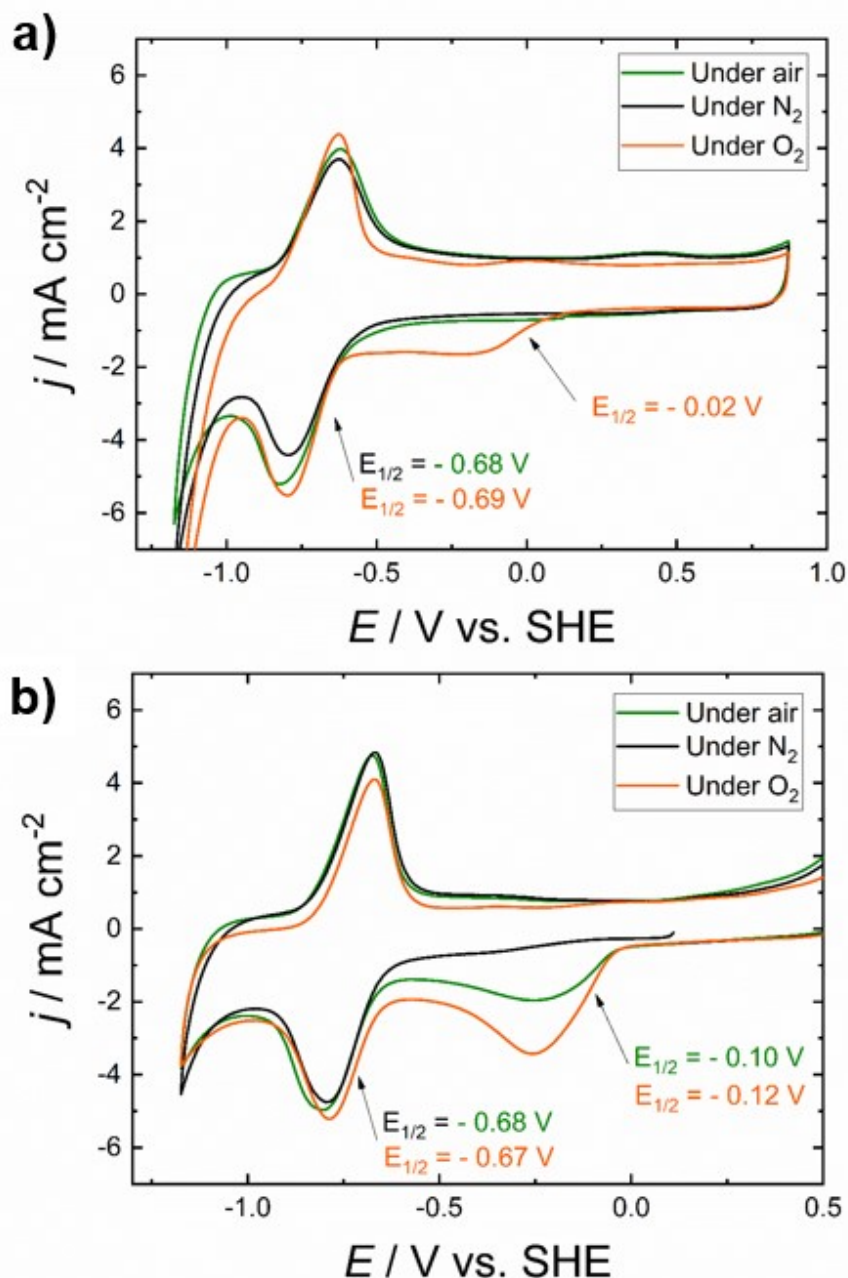
Figure 81: CV curves of AQ-MINT under aerated conditions (green line), N_2 (black line) and O_2 saturated conditions (orange line) in a) 0.1 M Na_2SO_4 and b) 0.1 M NaOH solution. Reproduced with permission from Wielend *et al.* (https://pubs.acs.org/doi/abs/10.1021/acsami.0c06516)[259]. © 2020 American Chemical Society.

The CV curves in Figure 81 show nearly identical j_p and redox potentials in neutral as well as in alkaline conditions. Such behavior is unexpected for freely-diffusing molecules like for

example AQS, but in accordance with the results of poly(anthraquinones) shown in Figure 64 & Figure 65. In contrast to the AQ redox potential, the potential for the oxygen reduction reaction is shifted due to an increase in pH from neutral to alkaline solution from -0.02 V to -0.12 V. On the other hand, in alkaline conditions this oxygen reduction feature is significantly more pronounced as reflected by a real peak shape and a current nearly twice the value compared to neutral conditions. This electrocatalytic effect is more pronounced as compared to bare GC or the poly(anthraquinones) as depicted in Figure 70. To emphasize this significant increase in electrocatalytic current, bare GC, SWCNT and AQ-MINT are compared as showed in Figure 82:
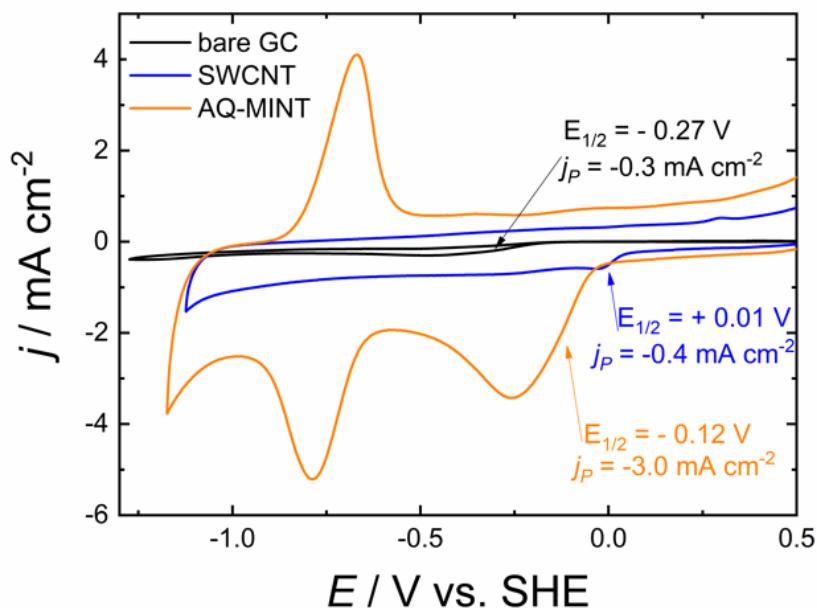
Figure 82: CV comparison of bare GC, SWCNT and AQ-MINT in 0.1 M NaOH under O_2 saturated conditions and recorded at 20 mV s^{-1}.

This comparison revealed that AQ-MINT exhibits an electrocatalytic current of nearly ten times the value compared to bare GC or SWCNTs. Although SWCNTs show a slightly more positive redox potential for the oxygen reduction reaction, the onset potentials are still quite comparable.

In order to investigate the electrocatalytic properties towards H_2O_2 production, chronoamperometry at -0.33 V was performed for 8 h and the amount of H_2O_2 was detected for aliquots taken and analyzed via a photometric method described in chapter 2.4. The results of the chronoamperometry are summarized in the following Table 4:

Table 4: Comparison of the moles H_2O_2 produced during 8 h electrolysis at -0.33 V and the according turnover numbers (TONs).

	0.1 M Na$_2$SO$_4$		0.1 M NaOH	
	n_{H2O2} / µmol	TON	n_{H2O2} / µmol	TON
AQ-MINT	1.9	116	7.0	417
AQ@SWCNT	1.4	75	4.4	236
SWCNT	0.5	-	2.2	-

For better visibility, the moles of H_2O_2 produced during 8 h electrolysis collected in Table 4 are also illustrated in the following bar chart:

Figure 83: Moles of H_2O_2 produced during 8 h electrolysis at -0.33 V in 0.1 M Na_2SO_4 and 0.1 M NaOH solution.
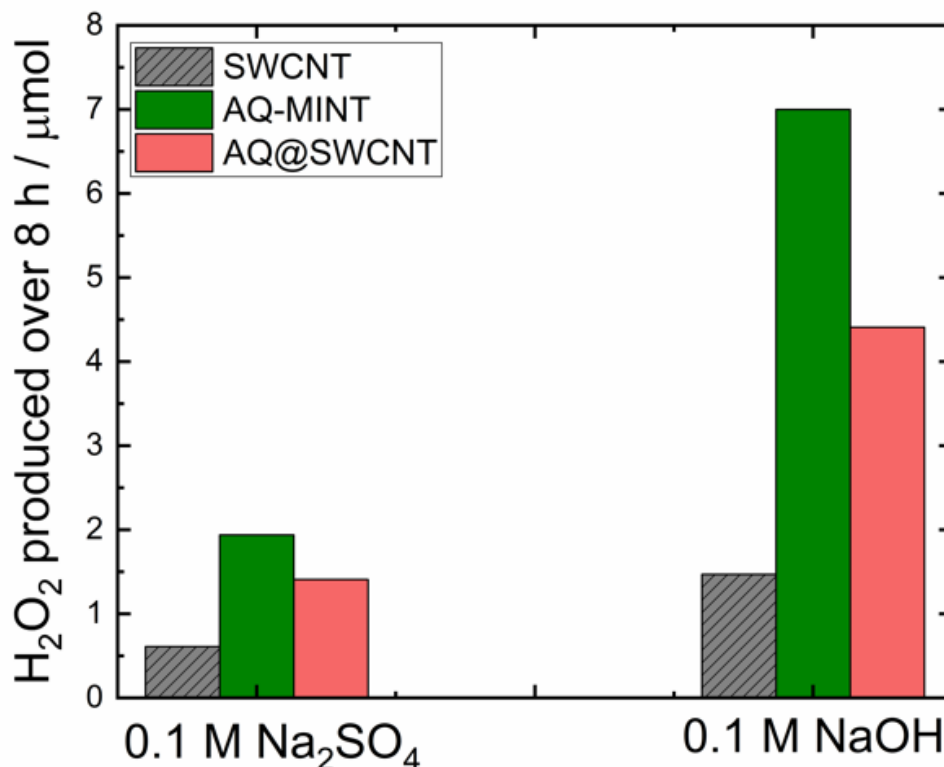
The overall results in Table 4 and Figure 83 reveal that under alkaline conditions higher yields of H_2O_2 upon electrochemical oxygen reduction are observed, which is in good agreement to literature.[7,118,269] In neutral conditions, AQ-MINT produced nearly four times the amount of H_2O_2 compare to SWCNTs and 35% more compared to the supramolecular species. This electrocatalytic effect was even more pronounced in the NaOH solution, where 7.0 and 4.4 µmols of H_2O_2 were produced over 8 h using AQ-MINT and AQ@SWCNT as catalyst. This corresponds to an increased production by a factor of 3 or 2 compared to SWCNTs. Considering the number of AQ macrocycles on the electrode, turnover numbers (TONs) were calculated. AQ-MINT in 0.1 NaOH reached a TON of 417 which further substantiates the electrocatalytic properties of this MINT approach. Upon consideration of the mass loading of AQ-MINT on the electrode, an average H_2O_2 production rate of 8.8 µmol mg^{-1} h^{-1} was achieved. Comparing this figure of merit with state-of-the-art H_2O_2 production rates from its elements on Pd nanoparticles[7] with a rate of 1100 µmol mg^{-1} h^{-1}, or the pigment epindolidione[202] upon photoelectrocatalysis having a rate of 120 µmol mg^{-1} h^{-1}, the value of AQ-MINT appears to be very low. Keeping in mind that the nano-hybrid AQ-MINT consists only of a small fraction of AQ units, this comparison considering the whole mass loading underestimates the electrocatalytic efficiency of the AQ moieties.

In addition to the sole consideration of the moles H_2O_2 produced, also the transient curves (current-time graphs) of the electrolysis of AQ-MINT and AQ@SWCNT in 0.1 M NaOH solution are compared in Figure 84:
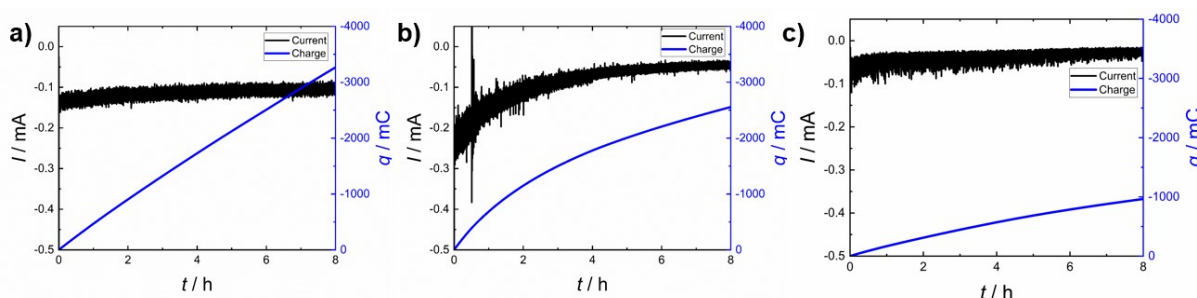
Figure 84: Chronoamperograms and accumulated charges recorded at -0.33 V in 0.1 M NaOH of a) AQ-MINT, b) AQ@SWCNT and c) SWCNT.

According to these electrolysis data, AQ-MINT results in a very stable current over time scale of 8 h, whereas in case of the supramolecular species a higher current in the beginning ceases within 2 h and resulting a finally lower accumulated charge. This result is in good agreement to the CV cycle stability tests in Figure 80, where also AQ-MINT shows only a slight loss in j_p over time. To prove this assumption of reductive delamination during electrolysis, CV graphs were recorded before and after electrolysis and compared in Figure 85:
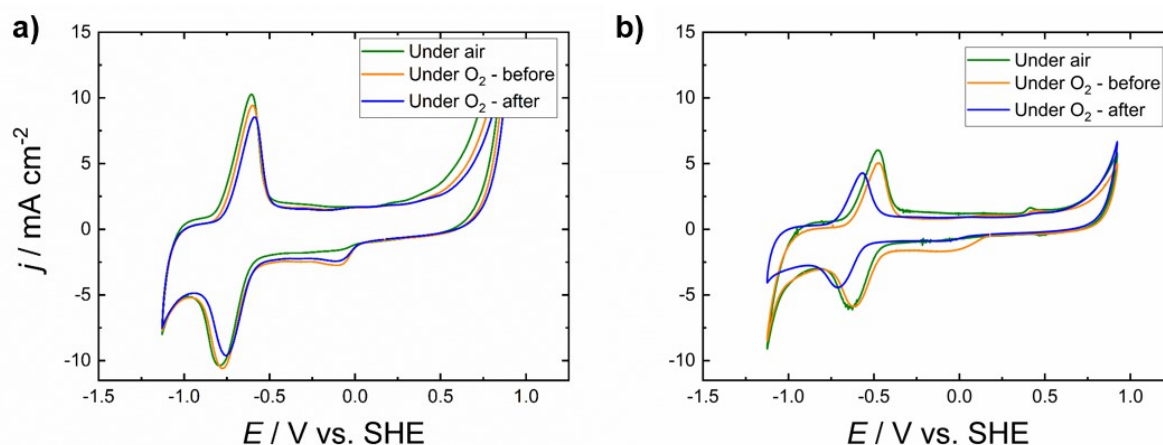
Figure 85: CV graphs recorded in 0.1 M NaOH solution before and after 8 h electrolysis of a) AQ-MINT and b) AQ@SWCNT. Part a) was reproduced with permission from Wielend *et al.* (https://pubs.acs.org/doi/abs/10.1021/acsami.0c06516)[259]. © 2020 American Chemical Society.

The comparison of the CV curves recorded before and after the electrolysis of AQ-MINT in Figure 85a clearly confirm the aforementioned theory that AQ-MINT is highly stable under reductive conditions as nearly no change in j_p is observed. In contrast, the j_p of the supramolecular species decreases significantly during the electrolysis, and furthermore, even a shift in the AQ redox potential is observed.

In addition to the electrocatalytic studies at constant potential, also hydrodynamic voltammetry using a rotating disc electrode (RDE) was performed. Using the same loading of nano-composites per electrode area as before, linear sweep voltammograms (LSV) were recorded in O_2 saturated 0.1 M NaOH solution as shown in Figure 86:

Figure 86: a) RDE-LSV curves of AQ-MINT, AQ@SWCNT and SWCNT in 0.1 M NaOH at a rotation speed of 1200 rpm and b) I_K values calculated from the intercept of the Koutecky-Levich analysis. Reproduced with permission from Wielend *et al.* (https://pubs.acs.org/doi/abs/10.1021/acsami.0c06516)[259]. © 2020 American Chemical Society.

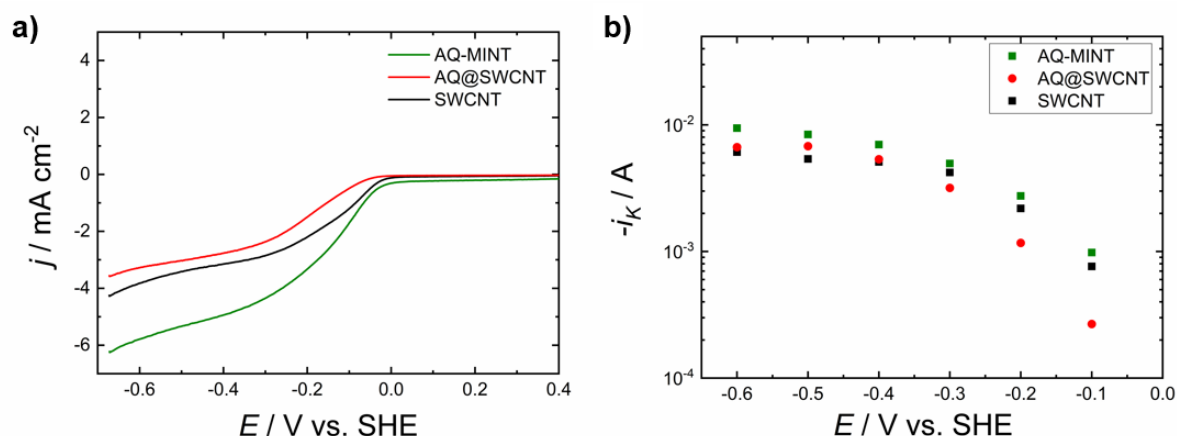At a first glance at the LSV curves in Figure 86, AQ-MINT shows the highest current density of all three materials. The detailed analysis of the curves turns out to be very tricky, as the actual electroactive surface area seems to be different for every system. As the currents were related to the geometric surface area, the actual electroactive surface area was underestimated, which is a well-known problem upon surface modification.[86,88] One reason for these differences between the nano-hybrids used herein might be the re-organization through hybridization, which was also reported by Lee *at al.* for a similar system.[267]

Due to these aforementioned limitations, only the I_K value can be extracted as the intercept following Koutecky-Levich analysis (see Eq. 11). Comparing these I_K values – in view of the geometric electrode surface area – reveals that, upon the whole potential range considered between -0.1 V to -0.6 V AQ-MINT exhibits the highest value. This can be regarded as a hint for higher electrocatalytic activity according to Eq. 12. It is presumed, that different CNT hybrid-composites arrange in a different way on a GC surface upon drop-casting, which is reflected by a different electroactive surface area. Therefore, SEM images of drop-casted films were recorded as illustrated in the following Figure 87:
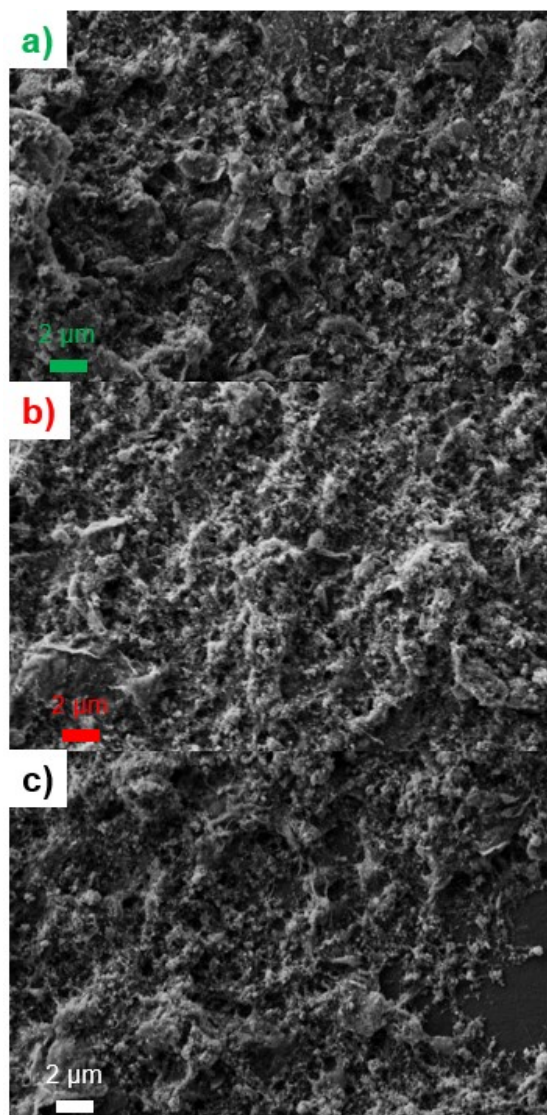
Figure 87: SEM images of a) AQ-MINT, b) AQ@SWCNT and c) SWCNT on GC.

Comparing these SEM images, no clear morphological difference at this magnification was revealed. In order to verify this assumption of organization on a nano-scale, more advanced SEM facilities with higher resolution than currently present would be necessary.

Summing up, the results presented herein clearly demonstrate the benefits of this non-covalent immobilization technique using rotaxane-type mechanically interlocked carbon nanotubes. This approach combines the benefits of unperturbed electrical and electrochemical properties with the extraordinary long-term cycle stability upon electrochemical treatment. As also pointed out in literature[102–104], besides the catalyst itself, also the molecular structure of the linker part as well as the anchor part are crucial for successful immobilization. Besides the usage of such MINTs as immobilization platform for organic molecules, the benefits of using AQ-MINT as electrocatalyst over simple adsorbed molecules were highlighted. The remaining problem of a possible reorganization on a nanoscopic scale limited further electrochemical investigation using hydrodynamic methods and should therefore be a target for future studies.

The results presented within this chapter are already published by Wielend *et al.* (2020) in *ACS Applied Materials & Interfaces*.[259]

3.5. Conductive polymers as heterogeneous electrocatalysts for oxygen reduction

The results from chapter 3.1. demonstrate the importance of thorough investigation of the electrode material used during electrocatalytic oxygen reduction studies. The studies presented in chapter 3.2. revealed an intrinsic electrocatalytic behavior of homogeneously dissolved AQS for the oxygen reduction reaction, which cannot only be sustained in heterogenized form via covalent linking as reported in literature[126,130,138] but also in a non-covalently immobilized approach using AQ-MINTs as described in the previous chapter 3.4. Although numerous reports on poly(anthraquinones) for battery research[227,229,230,270] exist, the results obtained in chapter 3.3. emphasized some problems for the usage of such poly(anthraquinones) for the electrocatalytic oxygen reduction reaction. The three major issues presented therein were an insufficient interaction of the hydrophobic polymer thin-film with the electrolyte solution, stability issues upon electrochemical treatment and the low conductivity.

One approach for overcoming all these three problems is the use of conductive polymers, as outlined in chapter 1.3.5. Already starting from the late 1980s, reports on the interaction of electrochemically reduced polymers with oxygen arose studying polymers, (showed in Figure 23, like polyaniline (PANI),[172,173] polypyrrole (PPy), polythiophene (PT) and PEDOT.[175]) Although these reports investigated the "same" polymer, regularly different trends regarding the oxygen reduction reaction, or sometimes even contradictive conclusions were reported.

In order to carefully look into the topic of using conductive polymers for the electrocatalytic oxygen to H_2O_2 reduction reaction, PANI and PPy were selected and extensively investigated. The approach presented herein is based on the electropolymerized polymer electrodes, which limits experimental errors and wrong conclusions from metal impurities which might be incorporated during chemical synthesis.[271]

The optimization of the electropolymerization procedure, as well as the chronoamperometric studies, were performed by Nikolas Heitzmann and Hannah Rabl, and can be found in detail in their respective theses.[163,164] The overall results of this study are already published in *ACS Applied Energy Materials* by Rabl *et al.* (2020).[209]

To obtain the optimized PANI result, a 0.1 M aniline solution in 0.5 M H_2SO_4 was used. The polymerization was performed potentiodynamically between +800 mV and -200 mV vs. saturated calomel electrode (SCE) for 25 cycles at a scan rate of 25 mV s^{-1}. The optimized electropolymerization procedure for PPy was found out to be performed in 0.45 M pyrrole in 0.1 M phosphate buffered saline (PBS) solution. 20 CV cycles at a scan rate of 50 mV s^{-1} were performed between +1000 mV and -400 mV. Polymerizations for both polymers were carried out on GC electrodes as well as on carbon paper (CP) electrodes with increased surface area. The results from SEM measurements of the electrodes are depicted in the following Figure 88:
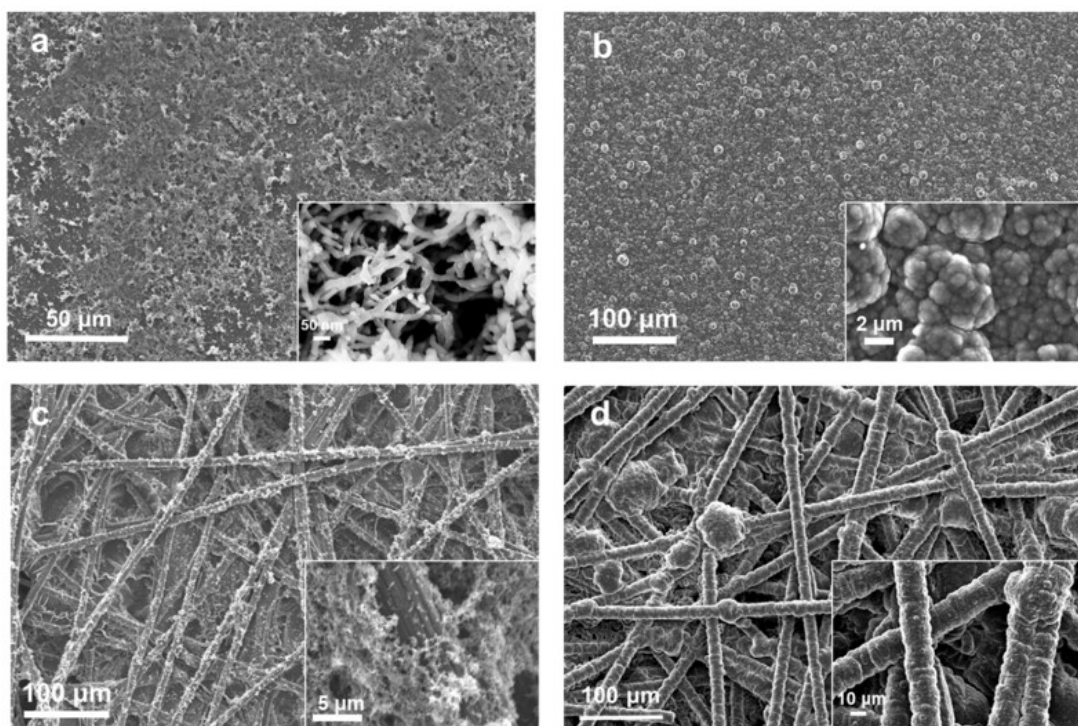
Figure 88: SEM images of polymers on electrodes. a) PANI on GC, b) PPy on GC, c) PANI on CP and d) PPy on CP. Reproduced with permission from Rabl *et al.* (https://pubs.acs.org/doi/abs/10.1021/acsaem.0c01663).[209] © 2020 American Chemical Society.

As can be seen from Figure 88, the microscopic morphology of PANI and PPy is significantly different. Whereas PANI only covers parts of the carbon electrode surface in a sponge-like structure, PPy is covering the whole electrode surface area. In contrast to PANI, the PPy structure is globule-like and the results obtained are in good agreement to a recent study on scanning tunneling microscopy on PPy films.[272] In addition, the largely increased electrode surface area of the CP fibers in contrast to the flat and smooth GC surface is visible.

In the next step, the polymer coated GC electrodes were investigated for the ORR in neutral, aqueous solution of 0.1 M PB as illustrated in Figure 89:

Figure 89: a) CV of GC/PANI and GC/PPy in 0.1 M PB under N_2 and O_2 saturated conditions and b) results of electrolysis of blank GC, GC/PANI and GC/PPy in 0.1 M PB recorded at -0.4 V showing the moles H_2O_2 produced and the according faradaic efficiencies. Data was recorded by Hannah Rabl. Reproduced with permission from Rabl *et al.* (https://pubs.acs.org/doi/abs/10.1021/acsaem.0c01663).[209] © American Chemical Society.

According to Figure 89, GC/PANI does not show a large faradaic current response, which can be explained by the fact that at a pH above PANI's pK_A value of 2.5, it is present in its deprotonated and non-conductive form.[273,274] Upon O_2 addition, GC/PANI shows a small reduction peak at around -0.25 V which is most likely just the GC response (according to Figure 37 & Figure 82). In contrast to PANI, GC/PPy under N_2 shows a reversible peak at around -0.5 V with nearly 2.5 mA cm^{-2} from the polymer redox behavior. Upon O_2 addition, this peak current density was increased by nearly 1 mA cm^{-2} and furthermore also the onset was positively shifted.

Comparing the results from chronoamperometry of GC/PANI with blank GC, the PANI coating causes a slightly lower production of roughly 52 µmoles H_2O_2. In contrast, PANI increases the *FE* by roughly 20% and the *FE* drops less compared to blank GC after 6 h. In accordance to the CV curves, GC/PPy increases both, the moles H_2O_2 produced as well as the *FE*, which was on average above 80% over 6 h.

The results of polymer coated CP electrodes from CV studies and chronoamperometry in 0.1 M PB are depicted in Figure 90:
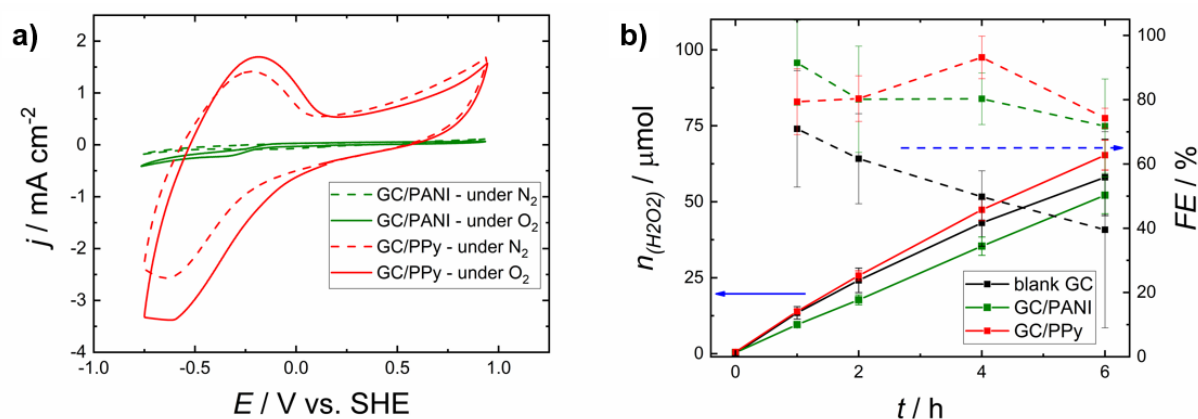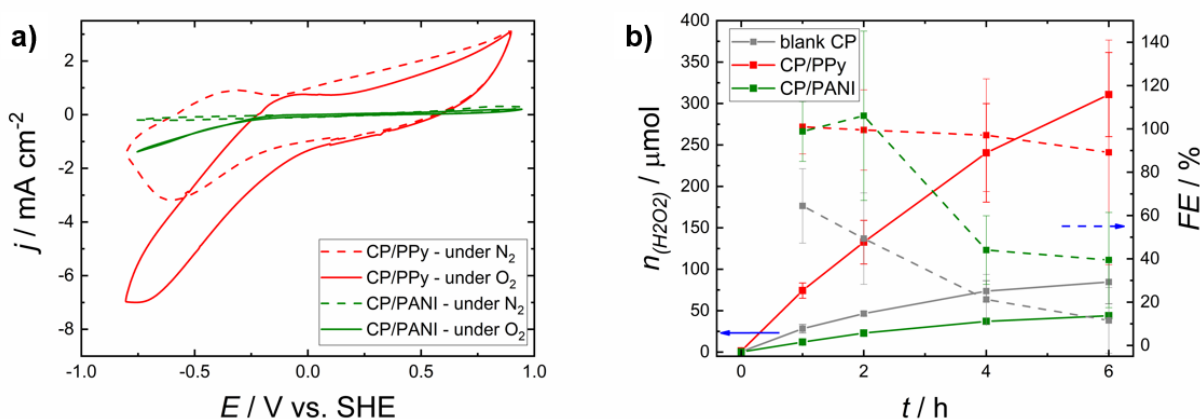

Figure 90: a) CV of CP/PANI and CP/PPy in 0.1 M PB under N_2 and O_2 saturated conditions and b) results of electrolysis of blank CP, CP/PANI and CP/PPy in 0.1 M PB recorded at -0.4 V showing the moles H_2O_2 produced and the according faradaic efficiencies. Data was recorded by Hannah Rabl. Reproduced with permission from Rabl *et al.* (https://pubs.acs.org/doi/abs/10.1021/acsaem.0c01663).[209] © 2020 American Chemical Society.

The CV curves of CP/PANI in Figure 90 look similar to the ones recorded on GC/PANI electrodes in Figure 89. Apart from the small peak of ORR in case of GC, CP/PANI shows only a linear electrocatalytic current increase at a similar onset potential. CP/PPy shows a comparable CV shape and reductive peak current density under N_2. CP/PPy under O_2 conditions though has a more anodic onset potential and a peak current density of around 7 mA cm^{-2} in comparison to 3 mA cm^{-2} of GC/PPy. This strong hint for an electrocatalytic effect is even more pronounced in the chronoamperometric results in Figure 90b where CP/PPy produced more than 310 µmoles of H_2O_2 over 6 h. These results reflect a significant increase in H_2O_2 production in comparison to the 65 µmoles of GC/PPy and around 84 µmoles of blank CP. In addition to this, the *FE* for H_2O_2 was close to unity throughout the 6 h of electrolysis, to be precise at an average value of 96%, which is superior compared to all other conditions reported herein.

As mentioned above, PANI only shows an electroactive redox behavior below its pK_A value of around 2.5, which is the reason why chronoamperometry of both polymers on GC and CP was also recorded at pH=2 as shown in Figure 91:
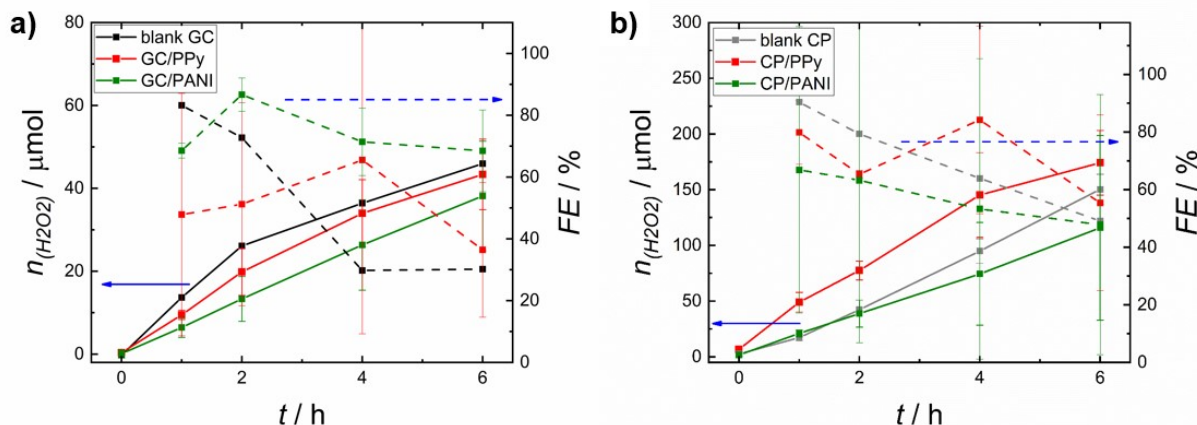
Figure 91: Results of electrolysis in 0.1 M NaHSO₄ at pH=2 recorded at -0.4 V of a) blank GC, GC/PPy and GC/PANI and b) blank CP, CP/PPy and CP/PANI. Data was recorded by Hannah Rabl.

In contrast to the results in neutral PB in Figure 89, GC in acidic media always shows a higher H_2O_2 production compared to the polymer modified GC electrodes, as depicted in Figure 91a. In this acidic solution in addition, GC/PPy does not show a significant increase in *FE*, whereas GC/PANI does significantly increase the *FE*. This behavior is attributed to the aforementioned redox-activity at pH values below the pK_A of PANI. Blank CP produces nearly twice the amount of H_2O_2 in acidic medium compared to neutral PB and the CP/PANI produces less H_2O_2 at a lower *FE* in pH=2. CP/PPy again produces slightly more H_2O_2 compared to blank CP in pH=2, although the difference is smaller compared to neutral PB. In addition, also the *FE* is significantly lower compared to neutral pH and on average comparable to blank CP.

These results reveal that, although GC/PANI is a moderate electrocatalyst for H_2O_2 production in acidic medium, in overall the electrocatalytic activities of PANI and PPy are more pronounced in neutral PB.

In order to gain a deeper understanding in the electrocatalytic trends depicted in Figure 89 on GC electrodes, hydrodynamic linear sweep voltammograms (LSV) on GC rotating disc electrodes (RDE) was performed. The following Figure 92 shows the LSV curves of GC/PANI under O_2 as well as with 5 mM H_2O_2 added in 0.1 M PB and the according number of transferred electrons:
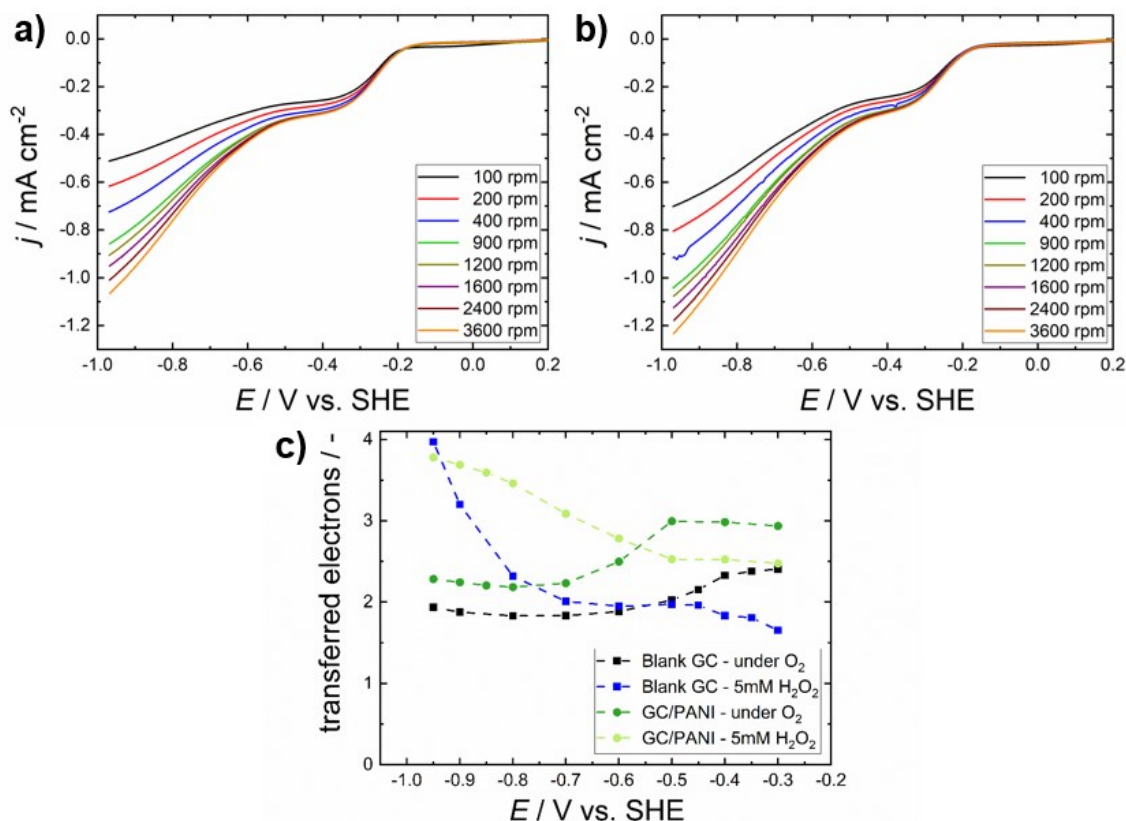
Figure 92 : a) LSV curves of GC/PANI in 0.1 M PB under O_2 and b) LSV curves of GC/PANI in 0.1 M PB under O_2 and with 5 mM H_2O_2 added and c) number of electrons transferred as calculated via Koutecky-Levich analysis. Reproduced with permission from Rabl *et al.* (https://pubs.acs.org/doi/abs/10.1021/acsaem.0c01663).[209] © 2020 American Chemical Society.

As can be seen from the measurements with and without additional H_2O_2 added in Figure 92, GC/PANI in both cases shows a reduction step at -0.4 V and a linear increase in reductive current at more negative potentials. Comparing these two conditions, the first reduction plateau is not influenced by the additional H_2O_2, whereas at more negative potentials a higher current is observed. These qualitative observations are proven by the number of transferred electrons *n* in Figure 92c, where GC and GC/PANI under O_2 both are close to a value of 2, which would correspond to H_2O_2 as only product. Upon H_2O_2 addition, with and without PANI, the value increases up to nearly 4 at -0.9 V which means that the system is also capable of reducing H_2O_2 further to water. A qualitative analysis is again hard to perform, as due to the PANI coating the electroactive surface area changes. Exactly this change in area is introducing significant errors in Koutecky-Levich analysis, as also already discussed in chapter 3.4.

The same investigations were also performed in 0.1 M $NaHSO_4$ solution at pH=2, as depicted in the following Figure 93:
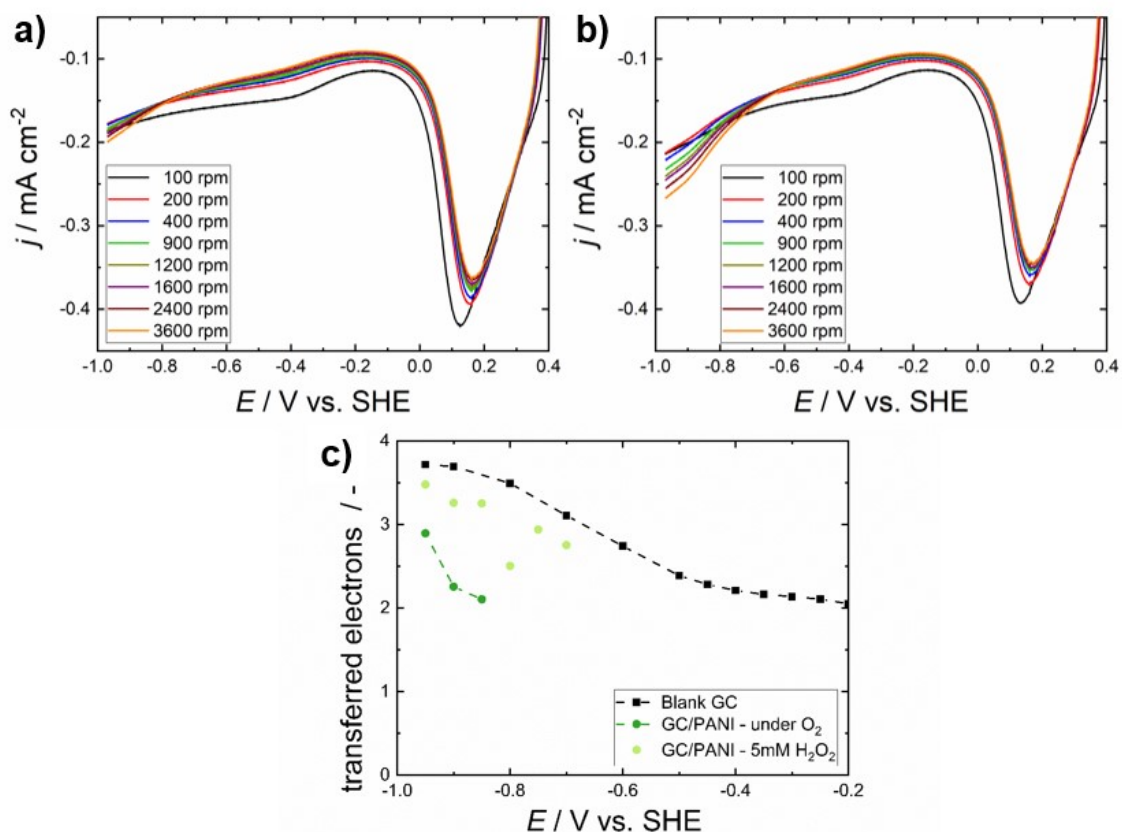
Figure 93: a) LSV curves of GC/PANI in 0.1 M $NaHSO_4$ under O_2 and b) LSV curves of GC/PANI in 0.1 M $NaHSO_4$ under O_2 and with 5 mM H_2O_2 added and c) number of electrons transferred as calculated via Koutecky-Levich analysis. Reproduced with permission from Rabl *et al.* (https://pubs.acs.org/doi/abs/10.1021/acsaem.0c01663).[209] © 2020 American Chemical Society.

Figure 93 shows that in those acidic conditions, a PANI reduction peak at +0.2 V is observed whereas in the more reductive regime nearly no current from ORR is observed under O_2. Upon H_2O_2 addition, starting at -0.7 V an increasing current upon faster rotation is observed. This behavior is reflected in detail by the number of transferred electrons. In acidic solution, blank GC shows increasing n-values below -0.5 V, whereas GC/PANI still exhibits lower values between 2 and 3 at -0.9 V. Even in 5 mM H_2O_2 solution, GC/PANI shows lower *n*-values compared to blank GC which can be regarded as a proof, that PANI acts as a hydrogen peroxide directing layer. This means, that PANI is not an electrocatalyst in the classical way by enhancing the current or lowering the overpotential. Although the PANI coating lowers the current and even the moles H_2O_2 produced, it hinders the further reduction of H_2O_2 to water. In accordance with Figure 89 & Figure 91, this effect is more pronounced in acidic medium at pH=2, where PANI is in its protonated and conductive form.

The same RDE-LSV experiments were also performed using GC/PPy electrodes in acidic and neutral solutions as depicted in the following Figure 94:

Figure 94: LSV curves of GC/PPy in 0.1 M PB under O_2, without (a) and with 5 mM H_2O_2 added (b) and LSV curves of GC/PPy in 0.1 M $NaHSO_4$ under O_2, without (c) and 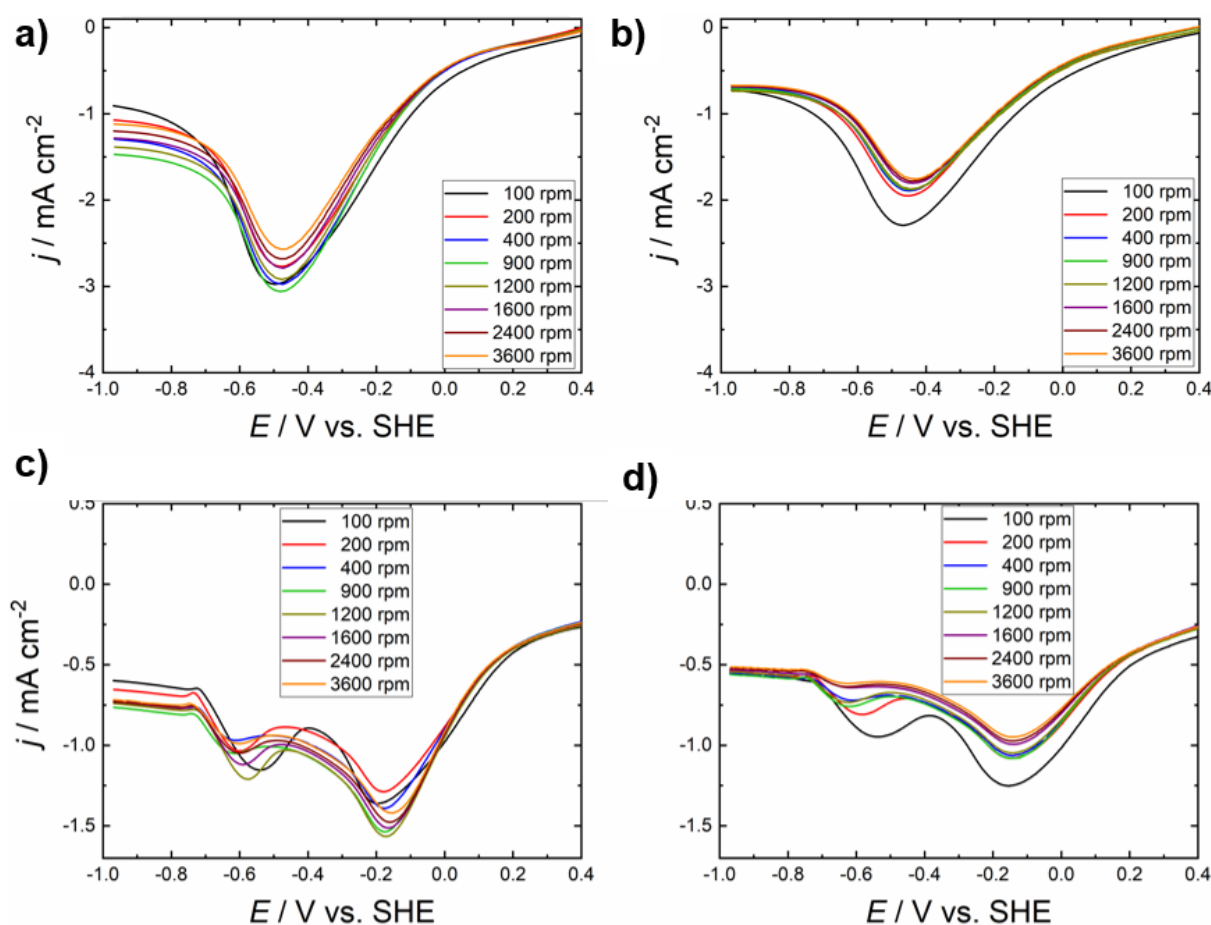with 5 mM H_2O_2 added (d). Reproduced with permission from Rabl *et al.* (https://pubs.acs.org/doi/abs/10.1021/acsaem.0c01663).[209] © 2020 American Chemical Society.

GC/PPy in Figure 94 shows an opposite trend compared to GC/PANI by exhibiting a larger current in neutral solution (upper images) compared to the acidic medium (lower images). A surprising fact from these results is that in both media, upon H_2O_2 addition, the reductive currents become less. Due to this fact, the Koutecky-Levich analysis was not feasible or possible, because this decrease in current by itself is the proof that PPy completely hinders the further reduction of H_2O_2 to water. This is in perfect agreement with the results from electrolysis observed in Figure 89 to Figure 91, whereas PPy modified electrodes always showed a superior H_2O_2 production rate and efficiency. Following the RDE-LSV curves, this effect is more pronounced in neutral solution, which is again in good agreement with the results from electrolysis, where in neutral solution PPy produced H_2O_2 over 6h at an average faradaic efficiency of 96%.

Summing up, the results presented herein highlight two very important aspects. The first aspect is that – although PANI and PPy are apparently molecular relatives – they appear to possess a completely different electrocatalytic behavior towards electrochemical oxygen to H_2O_2 reduction. Irrespective of the electrode material and the pH values used, a PANI coating on the one hand lowers the production of moles H_2O_2 but on the other hand increases the faradaic efficiency for the H_2O_2 production. Especially in neutral pH, the PPy film increases both, the

amounts of H_2O_2 produced and also significantly the faradaic efficiency for H_2O_2. These results from CV and chronoamperometry were further proven by RDE measurements and revealed, that PANI is acting as peroxide directing layer. PPy is a real electrocatalyst for the electrochemical H_2O_2 production and fully preventing any further reduction reaction to water.

The second aspect revealed throughout this work is, that especially when studying the electrochemical oxygen to H_2O_2 reduction with such conductive polymers on carbon based electrode materials, great care has to be taken regarding blank experiments. To determine the real electrocatalytic activity of the polymer, an electrochemical polymerization is recommended to prevent metal impurities within the system.[271] Furthermore, special attention should be drawn to the choice and thorough characterization of the respective electrode material chosen as valid blank experiments. As known from literature and chapter 3.1. herein, nearly all materials show an ORR activity, which might interfere with the polymer to be examined – or a synergistic directing layer phenomenon might be present.

Apparently some literature reports partially lack one of these aspects, which might be the reason why several publications regarding this topic of one polymer present different, or sometimes even contradictive results.

Some results presented and labelled within this chapter were recorded by Hannah Rabl and these results were published in her bachelor thesis[164] under the supervision of Dominik Wielend. All results presented within this chapter are already published by Rabl *et al.* (2020) in *ACS Applied Energy Materials*.[209]

4. Summary and Outlook

4.1. Summary

The target of this thesis is the understanding and further development of renowned and new heterogeneous electrocatalysts for the oxygen (O_2) to hydrogen peroxide (H_2O_2) reduction. Due to the fact that the *state-of-the-art* anthraquinone autooxidation processes (AO) requires elevated temperatures, high pressures, large organic solvent quantities followed by an energy intensive separation and purification procedure, the research for benign alternatives has gained increased attention throughout the last decades. Along the alternative approaches, the electrochemical production of H_2O_2 is one of the most promising candidates, also within the scientific framework of renewable energy storage and *solar-to-fuel* conversion. This heterogeneous electrocatalytic way, also referred to as *immobilized* approach, has great benefits over homogeneous catalysis with respect to industrial scalability and product and catalyst separation. One key parameter to be kept in mind for the chemical, as well as for the electrochemical H_2O_2 production processes, is the selectivity for the target product because also undesired side-products might be generated.

In a first step, exactly this selectivity issue was addressed and investigated for several metal and carbon-based electrode materials with cyclic voltammetry (CV), rotating disc electrode (RDE) and rotating ring-disc electrode (RRDE) techniques. These results and trends described in chapter 3.1. are in good agreement to literature reports and clearly demonstrated, that in all electrochemical ORR experiments the background activity of the electrode materials has to be considered.

Before moving on to heterogenized, organic electrocatalysts, a knowledge of the homogeneously dissolved molecules is required. Due to this reason, a renowned water-soluble anthraquinone derivate was investigated in homogenous solution throughout chapter 3.2. using RRDE and spectroelectrochemical techniques. Although such anthraquinones were already investigated for their ORR capability throughout the last decades, advanced RRDE techniques and the development of a new subtraction method were necessary to elucidate the electrocatalytic behavior when using common glassy carbon (GC) electrodes. The UV-Vis spectroelectrochemistry results substantiated mechanistic literature reports that no long-lasting $AQ-O_2$ intermediate species is formed but rather that the fully reduced AQ^{2-} bands disappear upon oxygen-saturated conditions.

Based on literature reports of poly(anthraquinone) based batteries, the three poly(anthraquinones) PDDA-SAQ, P14AQ and PVAQ were selected, synthesized and thoroughly characterized, as described in chapter 3.3. The investigation of those polymers revealed an ambiguous result. On the one hand, heterogenization via acid-base reaction of a small anthraquinone molecule to an innocent polymer matrix revealed a strong benefit compared to homogenous solutions with respect to electrochemical oxygen reduction during CV measurement. On the other hand, the two investigated covalent polymers with anthraquinone units appear to suppress the ORR activity of the GC electrode. An important message learned from this study is that this lack of electrocatalytic activity is most likely related to the complex and still not fully understood redox processes of such polymer thin-films in aqueous solutions. The main lesson learned is that the ability of such a redox-polymer to

undergo reversible electrochemical reduction and re-oxidation is related to its hydrophilicity and carbonyl IR frequency band $v_{C=O}$.

The approach investigated throughout chapter 3.4. aims at fixing the problem observed in chapter 3.3. Upon covalent immobilization of molecular (electro-) catalysts, frequently the catalytic activity of the molecule is decreased by an affixed orientation or the substrate electrode material is negatively affected. Non-covalent adsorption approaches do not suffer from such effects but lack long-term stability. Mechanically interlocked organic molecules on carbon nanotubes (MINT), described and synthesized by our collaborators, the group of Emilio Pérez, combine the benefits of both approaches. CV measurements clearly proved the superior CV cycle stability and furthermore a largely increased peak of oxygen reduction compared to the background electrode materials. In addition, AQ-MINT showed a superior electrocatalytic product rate of H_2O_2 which was also substantiated via RDE measurements, by means of an elevated kinetic current I_K.

The last chapter 3.5. focused on investigation of the conductive polymers polyaniline (PANI) and polypyrrole (PPy) as electrocatalysts for H_2O_2 production. Due to the fact that previous literature reports on this topic were inconsistent with one another, one source of error – metal impurities – was avoided by an electrochemical polymerization approach. Electrolysis results showed that PPy clearly enhanced the yield and faradaic efficiency (*FE*) whereas PANI lowered the yield but slightly increased the *FE* in comparison to the bare electrode material. RDE measurements revealed that PANI acted as a peroxide-directing-layer by suppressing the unwanted further reduction of H_2O_2 to water whereas PPy was identified as an electrocatalyst from a classical textbook point of view with a maximum *FE* of 96%.

4.2. Outlook

Throughout this work, numerous issues arose, some could be successfully addressed and many important as well as interesting lessons were learned. Concerning the electrochemical instrumentation and investigation, the following conclusions were drawn which are a recommendation for all future studies within this scientific area:

- Nearly all known metal and carbon-based electrode materials somehow show an electrocatalytic effect towards the oxygen reduction reaction. Due to this reason, during all electrochemical investigations this background catalytic activity should be considered and determined.
- The RRDE method is a powerful tool applicable for the investigation of electrocatalytic oxygen to H_2O_2 reduction, especially for bare electrodes and homogenous solutions. Nevertheless, great care and thorough experimental design are required when drop-casted or electropolymerized films are investigated, since this modification changes the electroactive surface area, and therefore the whole data analysis.
- On the way towards efficient heterogenized electrocatalysts for oxygen reduction, the scientific community should consider more parameters than the molecular unit and the specific energy density. As the polymer film-electrolyte interface is quite complex, the findings presented herein strongly suggest to include at least hydrophilicity and FTIR measurements within the routine methods for polymer material development.
- Purely covalent or purely non-covalent immobilization techniques were demonstrated to have severe drawbacks throughout the last decades. Based on the findings presented herein, investigations of new approaches like for example using MINTs is strongly recommended as this approach showed improved loading, stability and electrocatalytic activity

Although some of the aforementioned aspects were already well established within the scientific fields of hydrogen evolution reaction (HER) and the CO_2 reduction reactions (CO_2RR), quite some delay was observed in the field of electrocatalytic oxygen to H_2O_2 reduction. Only very recent publications were fully considering and investigating the background electrocatalytic activity of the electrode material used.
In my opinion, boron-doped diamond (BDD) with its large overpotential for ORR seems to be a promising candidate as *state-of-the-art* electrode material that should be used for ORR electrocatalyst screening. The increasing number of publications makes me confident that this special and expensive electrode material will be commonly available and used in this research within the near future.

One unique aspect of literature on electrocatalysts for ORR in contrast to HER and CO_2RR is the large number of purely organic molecules. Actually, in addition to less renowned mechanistic details also a smaller number of immobilization reports in contrast to the field of metal complex catalysis exist. In addition to very recent publications on poly(anthraquinone) development also the findings presented herein strongly suggest to include further standard characterization techniques in this research area. Apparently the solvent-polymer interaction, influenced by hydrophilicity, might be one key-issue for the redox behavior and electrocatalytic performance of immobilized systems like for example redox polymers. In my opinion, investigation of FTIR bands of the carbonyl groups and contact angle measurements of already

existing polymer materials might boost the research on fully organic materials for energy storage applications.

Regarding the *big-picture* of applying the electrochemically produced H_2O_2 as (solar) energy storage technology, one aspect has to be mentioned. Especially the energy storage applications explained in chapter 1.2. require quite high concentrations of H_2O_2, which can only be achieved via post-production concentration techniques. In this respect, the electrochemical production has to face the same problems as the AQ process. One common feature of nearly all reports on electrocatalytic H_2O_2 production is that only short-term electrolysis data are reported reaching concentrations of H_2O_2 of up to a few millimole per liter. Besides stability of the electrocatalysts used also the selectivity for H_2O_2, as well as the required potential are influenced by nature as described within the Nernst equation.

In general, heterogenized approaches facilitate the aforementioned issue of post-production H_2O_2 concentration and could furthermore be optimized by continuous-flow technologies. Organic electrocatalysts and carbon-based electrodes in general have a high selectivity for H_2O_2 and a rather low tendency for the further reduction to water. Keeping all those facts in mind, I am quite confident that carbon-based electrode materials will be highly relevant in the future development of electrocatalytic H_2O_2 production.

To know if H_2O_2 in general will be a major player in energy storage technologies is hard to predict, and definitely strongly depends on the future electrocatalyst development performance. Furthermore, the development of concurring technologies like normal batteries, redox-flow batteries or methanol fuel cells as well as the global trends with respect to fossil fuels like coal, oil and gas also have to be considered.

Nevertheless, besides this high concentration applications, I would like to draw the attention to the environmental applications described in chapter 1.2. As disinfection and water treatment processes do not require propellant-grade H_2O_2 concentrations, off-site electrochemical H_2O_2 production might be an important future technology for areas with limited access to the global power and fuel supply.

Summing up, for an industrial application of the electrochemical H_2O_2 production further research is required to obtain high H_2O_2 selectivity and stability through a more in-depth mechanistic insight. Thereby heterogenized and carbon-based materials are the most promising candidates. Regarding the application of the produced H_2O_2 one should consider more application fields besides energy-storage only and chose it according to the specific requirements of the country or production site.

5. Bibliography

[1]   G. Goor, J. Glenneberg, S. Jacobi, *Ullmann's Encycl. Ind. Chem.* **2012**, *18*, 393.
[2]   R. Ciriminna, L. Albanese, F. Meneguzzo, M. Pagliaro, *ChemSusChem* **2016**, *9*, 3374.
[3]   A. Sehrish, R. Manzoor, K. Dong, Y. Jiang, Y. Lu, *Chem. Reports* **2019**, *1*, 81.
[4]   H. Meidinger, *Justus Liebigs Ann. Chem.* **1853**, *88*, 57.
[5]   E. Berl, *Trans. Electrochem. Soc.* **1939**, *76*, 359.
[6]   W. Manchot, *Justus Liebigs Ann. Chem.* **1901**, *314*, 177.
[7]   J. M. Campos-Martin, G. Blanco-Brieva, J. L. G. Fierro, *Angew. Chemie - Int. Ed.* **2006**, *45*, 6962.
[8]   D. Wielend, Electrochemical Capture and Release of CO2 Using Organic Pigments, Johannes Kepler University Linz, **2017**.
[9]   S. Yang, A. Verdaguer-Casadevall, L. Arnarson, L. Silvioli, C. Viktor, R. Frydendal, J. Rossmeisl, I. Chorkendor, I. E. L. Stephens, *ACS Catal.* **2018**, *8*, 4064.
[10]   A. Uhl, M. Bitzer, H. Wolf, D. Hermann, S. Gutewort, M. Völkl, I. Nagl, *Ullmann's Encycl. Ind. Chem.* **2017**, 1.
[11]   M. Ventura, P. Mullens, in *35th Jt. Propuls. Conf. Exhib.*, The American Institute Of Aeronautics And Astronautics, Los Angeles, **1999**, pp. 1–19.
[12]   M. Ventura, G. Garboden, in *35th Jt. Propuls. Conf. Exhib.*, **1999**, pp. 1–17.
[13]   A. J. Musker, in *39th Jt. Propuls. Conf. Exhib.*, The American Institute Of Aeronautics And Astronautics, Huntsville, **2003**, pp. 1–11.
[14]   M. Ragnar, G. Henriksson, M. E. Lindström, M. Wimby, J. Blechschmidt, S. Heinemann, *Ullmann's Encycl. Ind. Chem.* **2014**, 1.
[15]   Y. Zeng, G. Wu, *Chinese J. Catal.* **2021**, *42*, 2149.
[16]   W. Zhou, X. Meng, J. Gao, A. N. Alshawabkeh, *Chemosphere* **2019**, *225*, 588.
[17]   I. Yamanaka, T. Murayama, *Angew. Chemie - Int. Ed.* **2008**, *47*, 1900.
[18]   L. An, T. Zhao, X. Yan, X. Zhou, P. Tan, *Sci. Bull.* **2015**, *60*, 55.
[19]   S. Fukuzumi, Y. Yamada, *ChemElectroChem* **2016**, *3*, 1978.
[20]   K. Mase, M. Yoneda, Y. Yamada, S. Fukuzumi, *Nat. Commun.* **2016**, *7*, 11470.
[21]   S. Yamazaki, Z. Siroma, H. Senoh, T. Ioroi, N. Fujiwara, K. Yasuda, *J. Power Sources* **2008**, *178*, 20.
[22]   R. S. Disselkamp, *Energy and Fuels* **2008**, *22*, 2771.
[23]   R. S. Disselkamp, *Int. J. Hydrogen Energy* **2010**, *35*, 1049.
[24]   S. Fukuzumi, *Biochim. Biophys. Acta - Bioenerg.* **2016**, *1857*, 604.
[25]   M. Fernández-Medina, M. A. Ramos-Docampo, O. Hovorka, V. Salgueiriño, B. Städler, *Adv. Funct. Mater.* **2020**, *30*, 1908283.
[26]   C. Fiedler, C. Ulbricht, T. Truglas, D. Wielend, M. Bednorz, H. Groiss, O. Brüggemann, I. Teasdale, Y. Salinas, *Chem. - A Eur. J.* **2020**, *27*, 3262.
[27]   H. Wang, G. Zhao, M. Pumera, *J. Am. Chem. Soc.* **2014**, *136*, 2719.
[28]   W. Z. Teo, H. Wang, M. Pumera, *Chem. Commun.* **2016**, *52*, 4333.
[29]   M. Kneidinger, A. Iturmendi, C. Ulbricht, T. Truglas, H. Groiss, I. Teasdale, Y. Salinas, *Macromol. Rapid Commun.* **2019**, *40*, 1900328.
[30]   A. A. Solovev, E. J. Smith, C. C. B. Bufon, S. Sanchez, O. G. Schmidt, *Angew. Chemie - Int. Ed.* **2011**, *50*, 10875.
[31]   K. Yuan, Z. Jiang, B. Jurado-Sánchez, A. Escarpa, *Chem. - A Eur. J.* **2020**, *26*, 2309.
[32]   B. Jurado-Sánchez, S. Sattayasamitsathit, W. Gao, L. Santos, Y. Fedorak, V. V Singh, J. Orozco, M. Galarnyk, J. Wang, *Small* **2014**, *11*, 499.
[33]   B. Jurado-Sánchez, J. Wang, *Environ. Sci. Nano* **2018**, *5*, 1530.
[34]   J. Zhang, H. Zhang, M. J. Cheng, Q. Lu, *Small* **2020**, *16*, 1.
[35]   P. Landon, P. J. Collier, A. J. Papworth, C. J. Kiely, G. J. Hutchings, *Chem. Commun.* **2002**, *18*, 2058.
[36]   S. Chinta, J. H. Lunsford, *J. Catal.* **2004**, *225*, 249.
[37]   Y. Yi, L. Wang, G. Li, H. Guo, *Catal. Sci. Technol.* **2016**, *6*, 1593.
[38]   S. C. Perry, L. Vieira, V. Sieber, L. Wang, C. P. De León, F. C. Walsh, *Nat. Rev. Chem.* **2019**, *3*, 442.
[39]   P. Vanýsek, in *CRC Handb. Chem. Phys.* (Ed.: D.R. Lide), CRC Press Taylor And Francis, Boca Raton, FL, **2008**, pp. 8.20-8.29.

[40] T. A. Faunce, W. Lubitz, A. W. B. Rutherford, D. Macfarlane, G. F. Moore, P. Yang, D. G. Nocera, T. A. Moore, D. H. Gregory, S. Fukuzumi, B. Yoon, F. A. Armstrong, R. Wasielewski, S. Styring, *Energy Environ. Sci.* **2013**, *6*, 695.

[41] K. Sayama, *ACS Energy Lett.* **2018**, *3*, 1093.

[42] A. Windsberger, M. Schick, B. Windsberger, *Perspektiven Der Decarbonisierung Für Die Chemische Industrie in Österreich*, St. Pölten, **2018**.

[43] M. Hronek, (TipsZeitung), "Start der Initiative H2Linz: „Linz soll Zentrum für Wasserstoff werden"," can be found under https://www.tips.at/nachrichten/linz/wirtschaft-politik/545348-start-der-initiative-h2linz-linz-soll-zentrum-fuer-wasserstoff-werden, **2021**.

[44] DerStandard, "Wo Sebastian Kurz' Wasserstoffpläne funktionieren könnten," can be found under https://www.derstandard.at/story/2000113395640/wo-sebastian-kurz-wasserstoffplaene-funktionieren-koennten, **2021**.

[45] Www.scopus.com, "Keyword Search results: Oxygen Reduction Reaction," can be found under https://www.scopus.com/term/analyzer.uri?sid=94762271b08613ae6d12a222a0ce3b11&origin=resultslist&src=s&s=KEY%28Oxygen+reduction+reaction%29&sort=plf-f&sdt=b&sot=b&sl=30&count=58273&analyzeResults=Analyze+results&txGid=12b24f360b242fc320e56ba8c52e7cdb, **2021**.

[46] S. Siahrostami, S. J. Villegas, A. H. Bagherzadeh Mostaghimi, S. Back, A. B. Farimani, H. Wang, K. A. Persson, J. Montoya, *ACS Catal.* **2020**, *10*, 7495.

[47] J. Stacy, Y. N. Regmi, B. Leonard, M. Fan, *Renew. Sustain. Energy Rev.* **2017**, *69*, 401.

[48] M. Shao, Q. Chang, J.-P. Dodelet, R. Chenitz, *Chem. Rev.* **2016**, *116*, 3594.

[49] L. Fan, Z. Tu, S. H. Chan, *Energy Reports* **2021**, DOI 10.1016/j.egyr.2021.08.003.

[50] V. Viswanathan, H. A. Hansen, J. Rossmeisl, J. K. Nørskov, *J. Phys. Chem. Lett.* **2012**, *3*, 2948.

[51] J. K. Nørskov, J. Rossmeisl, A. Logadottir, L. Lindqvist, D.- Lyngby, H. Jo, *J. Phys. Chem. B* **2004**, *108*, 17886.

[52] H. A. Hansen, V. Viswanathan, *J. Phys. Chem. C* **2014**, *118*, 6706.

[53] A. Kulkarni, S. Siahrostami, A. Patel, J. K. Nørskov, *Chem. Rev.* **2018**, *118*, 2302.

[54] R. Ma, G. Lin, Y. Zhou, Q. Liu, T. Zhang, G. Shan, M. Yang, J. Wang, *npj Comput. Mater.* **2019**, *5*, 78.

[55] Z. W. Seh, J. Kibsgaard, C. F. Dickens, I. Chorkendorff, J. K. Nørskov, T. F. Jaramillo, *Science* **2017**, *355*, 4998.

[56] M. Traube, *Berichte der Dtsch. Chem. Gesellschaft* **1887**, *884*, 3345.

[57] R. W. Haid, R. M. Kluge, T. O. Schmidt, A. S. Bandarenka, *Electrochim. Acta* **2021**, *382*, 138285.

[58] A. Shen, Y. Zou, Q. Wang, R. A. W. Dryfe, X. Huang, S. Dou, L. Dai, S. Wang, *Angew. Chemie - Int. Ed.* **2014**, *53*, 10804.

[59] X. Zhao, X. Zou, X. Yan, C. L. Brown, Z. Chen, G. Zhu, X. Yao, *Inorg. Chem. Front.* **2016**, *3*, 417.

[60] D. Zhang, C. Tsounis, Z. Ma, D. Djaidiguna, N. M. Bedford, L. Thomsen, X. Lu, D. Chu, R. Amal, Z. Han, *Small* **2021**, 2105082.

[61] J. S. Lim, J. H. Kim, J. Woo, D. S. Baek, K. Ihm, T. J. Shin, Y. J. Sa, S. H. Joo, *Chem* **2021**, *7*, 3114.

[62] V. Čolić, S. Yang, Z. Révay, I. E. L. Stephens, I. Chorkendorff, *Electrochim. Acta* **2018**, *272*, 192.

[63] M. Vikkisk, I. Kruusenberg, U. Joost, E. Shulga, I. Kink, K. Tammeveski, *Appl. Catal. B, Environ.* **2014**, *147*, 369.

[64] H. Yu, L. Shang, T. Bian, R. Shi, G. I. N. Waterhouse, Y. Zhao, C. Zhou, L. Z. Wu, C. H. Tung, T. Zhang, *Adv. Mater.* **2016**, *28*, 5080.

[65] T. Ikeda, Z. Hou, G. Chai, K. Terakura, *J. Phys. Chem. C* **2014**, *118*, 17616.

[66] L. Wang, Z. Sofer, M. Pumera, *ACS Nano* **2020**, *14*, 21.

[67] G. Chai, Z. Hou, T. Ikeda, K. Terakura, *J. Phys. Chem. C* **2017**, *121*, 14524−14533.

[68] Y. Sun, I. Sinev, W. Ju, A. Bergmann, S. Dresp, S. Kühl, C. Spöri, H. Schmies, H. Wang, D. Bernsmeier, B. Paul, R. Schmack, R. Kraehnert, B. R. Cuenya, P. Strasser, *ACS Catal.* **2018**, *8*, 2844.

[69] L. Dai, Y. Xue, L. Qu, H.-J. Choi, J.-B. Baek, *Chem. Rev.* **2015**, *115*, 4823.

[70] Y. Xue, Y. Wang, Z. Pan, K. Sayama, *Angew. Chemie - Int. Ed.* **2021**, *60*, 10469.

[71] T. Kang, B. Li, Q. Hao, W. Gao, F. Bin, K. N. Hui, D. Fu, B. Dou, *ACS Sustain. Chem. Eng.* **2020**, *8*, 15005.

[72] K. Mase, M. Yoneda, Y. Yamada, S. Fukuzumi, *ACS Energy Lett.* **2016**, *1*, 913.

[73] F. Dalton, *Electrochem. Soc. Interface, Fall 2016* **2016**, 50.

[74] A. Peroff, "Hydrodynamic Electrochemistry - Rotating Disk Electrode (RDE) Theory," can be found under https://pineresearch.com/shop/kb/theory/hydrodynamic-electrochemistry/rotating-disk-electrode-theory/, **2020**.

[75] V. G. Levich, *Physicochemical Hydrodynamics*, Prentice-Hall Inc., Englewood Cliffs, N. J., **1962**.

[76] S. Bruckenstein, B. Miller, *Acc. Chem. Res.* **1977**, *10*, 54.

[77] K. B. Prater, A. J. Bard, *J. Electrochem. Soc.* **1970**, *117*, 207.

[78] K. B. Prater, A. J. Bard, *J. Electrochem. Soc.* **1970**, *117*, 335.

[79] K. B. Prater, A. J. Bard, *J. Electrochem. Soc.* **1970**, *117*, 1517.

[80] V. J. Puglisi, A. J. Bard, *J. Electrochem. Soc.* **1972**, *119*, 833.

[81] A. J. Bard, L. R. Faulkner, *Electrochemical Methods*, John Wiley & Sons, Inc., New York, **2001**.

[82] X. Wei, G. Yin, J. Zhang, Eds. , *Rotating Electrode Methods And Oxygen Reduction Electrocatalysts*, Elsevier B.V., Amsterdam, **2014**.

[83] S. Treimer, A. Tang, D. C. Johnson, **2002**, 165.

[84] H. K. Kuiken, E. P. a. M. Bakkers, H. Ligthart, J. J. Kelly, *J. Electrochem. Soc.* **2000**, *147*, 1110.

[85] E. Lobyntseva, T. Kallio, N. Alexeyeva, K. Tammeveski, K. Kontturi, *Electrochim. Acta* **2007**, *52*, 7262.

[86] J. Masa, C. Batchelor-McAuley, W. Schuhmann, R. G. Compton, *Nano Res.* **2014**, *7*, 71.

[87] G. Zhang, Q. Wei, X. Yang, A. C. Tavares, S. Sun, *Appl. Catal. B Environ.* **2017**, *206*, 115.

[88] V. Di Noto, E. Negro, A. Nale, G. Pagot, K. Vezzù, P. Atanassov, *Curr. Opin. Electrochem.* **2021**, *25*, 100626.

[89] Y. Garsany, J. Ge, J. St-Pierre, R. Rocheleau, K. E. Swider-Lyons, *ECS Trans.* **2013**, *58*, 1233.

[90] Y. Hori, in *Handb. Fuel Cells - Fundam. Technol. Appl.* (Eds.: W. Vielstich, H.A. Gasteiger, A. Lamm, H. Yokokawa), John Wiley & Sons, Ltd, New York, **2010**, pp. 1–14.

[91] S. Berardi, S. Drouet, L. Francàs, C. Gimbert-Suriñach, M. Guttentag, C. Richmond, T. Stoll, A. Llobet, *Chem. Soc. Rev.* **2014**, *43*, 7501.

[92] D. Kim, K. K. Sakimoto, D. Hong, P. Yang, *Angew. Chemie - Int. Ed.* **2015**, *54*, 3259.

[93] B. Wang, *J. Power Sources* **2005**, *152*, 1.

[94] S. Dey, B. Mondal, S. Chatterjee, A. Rana, S. Amanullah, A. Dey, *Nat. Rev. Chem.* **2017**, *1*, 0098.

[95] G. Passard, D. K. Dogutan, M. Qiu, C. Costentin, D. G. Nocera, *ACS Catal.* **2018**, *8*, 8671.

[96] B. Šljukic, C. E. Banks, R. G. Compton, *J. Iran. Chem. Soc.* **2005**, *2*, 1.

[97] M. L. Pegis, C. F. Wise, D. J. Martin, J. M. Mayer, *Chem. Rev.* **2018**, *118*, 2340.

[98] J. P. Collman, M. Kaplun, R. A. Decréau, *Dalt. Trans.* **2006**, 554.

[99] W. Schöfberger, F. Faschinger, S. Chattopadhyay, S. Bhakta, B. Mondal, J. A. A. W. Elemans, S. Müllegger, S. Tebi, R. Koch, F. Klappenberger, M. Paszkiewicz, J. V. Barth, E. Rauls, H. Aldahhak, W. G. Schmidt, A. Dey, *Angew. Chemie - Int. Ed.* **2016**, *55*, 2350.

[100] C. Costentin, J. M. Savéant, *Nat. Rev. Chem.* **2017**, *1*, 0087.

[101] C. Costentin, J.-M. Savéant, *ChemElectroChem* **2014**, *1*, 1226.

[102] D. R. Whang, *Nano Converg.* **2020**, *7*, 1.

[103] H. D. Abruña, *Coord. Chem. Rev.* **1988**, *86*, 135.

[104] K. E. Dalle, J. Warnan, J. J. Leung, B. Reuillard, I. S. Karmel, E. Reisner, *Chem. Rev.* **2019**, *119*, 2752.

[105] D. H. Apaydin, H. Seelajaroen, O. Pengsakul, P. Thamyongkit, N. S. Sariciftci, J. Kunze-Liebhäuser, E. Portenkirchner, *ChemCatChem* **2018**, *10*, 1793.

[106] W. Keawsongsaeng, H. Seelajareon, S. Namuangruk, C. Chitpakdee, P. Chasing, V. Promarak, N. S. Sariciftci, P. Thamyongkit, *Isr. J. Chem.* **2021**, *61*, DOI 10.1002/ijch.202100077.

[107] C. C. L. McCrory, A. Devadoss, X. Ottenwaelder, R. D. Lowe, T. D. P. Stack, C. E. D. Chidsey, *J. Am. Chem. Soc.* **2011**, *133*, 3696.

[108] W. Zhang, A. U. Shaikh, E. Y. Tsui, T. M. Swager, *Chem. Mater.* **2009**, *21*, 3234.

[109] S. Gentil, D. Serre, C. Philouze, M. Holzinger, F. Thomas, A. Le Goff, *Angew. Chemie - Int. Ed.* **2016**, *55*, 2517.

[110] J. Qu, Y. Shen, X. Qu, S. Dong, *Electroanalysis* **2004**, *16*, 1444.

[111] N. U. Day, C. C. Wamser, *J. Phys. Chem. C* **2017**, *121*, 11076.

[112] T. Abe, M. Kaneko, *Prog. Polym. Sci.* **2003**, *28*, 1441.

[113] W. Ma, P. Yu, T. Ohsaka, L. Mao, *Electrochem. Commun.* **2015**, *52*, 53.

[114] M. Jahan, Q. Bao, K. P. Loh, *J. Am. Chem. Soc.* **2012**, *134*, 6707.

[115] L. Li, J. He, Y. Wang, X. Lv, X. Gu, P. Dai, D. Liu, X. Zhao, *J. Mater. Chem. A* **2019**, *7*, 1964.

[116] C. W. B. Bezerra, L. Zhang, K. Lee, H. Liu, A. L. B. Marques, E. P. Marques, H. Wang, J. Zhang, *Electrochim. Acta* **2008**, *53*, 4937.

[117] M. Ferrandon, A. J. Kropf, D. J. Myers, K. Artyushkova, U. Kramm, P. Bogdanoff, G. Wu, C. M. Johnston, P. Zelenay, *J. Phys. Chem. C* **2012**, *116*, 16001.

[118] H. Zhang, C. Lin, L. Sepunaru, C. Batchelor-McAuley, R. G. Compton, *J. Electroanal. Chem.* **2017**, *799*, 53.

[119] M. S. Hossain, D. Tryk, E. Yeager, *Electrochim. Acta* **1989**, *34*, 1733.

[120] R. Nissim, C. Batchelor-McAuley, Q. Li, R. G. Compton, *J. Electroanal. Chem.* **2012**, *681*, 44.

[121] Q. Li, C. Batchelor-Mcauley, N. S. Lawrence, R. S. Hartshorne, R. G. Compton, *Chem. Commun.* **2011**, *47*, 11426.

[122] Q. Li, C. Batchelor-Mcauley, N. S. Lawrence, R. S. Hartshorne, R. G. Compton, *ChemPhysChem* **2011**, *12*, 1255.

[123] J. Mason, C. Batchelor-Mcauley, R. G. Compton, *Phys. Chem. Chem. Phys.* **2013**, *15*, 8362.

[124] A. Sarapuu, K. Helstein, K. Vaik, D. J. Schiffrin, K. Tammeveski, *Electrochim. Acta* **2010**, *55*, 6376.

[125] K. Tammeveski, K. Kontturi, R. J. Nichols, R. J. Potter, D. J. Schiffrin, *J. Electroanal. Chem.* **2001**, *515*, 101.

[126] K. Vaik, U. Mäeorg, F. C. Maschion, G. Maia, D. J. Schiffrin, K. Tammeveski, *Electrochim. Acta* **2005**, *50*, 5126.

[127] F. Mirkhalaf, K. Tammeveski, D. J. Schiffrin, *Phys. Chem. Chem. Phys.* **2004**, *6*, 1321.

[128] M. Kullapere, G. Jürmann, T. T. Tenno, J. J. Paprotny, F. Mirkhalaf, K. Tammeveski, *J. Electroanal. Chem.* **2007**, *599*, 183.

[129] K. Vaik, A. Sarapuu, K. Tammeveski, F. Mirkhalaf, D. J. Schiffrin, *J. Electroanal. Chem.* **2004**, *564*, 159.

[130] G. Jürmann, D. J. Schiffrin, K. Tammeveski, *Electrochim. Acta* **2007**, *53*, 390.

[131] A. Sarapuu, K. Helstein, D. J. Schififrin, K. Tammeveski, *Electrochem. Solid-State Lett.* **2005**, *8*, 30.

[132] C. Batchelor-McAuley, B. R. Kozub, D. Menshykau, R. G. Compton, *J. Phys. Chem. C* **2011**, *115*, 714.

[133] Q. Zhu, Z. Pan, S. Hu, J. H. Kim, *ACS Appl. Energy Mater.* **2019**, *2*, 7972.

[134] C. M. Hanna, A. Luu, J. Y. Yang, *ACS Appl. Energy Mater.* **2019**, *2*, 59.

[135] Q. Lin, Q. Li, C. Batchelor-McAuley, R. G. Compton, *J. Phys. Chem. C* **2015**, *119*, 1489.

[136] H.-G. Korth, P. Mulder, *J. Org. Chem.* **2020**, *85*, 2560.

[137] K. Lopez, M. N. Groves, *Catal. Sci. Technol.* **2021**, *11*, 4979.

[138] M. Mooste, E. Kibena-Põldsepp, L. Matisen, K. Tammeveski, *Electroanalysis* **2017**, *29*, 548.

[139] T. Wilson, J. Zhang, C. C. Oloman, D. D. M. Wayner, *Int. J. Electrochem. Sci.* **2006**, *1*, 99.

[140] P. M. Hoang, S. Holdcroft, B. L. Funt, *J. Electrochem. Soc.* **1985**, *132*, 2129.

[141] M.-C. Pham, J.-E. Dubois, *J. Electroanal. Chem.* **1986**, *199*, 153.

[142] T. Brousse, C. Cougnon, D. Bélanger, *J. Braz. Chem. Soc.* **2018**, *29*, 989.

[143] S. Komorsky-Lovric, *J. Solid State Electrochem.* **1997**, *1*, 94.

[144] L. Chuang, I. Fried, P. J. Elving, *Anal. Chem.* **1965**, *37*, 1528.

[145] B. Šljukić, C. E. Banks, R. G. Compton, *Phys. Chem. Chem. Phys.* **2004**, *6*, 4034.

[146] C. P. Andrieux, P. Hapiot, J. M. Saveant, *J. Electroanal. Chem.* **1985**, *189*, 121.

[147] P. Audebert, P. Hapiot, *J. Electroanal. Chem.* **1993**, *361*, 177.

[148] T. Murata, K. Kotsuki, H. Murayama, R. Tsuji, Y. Morita, *Commun. Chem.* **2019**, *2*, 46.

[149] M. Jakesova, D. H. Apaydin, M. Sytnyk, K. T. Oppelt, W. Heiss, N. S. Sariciftci, E. D. Głowacki, *Adv. Funct. Mater.* **2016**, *26*, 5248.

[150] N. Wadnerkar, V. Gueskine, E. D. Głowacki, I. Zozoulenko, *J. Phys. Chem. C* **2020**, *124*, 9605.

[151] M. Warczak, M. Gryszel, M. Jakešová, V. Derek, E. D. Głowacki, *Chem. Commun.* **2018**, *54*, 1960.

[152] M. Gryszel, A. Markov, M. Vagin, E. D. Głowacki, *J. Mater. Chem. A* **2018**, *6*, 24709.

[153] M. K. Węcławski, M. Jakešová, M. Charyton, N. Demitri, B. Koszarna, K. Oppelt, S. Sariciftci, D. T. Gryko, E. D. Głowacki, *J. Mater. Chem. A* **2017**, *5*, 20780.

[154] M. Gryszel, M. Sytnyk, M. Jakešová, G. Romanazzi, R. Gabrielsson, W. Heiss, E. D. Głowacki, *ACS Appl. Mater. Interfaces* **2018**, *10*, 13253.

[155] H. Shirakawa, E. J. Louis, A. G. MacDiarmid, C. K. Chiang, A. J. Heeger, *J. Chem. Soc. Chem. Commun.* **1977**, *16*, 578.

[156] A. G. MacDiarmid, A. J. Heeger, *Synth. Met.* **1980**, *1*, 101.

[157] W. J. Feast, J. Tsibouklis, K. L. Pouwer, L. Groenendaal, E. W. Meijer, *Polymer (Guildf).* **1996**, *37*, 5017.

[158] Nobel Prize Outreach, "The Nobel Prize in Chemistry 2000," can be found under https://www.nobelprize.org/prizes/chemistry/2000/summary/, **2000**.

[159] H. S. Nalwa, Ed. , *Handbook of Organic Conductive Molecules and Polymers*, John Wiley & Sons, Inc., Chichester, **1997**.

[160] G. Hadziioannou, P. F. van Hutten, Eds. , *Semiconducting Polymers: Chemistry, Physics and Engineering*, WILEY-VCH Verlag GmbH, Weinheim, **1999**.

[161] T. A. Skotheim, J. Reynolds, Eds. , *Conjugated Polymers: Processing and Applications*, CRC Press, Boca Raton, **2006**.

[162] S. C. Rasmussen, *Substantia* **2017**, *1*, 99.

[163] N. Heitzmann, Electrochemical Behavior of Perylene Derivatives and Polyaniline towards CO2 Reduction, Johannes Kepler University Linz, **2019**.

[164] H. Rabl, Electrochemical Oxygen Reduction to Hydrogen Peroxide Using Conducting Polymers, Johannes Kepler University Linz, **2020**.

[165] H. Wang, J. Lin, Z. X. Shen, *J. Sci. Adv. Mater. Devices* **2016**, *1*, 225.

[166] A. Rochliadi, S. A. Akbar, V. Suendo, *Jt. Int. Conf. Electr. Veh. Technol. Ind. Mech. Electr. Chem. Eng. (ICEVT IMECE)* **2015**, 353.

[167] D. Werner, C. Griesser, D. Stock, U. J. Griesser, J. Kunze-Liebhäuser, E. Portenkirchner, *ACS Appl. Energy Mater.* **2020**, *3*, 3477.

[168] C. Dhand, N. Dwivedi, S. Mishra, P. R. Solanki, V. Mayandi, R. W. Beuerman, S. Ramakrishna, R. Lakshminarayanan, B. D. Malhotra, *Nanobiosensors Dis. Diagnostics* **2015**, *4*, 25.

[169] W. A. Marmisollé, D. Gregurec, S. Moya, O. Azzaroni, *ChemElectroChem* **2015**, *2*, 2011.

[170] W. Li, F. Gao, X. Wang, N. Zhang, M. Ma, *Angew. Chemie - Int. Ed.* **2016**, *55*, 9196.

[171] S. Tekoglu, D. Wielend, M. C. Scharber, N. S. Sariciftci, C. Yumusak, *Adv. Mater. Technol.* **2019**, *5*, 1900699.

[172] G. Mengoli, M. M. Musiani, G. Zotti, S. Valcher, *J. Electroanal. Chem.* **1986**, *202*, 217.

[173] L. Doubova, G. Mengoli, M. M. Musiani, S. Valcher, *Electrochim. Acta* **1989**, *34*, 337.

[174] C. Q. Cui, J. Y. Lee, *J. Electroanal. Chem.* **1994**, *367*, 205.

[175] V. G. Khomenko, V. Z. Barsukov, A. S. Katashinskii, *Electrochim. Acta* **2005**, *50*, 1675.

[176] A. Wu, E. C. Venancio, A. G. MacDiarmid, *Synth. Met.* **2007**, *157*, 303.

[177] M. Rafti, W. A. Marmisollé, O. Azzaroni, *Adv. Mater. Interfaces* **2016**, *3*, 1.

[178] G. E. Fenoy, J. Scotto, J. Azcárate, M. Rafti, W. A. Marmisolle, O. Azzaroni, *ACS Appl. Energy Mater.* **2018**, *1*, 5428.

[179] A. P. Mártire, G. M. Segovia, O. Azzaroni, M. Rafti, W. Marmisollé, *Mol. Syst. Des. Eng.* **2019**, *4*, 893.

[180] J. Hu, S.-S. Li, J.-F. Li, Y.-L. Wang, X.-Y. Zhang, J.-B. Chen, S.-Q. Li, L.-N. Gu, P. Chen, *Chem. Eng. J.* **2022**, *431*, 133921.

[181] B. Winther-Jensen, D. R. MacFarlane, *Energy Environ. Sci.* **2011**, *4*, 2790.

[182] E. Mitraka, M. J. Jafari, M. Vagin, X. Liu, M. Fahlmann, T. Ederth, M. Berggren, M. P. Jonsson, X. Crispin, *J. Mater. Chem. A* **2017**, *5*, 4404.

[183] E. Miglbauer, P. J. Wójcik, E. D. Głowacki, *Chem. Commun.* **2018**, *54*, 11873.

[184] E. Mitraka, M. Gryszel, M. Vagin, M. J. Jafari, A. Singh, M. Warczak, M. Mitrakas, M. Berggren, T. Ederth, I. Zozoulenko, X. Crispin, E. D. Głowacki, *Adv. Sustain. Syst.* **2019**, *3*, 1800110.

[185] M. Vagin, V. Gueskine, E. Mitraka, S. Wang, A. Singh, I. Zozoulenko, M. Berggren, S. Fabiano, X. Crispin, *Adv. Energy Mater.* **2021**, *11*, 2002664.

[186] Q. Cui, D. J. Bell, S. Wang, M. Mohseni, D. Felder, J. Lölsberg, M. Wessling, *ChemElectroChem* **2021**, *8*, 1665.

[187] L. Migliaccio, M. Gryszel, V. Đerek, A. Pezzella, E. D. Głowacki, *Mater. Horiz.* **2018**, *5*, 984.

[188] M. Warczak, M. Osial, M. Berggren, E. D. Głowacki, *J. Electrochem. Soc.* **2020**, *167*, 086502.

[189] K. Oka, H. Nishide, B. Winther-Jensen, *Adv. Sci.* **2021**, *8*, 1.

[190] X. Long, D. Li, B. Wang, Z. Jiang, W. Xu, B. Wang, D. Yang, Y. Xia, *Angew. Chemie - Int. Ed.* **2019**, *58*, 11369.

[191] S. G. Patnaik, R. Vedarajan, N. Matsumi, *ACS Appl. Energy Mater.* **2018**, *1*, 1183.

[192] N. G. Connelly, W. E. Geiger, *Chem. Rev.* **1996**, *2*, 877.

[193] G. Su, Y. Wei, M. Guo, *Am. J. Anal. Chem.* **2011**, *2*, 879.

[194] Nobel Prize Outreach, "The Nobel Prize in Physics 1986," can be found under https://www.nobelprize.org/prizes/physics/1986/summary/, **1986**.

[195] JEOLLtd., "Transmission Electron Microscope (TEM) Using Electrons to Explore the Micro World," can be found under https://www.jeol.co.jp/en/science/em.html, **2021**.

[196] H. Günzler, H.-U. Gremlich, *IR-Spektroskopie Eine Einführung*, WILEY-VCH Verlag GmbH & Co. KGaA, Weinheim, **2003**.

[197] M. Hesse, H. Meier, B. Zeeh, *Spektroskopische Methoden in Der Organischen Chemie*, Georg Thieme Verlag, Stuttgart, **2005**.

[198] Petergans, "FTIR Interferometer," can be found under https://commons.wikimedia.org/wiki/File:FTIR_Interferometer.png, **2013**.

[199] G. Xia, Y. Tian, X. Yin, W. Yuan, X. Wu, Z. Yang, G. Yu, Y. Wang, M. Wu, *Appl. Catal. B Environ.* **2021**, *299*, 120655.

[200] A. Sarapuu, K. Tammeveski, T. T. Tenno, V. Sammelselg, K. Kontturi, D. J. Schiffrin, *Electrochem. Commun.* **2001**, *3*, 446.

[201] M. T. M. Koper, *J. Electroanal. Chem.* **2011**, *660*, 254.

[202] M. Jakešová, D. H. Apaydin, M. Sytnyk, K. Oppelt, W. Heiss, N. S. Sariciftci, E. D. Głowacki, *Adv. Funct. Mater.* **2016**, *26*, 5248.

[203] R. J. Taylor, A. A. Humffray, *Electroanal. Chem. Interfacial Electrochem.* **1973**, *42*, 347.

[204] R. . J. Taylor, A. A. Humffray, *J. Electroanal. Chem.* **1975**, *64*, 63.

[205] R. J. Taylor, A. A. Humffray, *J. Electroanal. Chem.* **1975**, *64*, 85.

[206] J. Xu, W. Huang, R. L. McCreery, *J. Electroanal. Chem.* **1996**, *410*, 235.

[207] S. V. Mentus, *Electrochim. Acta* **2004**, *50*, 27.

[208] E. Verney, J. R. Martin, P. Clechet, *J. Electrochem. Soc.* **1985**, *132*, 2178.

[209] H. Rabl, D. Wielend, S. Tekoglu, H. Seelajaroen, H. Neugebauer, N. Heitzmann, D. H. Apaydin, M. C. Scharber, N. S. Sariciftci, *ACS Appl. Energy Mater.* **2020**, *3*, 10611.

[210] C. Oloman, A. P. Watkinson, *J. Appl. Electrochem.* **1979**, *9*, 117.

[211] C. Paliteiro, A. Hamnett, J. B. Goodenough, *J. Electroanal. Chem.* **1987**, *233*, 147.

[212] C. Batchelor-McAuley, I. B. Dimov, L. Aldous, R. G. Compton, *Proc. Natl. Acad. Sci. U. S. A.* **2011**, *108*, 19891.

[213] J. J. Pietron, R. W. Murray, *J. Phys. Chem. B* **1999**, *103*, 4440.

[214] D. Wielend, H. Neugebauer, N. S. Sariciftci, *Electrochem. Commun.* **2021**, *125*, 106988.

[215] A. C. Fisher, *Electrode Dynamics*, Oxford University Press, Oxford, **1996**.

[216] A. Goyal, G. Marcandalli, V. A. Mints, M. T. M. Koper, *J. Am. Chem. Soc.* **2020**, *142*, 4154.

[217] G. Marcandalli, A. Goyal, M. T. M. Koper, *ACS Catal.* **2021**, *11*, 4936.

[218] A. Babaei, P. A. Connor, A. J. McQuillan, S. Umapathy, *J. Chem. Educ.* **1997**, *74*, 1200.

[219] J. Revenga, F. Rodríguez, J. Tijero, *J. Electrochem. Soc.* **1994**, *141*, 330.

[220] N. Kornienko, Y. Zhao, C. S. Kley, C. Zhu, D. Kim, S. Lin, C. J. Chang, O. M. Yaghi, P. Yang, *J. Am. Chem. Soc.* **2015**, *137*, 14129.

[221] B. Reuillard, K. H. Ly, T. E. Rosser, M. F. Kuehnel, I. Zebger, E. Reisner, *J. Am. Chem. Soc.* **2017**, *139*, 14425.

[222] T. E. Rosser, E. Reisner, *ACS Catal.* **2017**, *7*, 3131.

[223] J. Luangchaiyaporn, D. Wielend, D. Solonenko, H. Seelajaroen, J. Gasiorowski, M. Monecke, G. Salvan, D. R. T. Zahn, N. S. Sariciftci, P. Thamyongkit, *Electrochim. Acta* **2020**, *367*, 137506.

[224] R. S. K. A. Gamage, A. J. McQuillan, B. M. Peake, *J. Chem. Soc. Faraday Trans.* **1991**, *87*, 3653.

[225] J. Sun, Y. Wu, *Angew. Chemie* **2020**, *132*, 10996.

[226] C. Schimanofsky, (Spectro)Electrochemical Investigation of Anthraquinone Derivatives under CO2 and O2, Johannes Kepler University Linz, **2021**.

[227] B. Häupler, A. Wild, U. S. Schubert, *Adv. Energy Mater.* **2015**, *5*, 1.

[228] N. Casado, G. Hernández, H. Sardon, D. Mecerreyes, *Prog. Polym. Sci.* **2016**, *52*, 107.

[229] C. Han, H. Li, R. Shi, T. Zhang, J. Tong, J. Li, B. Li, *J. Mater. Chem. A* **2019**, *7*, 23378.

[230] G. Zarren, B. Nisar, F. Sher, *Mater. Today Sustain.* **2019**, *5*, 100019.

[231] G. Hernández, M. Isik, D. Mantione, A. Pendashteh, P. Navalotro, D. Shanmukaraj, R. Marcilla, D. Mecerreyes, *J. Mater. Chem. A* **2017**, *5*, 16231.

[232] D. Wielend, Y. Salinas, F. Mayr, M. Bechmann, C. Yumusak, H. Neugebauer, O. Brüggemann, N. S. Sariciftci, *ChemElectroChem* **2021**, *8*, 4360.

[233] T. Yamamoto, H. Etori, *Macromolecules* **1995**, *28*, 3371.

[234] Z. Song, Y. Qian, M. L. Gordin, D. Tang, T. Xu, M. Otani, H. Zhan, H. Zhou, D. Wang, *Angew. Chemie - Int. Ed.* **2015**, *54*, 13947.

[235] W. Choi, D. Harada, K. Oyaizu, H. Nishide, *J. Am. Chem. Soc.* **2011**, *133*, 19839.

[236] C. Clausen, E. Drazevic, A. S. Andersen, M. L. Henriksen, M. Hinge, A. Bentien, *ACS Appl. Energy Mater.* **2018**, *1*, 243.

[237] Y. Li, L. Liu, C. Liu, Y. Lu, R. Shi, F. Li, J. Chen, *Chem* **2019**, *5*, 2159.

[238] Y. Zou, A. S. Walton, I. A. Kinloch, R. A. W. Dryfe, *Langmuir* **2016**, *32*, 11448.

[239] A. S. Shaplov, R. Marcilla, D. Mecerreyes, *Electrochim. Acta* **2015**, *175*, 18.

[240] P. W. Atkins, J. de Paula, *Physikalische Chemie*, WILEY-VCH Verlag GmbH, Weinheim, **2013**.

[241] R. A. Marcus, N. Sutin, *Biochim. Biophys. Acta* **1985**, *811*, 265.

[242] R. A. Marcus, *J. Chem. Phys.* **2020**, *153*, 210401.

[243] D. K. Garner, M. D. Vaughan, H. J. Hwang, M. G. Savelieff, S. M. Berry, J. F. Honek, Y. Lu, *J. Am. Chem. Soc.* **2006**, *128*, 15608.

[244] P. Hosseinzadeh, Y. Lu, *Biochim. Biophys. Acta - Bioenerg.* **2016**, *1857*, 557.

[245] T. Ma, A. D. Easley, S. Wang, P. Flouda, J. L. Lutkenhaus, *Cell Reports Phys. Sci.* **2021**, *2*, 100414.

[246] K. Oka, S. Murao, M. Kataoka, H. Nishide, K. Oyaizu, *Macromolecules* **2021**, *54*, 4854.

[247] Y. Chen, H. Wang, S. Ji, B. G. Pollet, R. Wang, *J. Ind. Eng. Chem.* **2019**, *71*, 284.

[248] M. C. Schulze, G. M. Carroll, T. R. Martin, K. Sanchez-Rivera, F. Urias, N. R. Neale, *ACS Appl. Energy Mater.* **2021**, *4*, 1628.

[249] D. Wakerley, S. Lamaison, F. Ozanam, N. Menguy, D. Mercier, P. Marcus, M. Fontecave, V. Mougel, *Nat. Mater.* **2019**, *18*, 1222.

[250] D. H. Apaydin, S. Schlager, E. Portenkirchner, N. S. Sariciftci, *ChemPhysChem* **2017**, *18*, 3094.

[251] S. Fukuzumi, Y. Yamada, K. D. Karlin, *Electrochim. Acta* **2012**, *82*, 493.

[252] N. S. Sariciftci, *Asia Chem* **2020**, 51.

[253] D. Canevet, M. Gallego, H. Isla, A. De Juan, M. P. Emilio, *J. Am. Chem. Soc.* **2011**, *133*, 3184.

[254] A. De Juan, Y. Pouillon, L. Ruiz-González, A. Torres-Pardo, S. Casado, N. Martín, E. M. Pérez, *Angew. Chemie - Int. Ed.* **2014**, *53*, 5394.

[255] A. López-Moreno, E. M. Pérez, *Chem. Commun.* **2015**, *51*, 5421.

[256] E. M. Pérez, *Chem. - A Eur. J.* **2017**, *23*, 12681.

[257] S. Mena-Hernando, E. M. Pérez, *Chem. Soc. Rev.* **2019**, *48*, 5016.

[258] D. Sluysmans, J. . F. Stoddart, *Trends Chem.* **2019**, *1*, 185.

[259] D. Wielend, M. Vera-Hidalgo, H. Seelajaroen, N. S. Sariciftci, E. M. Pérez, D. R. Whang, *ACS Appl. Mater. Interfaces* **2020**, *12*, 32615.

[260] M. V. Hidalgo, Novel Functionalization Methods of 1D and 2D Materials and Their Applications, Universidad Autónoma de Madrid, **2019**.

[261] M. Blanco, B. Nieto-Ortega, A. De Juan, M. Vera-Hidalgo, A. López-Moreno, S. Casado, L. R. González, H. Sawada, J. M. González-Calbet, E. M. Pérez, *Nat. Commun.* **2018**,

9, 2671.

[262] A. Ashnagar, J. M. Bruce, P. L. Dutton, R. C. Prince, *Biochim. Biophys. Acta* **1984**, *801*, 351.

[263] M. Shamsipur, A. Siroueinejad, B. Hemmateenejad, A. Abbaspour, H. Sharghi, K. Alizadeh, S. Arshadi, *J. Electroanal. Chem.* **2007**, *600*, 345.

[264] P. S. Guin, S. Das, P. C. Mandal, *Int. J. Electrochem.* **2011**, *2011*, 816202.

[265] S. Schwan, D. Schröder, H. A. Wegner, J. Janek, D. Mollenhauer, *ChemSusChem* **2020**, 5480.

[266] Z. Gong, G. Zhang, S. Wang, *J. Chem.* **2013**, *2013*, 756307.

[267] M. Lee, J. Hong, H. Kim, H. Lim, S. B. Cho, K. Kang, C. B. Park, *Adv. Mater.* **2014**, 2558.

[268] D. Wielend, D. H. Apaydin, N. S. Sariciftci, *J. Mater. Chem. A* **2018**, *6*, 15095.

[269] H.-H. Yang, R. L. McCreery, *J. Electrochem. Soc.* **2000**, *147*, 3420.

[270] Y. Lu, J. Chen, *Nat. Rev. Chem.* **2020**, *4*, 127.

[271] D. W. Hatchett, M. Josowicz, J. Janata, J. E. Soc, D. W. Hatchett, M. Josowicz, J. Janata, *J. Electrochem. Soc.* **1999**, *146*, 4535.

[272] R. Gonçalves, R. S. Paiva, A. M. R. Ramírez, J. A. Mwanda, E. C. Pereira, A. Cuesta, *Electrochem. Sci. Adv.* **2021**, e2100028.

[273] H. Kuzmany, N. S. Sariciftci, H. Neugebauer, A. Neckel, *Phys. Rev. Lett.* **1988**, *60*, 212.

[274] N. S. Sariciftci, M. Bartonek, H. Kuzmany, H. Neugebauer, A. Neckel, *Synth. Met.* **1989**, *29*, E193.

6. Appendix

6.1. List of Technical Abbreviations

ATR-FTIR … attenuated total reflection Fourier transformed infrared spectroscopy

BDD … boron-doped diamond

CE … counter electrode

CNT … carbon nanotube

CO$_2$RR … carbon dioxide reduction reaction

CP … carbon paper

CV … cyclic voltammetry

E$_{1/2}$ … electrochemical potential

FE … faradaic efficiency

GC … glassy carbon

HER … hydrogen evolution reaction

HR-TEM … high resolution transmission electron microscopy

I$_D$ … disc current

I$_K$ … kinetic current

I$_R$ … ring current

j$_P$ … peak current density

K-L … Koutecki-Levich analysis

LSV … linear sweep voltammetry

MINT … mechanically interlocked carbon nanotube

n … number of transferred electrons per reaction/elementary step

NMR … nuclear magnetic resonance

OER … oxygen evolution reaction

ORR … oxygen reduction reaction

PB … phosphate buffer solution

PBS … phosphate buffered saline solution

RDE … rotating disc electrode

RE … reference electrode

RRDE … rotating ring disc electrode

SCE … saturated calomel electrode

SEM … scanning electron microscopy

SHE … standard hydrogen electrode

TGA … thermogravimetric analysis

WE … working electrode

6.1. List of Tables

6.2. List of Figures

potential U_L in dependence of ΔG_{*OH} (upper part in blue). Reproduced with permission from Perry *et al.*[38]. © 2019 Springer Nature Limited.

Figure 17: a) Schematic depiction of an RDE experiment involving the electrochemical reduction of molecule A to molecule B. b) Schematic RDE voltammogram graph for such a reduction reaction A→B including the limiting disc current $I_{D,lim}$.

Figure 18: a) Schematic depiction of an RRDE experiment involving the electrochemical reduction of molecule A to molecule B and the back reaction on the ring electrode b) Schematic RRDE voltammogram graph for such a reduction reaction A→B and the reverse reaction including the limiting disc current $I_{D,lim}$ and limiting ring current $I_{R,lim}$.

Figure 19: Chemical structures of porphyrins, phthalocyanines and corroles, as examples of macrocyclic molecules used in ORR.

Figure 20: Covalent electrochemical grafting approaches reported by the group of Tammeveski.[125–128] a) oxidative electrochemical grafting of AQ-COOH and b) reductive electrochemical grating of AQ-N_2^+ salt.

Figure 21: Chemical structures of homogeneous catalysts for the oxygen reduction reaction: a) azobenzene, b) methylviologene (MV), c) 9-(4-R-phenyl)-*N*-methyl-acridinium, where R was H, F or Cl and d) a general trioxotriangulene (TOT) molecule as neutral radical species, where R was H, Cl, Br and phenyl.

Figure 22: Chemical structures of a) quinacridone (QNC), b) epindolidione (EPI) and c) perylene tetracarbonyl imide (PTCDI).

Figure 23: Schematic chemical structures of four conductive polymers: a) polyaniline (PANI), b) polypyrrole (PPy), c) polythiophene (PTh) and d) poly(3,4-ethylenedioxythiophene) (PEDOT).

Figure 24: Schematic chemical structures of four conductive polymers: a) Eumelanin[186] , b) Polyindole[187] ,

Figure 25: Polishing of GC electrodes with alumina pastes for a) disc-type GC electrode (black rod) with a polishing pad and the white Al_2O_3 polishing paste and b) a 1x4 cm GC plate (black) on a glass plate with white Al_2O_3 polishing paste.

Figure 26: Images of the potentiostats used. a) Jaissle Potentiostat-Galvanostat PGU10V-100 mA, b) Jaissle Potentiostat-Galvanostat 1030 PC-T with a 10 V application voltage but a maximum current range of 1 A and c) Ivium Vertex One.EIS with 10 V application voltage and a maximum current range of 100 mA.

Figure 27: a) One-compartment electrochemical cell with GC as WE, Pt as CE and Ag/AgCl (3M KCl) as RE and b) two-compartment electrochemical cell separated with a glass frit and GC as WE, Pt as CE and Ag/AgCl (3M KCl) as RE.

Figure 28: Conversion of potentials vs. QRE into vs. SHE via ferrocene calibration. Conversion potentials are reproduced from literature.[81,191]

Figure 29: a) Picture of the rotating (ring) disc electrode setup including the bipotentiostat, the rotator unit and the rotation controller and b) picture of the GC/Pt RRDE in PEEK and GC and Pt RDE's in PTCFE.

Figure 30: Reaction equation for the stoichiometric reaction of H_2O_2 with the *p*NBA forming *p*-nitrophenol.

Figure 31: a) Picture of the microplate with samples of increasing [H_2O_2], b) subtracted absorbance spectra of the H_2O_2 calibration and c) calibration curve of H_2O_2 for quantification.

Figure 32: a) Picture of the mainly used scanning electron microscope (SEM): JEOL JSM-6360LV, and b) sample holders used for SEM.

Figure 33: a) Photo of the Varian Cary 3G UV-Visible spectrophotometer, b) picture of the UV-Vis spectroelectrochemical cell, c) illustration of the mounting of the spectroelectrochemical cell inside the spectrophotometer and d) photo of the Perkin Elmer Lambda 1050 UV/VIS/NIR spectrometer with the reflectance unit mounted.

Figure 34: a) Scheme of an FTIR, reproduced from Wikimedia Commons[197], b) scheme of an ATR spectroscopy measurement mode, c) picture of the Vertex 80 FTIR and d) picture of the Platinum ATR unit.

Figure 35: Ossila Angle Goniometer setup for contact angle determination.

Figure 36: TGA/Perkin Elmer Q5000.

Figure 37: CV of Pt, GC, Ti and 5 nm Cr / 80 nm Au on glass electrodes recorded in 0.1 M NaOH under O_2 saturated conditions at a scan rate of 20 mV s^{-1}. For clarification, the large current responses from the platinum hydrogen evolution phenomena are not shown in detail here.

Figure 38: RDE-LSV curves of a) GC and c) Pt electrode recorded in 0.1 M PB at pH=7 at the rotation speeds given. The Koutecky-Levich plots are illustrated in the part b) and d).

Figure 39: Number of transferred electrons per reduction reaction *n* for GC and platinum determined in 0.1 M $NaHSO_4$ solution (pH=2), 0.1 M PB solution (pH=7) and 0.1 M NaOH solution (pH=13).

Figure 40: a) RRDE-LSV recorded in 1 mM $K_3[Fe(CN)_6]$ in 0.1 M PB at 100 rpm (Ring potential at +0.73 V) and b) the according plot of the experimental collection efficiency N_{exp}.

Figure 41: a) RRDE-LSV curves in 1 mM $K_3[Fe(CN)_6]$ in 0.1 M PB at rotation speeds between 100 and 3600 rpm and b) according average values of N_{exp} at the rotation speeds stated. Reproduced with permission from Rabl *et al.* (https://pubs.acs.org/doi/abs/10.1021/acsaem.0c01663)[208] © 2020 American Chemical Society.

Figure 42: CV of GC and Pt from the RRDE in 0.1 M PB under O_2 saturated conditions and with 5 mM H_2O_2 added

Figure 43: Faradaic efficiency values for H_2O_2 produced on a GC/Pt RRDE in various pH conditions: 0.1 M NaHSO4 solution at pH=2, 0.1 M PB at pH=7 and 0.1 M NaOH solution at pH=13. The error bars indicate the deviations from different rotation speeds. Reproduced with permission from Rabl *et al.* (https://pubs.acs.org/doi/abs/10.1021/acsaem.0c01663)[208]. © 2020 American Chemical Society.

Figure 44: CV curves of GC and 1 mM solutions of AQS under N_2 and O_2 saturated conditions. In all cases, 0.1 M PB at pH=7 was used as electrolyte solution. Reproduced from Wielend *et al.*[213]. © 2021 the authors.

Figure 45: CV studies of 1mM AQS in 0.1 M PB at different scan rates under a) N_2 saturated conditions and b) O_2 saturated conditions. Reproduced from Wielend *et al.*[213]. © 2021 the authors.

Figure 46: a) RRDE-LSV curves of blank GC electrodes in comparison with 1 mM AQS in 0.1 M PB solution under N_2 saturated conditions in comparison with O_2 saturated conditions, b) Ratio of ring current I_R and I_D from the LSV curves shown in a). For all measurements the ring was kept at +0.64 V and the rotation speed was 900 rpm. Figure a) was reproduced from Wielend *et al.*[213]. © 2021 the authors.

Figure 47: RRDE-LSV curves at 100 rpm (a & b) and 3600 rpm (c &d), where the excess currents were calculated and illustrated as red dots.

Figure 48: Illustration of the excess currents at the disc and ring at 100 rpm (a) and 3600 rpm (b) including the excess efficiency, c) Visualization of the excess current shifts upon increasing

the rotation speed from 100 to 2600 rpm in one graph. Reproduced from Wielend *et al.*[213]. (c) 2021 the authors.

Figure 49: a) Graphs of the excess efficiencies for all rotation speeds recorded between 100 and 3600 rpm, b) maximum current potentials of I_D and I_R at various rotation speeds vs. $\omega^{0.5}$. Reproduced from Wielend *et al.*[213]. © 2021 the authors.

Figure 50: In-situ UV-Vis spectroelectrochemistry graphs of 1 mM AQS in 0.1 M PB upon electrochemical reduction in a) &b) N_2 saturated conditions and c) & d) O_2 saturated conditions.

Figure 51: a) Reaction scheme for the synthesis of PDDA-SAQ, b) photographs taken during the synthesis of PDDA-SAQ. On the left picture, the 25 mM AQS solution is shown, then the reaction mixture is shown which is subsequently filtered with a filter paper and funnel, afterwards washed with MQ, dried and finally the yellow polymer collected as flakes.

Figure 52: a) Reaction scheme for the synthesis of P14AQ, b) photographs taken during the synthesis of P14AQ. The left image shows DCAQ, the blue color is observed for the reaction mixture right before the reaction start, during which the solution turns dark brown. After quenching with HCl, on top of the blue-green solution the brown polymer was precipitated. After washing, re-dissolving in $CHCl_3$ and precipitation with MeOH the polymer appears as yellow precipitate which can then be collected as powder via filtration or as film after slow evaporation when dissolved in $CHCl_3$.

Figure 53: a) Reaction scheme for the synthesis of PVAQ, b) photographs taken during the synthesis of PVAQ. On the left image the reaction setup is shown, then the reaction tube with already concentrated solution and faint polymer precipitation. The third image from the left shows the precipitated polymer upon toluene addition followed by centrifugation and drying, before collecting the light-yellow polymer powder.

Figure 54: a&b) ^{1}H-NMR spectra of monomer DCAQ and c&d) ^{1}H-NMR spectra of polymer P14AQ recorded as solution in $CDCl_3$ (marked as *). The presence of water in c) is marked with #. Spectra were recorded by Yolanda Salinas. Adapted from the Supporting Information of Wielend *et al.*[231] © 2021 the authors.

Figure 55: a) ^{1}H-NMR spectrum of monomer 2-vinyl AQ and b) ^{1}H-NMR spectrum of polymer PVAQ recorded as solution in $CDCl_3$ (marked as *). The presence of water in c) is marked with #. Spectra were recorded by Yolanda Salinas. Adapted from the Supporting Information of Wielend *et al.*[231] © 2021 the authors.

Figure 56: DOSY spectra a) P14AQ and two different samples of PVAQ. b) less purified PVAQ and c) more purified PVAQ. Spectra were recorded and fitted by Matthias Bechmann. a) & c) Reproduced from the Supporting Information of Wielend *et al.*[231] © 2021 the authors.

Figure 57 : UV-Vis absorption spectra of P14AQ and PVAQ dissolved in $CHCl_3$, the monomers DCAQ and 2-vinyl-AQ also dissolved in $CHCl_3$ whereas the monomer AQS was measured in homogeneous aqueous solution. The right graph shows a closer look at the regime between 250 and 500 nm. Reproduced from Wielend *et al.*[231] © the authors.

Figure 58: a) Photograph of the thin-films on quartz glass of PDDA-SAQ, P14AQ and PVAQ, b) Absorptance spectra measured of these polymer thin-films. Absorptance spectra were recorded and corrected for reflection by Felix Mayr. b) Reproduced from Wielend *et al.*[231] © 2021 the authors.

Figure 59: ATR-FTIR spectra of the polymers a) PDDA-SAQ, b) P14AQ and c) PVAQ in comparison with the respective monomers. Reproduced from the Supporting Information of Wielend *et al.*[231] © the authors.

Figure 60 :a) ATR-FTIR spectra of the three anthraquinone polymers where some of the most prominent bands are marked. The bands encircled in red correspond to the C=O vibration,

where a further zoomed area of these bands is shown in b). Reproduced from Wielend *et al.*[231] © 2021 the authors.

Figure 61: TGA graphs of a) PDADMAC and PDDA-SAQ, b) DCAQ and P14AQ and c) 2-vinyl AQ and PVAQ. The left y-axis and the solid lines refer to the weight whereas the right y-axis and the dashed lines refer to the derivatives of the weight. The TGA measurements were done and fitted by Maria Würflinger and Yolanda Salinas. Reproduced from the Supporting Information of Wielend *et al.*[231] © 2021 the authors.

Figure 62: Contact angle measurement with a water drop on blank GC, PDDA-SAQ, P14AQ and PVAQ on GC as well as on a P14AQ film on glass. Adapted from Wielend *et al.*[231] © 2021 the authors.

Figure 63: CV graphs testing 50 cycles stability of a) PDDA-SAQ, b) P14AQ and c) PVAQ recorded in 0.1 M PB at neutral pH=7. Reproduced from Wielend *et al.*[231] © 2021 the authors.

Figure 64: CV graphs testing 50 cycles stability of a) PDDA-SAQ, b) P14AQ and c) PVAQ recorded in 0.1 M NaOH at alkaline pH=13. Reproduced from Wielend *et al.*[231] © 2021 the authors.

Figure 65: CV graphs testing 50 cycles stability of a) PDDA-SAQ, b) P14AQ and c) PVAQ recorded in 2.5 M NaCl solution in 0.1 M NaOH at alkaline pH=13. Reproduced from the Supporting Information of Wielend *et al.*[231] © 2021 the authors.

Figure 66: CV graphs testing 50 cycles stability of a) PDDA-SAQ, b) P14AQ and c) PVAQ recorded in 0.1 M $NaHSO_4$ at alkaline pH=2. Reproduced from the Supporting Information of Wielend *et al.*[231] © 2021 the authors.

Figure 67: CV graphs testing 50 cycles stability of a) PDDA-SAQ, b) P14AQ and c) PVAQ recorded in 0.1 M $TBAPF_6$ in MeCN solution. Reproduced from the Supporting Information of Wielend *et al.*[231] © 2021 the authors.

Figure 68: SEM images of polymer films on GC electrode before and after the electrochemical treatment as stated: a-b) PDDA-SAQ, c-d) P14AQ and e-f) PVAQ. Reproduced from Wielend *et al.*[231] © 2021 the authors.

Figure 69: CV comparison of PDDA-SAQ comparing N_2 saturated conditions with O_2 saturated conditions with GC under O_2 in a) 0.1 M PB at pH=7 and b) 0.1 M NaOH at pH=13. Reproduced from Wielend *et al.*[231] © 2021 the authors.

Figure 70: CV comparison of a) P14AQ and b) PVAQ comparing N_2 saturated conditions with O_2 saturated conditions with GC under O_2 in 0.1 M NaOH at pH=13. Reproduced from Wielend *et al.*[231] © 2021 the authors.

Figure 71: CV comparison of a) PDDA-SAQ and b) PVAQ comparing N_2 saturated conditions with O_2 saturated conditions with GC under O_2 in 0.1 M NaOH at pH=13. "Full" refers to scans going beyond the onset of reduction of the polymer whereas the other scans were stopped at the edge of GC ORR.

Figure 72: a) ATR-FTIR spectra of the three anthraquinone polymers in the ragne of the C=O vibration modes and b) graphical illustration of the redox potentials at various electrolyte solutions in dependece of the C=O wavenumbers. Reproduced from the Supporting Information of Wielend *et al.*[231] © the authors.

Figure 73: Graphical correlation plots of a) redox potential *vs.* the contact angle θ and b) peak current density of the first reduction peak in MeCN *vs.* the contact angle *θ*. Part b) is reproduced from the Supporting Information of Wielend *et al.*[231] © 2021 the authors.

Figure 74: Graphical illustration of a general [2]rotaxane system and a mechanically interlocked carbon nanotube (MINT) system. In addition a single-walled carbon nanotube

(SWCNT) and a supramolecular assembly are also depicted. Reproduced with permission from Pérez [255] © 2017 Wiley-VCH Verlag GmbH&Co. KGaA, Weinheim.

Figure 75: a) graphical illustration of the MINT synthesis steps, b) energy-optimized simulation of a general MINT structure on a SWCNT and c) synthesis steps of MINT fabrication. Part a) was reproduced with permission from Pérez [255] © 2017 Wiley-VCH Verlag GmbH&Co. KGaA, Weinheim.and parts b&c) were reproduced with permission from DeJuan et al. [253] © 2014 Wiley-VCH Verlag GmbH&Co. KGaA, Weinheim.

Figure 76: Chemical structure of a) the AQ-MINT macrocycle and b) the octenyloxy-AQ.

Figure 77: a) Energy-minimized molecular geometry of AQ-MINT performed via DFT and b) HR-TEM image of AQ-MINT. Reproduced from Blanco et al. [260]. © 2018 these authors.

Figure 78: CV study of 2.5 mM AQ and 1 mM octenyloxy-AQ in 0.1 M TBAPF$_6$ in MeCN recorded at 20 mV s^{-1}. Reproduced with permission from the supporting information of Wielend et al. (https://pubs.acs.org/doi/abs/10.1021/acsami.0c06516)[258].) © 2020 American Chemical Society.

Figure 79: CV graphs of a) AQ-MINT and 1 mM octenyloxy-AQ in 0.1 M TBAPF$_6$ in MeCN and b) AQ-MINT and an evaporated 100 nm AQ thin film in 0.1 M Na$_2$SO$_4$ aqueous solution. All CVs were recorded under N$_2$ saturated conditions at a scan rate of 20 mV s^{-1}. Reproduced with permission from Wielend et al. (https://pubs.acs.org/doi/abs/10.1021/acsami.0c06516)[258]. © 2020 American Chemical Society.

Figure 80: CV curves of a) AQ-MINT in 0.1 M Na$_2$SO$_4$, b) AQ-MINT in 0.1 M TBAPF$_6$ in MeCN, c) AQ@SWCNT in 0.1 M Na$_2$SO$_4$ and d) Illustration of the normalized peak currents with respect to the first reduction peak. All CV's were recorded under N$_2$ saturated conditions at a scan rate of 20 mV s^{-1}. Reproduced with permission from Wielend et al. (https://pubs.acs.org/doi/abs/10.1021/acsami.0c06516)[258]. © 2020 American Chemical Society.

Figure 81: CV curves of AQ-MINT under aerated conditions (green line), N$_2$ (black line) and O$_2$ saturated conditions (orange line) in a) 0.1 M Na$_2$SO$_4$ and b) 0.1 M NaOH solution. Reproduced with permission from Wielend et al. (https://pubs.acs.org/doi/abs/10.1021/acsami.0c06516)[258]. © 2020 American Chemical Society.

Figure 82: CV comparison of bare GC, SWCNT and AQ-MINT in 0.1 M NaOH under O$_2$ saturated conditions and recorded at 20 mV s^{-1}.

Figure 83: Moles of H$_2$O$_2$ produced during 8 h electrolysis at -0.33 V in 0.1 M Na$_2$SO$_4$ and 0.1 M NaOH solution.

Figure 84: Chronoamperograms and accumulated charges recorded at -0.33 V in 0.1 M NaOH of a) AQ-MINT, b) AQ@SWCNT and c) SWCNT.

Figure 85: CV graphs recorded in 0.1 M NaOH solution before and after 8 h electrolysis of a) AQ-MINT and b) AQ@SWCNT. Part a) was reproduced with permission from Wielend et al. (https://pubs.acs.org/doi/abs/10.1021/acsami.0c06516)[258]. © 2020 American Chemical Society.

Figure 86: a) RDE-LSV curves of AQ-MINT, AQ@SWCNT and SWCNT in 0.1 M NaOH at a rotation speed of 1200 rpm and b) I$_K$ values calculated from the intercept of the Koutecky-Levich analysis. Reproduced with permission from Wielend et al. (https://pubs.acs.org/doi/abs/10.1021/acsami.0c06516)[258]. © 2020 American Chemical Society.

Figure 87: SEM images of a) AQ-MINT, b) AQ@SWCNT and c) SWCNT on GC.

Figure 88: SEM images of polymers on electrodes. a) PANI on GC, b) PPy on GC, c) PANI on CP and d) PPy on CP. Reproduced with permission from Rabl *et al.* (https://pubs.acs.org/doi/abs/10.1021/acsaem.0c01663).[208] © 2020 American Chemical Society.

Figure 89: a) CV of GC/PANI and GC/PPy in 0.1 M PB under N_2 and O_2 saturated conditions and b) results of electrolysis of blank GC, GC/PANI and GC/PPy in 0.1 M PB recorded at -0.4 V showing the moles H_2O_2 produced and the according faradaic efficiencies. Data was recorded by Hannah Rabl. Reproduced with permission from Rabl *et al.* (https://pubs.acs.org/doi/abs/10.1021/acsaem.0c01663).[208] © American Chemical Society.

Figure 90: a) CV of CP/PANI and CP/PPy in 0.1 M PB under N_2 and O_2 saturated conditions and b) results of electrolysis of blank CP, CP/PANI and CP/PPy in 0.1 M PB recorded at -0.4 V showing the moles H_2O_2 produced and the according faradaic efficiencies. Data was recorded by Hannah Rabl. Reproduced with permission from Rabl *et al.* (https://pubs.acs.org/doi/abs/10.1021/acsaem.0c01663).[208] © 2020 American Chemical Society.

Figure 91: Results of electrolysis in 0.1 M $NaHSO_4$ at pH=2 recorded at – 0.4 V of a) blank GC, GC/PPy and GC/PANI and b) blank CP, CP/PPy and CP/PANI. Data was recorded by Hannah Rabl.

Figure 92 : a) LSV curves of GC/PANI in 0.1 M PB under O_2 and b) LSV curves of GC/PANI in 0.1 M PB under O_2 and with 5 mM H_2O_2 added and c) number of electrons transferred as calculated via Koutecky-Levich analysis. Reproduced with permission from Rabl *et al.* (https://pubs.acs.org/doi/abs/10.1021/acsaem.0c01663).[208] © 2020 American Chemical Society.

Figure 93: a) LSV curves of GC/PANI in 0.1 M $NaHSO_4$ under O_2 and b) LSV curves of GC/PANI in 0.1 M $NaHSO_4$ under O_2 and with 5 mM H_2O_2 added and c) number of electrons transferred as calculated via Koutecky-Levich analysis. Reproduced with permission from Rabl *et al.* (https://pubs.acs.org/doi/abs/10.1021/acsaem.0c01663).[208] © 2020 American Chemical Society.

Figure 94: LSV curves of GC/PPy in 0.1 M PB under O_2, without (a) and with 5 mM H_2O_2 added (b) and LSV curves of GC/PPy in 0.1 M $NaHSO_4$ under O_2, without (c) and with 5 mM H_2O_2 added (d). Reproduced with permission from Rabl *et al.* (https://pubs.acs.org/doi/abs/10.1021/acsaem.0c01663).[208] © 2020 American Chemical Society.

7. Curriculum Vitae

Name	Dominik Wielend
Address	Linz Institute for Organic Solar Cells (LIOS) / Institute of Physical Chemistry Johannes Kepler University (JKU) Linz Altenberger Straße 69 4040 Linz / Austria
E-mail	dominik.wielend@jku.at

Academic education

2018 - present	<u>PhD studies</u> in "**Engineering Sciences**" (Main subject: Chemistry) at the Johannes Kepler University (JKU) Linz, Austria Thesis topic: "*Electrochemical H_2O_2 production using immobilized organic catalysts*"
2015 - 2017	<u>Master studies</u> in "**Chemistry and Chemical Technology**" at the Johannes Kepler University (JKU) Linz, Austria Thesis topic: "*Electrochemical capture and release of CO_2 using organic pigments*" Passed with distinction
09/2016 – 02/2017	<u>Erasmus+ internship</u> at the Christian Doppler Laboratory for Sustainable Syngas Chemistry / Erwin Reisner Lab at the University of Cambridge, United Kingdom Research topic: "*Photocatalytic water reduction with ZnSe nanocrystals*"
2012 - 2015	<u>Bachelor studies</u> in "**Chemistry and Chemical Technology**" at the Johannes Kepler University (JKU) Linz, Austria Thesis topic: "*Investigations of Polypyrrole based electrodes towards electrochemical reduction of CO_2*" Passed with distinction

Language skills

German	Mother tongue
English	Proficient user (C1)
Spanish	Basic knowledge (B1)

Society memberships

Austrian Chemical Society (GÖCH)   since 2016
International Society of Electrochemistry (ISE)   since 2020
Royal Society of Chemistry (RSC)   since 2019

Teaching experience

Exercise lecturer
Exercises in Physical Chemistry for Biological Chemistry I (WS 2018/2019, WS 2019/2020)
Exercises in Physical Chemistry I (WS 2020/2021, WS 2021/2022)
Exercises in Physical Chemistry II (SS 2021)
KV Chemical Thermodynamics (SS2020, SS2021)

Exercise tutor
Tutorial for Exercises in Physical Chemistry I (WS 2018/2019, WS 2019/2020)
Tutorial for Exercises in Physical Chemistry II (SS 2018, SS 2019, SS 2020)

Laboratory supervisor
Lab course in Physical Chemistry III (SS 2018 until WS 2021/2022)

Conferences

D. Wielend, H. Rabl, S. Tekoglu, H. Seelajaroen, H. Neugebauer, N. Heitzmann, D. H. Apaydin, M. C. Scharber, N. S. Sariciftci: The study of oxygen reduction reactions with carbon based electrode materials: problems and solutions using rotating electrodes, 72nd Annual meeting of the International Society of Electrochemistry (ISE), Jeju Island (Korea) / Online (2021), Oral presentation

D. Wielend, M. Vera-Hidalgo, H. Seelajaroen, N. S. Sariciftci, E. M. Pérez, D. R. Whang: Mechanically interlocked carbon nanotubes as a stable electrocatalytic platform for oxygen reduction, Electrochemistry Undercover, Berlin (GER) / Online (2020), Poster talk

D. Wielend, M. Vera-Hidalgo, H. Seelajaroen, N. S. Sariciftci, E. M. Pérez, D. R. Whang: Mechanically interlocked carbon nanotubes as versatile and stable platform for nano electrocatalysis, 71st Annual meeting of the International Society of Electrochemistry (ISE), Belgrade (SRB) / Online (2020), Poster talk

D. Wielend, D. H. Apaydin, D. R. Whang, N. S. Sariciftci : Electrochemical capture and release of CO_2 using anthraquinone, 18. Österreichische Chemietage, Linz (AT) (2019), Oral presentation

D. Wielend, D. H. Apaydin, D. R. Whang, N. S. Sariciftci: Reversible electrochemical capture and release of CO_2 using anthraquinone, Europe-Korea conference on Science and Technology (EKC), Vienna (AT) (2019), Poster presentation

D. Wielend, D. H. Apaydin, D. R. Whang, N. S. Sariciftci: Electrochemical capture and release of CO_2 using anthraquinone, Faraday Discussion Artificial Photosynthesis, Cambridge (UK) (2019), Poster presentation

List of publications

2021

1. **Wielend, D.***; Salinas, Y.; Mayr, F.; Bechmann, M.; Yumusak, C.; Neugebauer, H.; Brüggemann, O.; Sariciftci, N. S. Immobilized Poly(Anthraquinones) for Electrochemical Energy Storage Applications: Structure-Property Relations. *ChemElectroChem* **2021**, *8*, 4360–4370.

2. Hofinger, J.; Putz, C.; Mayr, F.; Gugujonovic, K.; **Wielend, D.**; Scharber, M. C. Understanding the Low Voltage Losses in High-Performance Non-Fullerene Acceptor-Based Organic Solar Cells. *Mater. Adv.* **2021**, *2*, 4291–4302.

3. Griesser, C.; Li, H.; Wernig, E.; Winkler, D.; Nia, N. S.; Mairegger, T.; Götsch, T.; Schachinger, T.; Steiger-Thirsfeld, A.; Penner, S.; **Wielend, D.**; Egger, D.; Scheurer, C.; Reuter, K.; Junze-Liebhäuser, J. True Nature of the Transition-Metal Carbide / Liquid Interface Determines Its Reactivity. *ACS Catal.* **2021**, *11*, 4920–4928.

4. **Wielend, D.***; Neugebauer, H.; Sariciftci, N. S. Revealing the Electrocatalytic Behaviour by a Novel Rotating Ring-Disc Electrode (RRDE) Subtraction Method : A Case-Study on Oxygen Reduction Using Anthraquinone Sulfonate. *Electrochem. Commun.* **2021**, *125*, 106988.

5. Werner, D.; Apaydin, D. H.; **Wielend, D.**; Geistlinger, K.; Saputri, W. D.; Griesser, U. J.; Drazevic, E.; Hofer, T. S.; Portenkirchner, E. Analysis of the Ordering Effects in Anthraquinone Thin Films and Its Potential Application for Sodium Ion Batteries. *J. Phys. Chem. C* **2021**, *125* (7), 3745–3757.

6. Richtar, J.; Ivanova, L.; Whang, D. R.; Yumusak, C.; **Wielend, D.**; Weiter, M.; Scharber, M. C.; Kovalenko, A.; Sariciftci, N. S.; Krajcovic, J. Tunable Properties of Nature-Inspired N,N′-Alkylated Riboflavin Semiconductors. *Molecules* **2021**, *26* (27), 1–16.

2020

7. Fiedler, C.; Ulbricht, C.; Truglas, T.; **Wielend, D.**; Bednorz, M.; Groiss, H.; Brüggemann, O.; Teasdale, I.; Salinas, Y. Reversible Speed Regulation of Self-Propelled Janus Micromotors via Thermoresponsive Bottle-Brush Polymers. *Chem. - A Eur. J.* **2020**, *27*, 3262–3267.

8. Luangchaiyaporn, J.; **Wielend, D.**; Solonenko, D.; Seelajaroen, H.; Gasiorowski, J.; Monecke, M.; Salvan, G.; Zahn, D. R. T.; Sariciftci, N. S.; Thamyongkit, P. High-Performance Co^{II}-Phthalocyanine-Based Polymer for Practical Heterogeneous Electrochemical Reduction of Carbon Dioxide. *Electrochim. Acta* **2020**, *367*, 137506.

9. Rabl, H.; **Wielend, D.***; Tekoglu, S.; Seelajaroen, H.; Neugebauer, H.; Heitzmann, N.; Apaydin, D. H.; Scharber, M. C.; Sariciftci, N. S. Are Polyaniline and Polypyrrole Electrocatalysts for Oxygen (O_2) Reduction to Hydrogen Peroxide (H_2O_2)? *ACS Appl. Energy Mater.* **2020**, *3* (11), 10611–10618.

10. Liebl, S.; Werner, D.; Apaydin, D. H.; **Wielend, D.**; Geistlinger, K.; Portenkirchner, E. Perylentetracarboxylicdiimide (PTCDI) as Diffusion-Less Electrode Material for High Rate Organic Na-Ion Batteries. *Chem.-A Eur. J.* **2020**, *26*, 17559 –17566.

11. **Wielend, D.**; Vera-Hidalgo, M.; Seelajaroen, H.; Sariciftci, N. S.; Pérez, E. M.; Whang, D. R. Mechanically Interlocked Carbon Nanotubes as a Stable Electrocatalytic Platform for Oxygen Reduction. *ACS Appl. Mater. Interfaces* **2020**, *12* (29), 32615–32621.

2019

12. Tekoglu, S.; **Wielend, D.**; Scharber, M. C.; Sariciftci, N. S.; Yumusak, C. Conducting Polymer-Based Biocomposites Using Deoxyribonucleic Acid (DNA) as Counterion. *Adv. Mater. Technol.* **2019**, *5*, 1900699.

13. Hailegnaw, B.; Adam, G.; **Wielend, D.**; Pedarnig, J. D.; Sariciftci, N. S.; Scharber, M. C. Acetylacetone Improves the Performance of Mixed Halide Perovskite Solar Cells. *J. Phys. Chem. C* **2019**, *123* (39), 23807–23816.

14. Abe, R.; Bajada, M.; Beller, M.; Bocarsly, A. B.; Butt, J. N.; Cassiola, F.; Domcke, W.; Durrant, J. R.; Gavrielides, S.; Grätzel, M.; Hammaström, L.; Hatzell, M. C.; König, B.; Kudo, A.; Kuehnel, M. F.; Lage, A.; Lee, C. Y.; Maneiro, M.; Minteer, S. D.; Paris, A. R.; Plumeré, N.; Reek, J. N. H.; Reisner, E.; Roy, S.; Schnedermann, C.; Shankar, R.; Shylin, S. I.; Smith, W. A.; Sen Soo, H.; Wagner, A.; **Wielend, D.** Beyond Artificial Photosynthesis: General Discussion. *Faraday Discuss.* **2019**, *215*, 422–438.

15. Abe, R.; Aitchison, C. M.; Andrei, V.; Beller, M.; Cheung, D.; Creissen, C. E.; De La Peña O'Shea, V. A.; Durrant, J. R.; Grätzel, M.; Hammarström, L.; Haussener, S.; Il In, S.; Kalamaras, E.; Kudo, A.; Kuehnel, M. F.; Kunturu, P. P.; Lai, Y. H.; Lee, C. Y.; Maneiro, M.; Moore, E. E.; Nguyen, H. C.; Paris, A. R.; Pornrungroj, C.; Reek, J. N. H.; Reisner, E.; Schreck, M.; Smith, W. A.; Sen Soo, H.; Sprick, R. S.; Venugopal, A.; Wang, Q.; **Wielend, D.**; Zwijnenburg, M. A. Demonstrator Devices for Artificial Photosynthesis: General Discussion. *Faraday Discuss.* **2019**, *215*, 345–363.

16. Aitchison, C. M.; Andrei, V.; Antón-García, D.; Apfel, U. P.; Badiani, V.; Beller, M.; Bocarsly, A. B.; Bonnet, S.; Brueggeller, P.; Caputo, C. A.; Cassiola, F.; Clausing, S. T.; Cooper, A. I.; Creissen, C. E.; De La Peña O'Shea, V. A.; Domcke, W.; Durrant, J. R.; Grätzel, M.; Hammarström, L.; Hankin, A.; Hatzell, M. C.; Kardas, F.; König, B.; Kuehnel, M. F.; Lamaison, S.; Lin, C. Y.; Maneiro, M.; Minteer, S. D.; Paris, A. R.; Pastor, E.; Pornrungroj, C.; Reek, J. N. H.; Reisner, E.; Roy, S.; Sahm, C.; Shankar, R.; Shaw, W. J.; Shylin, S. I.; Smith, W. A.; Sokol, K.; Sen Soo, H.; Sprick, R. S.; Viertl, W.; Vogel, A.; Wagner, A.; Wakerley, D.; Wang, Q.; **Wielend, D.**; Zwijnenburg, M. A. Synthetic Approaches to Artificial Photosynthesis: General Discussion. *Faraday Discuss.* **2019**, *215*, 242–281.

17. Badiani, V.; Bajada, M.; Beller, M.; Bocarsly, A. B.; Bonnet, S.; Bozal-Ginesta, C.; Brueggeller, P.; Butt, J. N.; Cassiola, F.; Grätzel, M.; Hammarström, L.; Hatzell, M. C.; Jeuken, L. J. C.; König, B.; Kuehnel, M. F.; Lawrence, J.; Lee, C. Y.; Maneiro, M.; Minteer, S. D.; Moore, E. E.; Piper, S. E. H.; Plumeré, N.; Reek, J. N. H.; Reisner, E.; Roy, S.; Shears, J.; Shylin, S. I.; Sen Soo, H.; Wagner, A.; **Wielend, D.**;Zhang, J.; Zwijnenburg, M. A. Biological Approaches to Artificial Photosynthesis: General Discussion. *Faraday Discuss.* **2019**, *215*, 66–83.

18. Kuehnel, M. F.; Creissen, C. E.; Sahm, C. D.; **Wielend, D.**; Schlosser, A.; Orchard, K. L.; Reisner, E. ZnSe Nanorods as Visible-Light Absorbers for Photocatalytic and Photoelectrochemical H_2 Evolution in Water. *Angew. Chemie - Int. Ed.* **2019**, *58*, 5059–5063.

2018

19. **Wielend, D.***; Apaydin, D. H.; Sariciftci, N. S. Anthraquinone Thin-Film Electrodes for Reversible CO_2 Capture and Release. *J. Mater. Chem. A* **2018**, *6*, 15095–15101.